UNIVERSIDAD
NACIONAL
DE COLOMBIA

Magnesium-Based Bioresorbable Cellular Metal as Bone Substitute

Viviana Marcela Posada Pérez

Universidad Nacional de Colombia

Facultad de Minas

Medellín, Colombia

2021

Magnesium-Based Bioresorbable Cellular Metal as Bone Substitute

Metal celular bioabsorbible a base de magnesio como sustituto óseo

Viviana Marcela Posada Pérez

Thesis submitted in partial fulfillment of the requirements for the degree:

Doctora en Ingeniería Mecánica y Mecatrónica

Director:

Ph.D., Juan Fernando Ramírez Patiño

Codirector:

Ph.D., Gloria Patricia Fernández Morales

Line of research:

Biomaterials

Research group:

Grupo de Investigación en Biomecánica e Ingeniería de Rehabilitación (GI-BIR)

Universidad Nacional de Colombia

Facultad de Minas

Medellín, Colombia

2021

A mi madre.

Por enseñarme del amor al conocimiento.

Acknowledgments

I would like to thank my advisors Prof. Juan Fernando Ramírez and Prof. Patricia Fernandez-Morales, who have believed in this project, in my abilities, and created this *espumas* crew. Thanks, especially for the unconditional support and advice. I also want to thank Prof. Jean Paul Allain for his advice and discussion sessions that were an important part of the development of this thesis.

Thanks to *Ministerio de Ciencia Tecnología e Innovación* (MINCIENCIAS) for the financial support (Contract No. 392-2016) and my scholarchip (call 757-2016). Thanks to my home, the *Universidad Nacional de Colombia*, particularly to my research group *Grupo de investigación en biomecánica e ingeniería de rehabilitación* (GIBIR), to Camila Naranjo and Maria Camila Velasquez, who helped me with the volumetric analyses. Thanks to my friend Claudia Sabogal for the company and my friend Sofía Henao for making the time gentler while we were outraged by other world problems, thanks in particular for always being willing to make justice.

I also would like to mention my two-second homes, the *Universidad Pontificia Bolivariana* (UPB) and the *University of Illinois at Urbana-Champaign* (UIUC), where I did much of the experimental development. Thanks to Luisa Fernand Marulanda from UPB for helping me with the manufacture of the ordered foams.

Special thanks to my friends from UIUC, Dra. Ana Fatima Civantos, for her invaluable contributions in the characterization marathon and the biological part of this thesis. Thanks to Camilo Jaramillo for taking the time to help me with the irradiation experiments. Thanks to the *Corporación para Investigaciones Biologicas* (CIB), where we did the in vivo trials, and Prof. Tonny Williams Naranjo, who helped me plan and execute the experiments. Thanks also to his students Juan David and Andrés.

Gracias muy especiales a mi familia, por creer siempre en mí, a mi madre, mi hermano, mi abuela, mis tías y mis primos por sentir un orgullo que me sonroja. Y, finalmente, un agradecimiento con todo mi corazón a mi esposo Jaime Andrés por acompañarme, apoyarme y esperarme con su amor desinteresado: gracias, amor, por creer en mí y ser el lugar en el que siempre quiero quedarme.

Abstract

The design and development of an osteoinductive environment to reconstruct and treat large bone defects is still a challenge. Biodegradable porous metals have been proposed to bridge healthy parts of the tissue when the lesion overcomes the bone self-healing capacity. Mg-based scaffolds promise to assist in this bridging process, providing the mechanical properties and adapting to the new requirements such as weight and geometry as the healing time advances. Moreover, the porous condition guides the tissue and blood vessels' growth, and the release of Mg^{2+} accelerates the healing process. However, the Mg support is limited by its rapid degradation, which hinders the appropriate integration with the tissue. Additionally, the degradation is again accelerated in the porous condition, and the complex geometry limits the application of current protection methods.

The present thesis aims to create an open-porous Mg-based scaffold for bone tissue engineering, focused on enhanced corrosion resistance and biocompatibility. Porous Mg materials were then fabricated in various geometrical configurations: random pores, truncated octahedron, and diamond unit cells. The control over the degradation of the material was achieved by modifying the first nanometers of the surface, avoiding changes in the architecture of the structures, and preserving the bulk properties of the material such as open porosity and lightweight.

The nanometric modification was created via low-energy Ar^+ irradiation, which developed well-ordered nanostructures on the surface, followed by Al-rich nanoclusters' accumulation. The creation of the Al-rich nanoclusters accelerated the passivation kinetics of the porous Mg, enhancing the apatite nucleation ability when immersing the materials in physiological fluids. Moreover, the apatite formation ability was conditioned to the concentration of Al on the near-surface, which offered surfaces for different biological purposes by tailoring the CaP ratio.

Superior properties regarding in vitro biodegradation and biocompatibility were obtained on hydroxylapatite tailored surfaces, such as decreased weight loss, conservation of the strut size during the immersion time, and decreased H_2 and Mg^{2+} release. Furthermore, higher cell density was adhered to and proliferated on the DPNS surfaces indicating outstanding biocompatibility. The increase in biocompatibility was also supported by the formation of focal adhesion points and increased osteogenic potential, and the immune response modulation of the cells seeded on the modified surfaces. Finally, the material was tested in vivo, demonstrating steady corrosion and improved porous structure stability after 8 weeks of implantation in Wistar rats.

Keywords: Magnesium, degradation-controlled, biodegradable implant, porous magnesium, ion-enhanced Gibbsian segregation, Directed plasma nanosynthesis, nanostructured surface.

Resumen

El diseño y desarrollo de un entorno osteoinductivo para reconstruir y tratar grandes defectos óseos sigue siendo un desafío. Los metales porosos biodegradables se han propuesto para conectar partes sanas del tejido cuando le lesión supera la capacidad autoreparadora del hueso. Los *scaffolds* de Mg prometen ayudar en este proceso de soporte, proporcionando las propiedades mecánicas y adaptándose a los nuevos requisitos, como el peso y la geometría, a medida que avanza el tiempo de curación. Además, la condición porosa guiaría el crecimiento del tejido y de los vasos sanguíneos, y la liberación de Mg^{2+} aceleraría el proceso de curación. Sin embargo, las funciones de soporte del Mg están limitadas por su rápida degradación, lo que dificulta la integración con el tejido. Además, el proceso de corrosión se acelera con la condición de porosidad, y la geometría compleja limita la aplicación de los métodos de protección actuales.

La presente tesis tiene como objetivo crear un andamio basado en Mg de poros abiertos para reemplazo de hueso, centrado en una mayor resistencia a la corrosión y biocompatibilidad. Para este propósito, se fabricaron materiales porosos de Mg en varias configuraciones geométricas: poros aleatorios, octaedro truncado y celdas unitarias de diamante. El control sobre la degradación del material se logró modificando los primeros nanómetros de la superficie, para evitar transformaciones en la arquitectura del material y conservar de propiedades volumétricas como la porosidad abierta y el peso ligero.

La modificación nanométrica se creó mediante irradiación de baja energía con Ar^{+}, lo que desarrolló nanoestructuras ordenadas en la superficie, seguidas de la acumulación de nanoclusters ricos en Al. La creación de nanoclusters ricos en Al aceleró la cinética de pasivación del *scaffold* de Mg, mejorando su capacidad de nucleación de apatita al sumergir los materiales en fluidos fisiológicos. Además, dicha capacidad de formación de apatita estaba condicionada a la concentración de Al en la superficie, lo que ofrece superficies para diferentes propósitos biológicos al adaptar la proporción de CaP.

Se obtuvieron propiedades mejoradas en cuanto a biodegradación y biocompatibilidad *in vitro* en superficies irradiadas que formaron una relación Ca:P similar a la hidroxiapatita. Estas propiedades incluyen menor pérdida de peso, conservación del tamaño del *strut* durante el tiempo de inmersión y disminución de la liberación de H_2 y Mg^{2+}. Además, se adhirió y proliferó una mayor densidad celular en las superficies de DPNS, lo que indica una mejora sobresaliente también en la biocompatibilidad, que, además, está respaldada por la formación de puntos de adhesión focales y el aumento del potencial osteogénico y la modulación de la respuesta inmune de las células ahderidas a la superficie modificada de Mg. Finalmente, el material se evaluó in vivo, demostrando una corrosión constante y una estabilidad mejorada de la estructura porosa después de 8 semanas de implantación en ratas Wistar.

Palabras clave: Magnesio, implante biodegradable, controlado por degradación, magnesio poroso, segregación gibbsiana mejorada por iones, nanosíntesis de plasma directo, superficie nanostructurada.

Content

List of figures

List of tables

Introduction

Problem statement

Large size defects are lesions that overcome the self-healing ability of the bone. These critical size gaps are secondary to osteolytic deformities, traumatic bone loss, tumor resection, and infections [1,2]. Traditional treatments consist of natural grafting, which uses bone from somewhere else (self-donation or a cadaveric donor) to bridge the healthy tissue [2]. However, about 70% of the bone-related surgeries in the world require bone substitutions [3], which complicates the supply of the population demand. Other limitations include the shortage of natural bone graft [4,5] and local morbidity and infections associated with autologous tissue extraction [6]. Moreover, the requirement for bone grafting has increased due to the aging of the population and the advances in spine surgery [7,8].

Tissue engineering approaches seek to replicate (or improve) the osseoregenerative profile of the autologous graft. Porous complexes are expected to bridge the healthy parts of the tissue and guide the proper growth, thus providing a better load transfer, vascularization, and nutrient and metabolite interchange. Moreover, bone substitutes should safely degrade in vivo to provide space for new bone tissue and blood vessel growth [9]. Mg-based scaffolds promise to assist in bone tissue growth by providing mechanical properties and, as the healing time advances, adapting themselves to the new requirements, such as weight and geometry. This material has been widely proposed as an orthopedic implant because it avoids second removal surgeries and its complications (i.e., infections and new fractures). Mg devices also deliver Mg^{2+} during degradation. The accumulation of Mg^{2+} at the fracture site enhances bone tissue regeneration by promoting osteogenic cell spreading and proliferation [10–12]. The modulation of macrophage polarization through the release of Mg^{2+} ions has been suggested as another instrument of the osteogenic effect of Mg implants since Mg^{2+} mediates the immune response by decreasing proinflammatory cytokine secretion [13] [14].

Despite the advantages of Mg-based scaffolds, several challenges remain regarding the clinical implementation of this material. Mg by itself cannot efficiently integrate with the host tissue because of its high corrosion rate [15]. Moreover, in porous conditions, the corrosion rate is accelerated due to the increase in the exposed area [16] and the uneven distribution of surface defects [17]. Coatings have been proposed as the most common strategies to decelerate and control porous Mg corrosion rates [18,19]. The reported coatings include Ca-phosphate (CaP) [20] deposited through various methods, including micro-arc oxidation (MAO) [18]. Polymeric and hybrid coatings have also been reported for porous Mg [21,22]. These coatings have enhanced the mechanical integrity, corrosion resistance, and bioactivity of porous Mg implants. However, the surface modification of porous Mg frequently results in altering the scaffold geometry, such as clogging of the inner pores, reducing the pore size, or decreasing the strut thickness. Small pores can affect the bioactivity of materials by interfering with nutrient-interchange mechanisms of the body [23].In comparison, reduced struts compromise the mechanical stability of the device. Moreover, in complex structures, the surface coatings are hindered by their limited adhesive properties. Thus, they often suffer from delamination, causing leaching and local inflammation [24,25]. Additionally, the lightweight properties of Mg-based foams can be compromised if the surface is covered by a dense layer [26], resulting in surface cracking via strain relief and delamination.

Observations in nonporous Mg have demonstrated the efficiency of Al-alloying in the corrosion protection, especially when there is Al segregation on the near-surface [27–31]. The development of an Al-enriched layer on the surface provides better protection against corrosion than typical Mg corrosion products (i.e., Mg (OH)s) [32,33]. However, this passivation ability is conditioned to the Mg-Al ratio. A minor increase in Al content can reduce the degradation rate of Mg-Al systems [34]. Therefore, strategies for driving and controlling the Al supply from the interior of the alloy to the near-surface are required. Reichel et al. [35] modeled and experimentally confirmed the compositional changes of MgAl binary alloys under Ar^+ bombardment as a function of the energy of the incident Ar^+. They described a preferential sputtering of Mg and preferential segregation of Al as a consequence of the bombardment-enhanced Gibbsian segregation caused by the intent of the system to reduce its surface free energy.

From this basis, in the present thesis, a multi-functional interface for bone tissue engineering is designed based on developing a suitable porous Mg matrix and the evolution of well-ordered nanostructures and preferential Al segregation along the foam outer surface driven by low-energy Ar^+ irradiation. Surface modification is achieved via low-energy directed plasma nanosynthesis (DPNS) introduced on Mg-based porous implants. DPNS is an atomic scale nanomanufacturing process that induces compositional and structural changes to the targeted solids. It is then hypothesized that DPNS causes an Al enrichment in the near-surface that improves the apatite formation ability of the Mg implants. The transformation of the surface into CaP phases is finely tuned by minor changes in the DPNS parameters (energy, fluence, and incidence angle) to yield HA interfaces enhancing the osteoconductive properties of the material and protecting the implant from fast corrosion.

Thesis goal

To develop an open-porous Mg-based scaffold for bone tissue engineering, focused on enhanced corrosion resistance and biocompatibility.

Specific goals

- To design a surface modification method that works in conjunction with the architecture of Mg implants to improve the corrosion resistance and the mechanical and biocompatibility properties.
- To elucidate the synergistic effect of the surface modification method and the surrounding media on the corrosion behavior of porous Mg.
- To determine the biocorrosion and biocompatibility performance of the finally obtained foam, in vivo and in vitro.

Research Overview

Chapter 1 reports a theoretical framework that describes the current understanding of the structural, biomechanical, and physicochemical properties of natural bone. Remodeling and fracture healing processes, including critical size bone defects and the tissue engineering approaches to assist their healing, are also described to provide useful insights to support the development of this thesis.

Chapter 2 reviews the current approaches to protecting porous Mg from rapid corrosion. Mg's general corrosion process is described, and two derived mechanisms for the corrosion behavior of porous Mg are proposed based on the literature reports. The advantages and disadvantages of current surface methods to protect Mg foams are also described and discussed.

Chapter 3 analyzes the mechanism of porous Mg surface modification via low-energy Ar^+ irradiation. The chapter begins by studying the chemical conversion of the surface, changing the irradiation parameters. Two energies (400 eV and 700 eV), two fluences (1×10^{17} cm^{-2} and 1×10^{18} cm^{-2}) and normal and off-normal incidence, and the combinations of them, are evaluated via in situ X-ray photoelectron spectroscopy (XPS) and ex-situ focused ion-beam (FIB), and grazing incidence X-ray diffraction (GIXRD). The nanostructures formation is also observed via scanning electron microscopy (SEM). In situ XPS and FIB results have shown that energies of ~400–700 eV can control surface topography and composition, which, in turn, influences the foam's corrosion mechanism via the progressive accumulation of Al. Studies examine the H_2 evolution and pH levels of irradiated and non-irradiated Mg-foam materials and correlate their corrosion rates to DPNS parameters. Samples are immersed in Dulbecco's modified eagle media (DMEM), and a synergistic reaction is found in which the irradiated samples enhance the formation of CaP phases to CaP ratios close to the hydroxylapatite (HA).

Chapter 4 Studies the bioactivity of the Mg-based scaffolds treated with low-energy Ar^+ ions. The porous materials were seeded with human bone marrow mesenchymal stem cells (hBM-MSC) to test adhesion and proliferation and J774A.1 macrophages to test immune response. MC3T3 preosteoblasts were seeded in the material's extracts to test the osteoblastic potential of the released Mg^{2+}. The limitations of the in vitro testing of Mg regarding the static conditions of the culture and the difficulties in imaging the cells are described and alternatives are proposed. The DPNS CaP-rich phases significantly promoted cell spread and focal adhesion points formation in hBM-MSC directly seeded on the DPNS-modified surfaces.

Furthermore, the ALP activity of DPNS samples (9,28 $U \times L^{-1}$) was significantly higher than the ALP activity of cells seeded on control wells and pre-treated samples. The regulation of TNF- α from J774A.1 macrophages is also observed. This material also releases active Mg^{2+} ions, which promote the relative fold expression of OPN, ALP, and RunX2 osteogenic related genes.

Chapter 5 Uniform Mg-based cylindrical grids, populated with diamond and truncated octahedron unit cells, were fabricated via combined processes: 3D printing and infiltration casting. The porosity was 83.4 % for truncated octahedron and 77.9 % for the diamond lattice structure. The samples presented similar alloy composition (Mg bal., 2.02 % Al, 0.24 % Mn, and 1.07 % Zn.) and microstructure. Both scaffolds' Young modulus (1.6 GPa for the diamond and 0.9 GPa for the diamond) was between the range of the cancellous bone (0.3–5 GPa).

After DPNS, the samples developed nanostructures followed by an accumulation of Al on the surface, dependent on the irradiation parameters and the local conditions of the lattice structures. When immersed in DMEM, the DPNS treatment enhanced the apatite nucleation ability of the surfaces, which, in turn, enhanced cell attachment and proliferation. Moreover, fold expression of osteogenic related genes ALP, OPN, and Runx2 of MC3T3 cells cultured in the samples extracts demonstrated a significant increase in ALP fold expression ($p<0.05$) for DPNS modification in the truncated octahedral cell geometry and a significant increase in fold expression of Runx2 in the diamond cell geometry. The evolution of the structures during immersion was evaluated via micro-CT. Moreover, the DPNS treatment significantly decreased the truncated octahedron structures' corrosion rate, and the Mg ions release was decreased up to 60% after seven days of immersion.

Chapter 6 presents the in vivo testing of DPNS-samples and controls. Wistar rats are uses as in vivo model, and the scaffolds are implanted under the rat's back skin. The controls are entirely dissolved after 4 weeks of implantation; then, the samples are no retrieved to further chemical and morphological evaluation. On the contrary, DPNS samples are tested during 1, 4, and 8 weeks of implantation to describe the in vivo corrosion mechanism. After 1 week, an H_2 gas cavity forms around the implant; the gas cavity safely dissolves, and after 8 weeks, healthy tissue is observed in the implant location. The in the vivo corrosion rate of the DPNS structures is constant during the time; however, the thickness of the struts shows significant differences between weeks 1 and 8. These results describe an in vivo biocompatible material and significantly improved corrosion resistance after the DPNS modification.

Chapter 7 summarizes the current developments and proposes future research directions.

1. Tissue-engineered bone replacements

The ideal biomimetic scaffold's design requires a full understanding of the structural, biomechanical, and physicochemical properties of natural bone. The comprehensive study of these biological and structural events provides useful insights into superior implants to produce engineered responses in the living targets. Hence, this theoretical framework chapter pretends to describe the current understanding of bone architecture, composition, and mechanical properties. This knowledge is then related to bone remodeling and fractures healing processes focusing on critical size bone defects. Tissue-engineered strategies to support critical-sized bone healing are also described, considering the characteristics of porous tissue engineering materials.

1.1 The demand for artificial bone replacements

About 70 % of the 20 million orthopedic surgeries around the world need bone substitutions. Hence, bone implants' global market capacity has increased with a compound annual growth rate (CAGR) of 8.2 % [36]. This market was expected to witness a CAGR of 4.7 % for the period 2019 to 2023. The aging of the population and the consequently increased spinal fusion surgeries are the principal growth drivers [7,8]. Information on the impact of fractures and bone substitutions in the Latin American economy is limited. However, Latin American countries are crossing a demographic transition, and one of the consequences is the aging of the population [37]. Aziziyeh et al. [38] estimated 840,000 osteoporosis-related fractures in adults aged 50 to 89, with an associated annual cost of ~1.17 billion USD for Brazil, Mexico, Colombia, and Argentina.

In Colombia, 10,174 osteomuscular donor alerts were activated in 2018. 69.8 % of those alerts were discarded due to breach of tissue donation protocol, i.e., the donor age (3,661) and cadaver transportation time (1,351). Other alerts were discarded due to diagnostic contraindications and positive tests for infectious diseases (20.1 %). Additionally, no specific causes of rejection reached 6.7 %. Therefore, it was a total of 256 cadaveric donors of bone tissue, which represent a total of 15,196 bone grafts. There were also 881 bone grafts obtained from living donors submitted to osteoarticular surgeries. From those, 242 were contraindicated for several causes, including infectious diseases and suspicious diagnosis [39]. There are also post-operatory outcomes that include immune rejection and infections [40].

The development of artificial bones is a flourishing market. The above scenarios revealed the difficulties in supplying the population demands, including the shortage of natural bone graft. Furthermore, the restrictive measures in responding to the COVID-19 pandemic have complicated the supply channels and deprioritized some orthopedic-related surgeries [41]. The delay in the supply of components and materials [42] has highlighted the necessity of developing distributed manufacturing capabilities. Disruptions on health care to mitigate the COVID-19 crisis spotlighted the supply chain of devices that depend on centralized manufactures. Then, the discussion of medical device manufacturing is recently having a paradigm change in terms of cost-benefit, risk, and mitigation. The development and production of bioresorbable devices are taking a new emerging direction that should consider local manufacturing and the use of materials that simplify clinical work (i.e., biodegradable metals that reduce the number of surgical interventions).

1.2 The bone architecture and chemistry

The human bone tissue comprises around 10% collagen, 70% bone mineral, 20% water, and other organic materials in balance, such as proteins, polysaccharides, and lipids. The primary components of the bone are the mineralized collagen fibers known as lamellae. The elemental composition of the bone mineral is hydroxyapatite (HA), with a Ca: P ratio of 1.67 and a chemical formula $Ca_{10}(PO_4)_6(OH)_2$. However, it is common to find bone HA with ratios varying from 1.37 to 1.87 [5]. The variation in the HA ratio is usually attributed to the substitution of ions [43]. Hence, besides being the central supporting system in the human body, the bone tissue regulates the Ca and P blood levels [44].

Macroscopically, the skeleton consists of long, flat, irregular, and sesamoid bones [45]. Typically, long bones are divided into their internal structures: trabecular, compact bone, periosteum, endosteum, and cartilage [46]. Compact bone is denser and more static than the trabecular, and its

Young's modulus ranges from 3.3 GPa to 18 GPa. At smaller scales, cortical bone consists, from larger to smaller, of osteons, collagen fibers, and collagen molecules. The cortical bone's basic units are the Haversian canals located in each osteon center and are in charge of the nutrition and metabolic transport structure within the bone; they house the nerves and blood vessels. Haversian canals are communicated by a canaliculi system, lacunae, and Volkmann's canals, interconnected arrangements inside osteons; they also transport the metabolic substances [47] **(Figure 1-1)**.

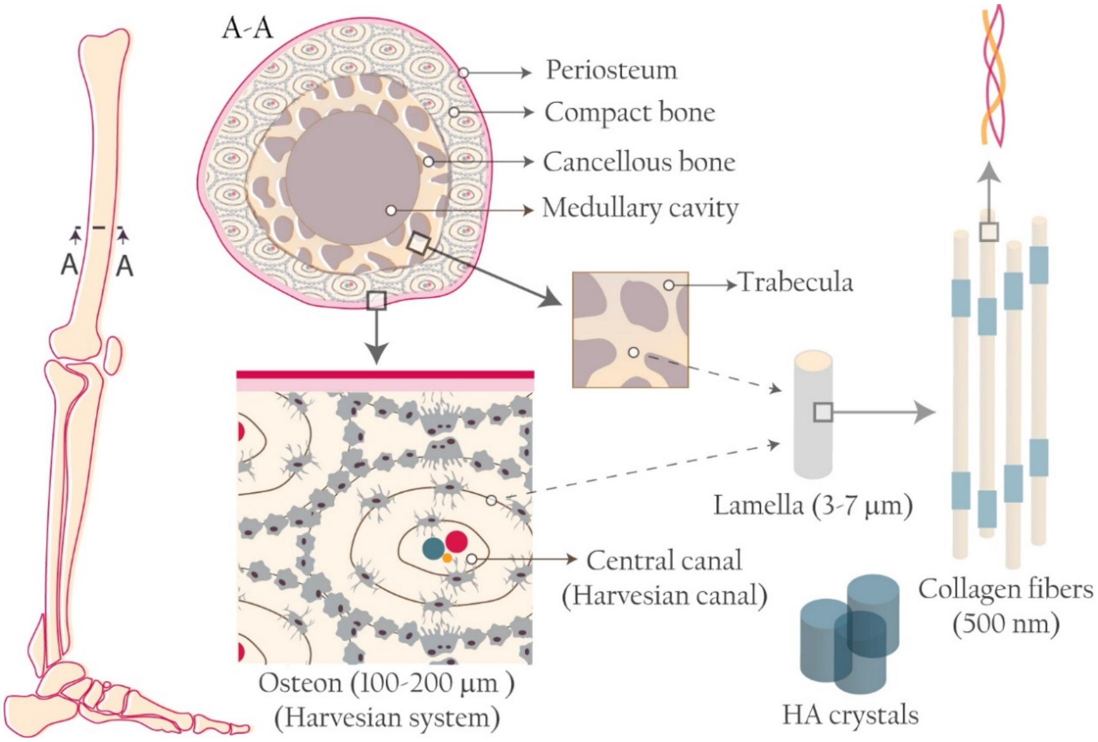

Figure 1-1 Human bone architecture and composition. The schematic representation of a long bone's cross-section shows the different layers of the structure starting at the periosteum, followed by the compact and cancellous bone, and ended at the medullary cavity. The hierarchical structure continues with the trabecula and the osteons as the cancellous and compact bone base units. Both base units are composed of the lamella formed with collagen fibers and hydroxyapatite crystals.

Trabecular or spongy-like bone is more active and is the center of the hemopoiesis and homeostatic functions. Since it can adopt particular alignments to deal with sudden stress, trabecular bone also has a supporting role in compression type loadings such as vertebras or joints. The typical Young's modulus of the cancellous bone ranges from 0.1 to 5 GPa [5]. At a smaller scale, trabecular bone consists of a porous structure with intersecting plates that are aligned with the mechanical stress. In the lattice space resides the bone marrow [48].

Contrary to the cortical bone, the lamellae in the trabecular bone are organized in parallel sheets that form the matrix. There is also a canaliculi communication system but without the Haversian canals [45]. Cartilage and periosteum are connective tissues; cartilage is a smooth surface that allows joint movement in the presence of synovial fluid, and periosteum covers the bone's surface. Endosteum is a thin layer present in the medullary cavity [5].

1.2.1 Bone healing process

Cells orchestration

After a tissue injury, a cascade of inflammatory processes is orchestrated to the wound site. There is an initial agglomeration of immune cells (platelets, neutrophils, and macrophages) in response to the vascular disruption. These cells cause an inflammation that forms a hematoma that further acts as a template for bone growth [49]. The macrophages' modulation in the first state is an important event in fracture healing. These cells release signals that regulate differentiation. Macrophages activation is classified into two groups: M1, the group of macrophages activated in the acute phase (immediately after the injury), in the presence of inflammatory cytokines. Macrophages with M1 phenotype further produce IL-1, IL-6, TNF-α, MCP-1, and MIP-1 to preserve cells' recruitment [49]. M2 phenotype activates in the subacute phase (when inflammation begins to subside) to initiate an anti-inflammatory response. M2 phenotype is associated with tissue regeneration; hence, macrophages secrete repairing signals such as IL-10, TGF-β, BMP-2, and VEGF [49,50].

Bone callus formation and remodeling phase

It has been proposed that mesenchymal cells “listen” to the macrophage’s signals. They also produce an anti-inflammatory response to the initial inflammatory cytokines. Donrronsoro et al. [51] described the mesenchymal cells' activation pathway after stimulation with TNF-α, a cytokine involved in the systemic inflammatory process (**Figure 1-2**). Mesenchymal cells can differentiate themselves into chondrocytes and osteoblasts, and they express genes such as Runx2, Sox9, and Col9α1 when populating the fracture site. This mix of cells forms a callus that bridges the bone's healthy fragments with an avascular tissue that stabilizes the fracture space for further vascularization. Then, chondrocytes hypertrophy and start secreting factors such as VEGF that induce new blood vessel formation [52]. This callus starts with a cartilage matrix and then turns into a hard callus that is further replaced by a matrix of collagen fibers that form the bone.

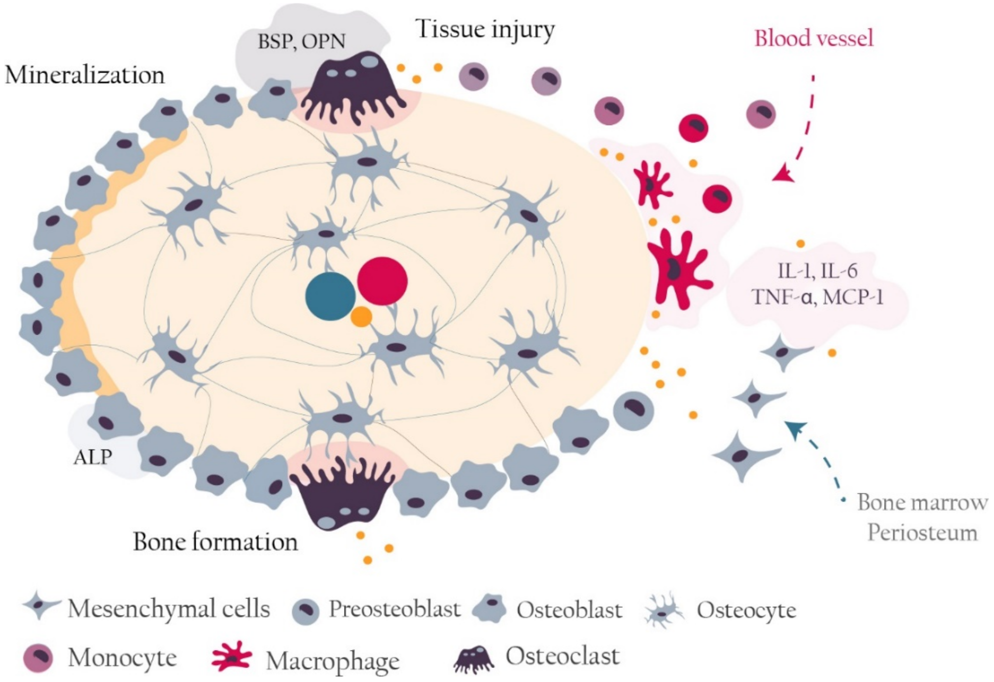

Figure 1-2. Schematic representation of the bone remodeling units. In the injury place, different inputs start the orchestration of immune cells and trigger the osteoclast differentiation. Osteoclasts resorb the bone, produce sialoprotein (BSP) and osteopontin (OPN) sensed by the osteoblasts. Osteoblasts mineralize the matrix and produce alkaline phosphatase (ALP) to support the mineralization process. Osteoblasts are finally embedded in the mineralized matrix in the form of osteocytes.

As shown in **Figure 1-2**, the bone matrix deposition process is driven by the synchronicity of resorption and remodeling bone cells: osteoclasts, and osteoblast, respectively [49]. Meanwhile, macrophages moderate communication and maintain the balance of the healing process. Osteoclasts are specialized in bone phagocytosis. They resorb the callus and build the tunnels required for vascularization. After osteoclasts are activated, they create a compartment known as a resorption pit and consists of a border that forms a seal with the mineralized surface. Hydrogen ions are pumped into the resorption pit to dissolve the hydroxyapatite crystals, and lysosomal enzymes digest the proteinaceous materials. While osteoclasts resorb the bone, they secrete sialoprotein (BSP) and osteopontin (OPN) sensed by the local osteoblasts [49]. Osteoblasts produce complex organic matrix within the resorption compartment [53]. They also generate alkaline phosphatase (ALP) that supports the mineralization of the osteoid (the collagen-rich substance of the bone [54]) and is commonly used as an early osteogenic marker [55]. Finally, osteoblasts are embedded as osteocytes into the mineralized matrix [56].

The overall function of the osteocytes is still not well understood [56,57]. However, Choy et al. [57] reviewed emerging evidence and described that osteocytes play a regulatory function in callus formation, mineralization, and callus remodeling. Once osteocytes are "buried" within the bone matrix, they act as "masterminds" that coordinate the osteoclasts and osteoblasts activities in response to the physical and biochemical signals. They also release OPN for the recruitment of multiple cell types [58].

1.2.2 Mechanical aspects of fracture healing

The overall size and shape of bone are genetically defined across the species. However, since the bone cells, as executors of the bone adaptation, are sensitive to mechanical stimulus, the mechanical loadings naturally optimize bone configuration in an individual [58]. According to its arrangement **(see 1.1)**, bone tissue can be compared to a fiber-reinforced composite on the microscopic scale, where mineral crystal platelets are embedded within the collagen matrix. This material is highly anisotropic along the longitudinal direction due to the lamellae's structural alignment [59].

The uniaxial stress-strain curve in compression of the cancellous bone behaves like the typical compression curve of metallic foams or cellular solids [60]. Three regimes of behavior are described for these materials **(Figure 1-3)**: linear elasticity in the small strain range, as the stress continues to increase, there is a non-linear response when the trabecular struts start to collapse; then, there is an anelastic region until the trabecular structures contact others and the stress abruptly increases again [5,59].

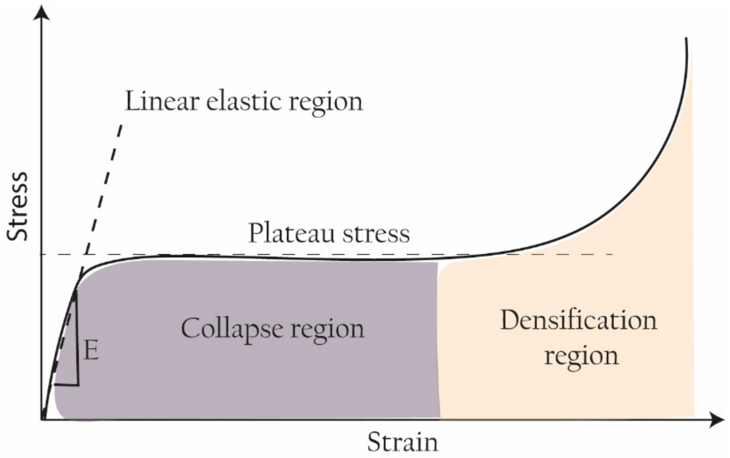

Figure 1-3. Typical compression behavior of porous metals. There is an initial linear-elastic region characterized by an early increase in stress. This initial high slope is associated with the stiffness of the sample. Due to the pores' collapse, there appears a wide stress plateau known as the collapse region. Finally, when the cells contact each other, the stress abruptly increases again in the densification region. Adapted from [61].

The mechanical properties of cancellous bone are also relative to the porosity, which varies with the collagen content and the age of the patient [5]. Then, the mechanical behavior of the bone has been widely explored and described as a function of its relative density [62–64]. Leng et al. [64] investigated the mechanical properties of demineralized cortical bone from the femur's anterior region at three different life stages, from 20 to 87 years old (where the sample size was 5). The study confirmed that the elastic modulus of the collagen phase depends on age and orientation; conversely, the maximum sustainable deformation was independent of age and orientation. The relationship between yield strain and apparent density in cancellous bone is also supported by Gibson and Ashby`s cellular solids theory [65].

The mineral phase has different mechanical properties than the collagen phase and influences bone's mechanical properties [66]. Keller [62] studied the mathematical dependency of adult bone on apparent density and mineral content. In the study, 496 cubical specimens of the human vertebral bone (ages 70, 77, 84 yr) and the femoral bone (46, 67 yr) were analyzed. As a result, the compressive mechanical properties showed mathematical dependency on the composition, which diverged between the vertebral and femoral specimens. Fratzl-Zelman et al. [66] showed that lower Ca content in the femoral neck is related to osteoporotic hip fractures. Hence, they suggest that fragility fractures are also related to changes in bone mineral properties.

Understanding the mechanical environment is crucial in the healing of the fracture. The mechanical properties of bone vary with the location and are influenced by different interfaces, i.e., trabeculae and interstitial liquid [67]. According to the mechanical environment, bone tissue self-repair is divided into primary and secondary healing. The primary or direct process occurs when the fracture area is reduced by internal fixation, ensuring rigidity and interfragmentary compression. During this process, the bone remodeling (see section **1.2.1**) avoids the callus formation. Hence, remodeling units restore Haversian systems [68] (**Figure 1-2**). On the contrary, the secondary process, the most common form of bone regeneration in clinical practice, highlights the importance of the hematoma formation and refers to the callus' intramembranous and endochondral ossification [69].

1.2.3 Large size bone defects

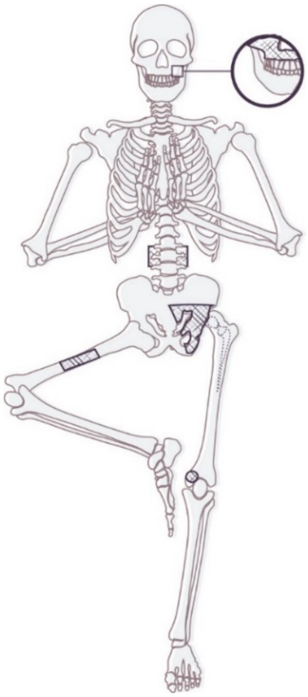

Figure 1-4. Critical size lesions that require bone grafting. From top to bottom: Mandibular segment, spine fusion, osteolytic defect, critical size bone loss, and joint arthrodesis.

The self-regulated process can repair small-size or well-stabilized fractures. However, when defects overcome the self-healing ability of the bone, improved strategies are required. Critical-sized bone defects refer to those fractures that will not spontaneously heal during the patient's lifetime [1,70]. Critical-size lesions that are secondary to osteolytic bone deformities due to stress shielding (when the implanted device overtakes the tissue's mechanical capacity), traumatic bone loss, bone resection in dental processes, tumor resection, infection, or developmental deformities [1,2] (**Figure 1-4**).

There are distinct approaches regarding the definition and treatment of critical size bone defects. Operative treatment strategies consist of bone grafting, which uses bone from somewhere else to repair the tissue. Other processes, such as spine fusion, also require grafting to bridge healthy tissue [2]. The grafting possibilities include autographs (autologous bone from donor site), allographs (bone from one person transplanted to another), and artificial and engineered strategies [5]. Grafting has been widely and comprehensively described, including the respective clinical outcomes [4,5].

Autograft continues to be the gold standard since the aim is to preserve the bone's natural properties; however, autograft possibilities are limited by the patient's self-donor capacity due to tissue availability and morbidity in the donor site [6]. Hence, the next sections focus on synthetic bone replacements conceived as tissue engineering strategies.

1.3 Artificial bone replacements

Tissue engineering consists of "*an interdisciplinary field that applies the principles of engineering and the life sciences toward the development of biological substitutes that restore, maintain, or improve tissue function* " [71]. In critical size bone defects, the tissue engineering approach intends to reconstruct the damaged bone. Despite the gold target of bone reconstruction is the autograph, other porous strategies have been developed to improve or mimic the autograph function. Numerous 3D materials have been designed to provide an environment for tissue to grow [5].

The porous bone replacement design should consider the understanding of the bone regeneration process and let the natural bone self-repair ability to continue its work. Thus, it is important to introduce the term "bioinspired," which, in the present work, describes designs conceived to intentionally produce a biological response on a living target instead of a structural or dimensional copy of a natural form. With this in mind, bone tissue engineering methods have two major requirements in common: first, biocompatibility, and second, a physical structure to bridge the damaged region. Other general desirable properties are open porosity, structural integrity during the regeneration process, radiolucency, and osteoconduction [72].

1.3.1 Scaffold design

The nature of the bone components dictates pore characteristics. The osteoblasts that lead the bone mineralization process during healing are cells around 10-50 µm in size; hence, they require a large area to operate. A pore size higher than 100 µm allows the osteoblasts colonization and favors macrophages infiltration. Macrophages also need enough space to eliminate bacteria and orchestrate the bone-forming cells. Smaller pore sizes are associated with no desirable fibrous tissue formation [73].

Several authors claim pore sizes between 100 µm to 1200 µm as the best platforms for mineralization and tissue formation. Relevant reports on porous scaffolds for bone replacement are summarized in **Figure 1-5**. The literature search was performed on PubMed and Scopus databases (last access 17/10/

2020) with the keywords *porous* AND *bone* AND *implant*. Works that evaluated the influence of pore size on the biological outcome were included. The pore sizes that provided the best results in the respective report are shown in **Figure 1-5**. The porosity, pore shape, and cell line or animal model in which the materials were tested are also summarized to allow comparisons. The largest pore sizes are seen in the hard metals, with 600 – 650 µm being the most popular. In the biodegradable metal scaffolds, there are mostly random pores in the range of 200 to 800 µm. Smaller pores are seen in natural polymers, ceramics, and composites. Pores between 200 to 800 µm had the best implant/tissue interactions in Sprague-Dawley rats and rabbits.

The conflicting results highlight the necessity for a balance between optimal cell attachment and proliferation. Then, the sustained bone ingrowth is typically associated with both pore interconnection site and pore extension. In the review of Hing [74] about the influence of pore and chemistry on bioceramic scaffolds, it was established that the pore size is not the critical parameter for bone ingrowth but the pore interconnection site. The critical pore interconnection size is 50 µm (reported on hydroxyapatite or β-TCP). Meanwhile, Xiao et al. [75] reported an interconnection size of 150 µm that improved vascularization in β-TCP implants. The pore interconnection's importance is not unexpected, considering the bone anatomy and the bone remodeling process (**see 1.1** and **1.1.1**), where the blood supply and the vascular network play a critical role. There is additional evidence that vascularization constructs require at least 300 µm pores [76].

Angiogenesis, or blood vessel formation, precedes osteogenesis. This process requires high cell density and local oxygenation for vasculogenic cells to differentiate [73]. Then, angiogenesis is highly sensitive to the pore size and interconnectivity [77]. Other variables, such as permeability, must enter into the equation. In addition to pore size, permeability depends on porosity and interconnectivity. The increased interconnectivity overcame pore size restriction since the cells can spread throughout the scaffold's length. Thus, higher permeability inhibits fibrous tissue formation, while restricted permeability and pore size force the cells to differentiate instead of proliferating [73].

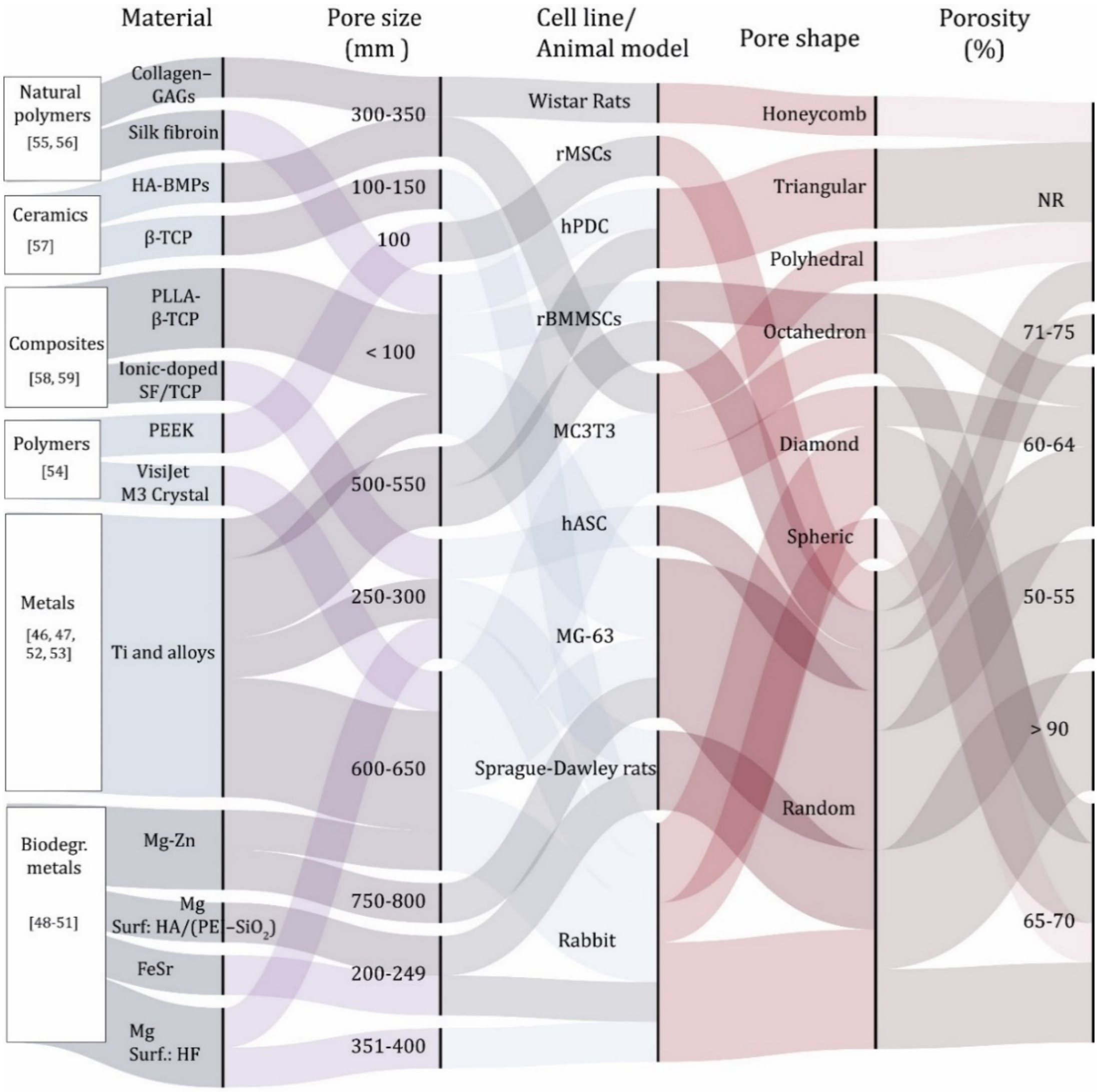

Figure 1-5 Alluvial plot of pore characteristics of different materials for orthopedic applications. The figure represents weighted flows among nodes. From left to right, data regroup on each node to represent the literature tendencies regarding material, pore size, cell line/animal model, pore shape, and porosity. The information was extracted from the following references: [78–91]. NR corresponds to non-reported data and Surf. corresponds to a surface modification of the respective material. The curves were plotted using Rawgraph [92].

1.3.2 Imitating bone structure

Predesigning a porous architecture for bone tissue engineering is attractive from diverse perspectives: first, the mechanical characteristics of the microenvironment for tissue integration are known and adjusted a priori; second, the structure can be designed given the degradation behavior of the base material; finally, the surface area can be considered taking into account the cell metabolism aspects. Cellular metals are classified into porous structures with random pores distribution and structures with periodic unit repetition.

The structures based on the repetition of equal unit cells are known as lattice or topologically ordered systems. The architectural lattice parameters are classified as topology (connectivity of the unit cells) and geometry (pore size and strut thickness) [93]. A lattice structure array guarantees a fully interconnected porous structure with predictable mechanical properties. It has been reported that structures colonized by the repetition of unit cells present superior mechanical properties compared to their random analogues at similar volume fractions [94].

Wettergreen et al. [67,95,96] reported a library of primitive bone unit cells to create a collage in a bone scaffold. The unit cells were imitative of the trabecular bone entities and were divided into two systems: analytically derived polyhedral and optimized abstract forms identified from tissue patterns (**Figure 1-6**). The units were combined to obtain 80% porosity (the volumetric porosity of the trabecular bone) and customizable mechanical properties. Likewise, several scaffold libraries for bone tissue engineering have been reported. Chua et al. [97,98] analyzed polyhedral shapes made of polygons whose segments were edges joined in vertices. The geometries of 11 polyhedral shapes were selected after their elimination criteria: structures with significant in-between gaps and structures with many edges (**Figure 1-6**). Chantarapanich et al. [99] reported 119 polyhedrons' evaluation presented in [100]; however, since not all polyhedrons were appropriate for bone tissue engineering, they only considered those suitable for additive manufacturing and with a surface area that allowed the combination of forms avoiding enclosed shapes.

As a result, truncated octahedron was considered in common as appropriate for bone tissue engineering [59,96,98,99,101]. This Archimedean solid can be obtained by truncating the corners of an octahedron. This cell has the lowest surface energy among single polyhedrons cells [59] and comprises 14 phases, eight regular hexagons, and six squares. Since trabecular bone (low-density) resembles an asymmetric network of rods, and the high-density trabecular bone resembles a network of platelets with perforations through the plates [60,102], several authors, including the author of this thesis [103], have reported the truncated octahedron, also known as *Kelvin cell*, as a local description of the trabecular bone [102,104,105]. Zysset et al. [105] demonstrated that the kelvin cell reproduces the trabecular bone's mechanical behavior for an extended sequence of volume fractions and anisotropy.

The diamond unit cell has also been proposed as an optimization strategy to promote osteogenesis, mostly in titanium implants [79,84,106,107]. This unit cell consists of 16 struts of equal length connected through 14 vertices with an angle of 109.5° every two struts [84]. Reznikov et al. [108] exanimated the geometric aspects of the cancellous bone via micro-CT scans and measured the inter-trabecular angles as a topological descriptor of cancellous bone. They reported a mean inter-trabecular angle of 120° in nodes with three connecting trabeculae and 109° in nodes with four connecting trabeculae.

The additive manufacturing process advances have introduced triply periodic minimal surfaces (TPMS) as candidates to produce biomorphic scaffold architectures (**Figure 1-6**). Schwarz's Diamond and Schoen's Gyroid have been successfully 3D printed in titanium-based scaffolds [109]. Then, it has been described that these surfaces could provide enhanced bone tissue-implant contact due to the low special curvature [110]. However, the experimental data to support this statement is limited so far. The literature reports are yet focused on the optimization of the additive manufacturing processes. However, Wang et al. [17] described the fabrication of three Mg-based scaffolds with different architectures. Their results showed that the TPMS scaffold had superior characteristics compared with the other two structures (with random and topologically ordered pores), although the samples had the same porosity and average pore size. Despite the good properties, Wang et al. highlighted the necessity of surface modifying the TPMS Mg-based scaffolds to provide appropriated biocompatibility.

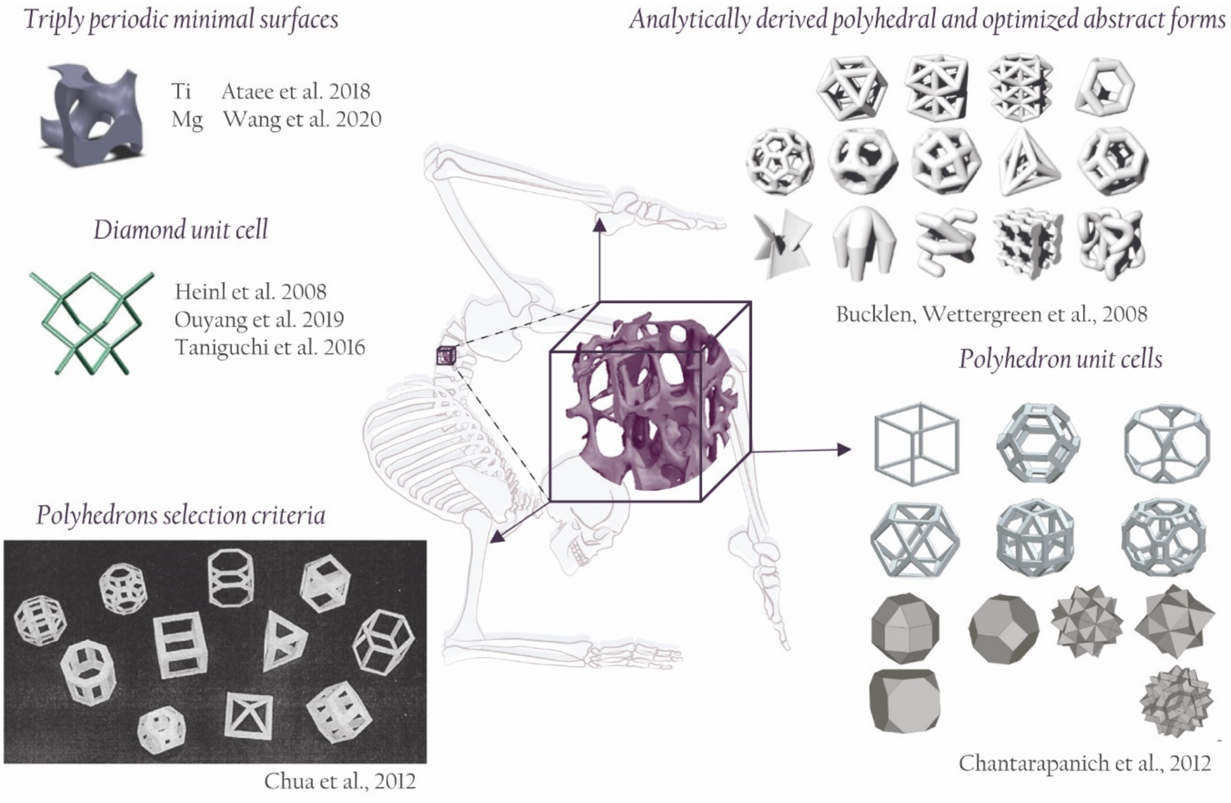

Figure 1-6 Unit cells for fabrication of geometrically and topologically ordered scaffolds. This figure shows the set of unit cells proposed to populate porous materials for bone replacement. Bucklen and Wettergreen et al. [95], Chantarapanich et al. [99], and Chua et al. [98] proposed unit cell libraries that are coincident in the use of polyhedrons (i.e., truncated octahedron). The proposed unit cells are analytical shapes extracted from the trabecular structures in the bone. Diamond unit cells and TPMS have also been presented as unit cell candidates.

1.3.3 Biodegradable metals for bone substitution.

Biodegradable implants are materials expected to have a controlled degradation profile with appropriate biocompatibility. Then, the degradation of products must be assimilated by cells or safely metabolized after fulfilling the reconstruction requirements. They are required to provide support for the bone during the healing process. The terms biodegradable, bioresorbable, and bioabsorbable are commonly used as synonyms of the materials named “absorbable metallic materials” in ASTM-F3160 [111]. The primary biodegradable metals for bone tissue engineering are Fe, Zn, and Mg. Of them, only Mg-based devices have been ultimately approved in Europe and South Korea [112]. There are available commercial versions, including the coronary scaffold Magmaris® by BIOTRONIK [113], Magnezix® screws for intraarticular fractures fixation by

Syntellix AG [114], and the MgCa alloy Resomet® by U&I that has been used in sutures, screws, and pins [115].

Iron

Fe is an abundant metal in the human body. This material is crucial for life since it is part of several metalloproteins and participates in biochemical activities such as oxygen sensing and transport, electron transfer, and catalysis [116]. However, the bioavailability of iron is hindered by its readily oxidized capacity. This condition also limits the use of Fe as a biodegradable implant. Fe's degradation products lead to an interruption in the transport of oxygen, which is necessary for the continuous release of the material [117]. Then, the study of Fe as a bioimplant is focused on the acceleration of its degradation rate. Alloying has been reported as a strategy to accelerate the corrosion and overcome other limitations such as Fe interference with MRI analysis [118]. However, more in vitro studies are required to test the Fe's biocompatibility. Moreover, the elastic modulus of Fe is higher than Mg, Zn, and bone; then, an implanted Fe device could exceed the mechanical capacity of the tissue and cause a phenomenon similar to stress shielding associated with the bioinert implants (i.e., Ti and alloys, Co-and Ta-based implants). Nevertheless, Fe's high strength makes it attractive in its porous form as it allows for thinner structures and greater porosity [119,120].

Zinc

On the other hand, Zn has demonstrated good biocompatibility in vivo and in vitro, and its corrosion rate is more appropriate for use as a bone replacement [121]. This material is part of the metabolism of the human body. It plays a vital role in several biological processes, including lipid and carbohydrate metabolism, enzymatic catalysis, collagen crosslinking, bone formation, and deoxyribonucleic acid replication. Moreover, around 300 zinc-containing enzymes have been reported [122]. As a bioimplant, Zn has been successfully proposed for stent applications [123] and recently considered orthopedic material [121]. However, the mechanical properties of Zn are not sufficient to fulfill the load-bearing requirements of the bone. Moreover, a porous configuration could be detrimental to the mechanical strength of Zn [124].

Magnesium

Mg is the second most abundant intracellular cation in the human body (first is potassium). Physicochemical processes depend on Mg, including its role as a cofactor of more than 300 enzymatic reactions, carbohydrate metabolism, protein, and nucleic acid synthesis [125]. This element is also highly involved in bone metabolism and bone remodeling (described in **1.2.1**). Its role in the bone remodeling process includes Ca adsorption, osteoblast adhesion, and bone formation [125]. Mg devices also deliver Mg^{2+} during degradation, and the accumulation of Mg^{2+} at the fracture site enhances bone tissue regeneration by promoting osteogenic cell spreading and proliferation [10–12]. The modulation of macrophage polarization (see **section 1.2.1**) has been suggested as another instrument of the osteogenic effect of Mg^{2+}, as Mg^{2+} ions mediate the immune response by decreasing proinflammatory cytokine secretion [13,14]. Despite the advantages of Mg-based implants, several challenges remain regarding the clinical implementation of this material. Mg by itself cannot efficiently integrate with the host tissue because of its high corrosion rate [15]. Then, the research efforts are focused on the control of the Mg rapid release.

This rapid corrosion could be an advantage if the physiological corrosion dynamics can be controlled. Therefore, it is imperative to understand Mg corrosion's complexity, as scaffold properties change dynamically during the healing process. Due to its high osteogenic potential, Mg was selected as the central element in the present thesis. Then, Mg's characteristics will be described in detail and context in the following section.

1.3.4 Homeostasis of Mg in the bone tissue

Since the surface is the earliest contact of the material with the tissue, surface characteristics are critical for implant success. This process starts with the signal collection and continues with the transduction, where the information about affinity is delivered. A cascade of enzymatic reactions is then initiated, and the signals are amplified, which influences gene regulation. In the next stage, there are integrins and transmembrane heterodimers attachment to the binding sites, which motivates the modulation of intracellular signals that influence cell mobility, shape, and feedback processes [5].

There are around 21-28 g of Mg in a healthy adult body. Slightly more than half of this Mg is in the bone tissue, 1% is present in the blood plasma, and the remaining amount is in the soft tissues [126]. In a regular intake, around 400 mg are consumed; however, excess of Mg is safely metabolized via excretion and reabsorption. In addition to being one of the most prevalent minerals in the human body, Mg is an essential element for constructing soft tissues and bone [127]. Mg is a small ion, smaller than Ca; however, this ion attracts water molecules more avidly, making it "larger" in practical terms [126]. Saris et al. [126] described the biochemistry of Mg and its role as a cofactor of hundreds of enzymatic reactions in the human body: it acts as a cofactor or substrate for phosphotransferases and –hydrolases that play a vital role in energy metabolism; moreover, Mg is part of the cell cycles, synthesis of proteins and nucleic acids, organelles integrity, modulation of some ions transport, among other processes.

The control of Mg homeostasis is crucial for skeletal tissue development and health. The Mg in skeletal tissue is partially stored in the cortical bone as a component of the hydroxyapatite crystal. It has been reported that in supersaturated solutions, Mg^{2+} participates in different stages of the crystallization of HA; i.e., surface absorbed Mg^{2+} inhibits HA crystallization [10]; accordingly, Mg deficiency leads to the larger and better-structured crystal, which makes the bone more brittle and fragile [127,128]. Dietary restriction of Mg is associated with osteoporosis development where the mechanical properties of the bone are severely affected [128]; experiments in rodents suggest that this affectation in bone characteristics is linked to a reduction in the osteoblastic activity [128,129].

Grünewald et al. [130] tracked the accumulation of Mg from degrading implants in rat bones. Their synchrotron microbeam X-ray fluorescence results showed that the corrosion products are temporarily stored in the bone matrix. Wang et al. [131] presented an improved mineralized matrix when using Mg screws to fix a tendon graph (contrasted with Ti screws). They suggested that the improvement is due to the stimulation of the bone marrow mesenchymal stem cells (BMSCs) with Mg ions released from the screw. These results coincide with the study of Zang et al. [12] that described the accumulation of Mg ions in the fracture following the degradation of the implant and proposed an enhanced bone regeneration due to local neuronal production of Calcitonin Gene-Related Peptide, CGRP.

1.4 Conclusions

The tissue engineering approach requires biocompatible materials and support and interaction with the tissue to enhance and accelerate the healing. In this respect, ideal bone implants' design requires a comprehensive understanding of the bone as host tissue. Hence, the present chapter described the current knowledge of bone composition, its complex hierarchical structure, and the mechanobiological aspects involved in its self-healing process. Moreover, engineering strategies for critical size bone defects are described. The descriptions in this chapter will be used as theoretical bases for the development of this thesis.

2. Controlling the corrosion of porous Mg

The magnesium scaffolds research has focused the efforts on optimizing the fabrication constraints, including the production method, space holder, and melt protection [132]. Processes such as powder metallurgy [133,134], metal/gas eutectic unidirectional solidification method, or GASAR process [135], laser perforation [23], and additive manufacturing approaches have been proposed [93,136]. Also, various space holders can be identified from the literature, including NaCl grains [18], NaCl salt patterns or negative salt predesigned templates [19,137], titanium wires [81], and flexible clay-like space holders [103,138]. The melt protection has been principally achieved with argon or other inert gasses [19,133,139], SF_6 with different carriers has also been reported [140], and the salt fluxes $MgCl_2$, MgO, CaF_2, and KCl [141].

Recent reviews comprehensibly cover aspects of the development of Mg as biomaterial such as bioactivity [142], microstructural characteristics [143], additive manufacturing [144], mechanical properties [145], surface treatments and coatings [24,146–148], alloying and alloying elements [149], corrosion mechanisms [150,151], clinical translation [152], among others. There is also information about manufacturing methods to obtain porous Mg [111,132,153,154]. However, a compendium of information about understanding and controlling the corrosion of porous Mg is still needed.

Despite the advances in porous Mg fabrication, there are still challenges regarding the corrosion rate of Mg. In porous Mg, the corrosion is fast and inhomogeneous. The rapid degradation makes the Mg poorly integrate with the tissue [155]. Moreover, the porous condition dramatically increases the surface area and, consequently, the degradation potential [132]. The geometry, which includes the porosity, the exposed surface, and the pore interconnection sites, creates a new challenge due to the increased ions' interchange during Mg dissolution [16,156]. Hence, this chapter presents a literature review to map out and categorize existing literature about surface modification of porous Mg. Moreover, Mg's corrosion mechanism is described to theoretically support the protection approaches presented.

2.1 Literature research

A literature search was performed on PubMed and Scopus databases (last access 30/06/ 2020); the keywords included were *porous* AND *magnesium*, *magnesium* AND *scaffold*, and *magnesium* AND *bone implant*. The inclusion criteria were studies that reported porous materials, metallic magnesium as a principal component, and surface modification or surface engineering strategies with corrosion protection purposes.

The following information was extracted from the reported data: material (i.e., alloy), methods for producing the porous structure, pore shape, characterization methods, and surface modification mechanism. A qualitative review was performed based on the surface modification outcomes regarding bioactivity, corrosion resistance, and scaffold geometry.

2.2 Results and discussion

2.2.1 Magnesium corrosion

Mg-based biomaterials have low thermodynamic stability; they quickly transform into their oxidation stages after exposure to aqueous environments. The correspondent chemical reactions are given in **Equations 2-1**, **2-2**, and **2-3** [157]:

$$Anodic\ reaction: Mg \rightarrow Mg^{2+} + 2e \quad \text{Equation 2-1}$$

$$Cathodic\ reaction:\ 2H_2O + 2e \rightarrow 2H_2 \uparrow + 2OH^- \quad \text{Equation 2-2}$$

$$Total\ reaction: Mg^{2+} + 2H_2O = Mg(OH)_2 + 2H_2 \uparrow \quad \text{Equation 2-3}$$

The macroscopic and observable results of reducing water (**Equation 2-1**) form H_2 bubbles and increase pH due to the release of hydroxyl ions. As noticed in **Equation 2-3**, in the presence of water, Mg-based materials liberate H_2 and form an $Mg(OH)_2$ product, which does not provide sufficient protection against corrosion in conditions that contain a high concentration of Cl^- ions. It has been reported that a concentration of Cl^- ions higher than 30 mM accelerates pit corrosion by transforming $Mg(OH)_2$ into $MgCl_2$, a more soluble product [158,159]. Hence, Cl^- ions concentration in simulated body fluid (SBF) or cell culture media (i.e., Dulbecco's modified eagle's medium, DMEM 90mM [160]) accelerates the samples' pit corrosion. The reactions are summarized in **Equation 2-4** and **2-5** [160]:

$$Mg + 2Cl^{-} \rightarrow MgCl_2 \quad \text{Equation 2-4}$$

$$Mg(OH_2) + 2Cl^{-} \rightarrow MgCl_2 \quad \text{Equation 2-5}$$

The formation of pits initiates at surface flaws that are nearby to the secondary phases as a consequence of the breakdown of passivity. Electrolytic cells are then formed, with the second phase playing as the cathode and the Mg matrix as the anode [161]. Then the grain boundaries and the second phases are the places leading the corrosion. **Figure 2-1** shows a 0.04 µm polycrystalline diamond polished AZ31 surface before and after 15 min of immersion in DMEM. The material embedded in epoxy resin and etched with a solution containing 1ml of acetic acid, 1 ml water, 420 mg picric acid, and 7 ml ethanol to reveal the microstructure. After immersion, all the initial microconstituents were still recognized on the surface. Some crack points were visible in the Mg matrix. The cathodic intermetallic reactions were evidenced in the accumulation of Ca-phosphate rich products precipitated along the Mg matrix's weaker parts. Meanwhile, the Al content increased in the second phase related to strong corrosion processes [162]. In contrast, the O/Mg ratio changed in the more visible cracked regions.

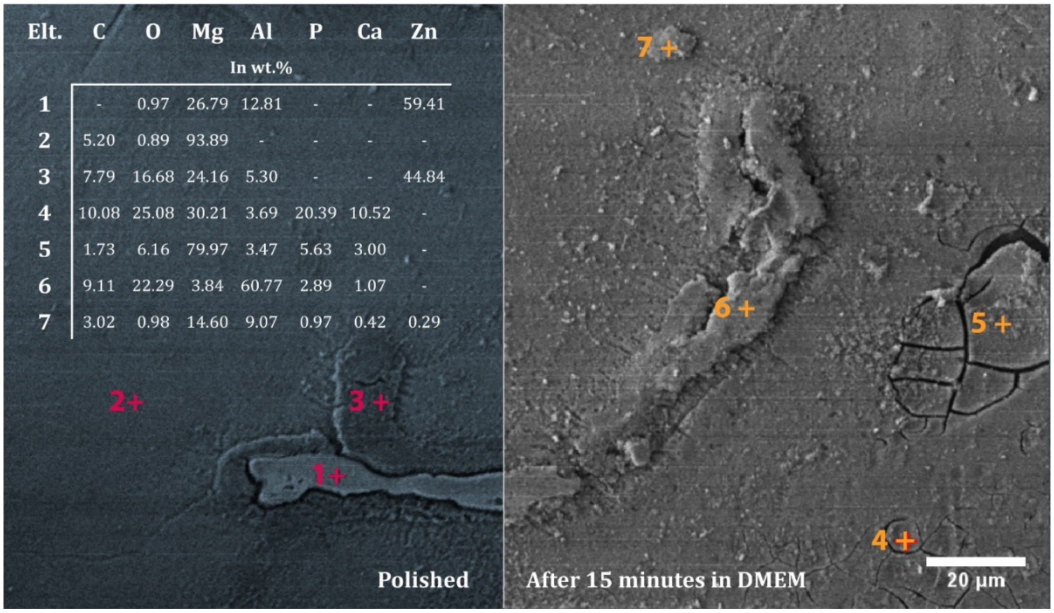

Elt.	C	O	Mg	Al	P	Ca	Zn
	In wt.%						
1	-	0.97	26.79	12.81	-	-	59.41
2	5.20	0.89	93.89	-	-	-	-
3	7.79	16.68	24.16	5.30	-	-	44.84
4	10.08	25.08	30.21	3.69	20.39	10.52	-
5	1.73	6.16	79.97	3.47	5.63	3.00	-
6	9.11	22.29	3.84	60.77	2.89	1.07	-
7	3.02	0.98	14.60	9.07	0.97	0.42	0.29

Figure 2-1 AZ31 surface polished surface before and after 15 mins of immersion in DMEM. The images were obtained via SEM, and the distribution of elements on the surface was acquired via EDS. This figure is representative of the corrosion process around the second phase in Mg-Al systems.

It could be assumed that the microstructural components control the corrosion of Mg systems [163]. However, Mg corrosion is also sensitive to immersion media [164], the alloy's composition, metallurgical and surface treatments, pH of the environment, mechanical inputs, and biological molecules' presence [165]. Due to the diversity, there is no consensus about the best practices to test Mg dissolution, and several media have been used to evaluate Mg-based devices with biological intentions. Among them, saline (NaCl) and complex saline solutions (phosphate-buffered saline; PBS) [166]. Likewise, SBFs such as Hank's balanced salt solution and Earle's balanced salt solution containing all the major inorganic ions present in the human serum [167]. Also, cell culture media such as minimum essential medium (MEM) and DMEM are similar to the SBFs but include small-molecule organic components [168]. Moreover, some authors have added protein supplies to the test solutions [16]. **Table 2-1** shows that mostly SBF and DMEM supplied with fetal bovine serum (FBS) are used to test surface-treated porous Mg. As mentioned, there is no consensus about the relation of sample and medium volume; then, comparisons among studies are difficult to carry out.

Table 2-1 Immersion media and sample characteristics of surface-modified porous Mg.

Modification	Material	Immersion media		Sample characteristics			Ref.
		Solution	Volume	Porosity	Diameter	Length	
				(%)	(mm)	(mm)	
Chemical conversion	LAE442	Oyane SBF	50 ml	41.4	4	5	[19]
Chemical conversion	Mg	DMEM + FBS	50 ml cm^{-2}	54.31	-		[81]
Polymeric	LAE442	Oyane SBF	50 ml	41.4	4	5	[19]
Polymeric	Mg	PSS	25 ml	40	-		[169]
Ceramic	Mg	DMEM + FBS	3 ml	75	10	12	[17]
Ceramic	Mg	Kokubo SBF	80 ml	69	12	1.5	[170]
Hybrid	Mg	Kokubo SBF	80 ml	69	12	1.5	[170]
Hybrid	Mg	Kokubo SBF	25 ml	40	12	6	[22]

The release of Mg^{2+} ions and OH^- also alters the conditions of the medium and the phosphate groups available in the bath that are a function of pH. The acid dissociation constants are shown in **Equation 2-6** [162].

$$H_3PO_4 \leftrightarrow H_2PO_4^- \leftrightarrow HPO_4^{2-} \leftrightarrow PO_4^{3-}$$

pK1 = 2.14 pK2 = 6.87 pK3 = 12.32 **Equation 2-6**

When immersing Mg samples in SBF or cell culture media, Ca-phosphates are precipitated on the surface. The deposited Ca-phosphate characteristics (i.e., density, thickness, and crystallinity) are a function of the environmental conditions such as the use of CO_2, temperature, and pH [164]. A proposed mechanism for the deposition of Ca-phosphate products onto Mg-based surfaces is shown in **Equation 2-7** [162,171].

$$10Ca^{2+} + 6PO_4^{3-} + 2OH^- \rightarrow Ca_{10}PO_6OH_2 \quad \text{Equation 2-7}$$

2.2.2 Corrosion mechanism of porous Mg

In a porous structure, the reaction conditions can easily and locally change. The morphology of the material detachment and oxides precipitation varies with the scaffold's location [16,156]. The geometry, which includes the porosity, the exposed surface, and the pore interconnection sites, influences ions' interchange during Mg dissolution. In static conditions, the accumulation of corrosion products clogs small pore interconnections [16]. Moreover, high porosity samples degrade faster at the initial stages of static immersion. They have more connected areas that allow the ions to interchange [16,139,172]. During dynamic immersion, porosity also affects the samples' deterioration; this effect is attributed to porosity's direct relation with permeability [173].

Distinct corrosion behaviors have been noticed between the external and internal pores in the same structure [16,136,174]. Li et al. [136] described accelerated corrosion in the scaffold's center compared to the periphery. The mechanism of the local increase in degradation was attributed to a higher increase of pH at the center of the scaffolds than the periphery, which causes more stable corrosion products that clog the pores. Then, there is a limited diffusion of Mg ions due to the clogged pores, and the accumulation of Mg^{2+} attracts Cl^- negative charged ions to the site. On the other side, ions' continuous interchanges in the struts that are more exposed to the medium reduce the struts' thickness and earlier strut losses [16]. Hence, the topological design is an essential variable in the corrosion complex. Different corrosion rates and mechanisms have been reported for samples with varying pore shapes but similar dimensions, porosity, and pore quantity [16,17].

Two proposed mechanisms for porous Mg corrosion are summarized in **Figure 2-2**, where a) is a schematic representation of the continuous ions interchange between the medium and the pores at the periphery, causing the replacement of the strut by corrosion products, followed by earlier strut losses, and faster corrosion from the periphery to the center. The second case (**Figure 2-2**b) is the schematic representation of the accumulation of denser corrosion products at the scaffold's center due to the limited diffusion. This results in a corrosion cell between the center and the periphery. The loss of material starts at the core of the scaffold.

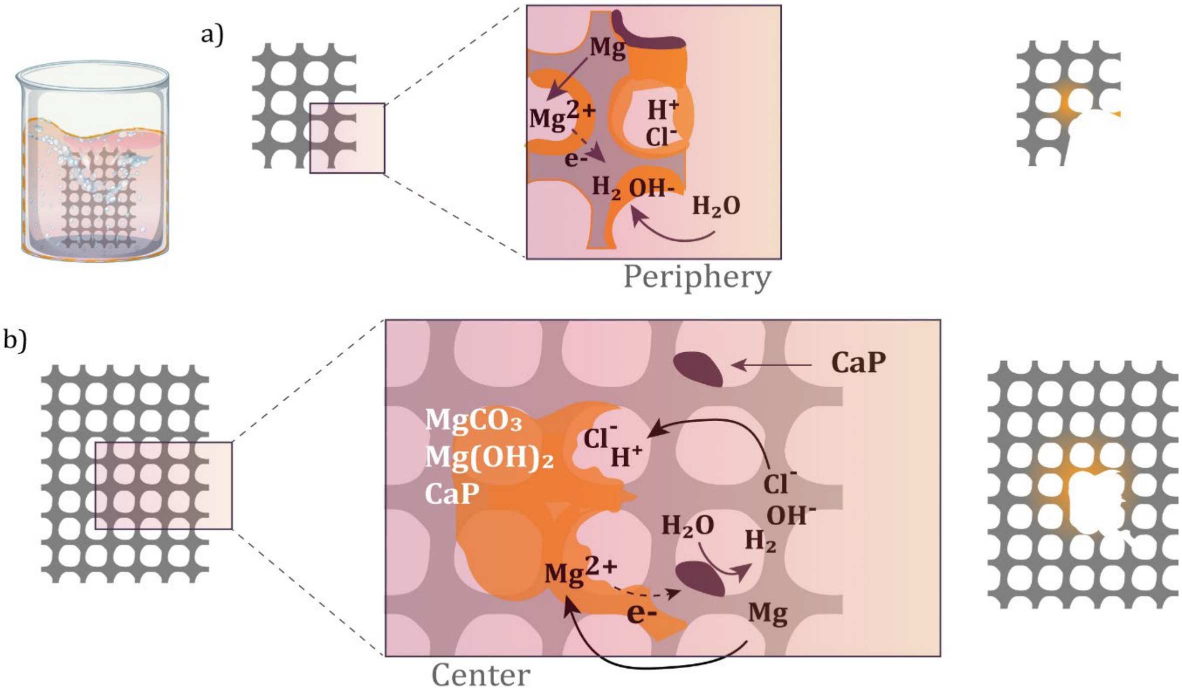

Figure 2-2 Schematic representation of two proposed mechanisms of porous Mg corrosion. a) corrosion is stronger in the outer pores that are in a continuous interchange of ions with the medium. b) corrosion products clog the inner pores, and the accumulation of Mg^{2+} attracts negative charged Cl ions. The formation of a corrosion cell within the external and internal pores leads to a material loss in the pores' center.

Jia et al. [16] evaluated two different Mg porous scaffolds and a bulk disc with similar dimensions. Their results showed that the exposed area highly influenced the Mg corrosion; then, the scaffolds that had enlarged surface contact with the corrosive medium degraded faster. On the contrary, Kim et al. [175] exposed different surface areas to a similar simulated body fluid volume. Their results showed that the increased surface area accelerated the passivation kinetics, which caused the deposition of products that protected the samples from further corrosion. Hence, although the corrosion rate certainly changes with the geometrical design of the scaffolds [17], the role of the specific surface area is still debatable.

The sample-medium-volume-to-surface-area ratio has also been considered to influence the corrosion behavior of the samples. The weight loss measurement is shown in **Equation 2-8**. Where A is the exposed area, and t is the time of immersion. It should be noticed that the initial exposed area has an inverse relation with the mass-loss rate. Moreover, the surface area increase decreases the weight, making the weight-surface area ratio the parameter that affects the Mg corrosion rate [176]. **Table 2-1** shows porous Mg surface-modified samples that reported the medium volume and sample size of the corrosion test. Again, the lack of consensus makes it challenging to compare reports, formulate models for the prediction, and further control porous Mg corrosion. ASTM standards recommend a sample-medium-volume-to-surface-area ratio of 0.2–0.4 ml mm^{-2}, which results in a small ratio for Mg since the samples' corrosion is conditioned by the ions receiving capacity of the media [177]. The ideal medium-volume-to-sample-area ratio is still controversial since several variables come into the reaction. The volume of medium for in vitro corrosion tests must also be considered in terms of what is relevant in the clinical practice, for instance, implant size [177]. Kirkland et al. [177] indicate that the best approach is to keep the medium volume as large as possible. Other authors suggest adding synthetic pH buffers to simulate the living systems' buffering capacity [164].

$$\Delta W_m = \frac{W_0 - W_f}{At} \quad \text{Equation 2-8}$$

2.2.3 Assessing the corrosion of porous Mg

Immersion methods are the most widely reported strategies to assess Mg corrosion [150]. This set of measurements includes mass loss, pH monitoring, and hydrogen evolution included in static [178] and dynamic [176] corrosion setups. Mass loss measurement consists of weighing the sample before and after different stages of the corrosion process. The weight loss measurement equation is given in **Equation 2-8.** This method requires removing Mg corrosion products using chromic acid to calculate the metal's degradation accurately, according to ASTM G1-90. Early reports avoided this step, then the porous Mg's weight was reported to increase in the initial stages of the immersion [172]. Moreover, for porous Mg with small pore interconnections, this technique becomes less reliable in removing corrosion products step [136].

Since Mg's cathodic reaction releases H_2 (**Equation 2-2**), hydrogen gas collection is another common approach to test porous Mg. Like mass loss, the complete sample is immersed in the corrosion medium; however, the hydrogen is collected with an inverted funnel into a burette, also filled with the medium [139]. Despite the direct relation of the H_2 evolution with the Mg degradation (**Equation 2-2**), this method could delay the corrosion information since the hydrogen bubbles could be trapped in the porous structure [136].

Inductively coupled plasma-atomic emission spectroscopy (ICP-AES), also known as inductively coupled plasma-optical emission spectroscopy (ICP-OES), is another popular approach to test porous Mg after immersion in corrosion media [23,81,179]. This technique is a spectroscopy type that uses ICP to produce excited atoms/ions that finally produce electromagnetic radiation at characteristic wavelengths [180]. This technique is then used to estimate the ions accumulated on an immersion media, such as Mg^{2+} (to test the Mg dissolution) and Ca (to test the apatite formation).

Electrochemical measurements have also been used to test porous Mg. The method consists of imbibing the porous sample in epoxy resin with a limited area exposed to the assessment. A conventional three-electrode electrochemical cell setup consists of a counter electrode (i.e., platinum mesh), a reference electrode (i.e., Ag/AgCl), and the Mg sample as the working electrode [136,181]. The slope of a linear plot of current vs. potential when the current changes polarity reveals the polarization resistance inversely proportional to the corrosion rate [150]. The electrochemical test then exposes the participation of the anodic and cathodic branches in Mg's corrosion. Despite the advantages, the electrochemical measurements are hindered by the limited exposed area of the setup; thus, the porous samples' structural characteristics (i.e., pore size and porosity) are excluded from the corrosion information.

Additional assessments are required to understand the corrosion kinetics of porous Mg. Micro-CT scans at different stages of the immersion provide an inside view of the corrosion process, i.e., accumulation of corrosion products and localized volume losses [19,136]. This characterization technique also provides corrosion information regarding volume loss and implant integration in the in vivo testing [81].

2.2.4 Surface modification of porous Mg

The protection of porous Mg requires consideration of additional parameters from the complex geometry condition. The modification method must infiltrate the structure and homogeneously treat the surface without clogging the pores with the coating material. As shown in **Figure 2-3**, the reports about surface modification of porous Mg consist mainly of chemical conversion processes and the use of ceramics as barrier layers against corrosion. Fluoride conversion is the most popular method since the coating solution can penetrate the pores and creating an MgF_2 protective layer. Other methods consist of polymeric and polymeric/ceramic (hybrid) coatings that deal with the limited adhesion properties of the ceramic layers. The effect of each modification method on the corrosion protection of Mg will be discussed below.

Regarding the geometry of the samples (pore shape and porosity), several results depend on the role of the Mg substrate in the modification process. The geometry changes after surface treatment related to the sample characteristics are shown in **Figure 2-4**. The outcomes include decreased or increased porosity, reduced pore size, and the formation of thin layers that are more convenient to protect the scaffold. In this respect, an increase in porosity can compromise the mechanical properties of the sample. Simultaneously, the decrease in the pore size [141] can be detrimental to material integration and bioactivity **(see 1.3.1)**.

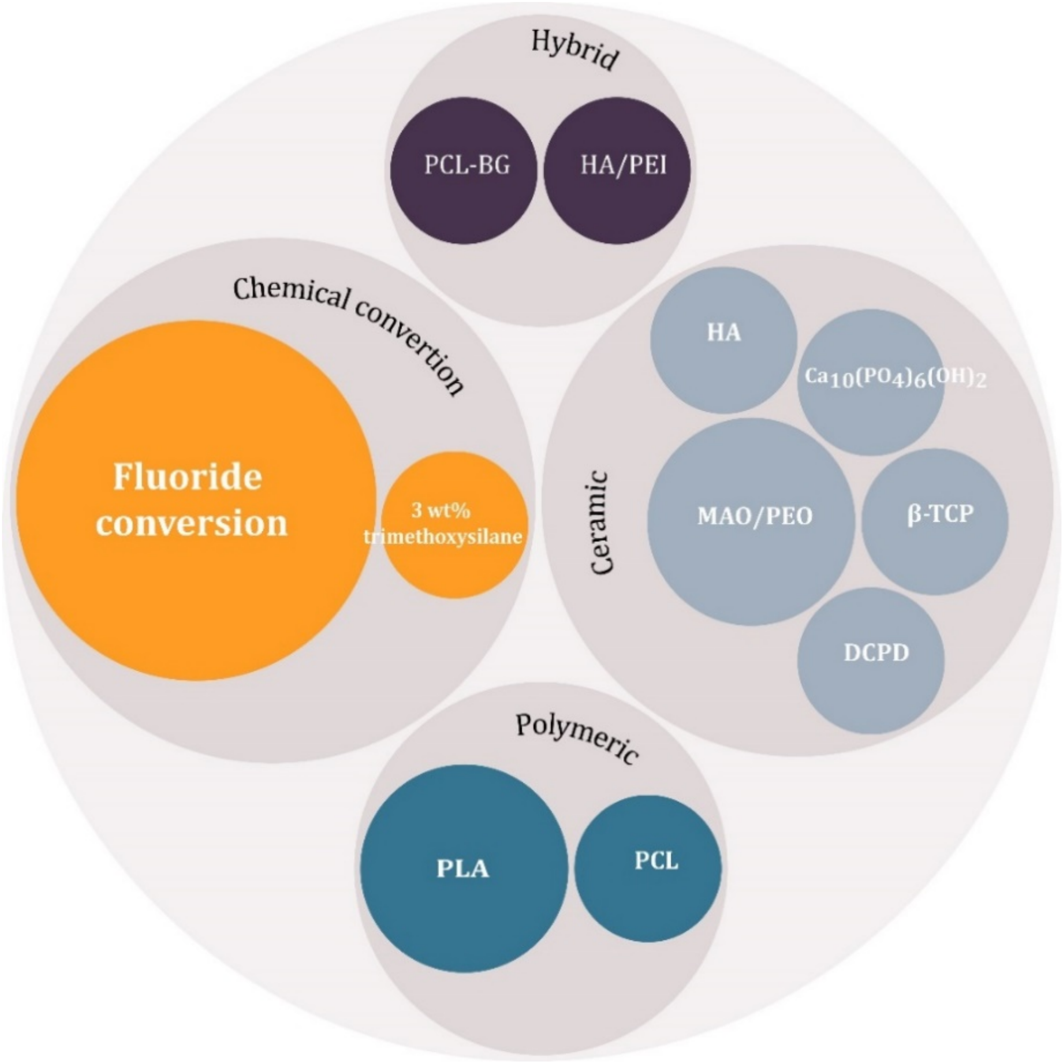

Figure 2-3 Surface coating methods on porous Mg. Each big circle represents a classification of the modification methods (chemical conversion, hybrid, ceramic, and polymeric). The circles inside correspond to specific coating methods within each category. The circle's size represents the frequency of the method in the literature reports [17,19,22,23,81,82,136,169,178,179,181–184].

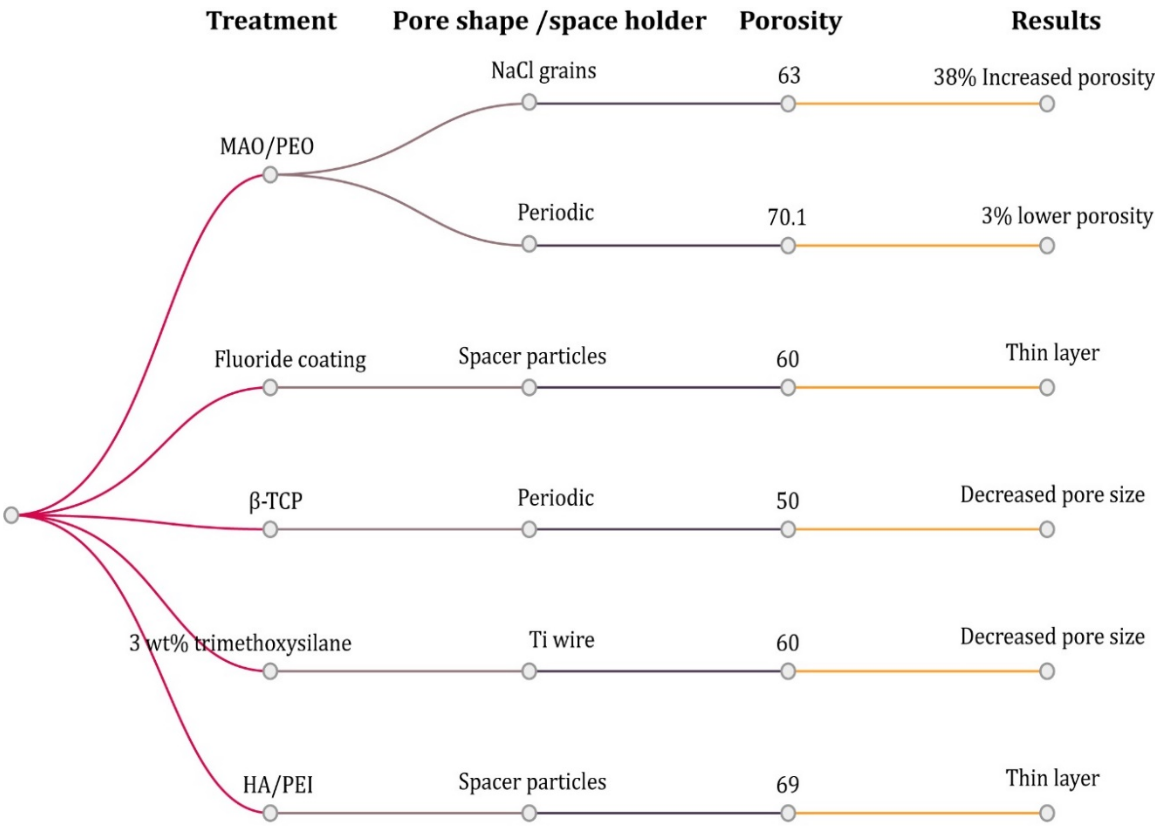

Figure 2-4 The effect of the surface treatments in the sample geometry. The surface treatments that reported an impact in the sample geometry were classified and associated with the surface treatment and geometry characteristics (pore shape and porosity) to allow comparisons.

Chemical conversion

These surface modification processes are the chemical reaction product between the Mg-based substrate and the coating solution [24]. For instance, Singh et al. fabricated $Mg_{10}Zn_4Y$ scaffolds via powder metallurgy using Ti-woven wire to create the pores. They obtained 300 µm pores that were then coated with a solution of 3 wt% trimethoxysilane, ethanol, and deionized water. The samples were immersed in an ultrasonic bath to ensure coating each pore. Their results showed that the solution covered the pores without blocking the paths with the coating material. Moreover, the achieved surface was effective against corrosion, as reflected in the decrease in weight loss. However, the deposited coating influenced the sample's geometry, and the pore diameter of 300 µm was reduced to 200 µm after the coating process [178].

Fluoride conversion.

Pretreating the samples with hydrofluoric acid (HF) produces an MgF_2 layer that is also biocompatible and protects Mg samples against corrosion. The MgF_2 layer is formed via the following reaction (Equation 2-9) [178,182].

$$Mg_{(s)} + 2HF_{(s)} \rightarrow MgF_{2_{(s)}} + H_{2_{(g)}} (\uparrow) \quad \textbf{Equation 2-9}$$

The coating process, which consists of immersing the sample in liquid HF, can cover the entire complex structure. The MgF_2 film is about 0–2 μm in thickness and encapsulates the sample avoiding the reaction between the Mg matrix and the intermetallic phases [183]. Moreover, the MgF_2 product is insoluble in water, eliminating the initial sharp hydrogen release [19]. Julmi et al. [19] demonstrated that the HF treatment, which comprised a pretreatment with sodium hydroxide (NaOH), covered the whole outer surface of a periodic scaffold with the MgF_2 layer. The MgF_2 cover had a flattened effect on the surface, decreasing the exposed area.

Similarly, Yu et al. [179] reported porous AZ31 scaffolds produced via laser processing with shield oxygen. The samples were cleaned and immersed in HF 40% (v/v) for 12 h at 30 °C. After immersion, both treated, and no treated samples showed a similar geometry with an average pore diameter of 300 μm. They suggested the formation of a thin coating that significantly decreased the corrosion rate. The MgF_2 layer in porous Mg has been reported to have an appropriate in vitro cytotoxicity. In the in vivo application, it reduces the formation of the H_2 gas cavities [81,179]. There is no data in the literature that focuses on the effect of the MgF_2 layer on the geometry of porous Mg samples; however, this effect is expected to be not significant since the film thickness is a relatively small volume percentage of the total sample and could be canceled in the systematic errors.

Calcium Phosphate coatings.

Ca-phosphate coatings have been attractive alternatives to protect Mg against corrosion [185]. A significant limitation is the formation of brittle faces with little HA content [186]. However, the CaP-phases and crystal size have been adjusted in porous Mg-Zn samples via the pulse electrodeposition process. The obtained ceramic layer consisted of 2–3 μm crystals deposited on porous that were initially 200–400 μm in size [181]. Like bulk substrates, the CaP cover improves porous Mg's corrosion, acting as a barrier between the Mg and the corrosion medium, as observed in periodic and random Mg scaffolds coated with dicalcium phosphate dihydrate (DCPD) and HA, respectively [17,82,187].

β-tricalcium phosphate (β-TCP) has also been suggested for porous Mg via precipitating CaP products on the surface after alkali-heat treatment. This kind of conversion coating regulates the immune microenvironment to control the bone cells' reaction in Mg implants [23]. Nevertheless, the coating process with ceramic layers causes a change in the scaffolds' geometry, for instance, porosity and pore size [17,23]. Chen et al. [23] described a decrease in the pore size from 100 µm to 60 µm. After HF treatment, the deposition of CaP products also demonstrated the uneven distribution of the CaP-phases and coating thickness in periodic Mg-based foams.

MAO/PEO coatings

Electricity power has been widely used to generate ceramic and oxide coatings on the Mg surface via plasma electrolytic oxidation (PEO), also known as micro-arc oxidation (MAO; anodizing). A comprehensive review of PEO in Mg bulk substrates is given in [188], where corrosion protection is reported as the primary application. Generally, in PEO processes, the Mg is integrated onto the circuit serving as the anode; thus, the achieved surface consists of the implant elements together with the surrounding electrolyte. The high potential exceeds the dielectric breakdown of the growing oxide, and the physical events modify the resultant oxidation state [189]. Hence, PEO/MAO power consumption is a concern that becomes more problematic in porous materials because of the increased exposed area.

Furthermore, part of the substrate is dissolved during the process, which led to changes in the foam geometry. For instance, Rua et al. [18] treated with MAO AZ31 foams produced via infiltration casting. The electrolyte solution was obtained using deionized water to dissolve NaOH, $Ca(OH)_2$, $CaHPO_4$, and metallic Ca. After the coating process, the samples decreased by 28% in density and increased 38% percent in porosity. The in vitro corrosion and biocompatibility behavior of the coating were not reported.

Pre-designing the implant's architecture could help overcome the geometry affectation since it considers the dimensional change of the material during the PEO process. Kopp et al. [190] established a postprocessing routine, including PEO, as a surface modification. The samples were WE43 porous materials with cuboid lattice structures achieved via laser powder bed fusion. The process variables were set for the surface thickness of around 9 μm with a phosphate electrolyte. The coated implants showed a 3% lower porosity than the expected theoretical value, while uncoated samples were 2.5% higher in porosity. Their PEO coatings offered protection against corrosion and improved mechanical performance.

As expected, the corrosion mechanism of the PEO-coated porous materials is similar to PEO's corrosion process in bulk. The coating creates a barrier that protects the sample from corrosion at the initial stages [25]. After that, the propagation of cracks in the layer creates pathways that allow the interchange of ions and corrosion products to accumulate into the inner PEO layer. In Kopp et al. [190], this corrosion process led to selective corrosion at the inner part of the porous material.

Polymeric coatings

This coating method has been used to produce homogeneous thin films in Mg surfaces [191]. Polymetric coatings protect Mg from dissolution and increase the mechanical properties of the porous Mg materials [21,184]. Yazdimamaghani et al. [21,169] coated Mg-based scaffolds with polycaprolactone (PCL). The viscosity was decreased to allow the PCL to penetrate the 200 – 300 μm pores. The resultant polymeric film was effective against corrosion. After immersion in physiological serum saline (PSS), the samples coated with PCL gained more weight than the samples non-treated. This behavior was attributed to the take-up of water by the polymeric coating. The polymer's water absorption and swelling have been reported as undesirable effects of this kind of surface treatment since they can produce internal stresses and consequent peeling of the coatings [24].

Polylactide acid (PLA) has also been proposed for porous Mg using dichloromethane (DCM) as a solvent [19,184]. PLA has been reported to decrease Mg bulk and porous materials' corrosion rate by encapsulating the material into a protective barrier [19,192]. Despite the advantages, PLA coating resulted in an uneven distribution when used to cover porous materials with periodic structure [19]. Moreover, biodegradable polyesters have a weak bonding to Mg [186]; then, they are susceptible to mechanical failure during manipulation (i.e., during surgical procedures) and detachment. The limited adhesion properties could also hinder the PLA application in porous Mg structures due to the geometry's complexity.

Hybrid coatings

A strategy to suppress the cracking effect on ceramic coatings consists of the use of polymers to create hybrid layers since they can support deformation [186]. Hybrid coatings have been proposed to protect porous Mg [82]. Poly(ether imide) (PEI) and PEI–SiO_2 were used to preserve porous Mg already coated with HA [82]. The HA layer had a thickness of 2 µm, and the HA/ PEI–SiO_2 consisted of a layer of less than 200 nm, which could be convenient to protect the surface without clogging the pores. The layers were effective against corrosion and behaved better (corrosion resistance and stability) than the initial HA coating.

Similarly, PCL and bioactive glass (BG) have been proposed to coat porous Mg. The PCL-BG improved degradation, mechanical stability, and bioactivity of the coated samples [22,193]. Moreover, increasing the PCL-BG layers increase corrosion protection. However, the coating was 60 µm in thickness after three PCL-BG layers; increasing the layer thickness could also be detrimental and cause the coating's delamination [22].

2.3 Conclusion

Porous Mg is more vulnerable to corrosive attack than the fully solid counterparts due to the increased exposed area and the ions interchange's new conditions. An accurate corrosion mechanism for porous Mg is hard to establish, given the differences in testing conditions. However, general porous Mg degradation trends consist of localized corrosion boosted by the pores' clogging and the strut loss due to the accumulation of corrosion products. Hence, the protection mechanism must consider the samples' geometry to balance corrosion protection and open porosity. The approaches to protect porous Mg consist of conversion coatings, including chemical conversion and deposition of ceramic, polymeric, and hybrid coatings. Several coatings, such as the coatings obtained via MAO/PEO, produce significant changes to the sample's geometry. Fluoride conversion is the most popular modification method since it creates a thin layer of protective MgF_2. However, its effect is limited to the initial stages of immersion. Future research may improve the coatings adhesion properties and develop approaches that avoid depositing a material that can clog the pores.

3. DPNS for enhanced osseointegration and tunable resorption of Mg-based foams.

As seen in **chapter 2**, coatings have been proposed as the principal strategy to decelerate and control corrosion rates of porous Mg foams. Various degradable coatings, including those based on Ca-phosphate (CaP), have been proposed, owing to their favorable properties as biological implant materials [20]. Other degradable coatings, such as β-TCP [23], PCL, PCL-BG [21,22], have been reported for porous Mg. However, these coatings to protect metallic foams have modified the scaffold geometry and reduced or increased pore size. As mentioned, small pores can affect the bioactivity of materials by interfering with nutrient-interchange mechanisms of the body.

Meanwhile, increased pore size compromises the mechanical properties of the scaffold. Therefore, a desired surface modification strategy must adjust the Mg-based porous material biological environment interface without the use of a coating while maintaining the bulk properties. The transformation tendency of Mg and its alloys has highlighted the need for the development of surface-engineering technologies that can achieve protection and bioactive properties without affecting bulk characteristics. This chapter includes material published on [194].

3.1 Al-alloying to protect Mg corrosion.

Al-alloying has been considered a key strategy for improving the corrosion resistance, especially when there is Al segregation on the near-surface [27–31]. Although the toxicity of Al is still being discussed, the amount of Al released from MgAl systems having less than 5 wt % Al is below the weekly intake limits, and no toxic effects have been correlated in long-term in vivo studies [195]. Al-enrichment on the near-surface has been obtained by laser-surface melting and high-current pulsed electron beam [32,33], demonstrating that the development of an Al-enriched layer on the surface provides better protection against corrosion than typical Mg corrosion products (i.e., Mg

(OH)s). A minor increase in Al content can reduce the degradation rate of Mg-Al systems. However, this passivation ability is conditioned to the Mg-Al ratio. Pardo et al. [34] reported that 3 wt.% of Al decreased the degradation rate of Mg, whereas 9 wt% of Al significantly increased the corrosion rate because greater localized corrosion leads to greater Mg dissolution and a reduction of protective-layer formation. Similarly, Liao et al. [30] reported that rapid micro-galvanic corrosion on the AZ61 alloy promoted the precipitation of hydroxide species on the surface. Consequently, the new Al-rich surface layer significantly improved its corrosion resistance.

3.2 Directed plasma nanosynthesis

The affinity of Mg can be used to create an interaction between the tissue and the material to modulate the corrosion rate and H_2 release while designing Mg self-response systems to the environment in which they are placed. Thus, the use of alloying elements (e.g., Al), combined with tailored surface tunability, to modify the local surface chemistry of the implants provides an opportunity to control the corrosion response and surface transformation of Mg-based devices. Strategies for driving and controlling the Al supply from the interior of the alloy to the near-surface are therefore required. Reichel et al. [35] modeled and experimentally confirmed the compositional changes of MgAl binary alloys under Ar^+ bombardment as a function of the energy of the incident Ar^+. They also described a preferential sputtering of Mg and preferential segregation of Al as a consequence of the bombardment-enhanced Gibbsian segregation caused by the intent of the system to reduce its surface free energy.

From this basis, in the present work, a multi-functional interface is designed based on the evolution of well-ordered nanostructures and preferential Al segregation along the foam outer surface driven by low-energy Ar^+ irradiation. Surface modification is achieved via low-energy directed plasma nanosynthesis (DPNS) introduced on Mg-based alloy foams. DPNS is an atomic-scale nanomanufacturing process that induces compositional and structural changes to the targeted solids. Additionally, the process can be readily controlled by adjusting different parameters, such as gas species, energy, fluence, and incidence angle. In this study, DPNS is used to control the corrosion rate and, consequently, the bioactive properties of Mg-based foams that can adapt to the extreme environment of the body. This surface is designed such that, when combined with the inherent human-body fluid environment, it triggers specific bioactive functions, resulting in a biocompatible and bioactive interface without the need for complex coatings. Therefore, the present work studies the effect of different DPNS parameters on the transformation of the foam's surface; in particular variation in hydrogen evolution and the formation of CaP phases on immersed Mg-based foams.

3.3 Materials and methods

3.3.1 Foam fabrication and initial characterization

The foams were fabricated via infiltration casting, as was described in previous work [141]. The starting material was an AZ31 rod with a chemical composition of Mg at bal. and Al-3.3% Zn-1.1%. Salt particles sieved on average 500-µm sizes were used as space holders. 500-µm pore size has been selected because of its high vascularization and cell adhesion potential [73,141].

Moreover, 500 µm pore size has been shown in the author's previous work to mimic the mechanical properties of bone in scaffolds obtained via infiltration casting [141]. The melt was protected from ignition using salt fluxes: $MgCl_2$, MgO, CaF_2, and KCl. The Mg/NaCl-solidified composite was cut into cylinders of 8.0 -mm diameter and 2-mm height. Finally, the cylinders were leached via dissolution using NaOH in an ultrasonic bath for 15 min. The composition of the obtained foams was assessed via inductively coupled plasma-optical emission spectrometry (ICP-OES). Pictures of the machined samples are shown in **Figure 3-1**. The surface area was measured using N_2 gas by adsorption/desorption isotherms of pressure sorption using a Micromeritics ASAP 2020 surface-area analyzer.

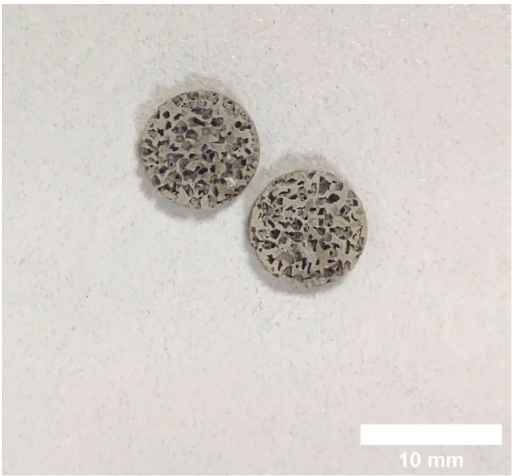

Figure 3-1. Photograph of the AZ31-based scaffolds obtained via infiltration casting.

3.3.2 Surface modification with DPNS

DPNS was introduced for porous materials and Mg-based foams. This surface treatment was carried out using ion–gas–neutral interactions with surfaces (IGNIS), a multi-purpose facility having an ultrahigh vacuum chamber operating at room temperatures, allowing surface modification and in situ characterization.

Before irradiation, the metallic foams were fixed to a molybdenum holder with double-sided adhesive carbon tape. The absorbed impurities on the surface were then cleaned using 1-keV Ar^+ ions at an angle of incidence of 45° for 5 min. After this step, the surface was irradiated with a Tectra GenII ion source, alternating a step of Ar^+ bombardment with *in-situ* X-ray photoelectron spectroscopy (XPS) scans to observe the transformation of the surface chemistry. All DPNS treatments and corresponding XPS measurements were performed in an ultrahigh vacuum (base pressure $<3\times10^{-8}$ Pa) operating at room temperature. The DPNS parameters are listed in **Table 3-1**.

Table 3-1 DPNS conditions of Mg alloy foams irradiated with normal incidence (0°)

Step	Energy [eV]	Fluence [cm^{-2}]	Angle [°]
1	400	1×10^{17}	0
2		5×10^{17}	
3		1×10^{18}	
1	700	1×10^{17}	0
2		5×10^{17}	
3		1×10^{18}	

Another set of samples was irradiated under the conditions listed in **Table 3-2**. Particularly, this set of samples was irradiated with an angle of incidence of 60º. In this case, XPS analysis was performed ex-situ at the IGNIS facility since the in-situ configuration was not available for oblique irradiation. This set of samples were analyzed immediately after irradiation; however, there was a short exposure to environmental conditions in the interval between irradiation and analysis. Details of the XPS analysis are described in the chemistry evolution section.

Table 3-2 DPNS conditions of Mg alloy foams irradiated with an off-normal incidence angle (60º).

Energy [eV]	Fluence [cm^{-2}]	Angle [°]
400	$1×10^{17}$	60
	$1×10^{18}$	
700	$1×10^{17}$	60
	$1×10^{18}$	

3.3.3 Characterization before and after DPNS

Surface morphology

Surface morphology before and after irradiation was evaluated with an SEM Hitachi 4800 at an acceleration voltage of 5 kV, a working distance of 8 mm, and a range of magnification of 35 kX. The surface was coated with Au and Pd sputtering to avoid the charging effects of Mg.

The Ga-ion beam in the Scios 2 focused ion beam (FIB; Thermo Scios 2 Dual-Beam SEM/FIB) was used to cut down vertically through the surface to observe the cross-section and the evolution of surfaces (**Figure 3-2**). The surfaces were prepared via a milling process and observed with the Scios 2 using backscattered electrons. A Pt coating was used to protect the surface from the Ga ions.

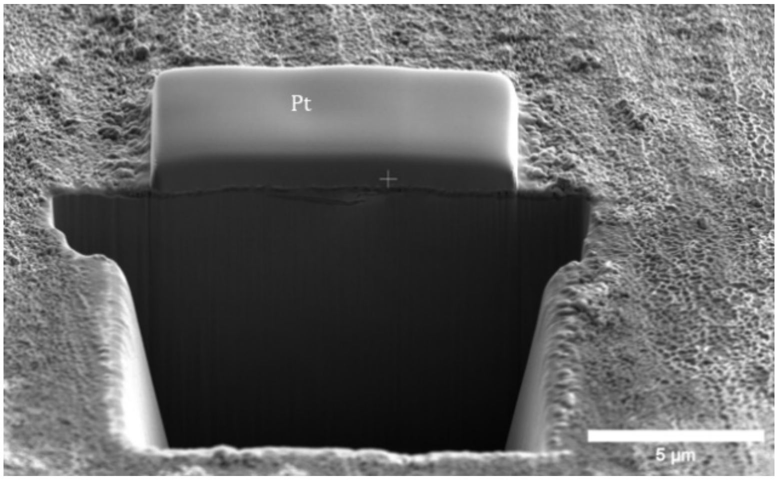

Figure 3-2 FIB sample preparation for cross-section analysis. A rectangular section was cut down vertically, and a layer of Pt was deposited on top to protect the surface of interest from the Ga ions.

Chemistry evolution

The surface chemistry of Mg foams was estimated via SEM (Hitachi 4700) equipped with energy dispersive spectroscopy (EDS) at an acceleration voltage of 15 kV. The surface was coated with Au and Pd sputtering.

X-ray diffraction (XRD) analyses were performed using a CuKα source using a Philips X'PERT diffractometer operating at 45 kV and 40 mA over the range of 10–90° (2θ) and a counting time of 2 s per step. The incidence angle omega was 2°.

XPS in situ (off-normal) and ex-situ (in 60 ° samples) measurements were carried out using the IGNIS facility on the same sample location as DPNS irradiations. An Al Kα (1486.6 eV) X-ray source (Specs XR-50) and hemispherical energy analyzer (Specs EP-150) were used to obtain full spectrum scans with 1 eV step size. The studied region scans were O1s and Mg2p peaks, mainly observing a complete reduction of C1s and small peaks of Al2p, all of them taken with 0.1 eV step size. All obtained spectra were analyzed using Casa XPS and Origin Pro software.

3.3.4 In vitro degradation

The samples were individually exposed to the Dulbecco's modified Eagles' medium (DMEM) solution under static conditions of 37 °C for 144 h with a DMEM volume corresponding to a surface-to-volume ratio of 50 ml cm^{-2}. H_2 release was monitored by the gas-collecting method, as suggested by [196]. The released gas was measured at seven different time points of 3, 24, 48, 72, 96, 120, and 144 h. The pH was measured at the same time points using a pH meter (Thermo Orion 720). Immersion media were collected at 24, 96, and 144 h, and the Mg-ion release and Ca present on the media were measured via ICP-OES.

3.3.5 Characterization during in vitro degradation

Surface morphology

Surface morphology after immersion was evaluated using SEM Hitachi 4800 at an acceleration voltage of 5 kV, a working distance of 7.4 mm, and ranges of magnification of 5 kX. The surface was coated with Au and Pd sputtering to avoid the charging effect of Mg.

Surface chemistry

The distribution of elements on the surface and the Ca:P ratio was measured using SEM/EDS at an acceleration voltage of 15 kV in secondary electron-detection mode.

The crystalline phases were studied with GIXRD with a CuKα source from a Philips X'PERT diffractometer, operating at 45 kV and 40 mA over the range, 10–90° (2θ), and a counting time of 2 s per step. The incidence angle omega was 2°.

3.3.6 Statistical design of experiments

A full factorial design was applied to find the levels of energy, fluence, and incidence angle that optimized the CaP ratio and minimized the H_2 evolution rate, where the levels of energy, fluence, and incidence angle were independent variables. The base designs consisted of three factors, eight combinations, and two replicates for a total of 16 runs. The runs were performed in random order. The factors and levels of the factorial design can be seen in **Table 3-3**. The obtained data were evaluated using an analysis of variance. Minitab software was used to perform this analysis. Significance was established at $p<0.05$. Details of the statistical design of experiments and analysis are shown in the supplementary material (**Appendix A**).

Table 3-3. The 2^3 factorial design, providing the lower (– 1) and upper (1) level.

	Level	
Variable	**-1**	**1**
Energy	400	700
Fluence	1×10^{17}	1×10^{18}
Angle	0	60

3.4 Results

3.4.1 Effect of irradiation conditions on surface morphology.

Figure 3-3 and **3-4** show the SEM images and their respective focused ion-beam cross-sections. The images were obtained using backscattered electrons in cross-section with a Pt cover deposited on the top to protect the surface during cutting and milling steps. Two different oxide layers can be identified in the pre-irradiated sample (**Figure 3-3**). A small dense layer adjacent to the metal (white) and a porous layer having a fibrous appearance on the top of the previous dense layer (yellow) are seen. The Pt cover on top was deposited by the FIB to protect the surface. After irradiation by DPNS, it can be seen that the significant thickness reduction of the oxide layer, compared to the untreated and the evolution of the surface, can be noted starting at 400 eV 1×10^{17} cm^{-2} when the oxide is transformed into a single and more compact porous layer (**Figure 3-3**).

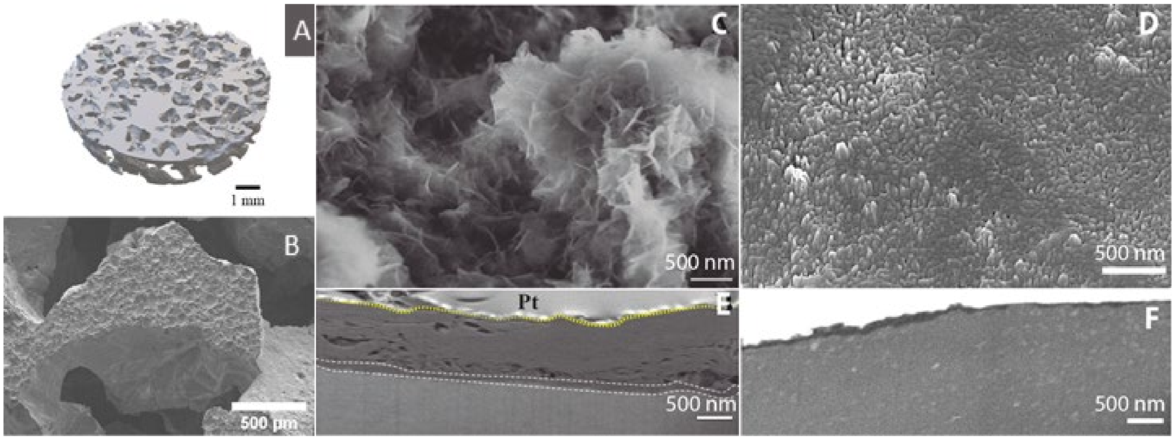

Figure 3-3. SEM images of Mg-based foams before irradiation highlighting the morphology of the corrosion layer forming on AZ31. a) volumetric representation of the scaffold. b) SEM of the as-cast scaffold. c) SEM images of Mg-based foams before irradiation highlighting the morphology of the corrosion layer forming on AZ31. top surface showing the hydroxide growth with a platelet-like morphology with random orientation. d) backscattered electrons cross-sectional images of the Mg-based foam before irradiation. White dotted lines mark the small dense layer of oxide adjacent to the metal, while the yellow dotted line shows a porous layer with a fibrous appearance on the top of the dense layer. This three-layer structure with random orientation platelet-like morphology on top (coexistence of MgCO3 and Mg(OH)2), dense oxide in the middle (MgO), and Mg matrix ad the end is typical for Mg surfaces after atmospheric exposure. A Pt layer was used to protect the surface from Ga ions. d) and e) show the surface after DPNS (700 eV, 1×1017 cm-2, 60o). The formation of nanostructures can be observed on the top surface, followed by the accumulation of Al-rich nanoclusters on the cross-section.

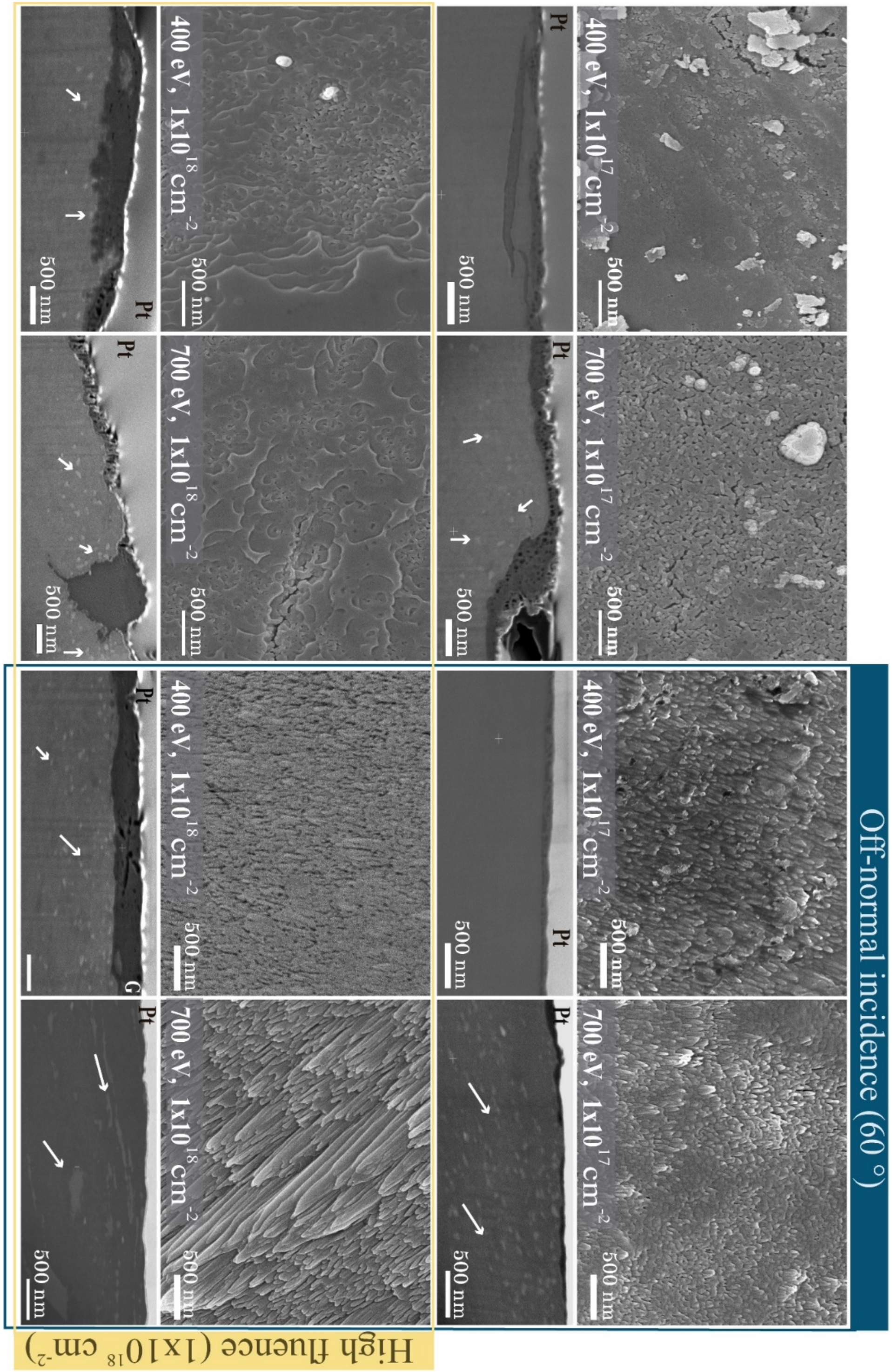

Figure 3-4. SEM micrographs of the surface transformation after different direct plasma nanosynthesis (DPNS) parameters. The top surface shows the oxide growth and backscattered electrons' cross-sectional images of the Mg-based foam after DPNS. White arrows show the Al nanoclusters formed on the adjacent subsurface. Mg-based foams after irradiation using normal incidence angle (0 °) presented the evolution of waves-like nanostructures on the top and the formation of Al-rich nanoclusters on the cross-section. Mg-based foams after irradiation with a 60° incidence angle: the

top surface shows the nanopillar-like nanostructures that are intensified with the increase in energetic conditions. Also, Aluminum nanoclusters formed at the interface are becoming larger and with remarkable orientation due to the incidence angle. Scale bars represent 500-nm.

Because the samples are porous, the near-surface region is rarely homogenous, and the surface transformation is influenced by the geometric configuration of the foams. Hence, the thickness of the oxide layer can follow the topographical characteristics, as observed in **Figure 3-4**. Because fluence and energy increased, the oxide layer reduced several nanometers to a relatively non-uniform thickness. Moreover, the surface was transformed into a more compact and less porous layer. Metallic-rich nanoclusters were observed below the oxide layers and were increased in quantity and size with the increase in energy, fluence, and angle.

Regarding the cross-section of 700 eV 1×10^{18} cm^{-2} 0° (**Figure 3-4**), the nanoclusters formed were intensified with the surface-angle modification. This hypothesis is in good agreement with the off-normal samples SEM images in **Figure 3-4**, which shows the irradiated surface having a 60º angle. The thickness of the oxide layer is higher in the 60º samples, whereas the formed nanoclusters are crowded and larger with specific orientations.

This surface transformation can be described by three principal events: elimination of the fibrous layer attributed to $MgCO_3$, nano-structuring of the oxide layer, and cross-section nanocluster formation. **Figure 3-4** shows the morphology and cross-section of the irradiated foams compared with the pre-irradiated sample in **Figure 3-3**. The figures show, for the 0º surface (see **Figure 3-4**), a reduction in the surface roughness occurring at higher energetic conditions. At 400 eV 1×10^{18} cm^{-2}, the surface is less homogeneous and could be described as the mix of 700 eV 1×10^{17} cm^{-2} and 700 eV 1×10^{18} cm^{-2} topographies. This surface behavior might be attributed to the inherited irregular geometry of the foam where the effective incident angles could locally have a distribution with respect to the surface normal near 0º incidence.

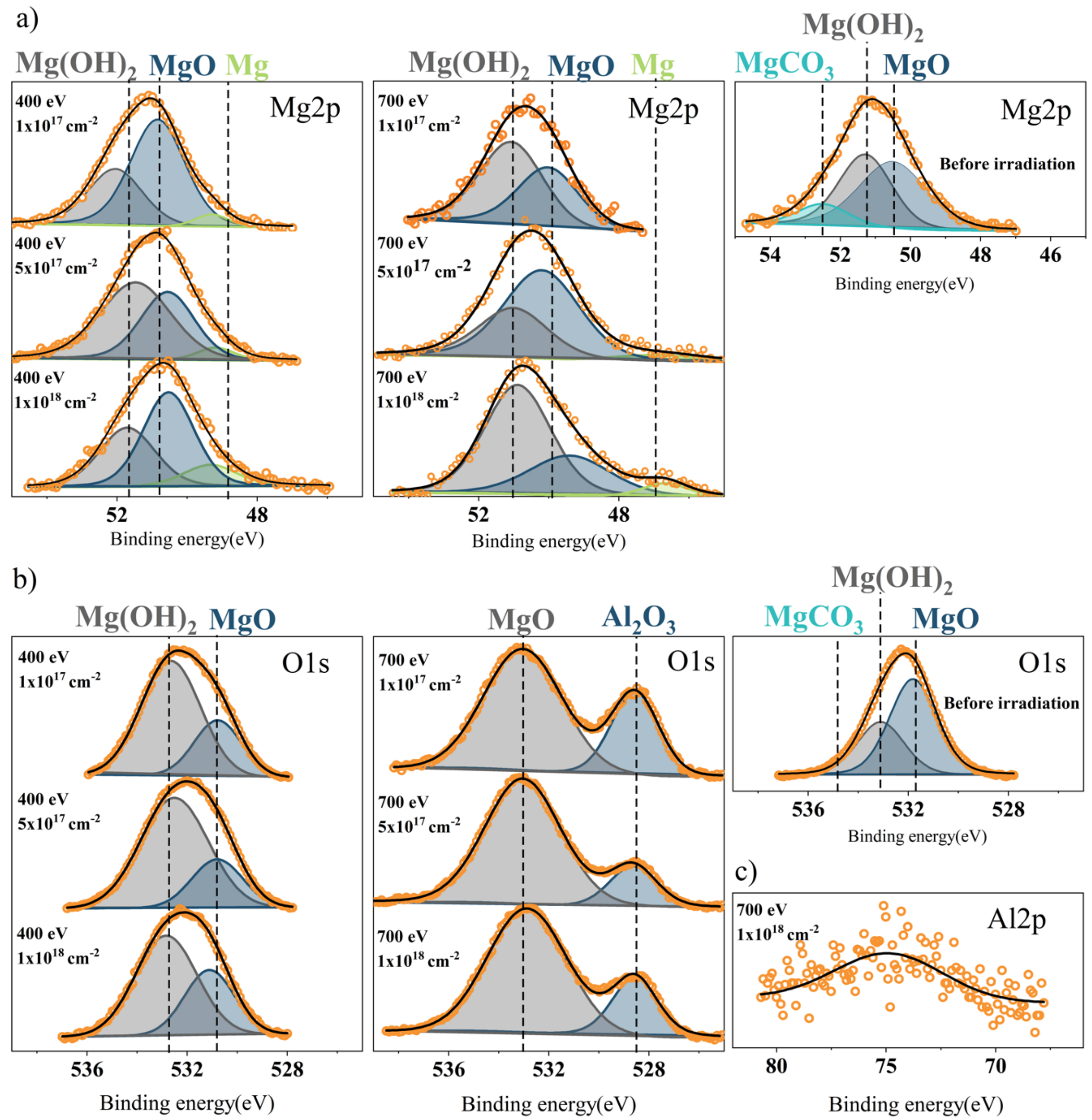

Figure 3-5. In situ X-ray photoelectron spectroscopy spectra of the Mg foams irradiated with normal incidence. a) shows Mg2p region for 400 eV and 700 eV varying the fluence from 1×10^{17} cm^{-2} to 1×10^{18} cm^{-2}. Mg(OH)$_2$ on the top surface is being eliminated to reveal the metallic Mg peak finally. The Mg2p peak before direct plasma nanosynthesis is also shown. b) shows O1s region for 400 eV and 700 eV varying the fluence from 1×10^{17} cm^{-2} to 1×10^{18} cm^{-2}. c) represents the Al2p region that appears at high fluence in 700 eV 1×10^{18} cm^{-2}.

For the case of oblique incidence (e.g.,> 45º), 60 º irradiations exhibited a greater degree of surface patterning and the formation of pillar-like nano and micro-structures inclined in the direction of the irradiation. The structures varied from a few 10's of nm to 1000's of nm at higher energetic conditions, as observed in 400 and 700 eV respectively at a fluence of 1×10^{18} cm^{-2}.

3.4.2 Effect of DPNS irradiation on surface chemistry evolution

The pre-irradiated surface observed in **Figure 3-3** can be principally described as the coexistence of MgO and $Mg(OH)_2$. **Figure 3-5** shows the in-situ XP spectra for Mg2p and O1s regions for the samples irradiated with normal incidence and pre-irradiated control surfaces. Ex-situ XPS of samples irradiated with 60 ° is shown in **Figure 3-6**. Shirley-Type background subtraction was used before peak fitting. Curve fittings were performed using mixed Gaussian/Lorentzian (GL) peaks. The Mg metallic peak was fitted with a GL ratio of 30/70 and an asymmetry of 40% [197]. Charge effects were corrected via C1s-peak at 286 eV. The substrate was cleaned via Ar^+-ion bombardment before DPNS.

A lower intensity peak was found after 5×10^{17} cm^{-2} at 49.1 eV, which is associated with the presence of metallic Mg. This surface chemistry change suggests that the irradiation altered the oxidation state of the surface species and that $Mg(HO)_2$ was eliminated to reveal the MgO nearest to the bulk. At 700 eV, Mg2p peaks BE decreased with the corresponding increase of the metallic Mg peak. The Al2p signal increased with the fluence, and it became visible with the combination of high energy and high fluence at 700 eV 1×10^{18} cm^{-2} 0° (**Figure 3-5**b). The Al2p presence suggests that the shift on the O1s peak on 700-eV species can also be attributed to the formation of Al_2O_3. Al2p peak particularly dominant in the 700 eV 1×10^{18} cm^{-2} 0° case had its highest and single intensity at 74.8 eV, indicating the presence of Al in the oxide form of Al_2O_3 (**Figure 3-5**b). **Figure 3-7** shows the changes in the concentration of the elements, on the 5-nm probing depth of in situ XPS, with the increasing fluence. It can be noticed the particular trend of the irradiation-enhanced Al segregation and the corresponding decrease of the oxygen atoms.

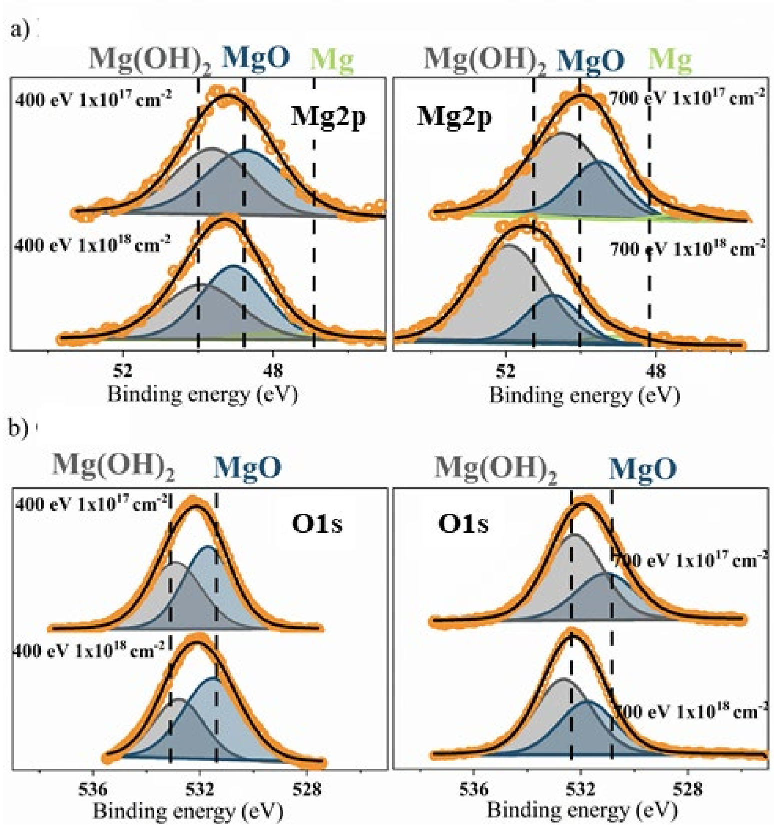

Figure 3-6. Ex-situ X-ray photoelectron spectroscopy spectra of the Mg foams irradiated with off-normal incidence (60°). a) shows Mg2p region for 400 eV and 700 eV with 1×10^{17} cm^{-2} and 1×10^{18} cm^{-2} fluences. $Mg(OH)_2$ is typical on Mg surfaces after atmospheric corrosion, even at short periods of exposure. This $Mg(OH)_2$ top layer is being eliminated via direct plasma nanosynthesis until the Mg metallic peak is visible after higher energetic exposures. b) represents O1s region for 400 eV and 700 eV at 1×10^{17} cm^{-2} and 1×10^{18} cm^{-2} fluences.

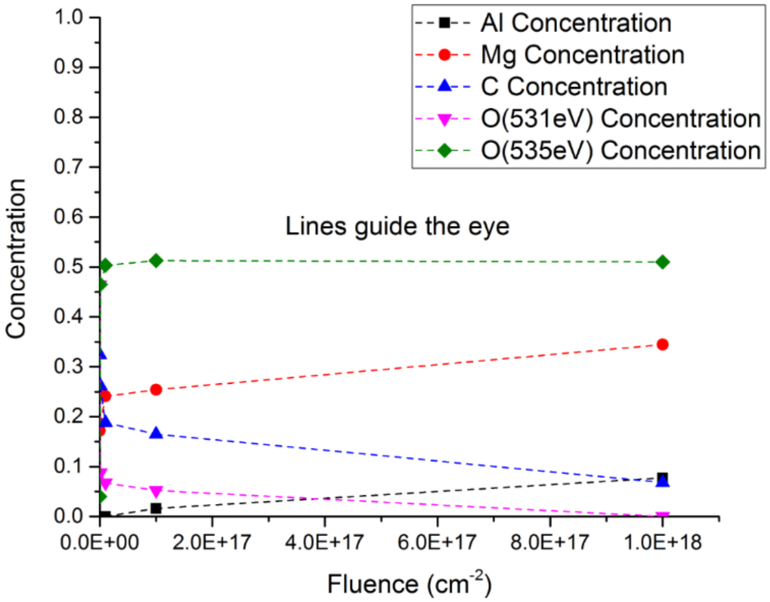

Figure 3-7. In-situ surface chemistry with XPS showing irradiation-enhanced Al segregation to the 5-nm probing depth of XPS to the surface of the Mg alloy. Also shown is the chemical behavior of oxygen atoms and their active chemical functionality during irradiation.

XPS at 60° is shown in **Figure 3-6**. Similar behavior can be observed in this set of samples. $Mg(OH)_2$ is most prominent in these cases since the samples were exposed to air before XPS analysis. Even after short periods of ambient exposure $Mg(OH)_2$ forms naturally on the MgO layer confirmed in these measurements [198]. It should also be pointed out the in situ measurements also mark the importance of running the experiments under these conditions. Unfortunately, the in situ configuration was not available for oblique irradiation. However, comparisons can still be made as to the irradiation over a sufficient time scale (e.g., fluence) removes any of the typical carbonaceous passivated layers on the surface of these Mg alloy foams and also helps drive Al atoms to the surface, which then reduces any remaining oxygen there.

EDS maps of the cross-sections reveal the general trend of the changes in the Al concentration on the foams subsurface with different DPNS parameters **(Figure 3-8,** page 57**).** According to cross-section FIB images, there is a region Al-enriched on the alloy substrate adjacent to the alloy/oxide interface that becomes detectable by XPS when the DPNS treatment almost eliminates the oxide layer. In agreement with FIB images and XPS spectra, Mg, MgO, and $Mg(OH)_2$ were the main products presented on the surfaces of the foam.

Figure 3-9 shows the diffraction patterns for pre-irradiated foam and all irradiated substrates. At a 2° angle of incidence, the XRD scan is much more surface-sensitive and offers information depth on the order of 200 nm [150]. All Mg peaks moved toward a high-angle direction, as illustrated for the 2θ=36.8 characteristic peaks. This effect was produced by a decrease in the lattice parameter of the Mg-rich phase with the enrichment of Al on the surface. A strong crystal texture plane was identified. This peak corresponds to the material bulk at 37°. The other Mg peaks were localized around 34.5°, 70.5°, and 48°, becoming more intense when increasing their energetic conditions. The MgO peak at 78° was only present in the pre-irradiated foam and 700 eV 1×10^{17} cm^{-2}. Some irradiated conditions exhibited additional peaks, suggesting the formation of new phases. The additional peaks coincided with $Mg(OH)_2$ (18.4°, 38°, and 58.9°), which is part of the corrosion nature of Mg, and Al_2O_3 (38°, 67.7°, and 78.3°) and is highly coincident with the data obtained via XPS and EDS.

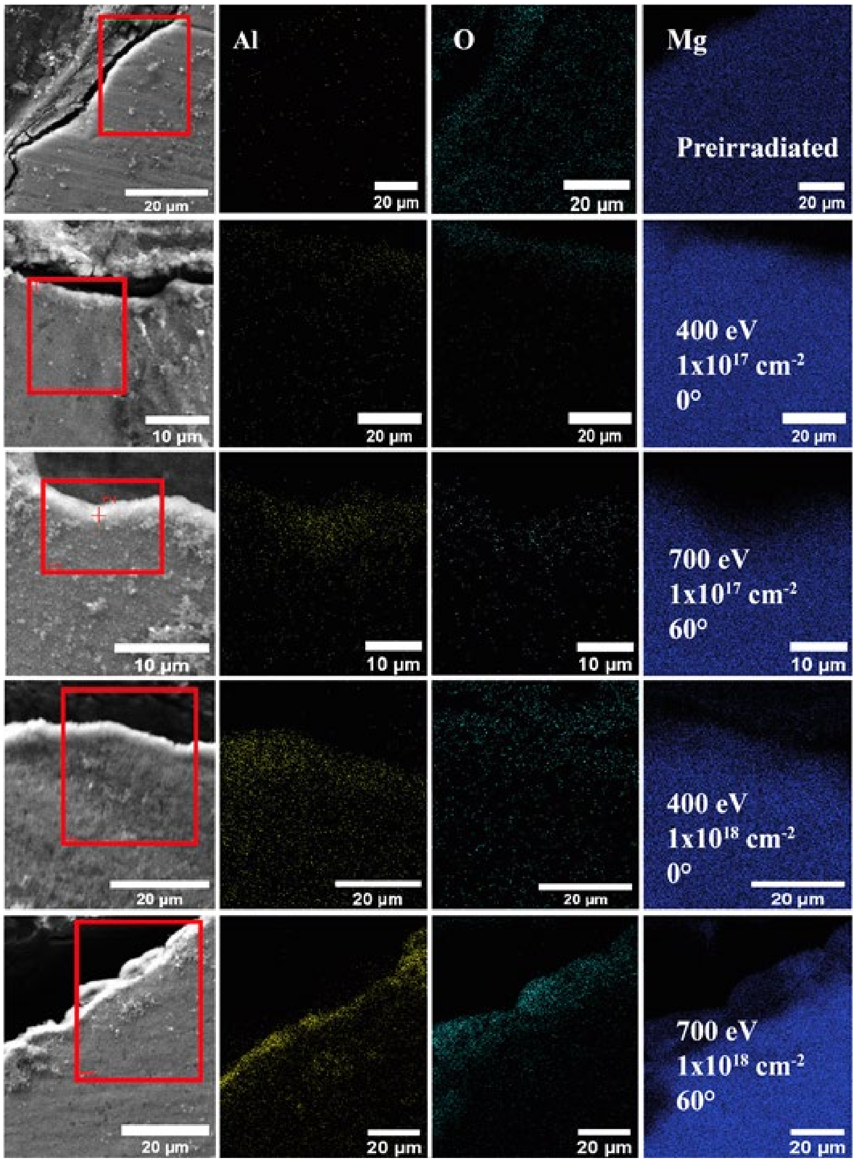

Figure 3-8 Al, O, and Mg EDS maps of the cross-section of different foams. Representative tendencies of the direct plasma nanosynthesis (DPNS) effect on Mg-based foam surfaces can be observed. Al increase in the near-surface is changing form barely detectable on the control sample and low energy conditions to visible higher concentrations after DPNS at high fluence, high energy, and high angle.

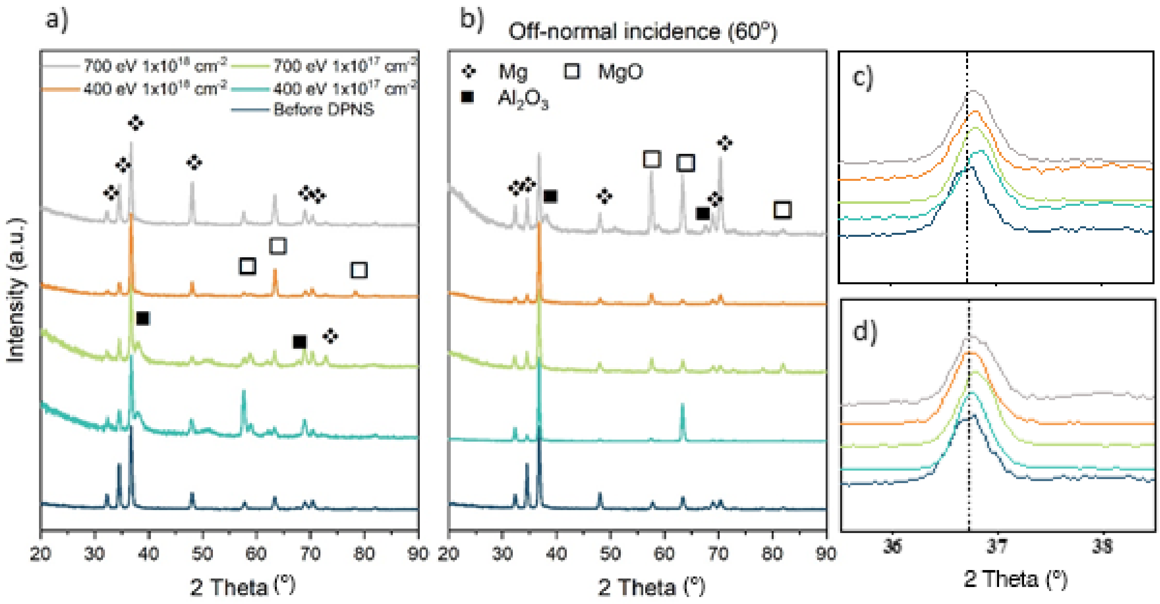

Figure 3-9. a) and b) GIXRD patterns of Mg foams after DPNS with the control spectra at the bottom. Mg and MgO were the principal phases on the pre irradiated surfaces. Al_2O_3 peaks are rising in the DPNS samples. c) and d) enlarged spectra of normal and off-normal incidence samples, respectively, near 2θ =36.8 to show peak shifts caused by a decrease in the lattice parameter of Mg-rich phase with the increased concentration of Al on the surface

3.4.3 Corrosion transformation mechanism

Pre-irradiated and modified foams were immersed in DMEM to evaluate their transformation properties and corrosion resistance. In this thesis, it is postulated that once an Al-rich interface is prepared with DPNS immersion in DMEM would enable the Mg alloy foam surface to transform into CaP phases that ultimately could be tuned to yield HA interfaces enhancing its osteoconductive properties. **Figure 3-10** shows the surface transformation after immersion in DMEM for 6 days. The pre-irradiated sample had a typical surface morphology with a great extension of mud cracking and plenty of white-product formation as a weakly protective layer. EDS was conducted on different random parts of the foam, and the distribution of elements is reported in **Figure 3-11**a. Mg and O were the principal elements on the surface. Ca, Na, and P from the DMEM were also present.

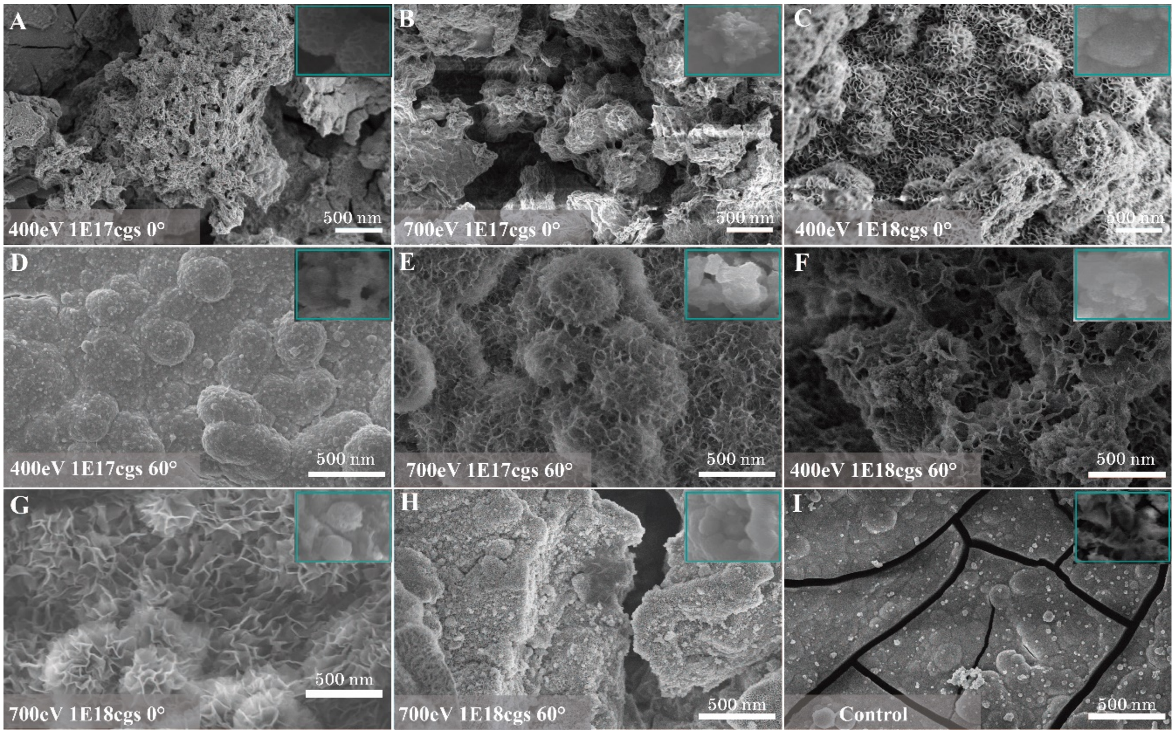

Figure 3-10. SEM micrographs of the samples after 144 hours of immersion in Dulbecco's modified eagle media with an upper inset of the area analyzed by EDS. The distribution of elements is shown in **Figure 3-10**a. Surface morphology is evolving from the cracks observed in I), no treated sample, to different oxides formed depending on the DPNS parameters. More uniform and protective surfaces are observed on samples B) and D). Cracks are again noticed in the surface of the samples irradiated with higher DPNS parameters in H). Scale bars represent 500 nm.

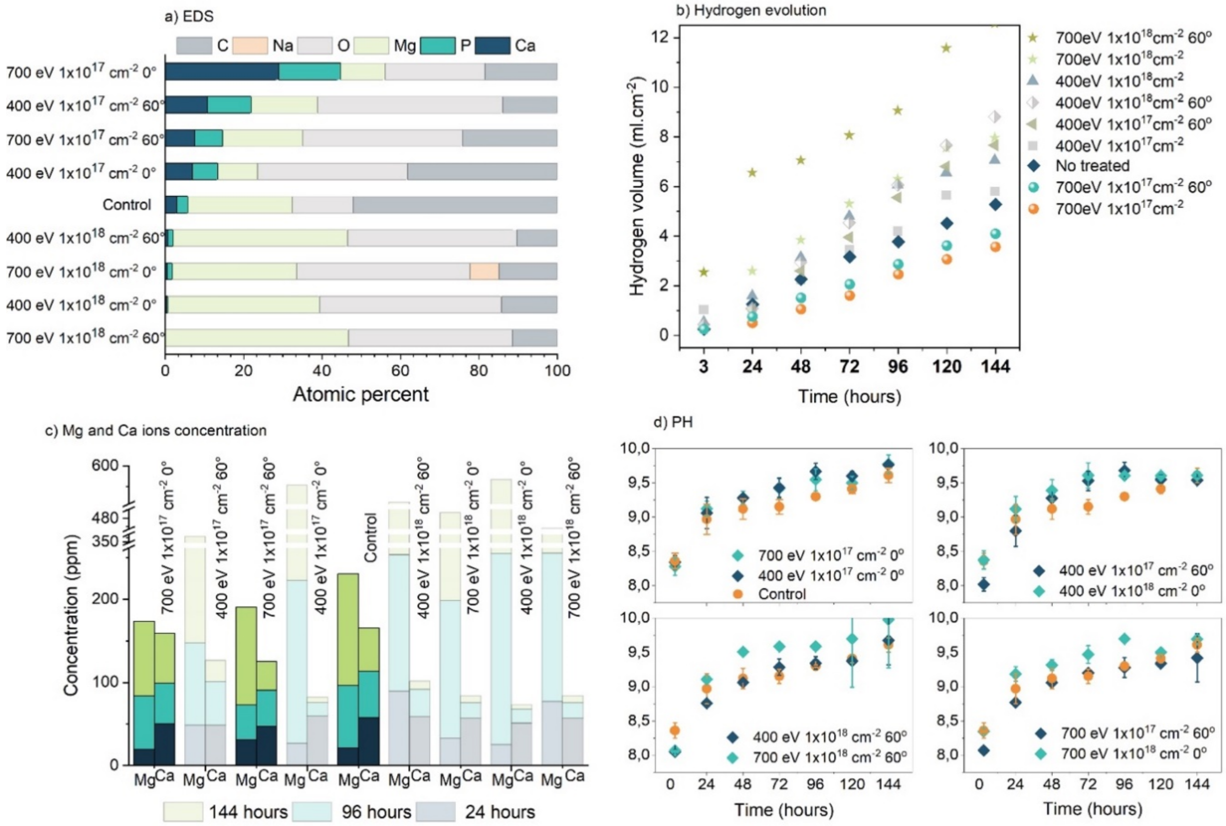

Figure 3-11 a) EDS showing the distribution elements on the surface of the sample after 144 hours of immersion. The modulation of the direct plasma nanosynthesis parameters led to a different distribution of elements on the surface. High fluence samples avoided Ca-phosphates depositions. Meanwhile, 700 eV 1x10^{17} cm^{-2} were more in favor of forming stable hydroxyapatites. b) Hydrogen volume calculated via the gas collecting method showing how H_2 release decreased in 700 eV 1x10^{17}cm^{-2} samples and highly accelerated with higher DPNS conditions. c) Mg release and Ca consumption calculated via ICP-OES. d) pH after different immersion periods. Data is shown as a mean ± standard deviation.

The transformation of the irradiated samples can be divided into two groups. The first group is low energy, low fluence, and zero-angle samples. In this group, a continuous and rough corrosion layer covered the surface, as **Figure 3-10**a shows. The nanostructures created with DPNS disappeared completely, and dense products configured in the form of half-spheres covered the substrate in surfaces irradiated under low energy, high fluence, and zero-angle degrees. The EDS analysis revealed that these spheres had Ca and P as their main elements. The second group showed island-like corrosion products corresponding to high energy, high fluence, and 0 and 60 substrates. Tiny nanosheets were formed on these surfaces, as **Figure 3-10**g and h shows. The size of the nanosheets increased with energy, angle, and fluence, and their assembly turned into spheres when increasing the energetic conditions.

Figure 3-11a shows the distribution of elements on the surface in atomic percent. Some tendencies can be identified: 1×10^{17} cm^{-2} fluence favored the formation of CaP phases and an increase of the CaP ratio. Minimal differences in the CaP ratio can be spotted between 400 and 700-eV energies at this fluence level. Particularly, 400eV 1×10^{17} cm^{-2} at 60 ° elements distribution ratios are coincident with calcium-deficient apatites [162,199]. A higher quantity of CaP appeared on the surface of 700 eV 1×10^{17} cm^{-2} samples. The CaP ratio increased from less than 1.0 to 1.8, indicating the formation of more stable CaP phases. At higher fluence levels, the accumulation of Ca and phosphate stopped. Mg and O were the main elements on the surface of 1×10^{18} cm^{-2} samples at both 400 eV and 700 eV. The EDS measurements showed that the corrosion layer comprised $Mg(OH)_2$ at an Mg:O ratio of 1:2 [30].

GIXRD analysis is shown in **Figure 3-11**, and the phases formed on the surfaces can be identified. 400eV 1×10^{17} cm^{-2} cases were very similar to the control samples having $Mg(OH)_2$ as the main transformation product. The 700 eV 1×10^{17} cm^{-2} samples showed the transformation of the surface into CaP-rich phases. Particularly, $CaHPO_4{\cdot}2H_2O$ was detected on the 700 eV 1×10^{17} cm^{-2} 0° substrate. Higher fluence samples showed more intense peaks of MgO and $Mg(OH)_2$.

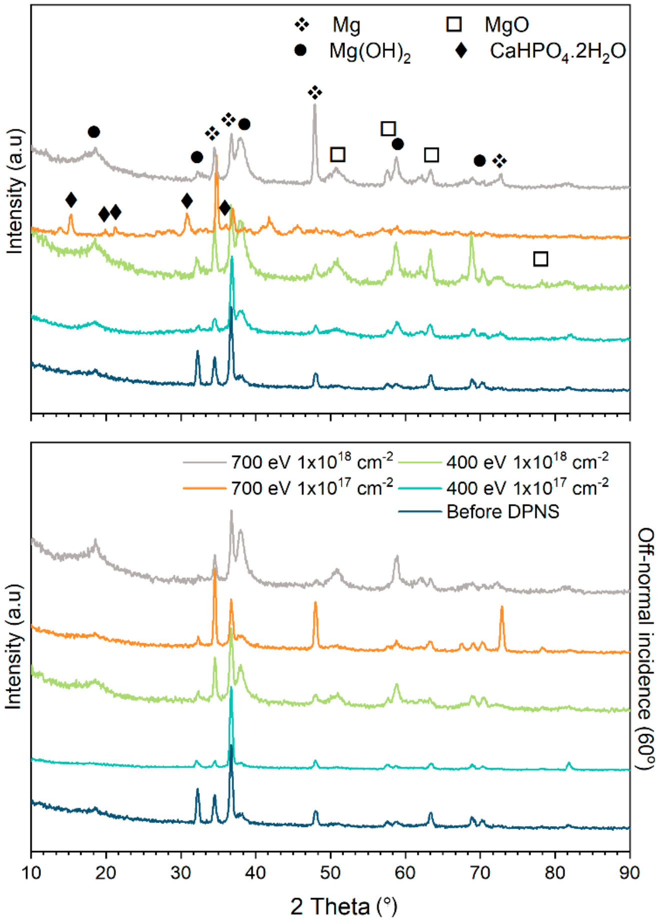

Figure 3-12. GIXRD patterns of Mg foams after immersion in DMEM. Normal (top) and off-normal incidence samples (bottom). $Mg(OH)_2$ is the principal corrosion product formed on the surface. $CaHPO_4.2H_2O$ phase is observed in the 700 eV 1x10^{17} cm^{-2} spectra after 144 hours of immersion.

The H_2 evolution curves of the samples immersed in DMEM for 144 h are shown in **Figure 3-11b**. The effects of DPNS in H_2 evolution were similar to those seen in the compositional analysis of EDS and XRD. The samples can be classified into two different groups matching the compositional data from **Figure 3-8**, **3-12**, and **3-11a**. The first group included samples that were less corrosive than the control. This group was coincident with the samples that formed CaP phases on the surface (i.e., 400 and 700 eV), irradiated using low fluence. Meanwhile, the second group was based on the samples having higher fluence and higher combinations of fluence and angle, which corresponds to the samples preventing the formation of CaP phases on the surface.

The plot shows that the H_2 evolution exhibited a decreasing trend when decreasing the DPNS parameters, such as with the surface irradiated with 700 eV 1×10^{18} cm^{-2} and 60 ° and the lowest rate for the 700 eV 1×10^{17} cm^{-2} 0 °. A comparable corrosion rate was noted between the Control, 700 eV

1×10^{18} cm^{-2} 0 °, and 400 eV 1×10^{17} cm^{-2} 0 °. However, 700 eV 1×10^{18} cm^{-2} 0 °, and 400 eV 1×10^{17} cm^{-2} 0 ° had a passivation tendency after 120 h of immersion.

3.4.4 Effect of DPNS conditions on CaP phases formation and hydrogen release

The Pareto chart of standardized effects at p = 0.05 is shown in **Figure 3-13**. All the values located at the right of the dashed line were significant for the treatment. The influence of the DPNS variables on the H_2 release is shown in **Figure 3-13**. H_2 release was influenced by fluence, and the interactions of fluence, energy, and angle. When energy increased, less fluence was required to produce a protective effect on the surface. On the contrary, an increase in the angle was detrimental to the corrosion of the foam. Because the goal was to minimize the H_2 evolution rate, the energy of 700 eV and fluence of 1×10^{17} cm^{-2} were the best combination of DPNS parameters to achieve that purpose.

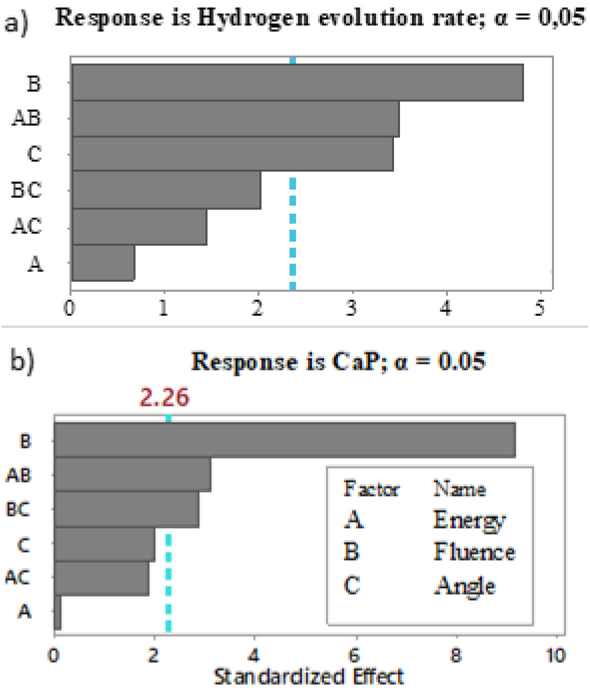

Figure 3-13 Pareto's chart of standardized effects for a) Hydrogen evolution and b) Ca-phosphate ratio. This chart reveals the absolute value of the magnitude of the effects. T-statistics that test the null hypothesis that the effect is 0 are considered standardized effects. A dotted line was also plotted to determine which effect was statistically significant. Bars that cross the dotted line are significant for the response at a 0.05 level of significance.

From the Pareto chart found in **Figure 3-13**b, one can conclude that there was a relation between CaP ratio, fluence, angle, and the interaction of fluence and angle. Energy by itself did not present a significant influence on the CaP ratio. However, the interaction between energy and fluence did influence the H_2 evolution rate. When energy increased, less fluence was required to produce a higher CaP ratio on the surface. According to the results, because our goal was to target a CaP ratio at 1.67 (to obtain hydroxyapatite stoichiometric ratio), the energy of 700 eV and fluence of 1×10^{17} cm^{-2} was the best combination of factors with the best response at 0 degrees. Details of the statistical and residuals analysis are shown in the supplementary material (**Appendix A**).

3.5 Discussion

3.5.1 DPNS effect on the topographic and compositional changes of Mg-based foams.

DPNS produced a multi-functional interface based on the evolution of well-ordered nanostructures and the preferential segregation of Al on the near-surface. The existence of topographical irregularities and surface chemistry of the foam were key factors involved in the different stages of the surface transformation. A well-defined DPNS process and its intrinsic high-fidelity control of surface properties enabled the mesoscale control of different material responses. In this context, "mesoscale control" is defined as changes in the nanometer-level scale tuned by DPNS manifesting themselves in macroscale properties such as corrosion rate, materials structure/morphology, and hydrogen production. In this sense, tunability of properties focused on the reduction of the H_2 release and the formation of a bioactive surface with the modulation of the CaP ratio. The preferential passivation points, even within the pores, acted as seeds to create CaP phases that protected the entire foam against corrosion processes.

As shown in **Figure 3-4**, during DPNS treatment, two consecutive processes occurred on the surface when the energy condition increased. Nanowaves, unperiodic nanowaves, and pillar-like nanostructures were produced as functions of energy, fluence, and incident angles with respect to the control or pre-irradiated surface. The initial processes were observed at 400eV 1×10^{17} cm^{-2} and were associated with morphological changes of the topography, including nanostructure formation and variations of the oxide states. The next processes were related to more complex compositional changes. Aluminum segregation from the interior of the alloy driven by low-energy irradiation was observed on the near-surface (**Figure 3-6** and **Figure 3-7**). This Al-enrichment is similar to the Al segregation produced by laser-surface melting [32,200] and high-current pulsed electron beam [33]. The preferential segregation of one alloy element can be explained as a strategy of the system to reduce its surface free energy [201]. Reichel et al. referred to this effect as bombardment-enhanced

Gibbsian segregation when there were nonequilibrium point defects on the alloy [35]. The GIXRD patterns presented in **Figure 3-8** support this conjecture because all Mg peaks moved toward high-angle directions, owing to the decrease in the lattice parameter of the Mg-rich phase with the increased concentration of Al on the surface [202–206]. Likewise, 400 eV 1×10^{17} cm^{-2} 0°, 700 eV 1×10^{17} cm^{-2} 0°, 700 eV 1×10^{18} cm^{-2} 0°, and 700 eV 1×10^{18} cm^{-2} 60° irradiated foams exhibited two additional weak peaks at $2\theta = 40.8$ and $2\theta = 68$, suggesting the formation of Al-rich phases in the form of Al_2O_3.

3.5.2 Effect of Al-enrichment on the corrosion mechanism of Mg-based foams

The increase in the Al content reduced the corrosion rate of Mg-Al systems. The formation of an Al-enriched layer on Mg surfaces enhanced passivation compared to typical Mg corrosion products ($Mg(OH)_s$). However, the improvement offered by Al on the alloy was conditioned by the Mg: Al ratio [30]. Feliu et al. reported higher corrosion rates on AZ61, compared to AZ31. They associated the lower corrosion rate with higher Mg–C content at the surface of the AZ31 samples [207]. Localized corrosion of AZxx systems was initiated at the interface between the Mg and Al-rich phases because of the galvanic coupling. The anodic dissolution of Mg took place, whereas the Al-rich phase acted as a cathode. This dissolution of Mg corresponded with the H_2 evolution and release of hydroxyl (OH^-) ions, increasing the local pH and that of the immersion solution. The local rise in pH was reported to catalyze the heterogeneous nucleation of CaP on the surface, which also changed the surface transformation dynamic, because the phosphate species present on the bath varied with the pH of the solution [162,208]. A high corrosion rate process was related to the rise in pH. In a strong corrosion process, the pH can rise to 10 and 11. In this case, the highest pH was seven, and the pH in the control sample was eight. This suggests that the foam may have had a better corrosion rate coming from the fabrication process. However, further comparisons are required to support this suggestion.

The modulation of DPNS parameters produced Al concentrations, on the subsurface, from undetected levels up to a 10% increase **(Figure 3-7)** and, consequently, the surface behaviors under immersion in DMEM also varied. From Pareto's chart, the CaP ratio was influenced by the fluence, angle, and the interaction fluence × angle and fluence × energy. A fluence value of 1×10^{17} cm^{-2} favors the formation of CaP phases on the irradiated surfaces. However, not all CaP phases obtained were effective against corrosion. There were no significant differences between 400 eV 1×10^{17} cm^{-2} 0° and 400 eV 1×10^{17} cm^{-2} 60° and the control. However, DPNS altered the corrosion mechanism, which can be noticed in the distribution of elements where a high content of carbon is observed in control (52 wt. %) after immersion in DMEM (**Figure 3-11**a).

The release of Mg ions can explain this effect. 1 ml of evolved H_2 roughly corresponds to 1 mg of dissolved Mg, and the dissolved Mg remains in the bath as Mg^{2+}. Released Mg^{2+} is necessary for the nucleation of CaP. However, an excess Mg^{2+} disturbs the CaP crystal growth and stabilizes amorphous CaP phases [162,209,210]. These surfaces showed thicker corrosion products associated with the $Mg/(Mg^{+}Ca)$ ratio and less developed structures with smaller crystals compared to 700eV 1×10^{17} cm^{-2} conditions (**Figure 3-10**).

When the energy was increased to 700 eV, the corrosion of the foams was reduced, probably by the increase in the percentage of passivating points (due to a slight Al-enrichment). Hence, an initial increase in pH caused by the precipitation of CaP phases was observed. However, the Mg^{2+} ions supply decreased due to the effect of the products deposited on the surface [211]. This decrease in the Mg^{2+} supply and the continuous exposure of the sample to Ca and P presented in DMEM media promoted the nucleation of more stable CaP phases. A reduction in hydrogen release is associated with a smaller rise in pH, which in turn influenced the precipitation process of CaP phases since fewer Mg^{2+} ions were present in the media. Small CaP crystals grew on semi-spheres, began to precipitate on all areas of the foam surface until they merge, and a continuous CaP film was formed (**Figure 3-10**). The sample of the series 700eV 1×10^{17} cm^{-2} (**Figure 3-12**), in which the $CaHPO_4 \cdot 2H_2O$ phase is present, showed well-developed crystals that are commonly associated with this phase [199]. The phases formed on these surfaces (700eV 1×10^{17} cm^{-2} 0° and 700eV 1×10^{17} cm^{-2} 60°) seemed more stable and were evolving towards the formation of HA since the pH of the samples was still increasing. Wang et al. [199] described the transformation of $CaHPO_4 \cdot 2H_2O$ into HA after a further increase in pH. The dissolution of $CaHPO_4 \cdot 2H_2O$ causes the release of CaP ions, and those ions are re-precipitated in the form of HA.

The second group consisted of higher energy that avoided the absorption of Ca and P from the immersion solution. Different hypotheses can be considered to explain this phenomenon; first, the excess of Al in the surface structure causes more intensive corrosion processes and faster Mg dissolution due to excess in galvanic sites [212]. Second, the increase in the hydrogen evolution rate caused an increase in the Mg^{2+} present in the media, and the excess of Mg^{2+} disturbed the CaP crystal growth process [210]. Finally, the poorly protective nature of the surface-induced a faster dissolution of the coating in the immersion solution, and the aqueous ions were still diffusing in and out of the coating [162]. Hence, although there is not a large amount of CaP on the surface, there is a low concentration of Ca is noticeable in the medium (**Figure 3-11c**). Avoiding the absorption of CaP on the surface is desirable for some Mg applications, such as vascular implants, when CaP deposits could block an artery near the Mg device [213].

3.6 Conclusion

In this study, DPNS was applied in open-porous Mg foams to modify their surface chemistries and topographies. The metallic foams were exposed to low-energy Ar^+ irradiation having two levels of energy, fluence, and angle. The surface morphology and chemistry were modified, observing an Al supply from the bulk content to the near-surface of the Mg-based foams. Then, samples were immersed in DMEM, which has an ionic composition similar to that of the human body. The surface behavior depended on combining the DPNS parameters and the synergistic interaction with the inorganic salts present in the DMEM. Hence, the foam surface can be tailored with one or more predetermined functionalities to design low H_2 corrosion or high CaP-ratio Mg foams for a tunable and intelligent design approach of future Mg-based biodegradable materials in biomedical implants.

4. DPNS-Mg scaffolds as osseointegration interfaces

4.1 introduction

As seen in **section 3.2**, directed plasma nanosynthesis (DPNS), an atomic-scale additive manufacture method, was used in the present thesis to transform AZ31-based foams into degradable porous scaffolds with a nanostructured surface and controllable degradation, to repair bone cavity defects. The combination of the DPNS parameters (energy, fluence, and incidence angle) was used to modulate the corrosion response of the scaffold via the nanostructuration of the surface and the Al supply on the subsurface via ion-assisted Gibbsian segregation. As a result of the screening in **chapter 3**, the surfaces of the scaffolds were customized with one or more predetermined functionalities to produce a lower H_2 release or high CaP-ratio for different purposes.

The Al bulk content in the methodology presented in **chapter 3** was kept constant; thus, fluence, energy, and angle were the only variables analyzed. However, preliminary assays in the author's master thesis showed that the degree of Al-enrichment in the foam-surface region after DPNS is also dependent on the appropriate Al weight fraction. Hence, samples having two different Al bulk contents (2.02 wt.% and 3.3 wt.%; Zn content was 1.1 wt.% in both cases) were irradiated with the same DPNS conditions (energy 400 eV, fluence 1×10^{18} cm^{-2}, and angle 0°). The Al concentration on the near-surface after DPNS varied with the alloy composition, and a more pronounced enrichment of Al was observed in the sample with 3.3 wt.% Al. The slight increase in the right sample favored the formation of CaP-rich phases on the surface after immersion in DMEM (see **Figure 4-1**).

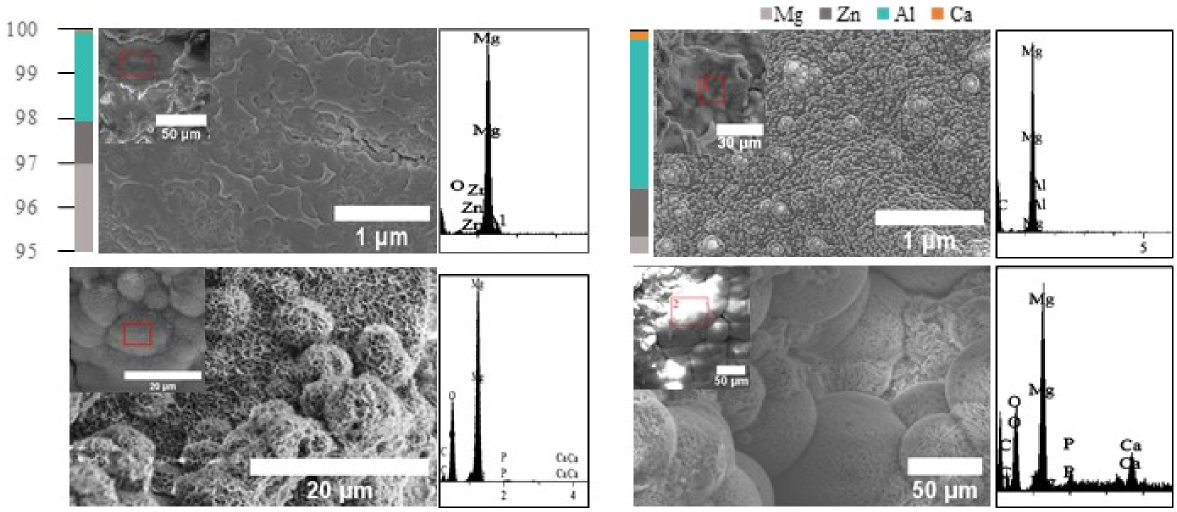

Figure 4-1. Scaffolds surface after DPNS and after immersion in Dulbecco's modified eagle medium (DMEM). The scaffolds had different Al bulk contents (2.02 wt.% left and 3.3 wt.% right), which produced different responses on the surface. The scaffold with 3.3 wt% Al bulk content favored the formation of CaP-rich phases when immersed in DMEM.

A remaining question is the nano topography's role on the surface evolution during the corrosion process. A controversial discussion about the role of surface topography in Mg's corrosion mechanism debates the statement that roughness influences Mg corrosion. Nguyen et al. [214] reported that the increase in R_a increases pure Mg corrosion. Similarly, Alvarez et al. [215] evaluated AE44 surfaces at different polishing levels and reported that the decrease in surface roughness caused strong corrosion and accelerated pits' formation. However, there are high dimensional differences in the reports mentioned above, and the surfaces by Alvarez et al. were comparatively smooth. Walter et al. [156] described that the surface roughness does not significantly affect Mg and alloys' general corrosion despite the rougher surface locally accelerated the pitting corrosion. Despite the last-mentioned data, the reports focused on the role of surface topography of Mg on corrosion resistance are limited to date.

To the best of the author's knowledge, this is the first report that describes the modulation of well-ordered nanostructures on porous Mg. During the ion's bombardment, the surface is far from equilibrium, and several processes are occurring, including the nanostructuration of the surface as an expression of the kinetic processes that are taking part. However, due to the evidence that the Mg-Al systems' passivation ability is highly conditioned to the Mg: Al ratio [30], the author postulated that the change in chemistry caused by DPNS is the dominant factor during the corrosion of Mg.

This chapter aims to evaluate the role of surface nanotopography on the apatite formation ability of Mg surfaces. It is then hypothesized that the ability of DPNS to control the corrosion dynamics and drive the formation of a high CaP-ratio and hydroxyapatites protects the surface from rapid corrosion resulting in a great biocompatible surface. Moreover, the material's bioactivity is enhanced by different mechanisms: the surface topography transformed via DPNS increases cell adhesion and proliferation. Concomitantly, the presence of Mg^{2+} promotes osteoblastic differentiation and the regulation of the secretion of proinflammatory cytokines towards greater osseointegration. Hence, the biological behavior of the DPNS-modified AZ31 scaffold regarding the surface transformation and Mg ions release is evaluated, including the behavior of bone marrow-derived human mesenchymal stem cells (hBM-MSCs), murine preosteoblast MC3T3.E1 cells, and the inflammatory response of J774A.1 murine macrophages

One key challenge related to work with Mg-based scaffolds is their continued reaction in different environments. Due to this reactive behavior, the in vitro cultured tests directly on the Mg surface subject the cells to constant surface changes, highly alkaline environments, and high concentration of Mg ions and hydrogen bubbles [216]. Besides, Mg continues to react with the commercial assays' solutions and components, interfering with the final result. For example, Mg concentration and pH are parameters that affect the tetrazolium-based tests that are used to quantify cellular growth and proliferation, leading mainly to false-positive results [217]. Similarly, Mg samples react with the phosphate-buffered saline (PBS) solution [139]. This solution is widely used to wash the samples between dying steps, and it probably buries the cells into a corrosion layer that hampers their identification in fluorescence tests [218]. On the other hand, manipulating porous structures introduces another challenging aspect, as a wider surface area is exposed to continuous corrosion and ion release and makes it harder to focus while using confocal or inverted fluorescence microscopy.

Therefore, most of the in vitro tests of Mg-based biomaterials use non-contact methods based on ISO 10993-12, in which the cells are exposed to a specified concentration of the corrosion products of the samples [219,220]. As these methods were initially developed for nondegradable materials, the dynamic corrosion of Mg is omitted from the test. The direct in vitro culture on Mg-based surfaces presents new aspects of the surface transformation that profoundly affect biological behavior. Cipriano et al. demonstrated that the surface topography transformation played a more critical role in the modulation of F-actin than did Mg ions or the pH of the extract of the material [216]. However, some researchers have avoided the implications of the in vitro tests by directly performing in vivo trials after the in vitro corrosion and mechanical characterization [220]. Because of ethical implications, the effect of metal ions, insoluble corrosion products, and the surface transformation characteristics on the cellular behavior, the in vitro response should be analyzed to provide unambiguous evidence for subsequent in vivo trials.

4.2 Methods

4.2.1 Surface modification via DPNS

The specimens were fixed on a molybdenum sample holder with double-sided carbon tape. The foams were cleaned using 1-keV Ar^+ ions at an angle of incidence of 45° for 5 min. Subsequently, the surfaces were irradiated at the IGNIS facility using a Tectra GenII ion source operating at room temperature in ultrahigh vacuum (base pressure $< 3 \times 10^{-8}$ Pa). The applied energy was 400 eV, the fluence was 1×10^{18} cm^{-2}, with the target holder directed onto the beam.

4.2.2 Surface characterization before and after DPNS

The compositional changes of the surfaces were evaluated via X-ray diffraction (XRD) analyses in a Philips X'pert diffractometer with a CuKα source at 45 kV, 40 mA, and 2 s counting time per step. The scaffolds were covered with Au and Pt and were evaluated using scanning electron microscopy (SEM; Hitachi 4800) at an acceleration voltage of 5 kV. The distribution of elements on the surface was analyzed via SEM on an instrument equipped with energy-dispersive spectroscopy (EDS; Hitachi 4700) at an acceleration voltage of 15 kV in secondary electron-detection mode. Control sample XPS and in situ XPS after DPNS were carried out in IGNIS with the conditions described in **section 3.3.3**.

Contact angle measurements were carried out with a deionized water droplet volume of 3 µL on an optical apparatus (Ramé-hart 250 contact angle goniometer) with DROP image Advanced Software.

4.2.3 Degradation test

The samples were individually exposed to DMEM at 37 ºC under static conditions for 7 d using a volume of DMEM corresponding to a surface-to-volume ratio of 50 ml cm^{-2} [81,221]. The samples were evaluated via SEM/EDS after 5 h of immersion. The cross-section of the DPNS sample after 5 h of immersion was analyzed via FIB as described in **section 3.3.3**.

The samples were removed from the media at three different time points: 24, 96, and 144 h. The pH was measured at the same time points using a pH meter (Thermo Orion 720). The corrosion products were removed after ASTM G1 by dipping them in a solution of 150 g CrO_3+10 g Ag_2CrO_4 in 1 L deionized water in boiling conditions. Subsequently, the weight loss (W) was measured to calculate the corrosion rate (Cr) using **Equation 2-8**. Immersion media were collected, and the Mg-ion release was measured via inductively coupled plasma optical emission spectroscopy (ICP-OES).

The compositional changes of the corroded surfaces after 144 h were re-evaluated via XRD, SEM, and SEM/EDS, as described in **section 4.2.2**. All experiments were run in triplicate in independent tests.

4.2.4 In vitro biological response

Cell culture

hBM-MSCs were purchased from the American Tissue Culture Collection (ATCC®-PCS-500-012) and cultured following the manufacturer's protocol. In short, hBM-MSCs were cultured using Mesenchymal Stem Cell Basal Medium (MSCBM; ATCC PCS-500-030) supplemented with Mesenchymal Stem Cell Growth for Bone Marrow-derived MSCs (ATCC PCS-500-041). These cells were used for cell proliferation and adhesion tests and alkaline phosphatase (ALP) enzyme quantification tests.

Murine preosteoblast (MC3T3-E1; subclone 4), from ATCC (ATCC®CRL-2594) and used to evaluate the expression of bone-related genes. MC3T3 cells were cultured in Alpha-Minimum Essential Medium (α-MEM) supplemented with 10% FBS at 37 ºC, 5% CO_2, and 95% humidity. Finally, the inflammatory response was analyzed using a murine macrophage cell line (J774A.1) from the ATCC (ATCC®TIB-67). These cells were cultured in DMEM supplemented with 10% fetal bovine serum (FBS) at 37 ºC, 5% CO_2, and 95% humidity.

Cell adhesion, focal points, and cell spreading

The samples were autoclaved and preincubated in MSCBM 16 h before the seeding step, as suggested in [222]. Sterile samples were placed on 48-well culture plates and seeded without removing the media at a cell density of 10,000 hBM-MSCs/cm^2 at 37°C, 5% CO_2, and 95% humidity. Empty tissue culture plastic (TCP) wells (without scaffolds) were used in parallel in the same plate as Mg samples as a positive control (with cells) and negative control (only media). Forty-eight-well plates were strategically selected to limit the movement of the sample inside the well and avoid the upside-down of the sample. After 24 h, the culture media was removed (800 µl) and consecutively renewed every 48 h by the addition of 800 µl of fresh medium.

Fluorescence stains were used to assess cell spreading and the formation of focal adhesions after 4 h, 24 h, and 7 d of culture using the following procedure: cells on the scaffolds were washed with deionized water and fixed with 3.7% formaldehyde for 15 min. Each step was followed by quick rinses with deionized water to avoid further reaction of the material with PBS. The samples were then permeabilized with 0.1% Triton X-100 in PBS for 3 min and blocked with 1% bovine serum albumin (BSA). Finally, the specimens were covered for 30 min with a solution containing Texas Red®-X phalloidin (Thermo Fisher) and vinculin (H-10, Sc-25336, from Santa Cruz Biotechnology) dissolved in 100 mM Tris-HCl, 0.3% Triton X-100, and 5% BSA in PBS. Simultaneously, 4,6-diamidino-2-phenylindole (DAPI, Sigma) was used to stain cell nuclei as a contrast staining. Fluorescence micrographs were taken by confocal laser scanning microscopy (Leica SP8 UV/Visible).

Similarly, after the specified incubation periods, the specimens were washed with deionized water and fixed with 3.7% formaldehyde for 30 min at room temperature. Subsequently, fixated samples were subjected to stepwise dehydration with a progressive series of ethanol–water solutions (50% to 100%) for 15 min each. Finally, the surfaces were covered with Au and Pt and observed using SEM (Hitachi 4800).

Alkaline phosphatase activity

DPNS and control Mg scaffolds were seeded as previously described (using hBM-MSCs and 10,000 cells/cm^2). After 48 h in culture, cell differentiation was induced by adding 10 nM dexamethasone, 6 μM ascorbic acid, and 10 mM β-glycerophosphate sodium to the MSCBM. Wells without materials were used in parallel as TCP and were also induced to cell differentiation. After 4 and 7 d, the differentiation behavior was estimated based on ALP activity, as assessed using the colorimetric ALP assay kit (Abcam, ab83369), an early osteogenic differentiation marker that turns yellow after the dephosphorylation of *p*-nitrophenyl-phosphate by ALP. The cell lysates were obtained by rinsing the disks with PBS and applying osmotic and thermal shocks with ultrapure deionized water. Disks without cells were subjected to the same procedure and were used to exclude the material's effect.

Osteogenic differentiation via real-time polymerase chain reaction (RT–PCR)

Extraction media of DPNS samples and controls were prepared after ISO 10993-12. The extraction vehicle was the culture medium α-MEM completed with FBS to extract both polar and nonpolar substances. The scaffolds were incubated in a completed α-MEM with a surface area to medium volume of 1.25 cm^2/ml at 37°C. After 24 h, MC3T3 cells were cultured with the extracts without further filtration at a density of 5×10^4 cells/cm^2 in 24-well plates for 48 h. Subsequently, the osteogenic inductive supplements listed above were added to the extracts. This media was renewed every 48h.

After 7 and 14 days of cell incubation, the extracts were collected to evaluate the expression of the *ALP*, Runt-related transcription factor 2 (RunX2), and osteopontin (OPN) genes via real-time polymerase chain reaction (RT–PCR). Total RNA was extracted using the PureLink RNA Mini Kit (Invitrogen). The RNA quality was measured was assessed via Nanodrop Absorption Spectroscopy. Only samples with absorbance readings 260/230 nm between 1.8 and 2.0 were used for the following steps. Quantification of the selected genes was performed using the SYBR green PCR master mix (Invitrogen). The sequences of the forward and reverse primers used in this study are listed in **Table 4-1**. The mean cycle threshold (Ct) value of each target gene was normalized against the Ct value of the glyceraldehyde 3-phosphate dehydrogenase (*GAPDH*) housekeeping gene. The ΔΔCt method was used to compare mRNA expression levels. The results are expressed as fold changes in gene expression using the mean and standard deviation of the level of expression of the target gene (2−ΔΔCT). MC3T3 cells cultured in alpha-MEM supplemented with the osteogenic inductive supplements listed above were used as a tissue plastic control.

Table 4-1. RT-PCR primers

Gene	Primers (F, forward; R, reverse)
OPN	F:TCTGATGAATCTGATGAACTGGTC R:GGTGATGTCCTCGTCTGTAGCA
ALP	F:GACAATCGGAATGAGCCCACAC R:GTACTTATCCCGCGCCTTCACCAC
Runx2	F:TGCGGCCGCCCCACGACAA R:ACCCGCCATGACAGTAACCACAGT
GAPDH	F: TGT GTC CGT CGT GGA TCT GA R: TTG CTG TTG AAG TCG CAG GAG

Measurement of pro and anti-inflammatory cytokines

The J774 cells were cultured in direct contact with the preincubated surfaces at a density of 10,000 cells/cm^2 in 48-well plates. After 1 and 4 d in culture, the amounts of IL-10 (Legend Max, BioLegend) and TNF-α (eBioscience) in the macrophage culture were detected using ELISA kits according to the manufacturers' instructions. Wells without materials were used in parallel as TCP. Disks without cells were subjected to the same procedure and were used to exclude the material's effect.

4.2.5 Statistics

All experiments were run in triplicates using three samples per condition. The experimental results were expressed as mean ± standard deviations. Statistically significant differences were checked using one-way ANOVA, followed by Dunnet's multiple comparison test. Statistical analysis was carried out using the Minitab software. $P < 0.05^*$ was considered statistically significant and $P < 0.01^{**}$ was considered highly significant.

4.3 Results

4.3.1 Characteristics of samples before and after DPNS

Similar to the results in **chapter 3**, DPNS generated nanometric modifications as well as changes in mesoscale surface characteristics. **Figure 4-2**a shows the rust layer formation on the as-received sample, and **Figure 4-2**b shows the distribution of elements on the pre-treated surface where Mg and O were the governing elements, followed by Cl and Al. **Figure 4-3** and **Figure 4-4** show that the platelets from the preirradiated scaffold disappeared and were replaced by nanostructures that differed regarding the location and geometry on the scaffold. Notably, at the top surface (**Figure 4-3**a), after Ar^+ irradiation at 400 eV, the morphology of the scaffold exhibited a new boundary shape filled with bean-like nanostructures that became progressively elongated with the increase in the distance from the surface to the pore center (**Figure 4-3**b). The element distribution on the DPNS samples consisted principally of Mg, O, and Al (**Figure 4-4**b). The new presence of Al (11.79 wt.%) on the surface should be noticed. The XRD patterns also exhibited differences, as reflected in the shift of the Mg peaks (**Figure 4-5**b).

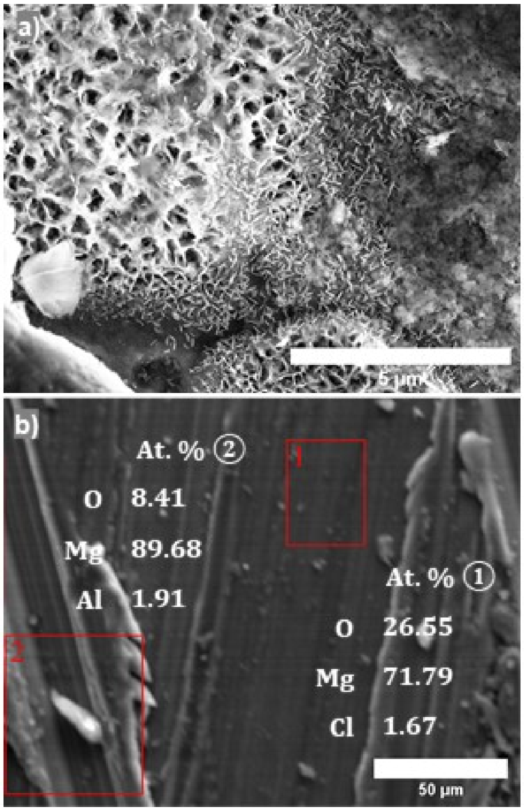

Figure 4-2. SEM micrographs and EDS analysis of the pre-treated sample. a) the SEM micrograph reveals the platelet layer formed on the surface due to atmospheric corrosion. b) is a less magnified view of the surface, showing the spots for EDS analysis and the distribution of elements on the surface.

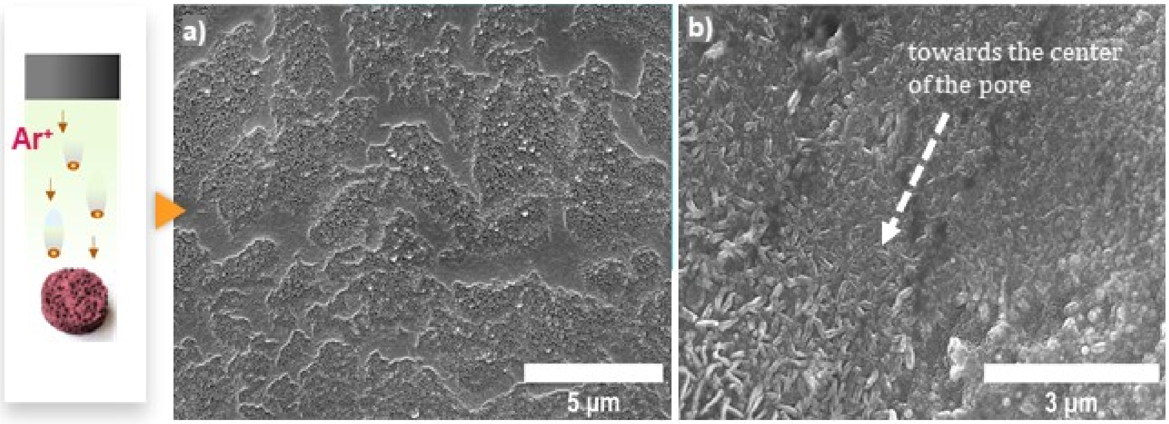

Figure 4-3. SEM micrographs of DPNS scaffolds. e). After direct plasma nanosynthesis (DPNS; Ar^+ ions bombardment), beams-like nanostructures were formed on the surface. b) is the DPNS surface of the inside of a pore where it is observed that nanostructures size is increasing directly with the distance from the surface.

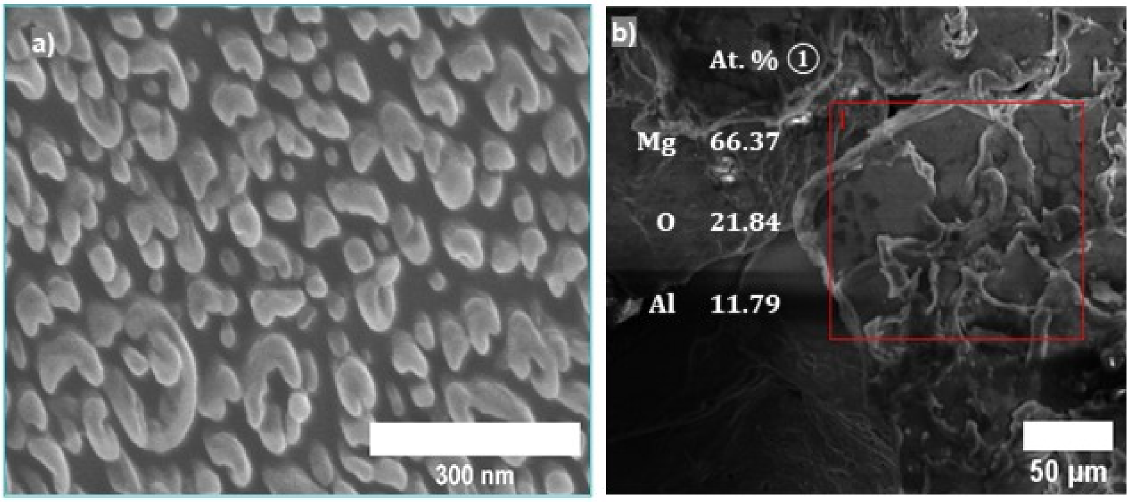

Figure 4-4. SEM and EDS evaluation of DPNS scaffolds. a) DPNS sample at higher magnification reveals the formation of beans-like nanostructures. b) higher magnification showing the distribution of the elements on the surface calculated via EDS.

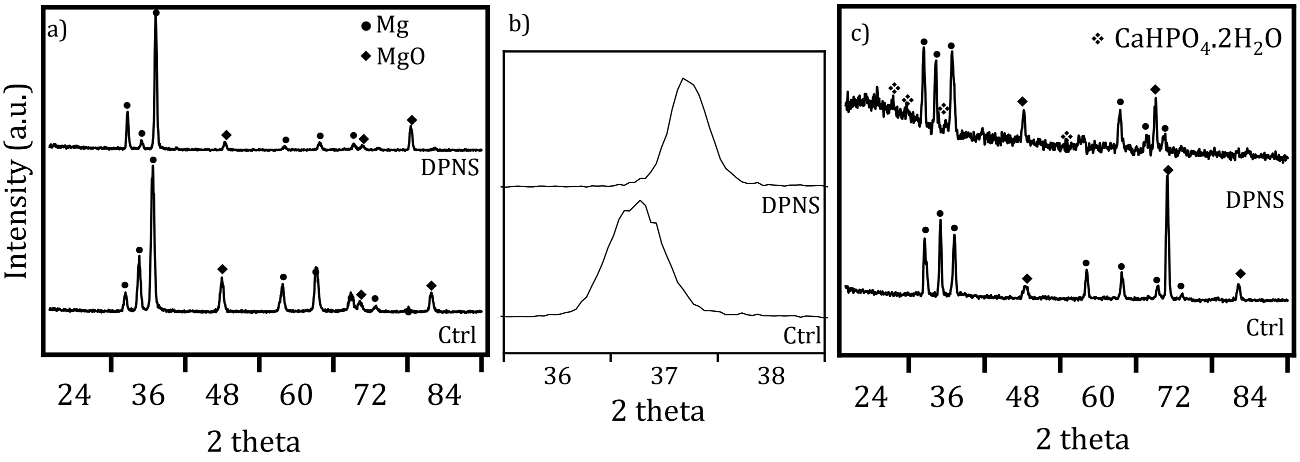

Figure 4-5. XRD measurements of Mg scaffolds before and after direct plasma nanosynthesis (DPNS) treatment. a) complete spectra of Ctrl and DPNS samples. b) presents the enlarged spectra near the 36.5 peak of Ctrl and DPNS samples. Mg peaks after DPNS moved toward high-angle directions, owing to the decrease in the Mg-rich phase's lattice parameter with Al's increased concentration on the surface. c) complete spectra of DPNS and Ctrl samples after immersion in Dulbecco's modified eagle media. The $CaHPO_4$-$2H_2O$ phase is formed on the surface of the DPNS sample.

Figure 4-6 shows the surface topography and wettability. The control surface corresponds to a significantly oxidized surface with broad O1s spectra indicating the coexistence of MgO, $Mg(OH)_2$, and $MgCO_3$ (see **section 3.4.2**). A complete spread of the water was observed on this control sample. Comparatively, the DPNS sample exhibited a significant change in the wettability reflected in an increase in the contact angle (100.7 ± 6.9°). Moreover, the XP spectra revealed a negative shift corresponding to eliminating the hydroxide and carbonate layers.

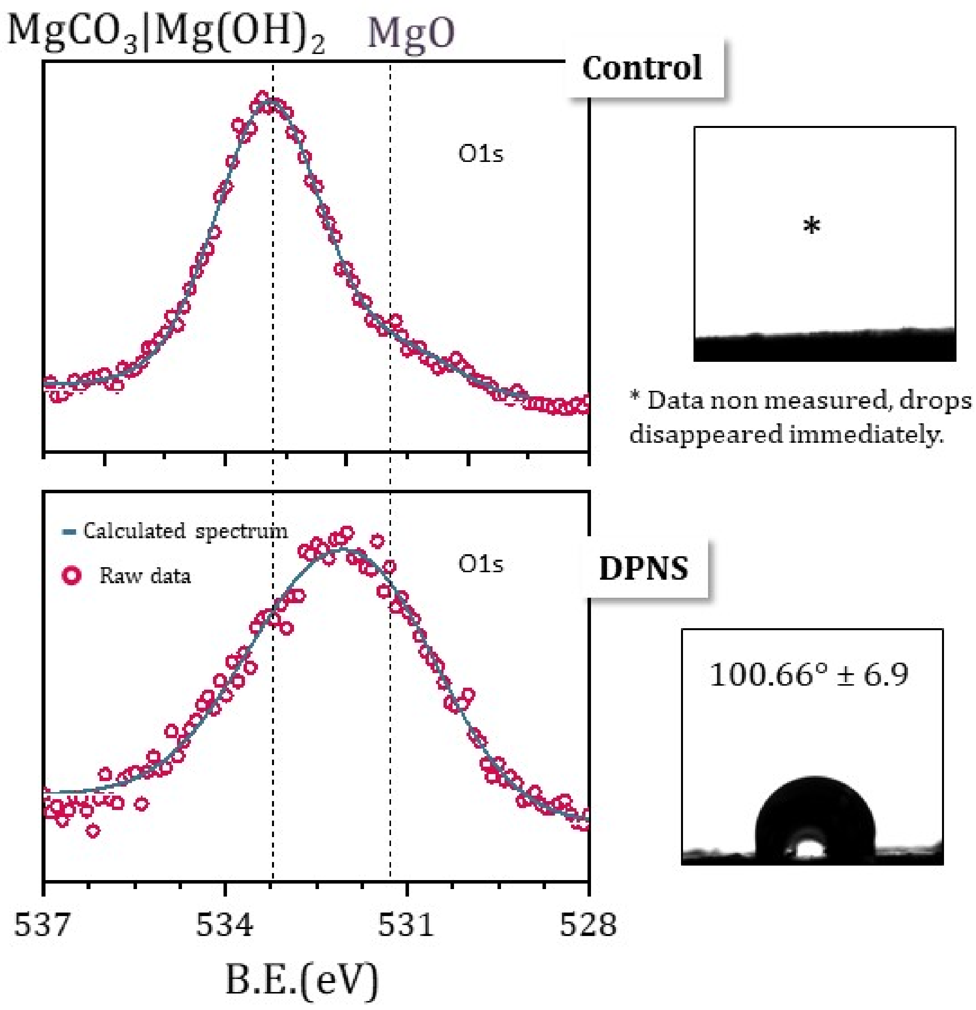

Figure 4-6 in situ XPS analysis (O1s) and contact angle measurements before and after DPNS. Top, XP spectrum, and contact angle showing the complete spread of the water on the control surface. b) XP spectrum shows the elimination of the hydroxide and carbonate layers after DPNS and increases the contact angle, indicating a more hydrophobic behavior.

4.3.2 Surface transformation after immersion in DMEM

After 5 hours of immersion, the DPNS surface showed a significantly higher Ca: Mg ratio (0.93 vs. 0.22) than the control (**Figure 4-7**). **Figure 4-8** shows the DPNS surface, after 5 hours of immersion, coated with a continuous layer of corrosion products that replaced the initial nanostructures' formation at the near-surface.

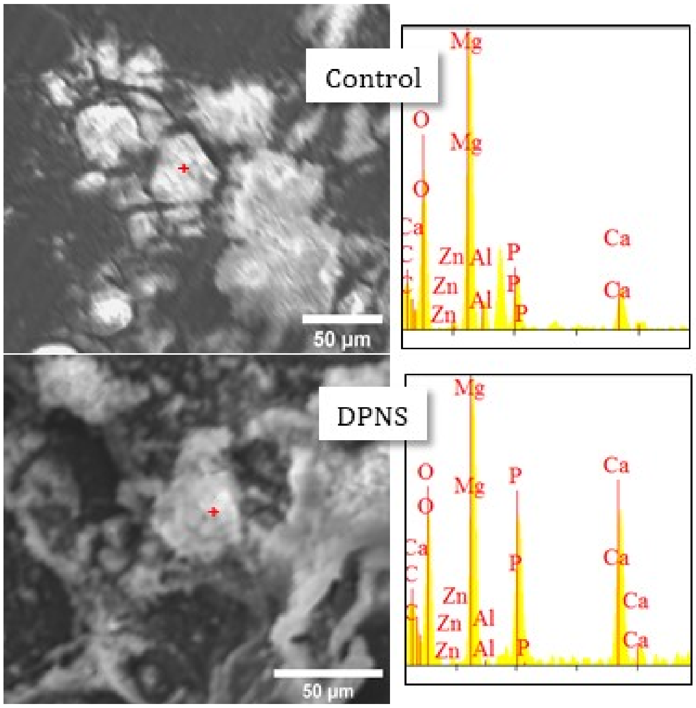

Figure 4-7. SEM/EDS analysis of control and DPNS samples after five hours of immersion in DMEM. CaP deposition is accelerated after the DPNS treatment.

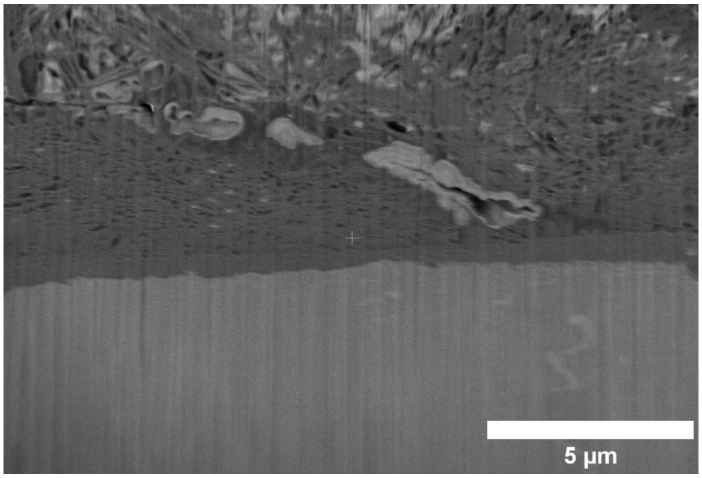

Figure 4-8 Cross-section SEM micrograph of the DPNS surface after five hours of immersion in DMEM. The initial nanostructures at the top surface were entirely covered by the corrosion products deposited on the surface.

After 48 hours of immersion in DMEM, the pretreated scaffold disks exhibited considerable structural changes, which varied from small surface erosional pits to a severely cracked surface. A network structure could be observed because of the presence of the cracks. A thin film was observed under the cracks after 4 d of immersion (**Figure 4-9**a). DPNS samples also showed significant structural changes. These structural changes were governed by outgrowths of deposited crystal structures (**Figure 4-10**a and **4-10**b). The presence of cracks was dramatically reduced compared with the pretreated samples, and, after four days of immersion, the crystal outgrowths were replaced by small crystals that grew on semi-spheres **Figure 4-10**d. At high magnification, packed flakes were identified (**Figure 4-10**e and **4-10**f). Those structures merged with adjacent structures to form a continuous film of semi-spheres.

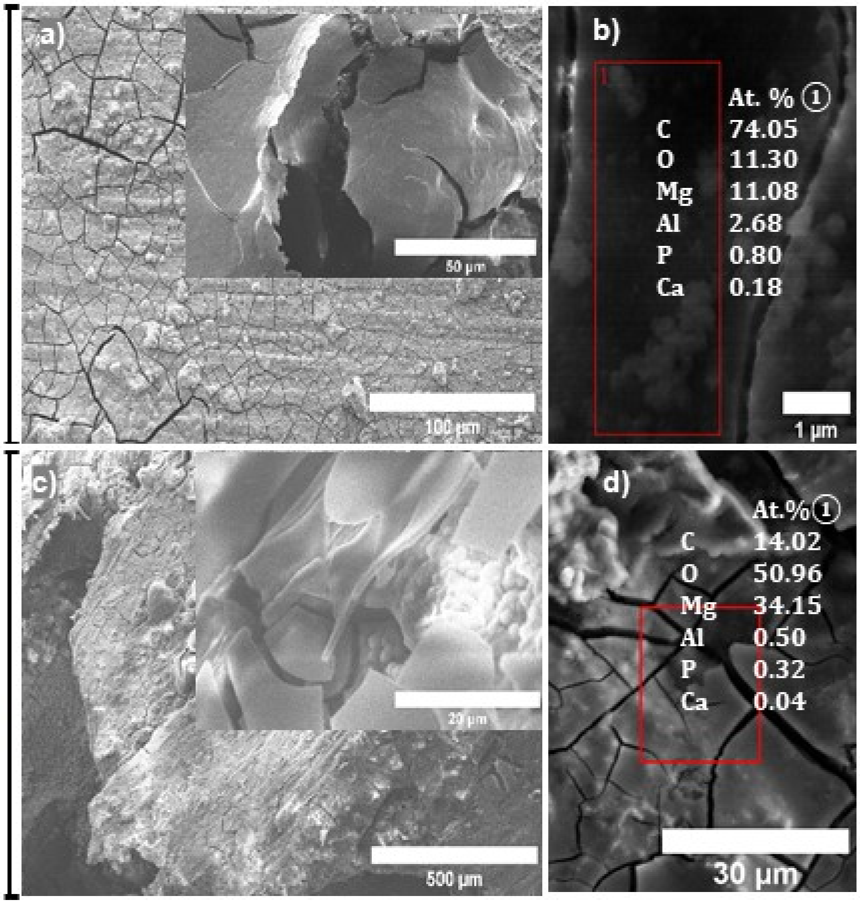

Figure 4-9 SEM micrographs of the control samples after 48 hours and 96 hours of immersion with respective EDS analysis. a) samples after 48 hours of immersion with an inset of a higher magnification view. b) EDS after 48 hours. c) sample after 96 hours of immersion with an inset of higher magnification. d) EDS analysis after 96 hours of immersion in DMEM.

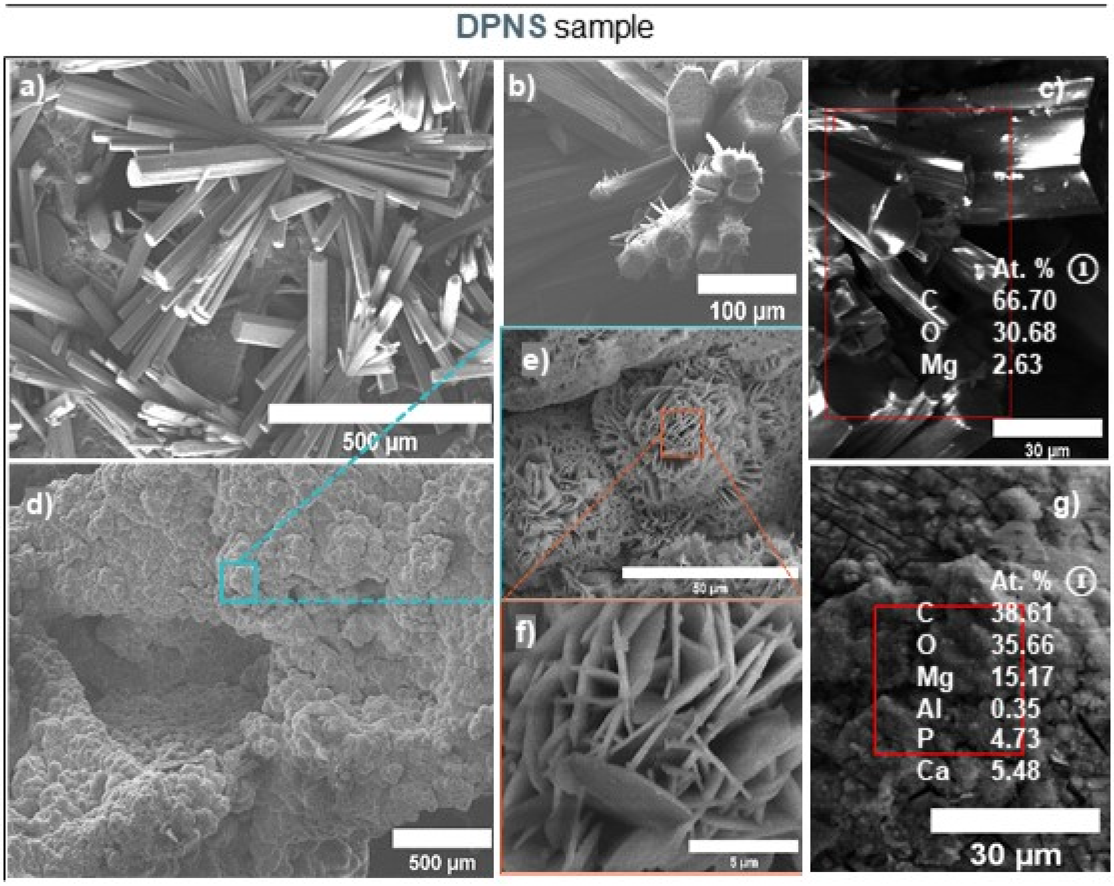

Figure 4-10. SEM micrographs of the DPNS samples after 48 hours (top) and 96 hours (bottom) of immersion with respective EDS analysis. a) samples after 48 hours of immersion with an inset (b) of a higher magnification view. c) EDS after 48 hours. d) sample after 96 hours of immersion with insets (e and f) of higher magnification. g) EDS analysis after 96 hours of immersion in DMEM.

The chemistry of the corroded bare samples revealed a high C and O content on the surface. This C and O content was then replaced by small traces of Ca and P. However, only Mg and MgO phases were detected under the sensitivity limits of the XRD (**Figure 4-5**). In comparison, the DPNS samples favored the formation of CaP phases. The content of Mg, Ca, C, O, and P in the films grown on the DPNS scaffold suggests that different compounds are present on this surface, such as the coexistence of $Mg(OH)_2$ with CaP supported by the strong presence of Mg (15.17 wt.%). There was also an increase in the C content, which indicates the formation of carbonates containing hydroxyapatite. The CaP-ratio on the DPNS surface was ~1.16:1, which was slightly higher than the 1:1 ratio predicted by dicalcium phosphate dihydrate (DCPD) [223]. The additional Ca can be attributed to other mechanisms, such as Ca or CaO incorporation in the rising structures. Moreover, the peaks present on the XRD pattern of the DPNS samples (**Figure 4-5c**) were attributed to $CaHPO_4$-$2H_2O$.

The pH values of the immersion solutions and the release of Mg ions measured via ICP-OES were recorded and are shown in **Figure 4-11**. In all cases, i.e., treated and non-treated scaffolds, it can be seen that the pH value increased abruptly and decreased after 20 h of immersion. However, before 24 h of immersion, the pH values on DPNS scaffolds (8.81 ± 0.21) were similar to those of the pretreated samples (8.77 ± 0.14), and there were no significant differences in the quantity of Mg ions released. Nevertheless, pretreated samples exhibited a faster ascending curve. After 48 h of immersion, the pH values of the treated samples were lower than those of the pretreated samples, suggesting that a more stable and protective surface was obtained after the DPNS treatment. These results were also confirmed by lower Mg ions released and corrosion rate on DPNS scaffolds compared to control samples, denoting significant differences at 2, 7, and 14 days.

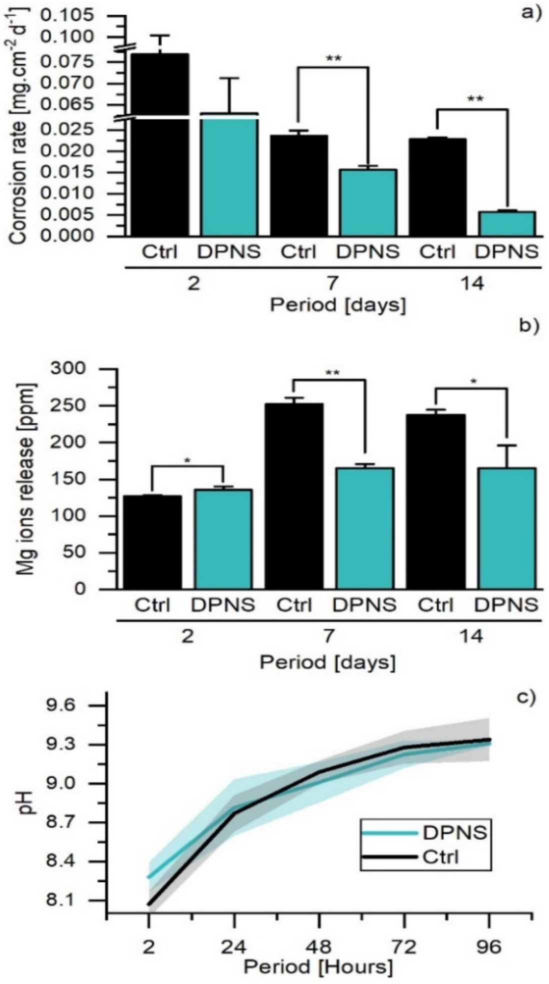

Figure 4-11 Samples degradation in Dulbecco's modified eagle medium (DMEM) after different time points. Results were $p < 0.05$ (*) were considered statistically significant, and $p < 0.01$ (**) highly statistically significant. a) corrosion rate calculated via mass loss after 2, 7, and 14 days of immersion in DMEM via the gas collecting method. Highly significant lower corrosion rates are observed on the DPNS samples after 7 days of immersion. b) Mg ions evaluated via ICP-OES also showed a significant decrease in the release after 7 days of immersion. pH in c) was calculated at the first 96 hours.

4.3.3 Cellular response

Figure 4-12a shows the adhering process of hBM-MSCs on both surfaces after various periods. After cultivation for 4 h, most of the hBM-MSCs seeded on the two types of surfaces seemed spherical without spreading out. However, it should be noticed an advanced cell adhesion and higher cell density attached to the DPNS surface; hBM-MSCs on DPNS samples showed filopodia prolongations interacting directly with the scaffold surface, which is a sign of initial and stable adhesion process (**Figure 4-13**; white arrow). Twenty-four h later, pretreated samples exhibited more independent cells that lacked contact between cells and with the surface and had less expanded and round nuclei. The hBM-MSCs grown on DPNS samples for 24 h showed a greater number of cells with a more elongated cell morphology and evident filopodia and lamellipodia formation.

Moreover, focal adhesion points were observed via vinculin staining (**Figure 4-12**b). SEM micrographs evidenced the interaction of the cells with the evolving surfaces (**Figure 4-13**). After 24 h of cell culture, hBM-MSCs were spread over the crystal outgrowths, and after 4 d of culture, they were extended over the continuous CaP surface, with the fluorescence in **Figure 4-12**a indicating cells with well-developed nuclei and widespread fibroblastic phenotype shapes. The staining of vinculin protein, which participates in focal adhesion points, was observed (**Figure 4-12**b). The scaffolds exhibited strong autofluorescence, despite the use of BSA to block the nonspecific background signal.

SEM micrographs acquired after 24 h and 4 d of culture showed cells attached to the crystal outgrowths on the DPNS samples, followed by the spreading of the cells over the CaP crystals that formed on the surface. In contrast, cells in pretreated samples exhibited a more rounded morphology and lowered filopodia contacts indicative of an immature adhesion state.

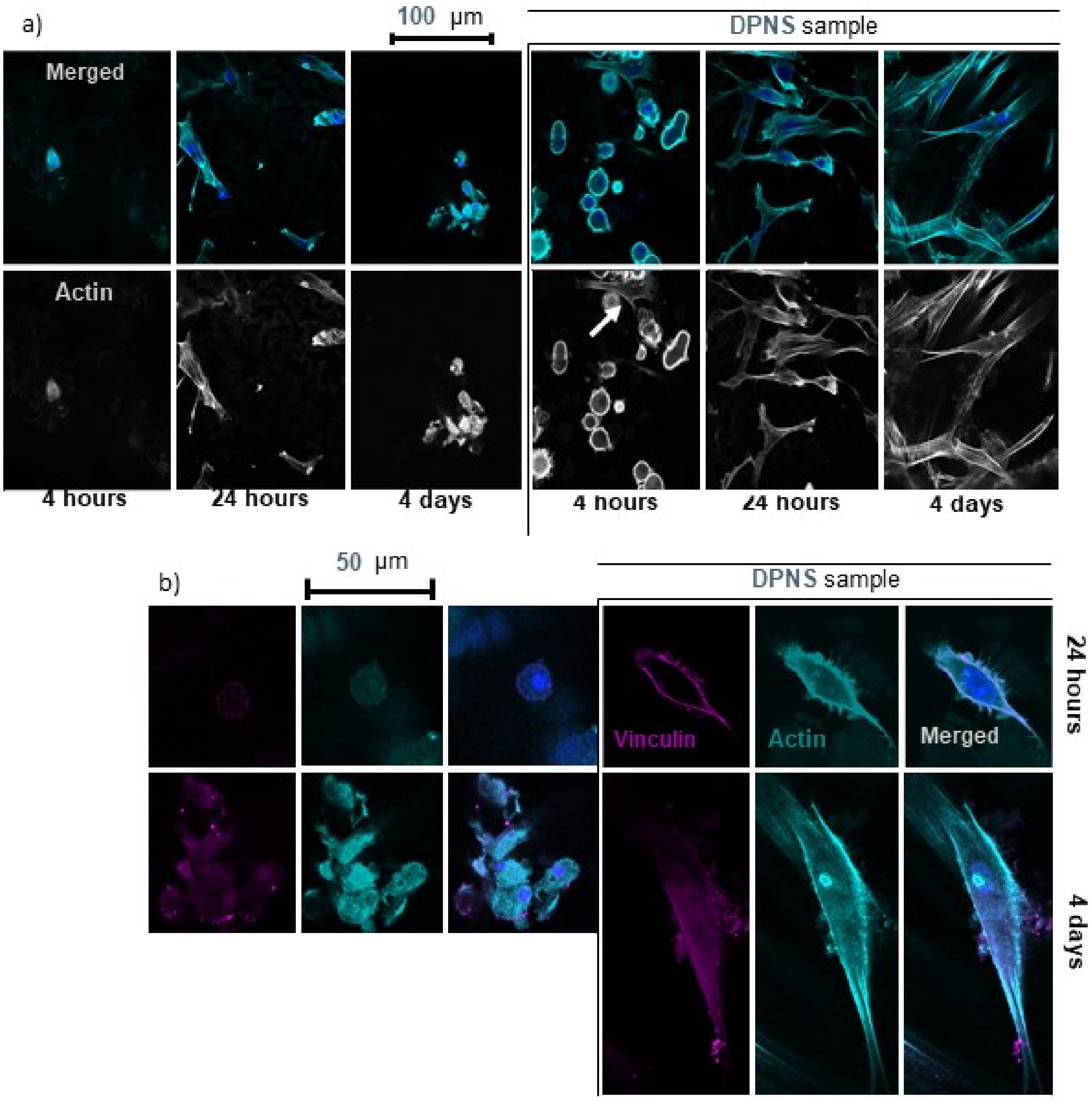

Figure 4-12 Cells adhesion, spreading, of hBM-MSC on DPNS and control surfaces. a) actin and DAPI fluorescence of Ctrl (left) and DPNS sample (right). More extensive and well-developed cells can be seen on the surface of the DPNS samples. Higher magnification of actin, DAPI, and vinculin fluorescence is shown in b) where the cells' interaction with the DPNS surface is observed via the focal adhesion points (Vinculin).

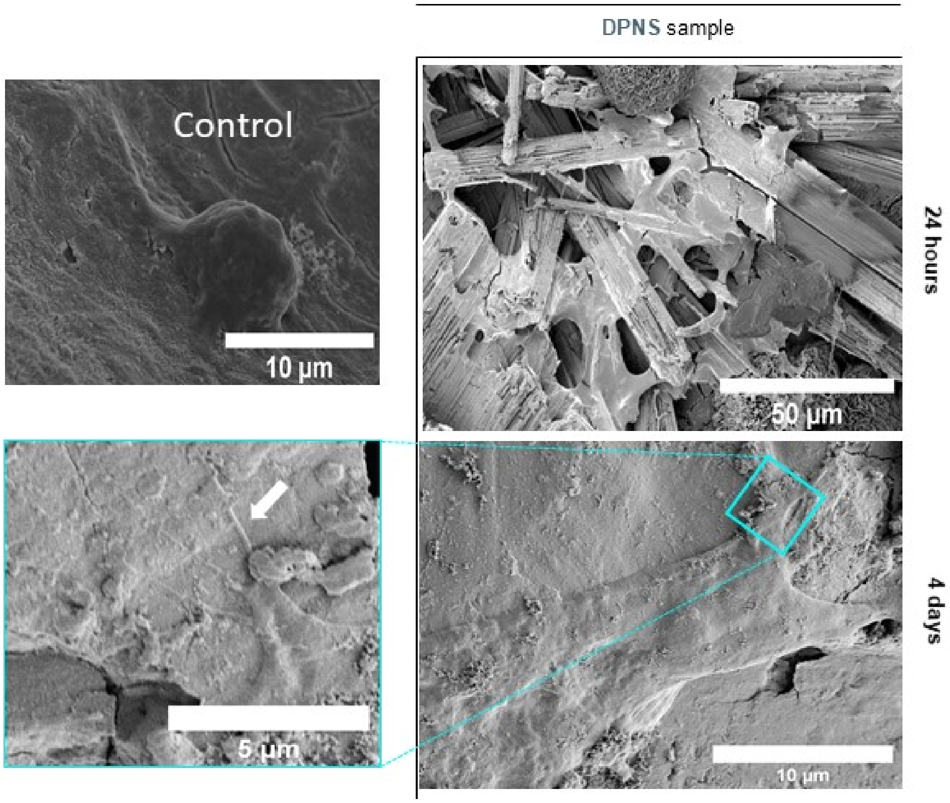

Figure 4-13 SEM micrographs of the hBM-MSC after 24 hours and 4 days on the control. Control sample after 24 hours of cell culture (top left). DPNS CaP-rich surfaces (right) after 24 hours and 4 days of cell culture with a high magnification view on the left showing the formation of stronger adhesion.

The levels of the early osteogenic marker ALP were assessed in hBM-MSCs after 4 and 7 d in culture (**Figure 4-14**b). The levels of ALP were significantly higher in DPNS and TCP than they were in the Ctrl. ALP activity increased with increasing time in all cell cultures. After 7 d in culture, the levels of ALP were significantly higher in DPNS than they were in TCP and Ctrl, suggesting an improvement in hBM-MSC osteoblastic differentiation in the DPNS samples.

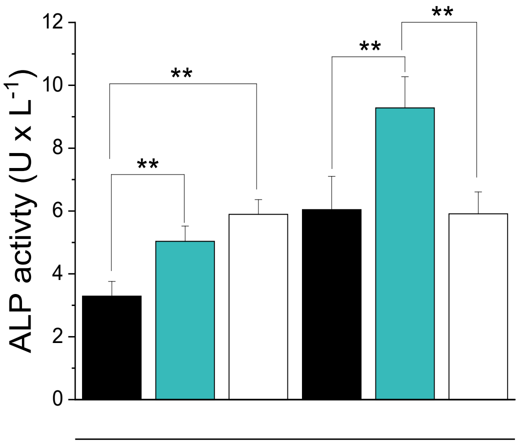

Figure 4-14. ALP activity of Ctrl and DPNS samples compared to a tissue control plastic (TCP) after 4 days and 7 days. ALP activity on DPNS and TCP are highly statistically higher than ALP in Ctrl. Results were $p < 0.05$ (*) were considered statistically significant, and $p < 0.01$ (**) highly statistically significant

4.3.4 Measurement of pro-and anti-inflammatory cytokines

The J774A.1 cells used in this work displayed different behaviors when in contact with the surface of the scaffolds (Figure 4-15). After 24 h in cell culture, macrophages in the DPNS samples secreted a higher concentration of the proinflammatory cytokine TNF-α than pretreated samples and TCP and secreted a lower concentration of the anti-inflammatory cytokine IL10 than did the Ctrl. After 72 h in culture, the concentration of TNF-α in the DPNS sample was comparable to TCP concentration. The concentration of TNF-α in the pretreated samples was significantly decreased, which may have been related to a lower cellular density (as we have seen in the previous results for the cell adhesion process). The concentration of IL10 in the DPNS sample was significantly increased after 72 h in cell culture, even higher than TCP.

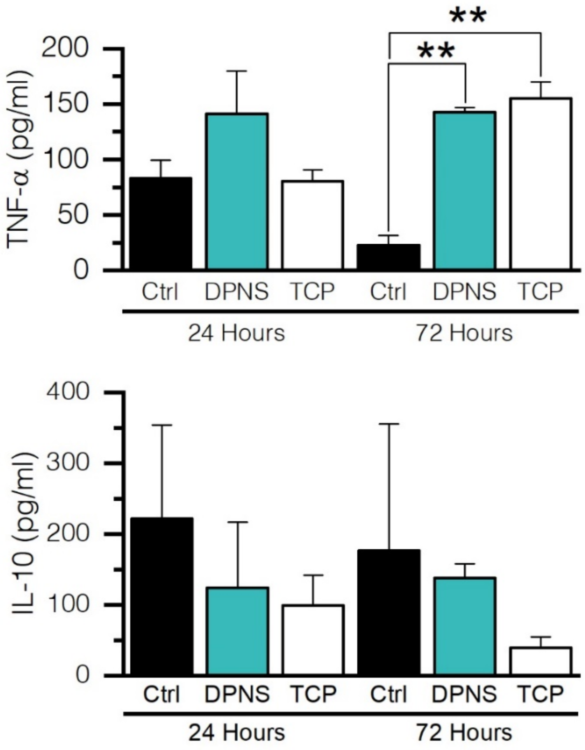

Figure 4-15 The anti-inflammatory and the pro-inflammatory response of J774A.1 macrophages seeded on the Ctrl and direct plasma nanosynthesis (DPNS) scaffolds surfaces compared to a tissue control plastic (TCP) after 24 hours and 72 hours in culture. a) shows an initial increase in the TNF-secretion for DPNS samples. After 72 hours in culture, this increase is comparable to the increase in TCP. b) more noticeable concentration variation of IL 10 is observed in Ctrl samples; however, there are no significant differences. Results were $p < 0.05$ (*) were considered statistically significant, and $p < 0.01$ (**) highly statistically significant

4.3.5 Osteogenic differentiation

The expression of genes associated with osteoblastic differentiation was analyzed in MC3T3.E1 cells via RT–PCR. After 7 d in cell culture, the levels of *ALP*, *OPN*, and *RunX2* were similar in all samples (**Figure 4-16**). Subsequently, after 14 d in culture, the DPNS and Ctrl samples showed higher and significantly higher ALP relative expression, respectively, compared with TCP. Another gene related to late osteogenesis, *OPN*, showed a similar tendency after 7 d in cell culture when all samples had a comparable expression; however, after 14 d, its expression level was significantly elevated in TCP compared with DPNS and Ctrl samples, as well as in Ctrl compared with DPNS samples. The level of expression of *RunX2* was comparable in all samples and time points.

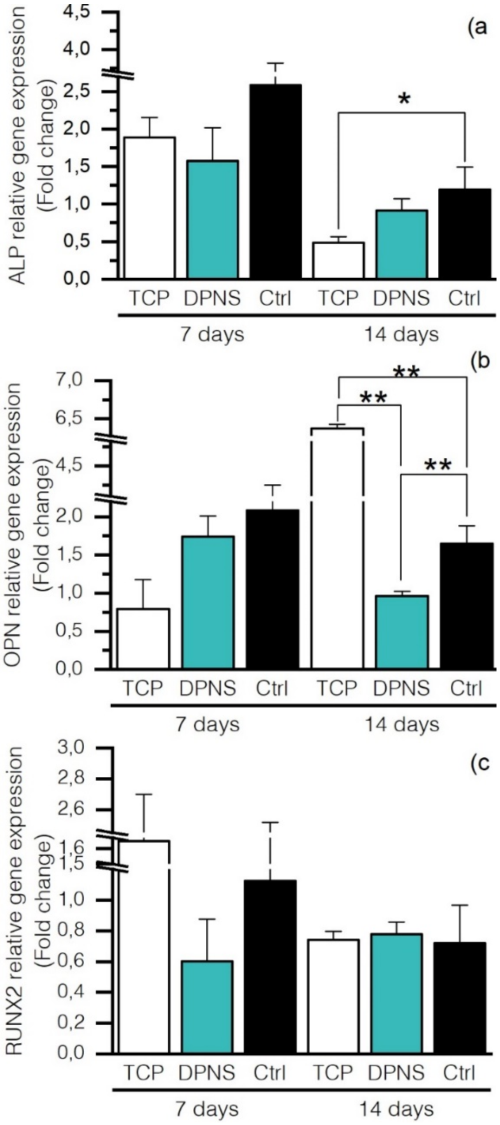

Figure 4-16. Relative gene expression of osteogenic-related genes measured in MC3T3 cells. Cells cultured on direct plasma nanosynthesis and control extracts were compared to tissue plastic control (TCP) cultured with culture media and osteogenic inductive supplements. a) higher alkaline phosphatase (ALP) relative expression is observed on the scaffold's extracts. b) higher osteopontin (OPN) relative expression is observed in TCP. c) no significant differences were observed on Runt-related transcription factor 2 (RunX2) relative expression. Results were $p < 0.05$ (*) were considered statistically significant, and $p < 0.01$ (**) highly statistically significant.

4.4 Discussion

The hydrogen evolution rates of several AZ31 surfaces modified with DPNS at varied parameters are shown in **Figure 4-17**. The data were collected in different experiments with similar conditions (immersion in DMEM at 50 ml cm^{-2}, 37 °C for 144 h). the corrosion values were normalized with the corresponding control. A strong dependency on Al accumulation on the surface and corrosion rate can be observed on the samples. The protection effect is noticed until 7.1 ± 0.4 at.% of Al. Despite the strong influence of the surface chemistry, some tendencies relate the corrosion rate with the surface nanotropography: the formation of nanoripples (irradiation cases 2, 3, 4, and 5) is associated with lower corrosion rates.

On the contrary, the formation of deeper nanostructures (case 6), such as nanopillars, is correlated with higher corrosion rates. This result followed the tendency that associates the deep valleys with higher corrosion rates [224]. Nevertheless, making exact comparisons is complicated due to dimensional differences.

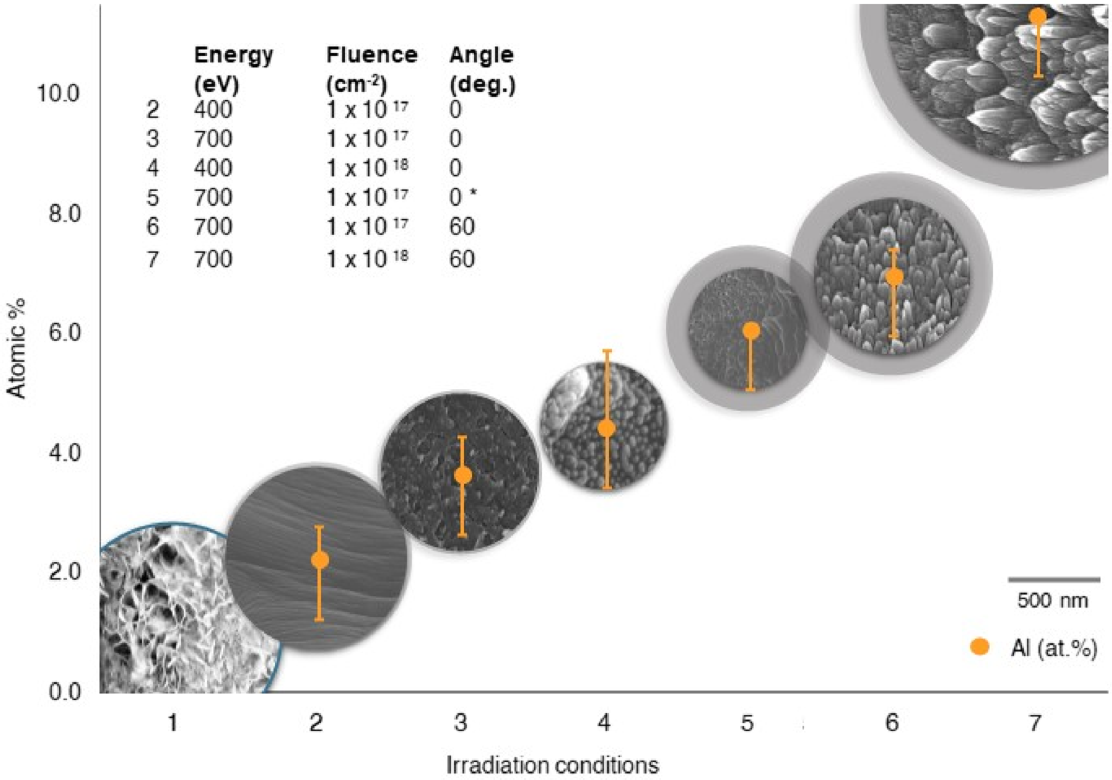

Figure 4-17. Surface nanotropography, obtained via directed plasma nanosynthesis, correlated with Al at.% and hydrogen evolution rate. The control sample (Case 1) represents 100%. The hydrogen evolution rates were collected via immersion in DMEM at 50 ml cm^{-2}, 37 °C for 144 h. The bubble size represents the hydrogen evolution rate (% of control). Bubble shade represents standard deviation. * 700 eV $1x10^{17}$ cm^{-2}, was applied to a foam with different bulk Al concentration.

The corrosion process was "step by step" followed to elucidate the role of the nanotopography on the corrosion rate of the porous AZ31 substrates in the 400 eV, 1×10^{18} cm^{-2} case. The control sample (no irradiated) generated complete water spread over the surface; this immediate absorption of the water can result from the oxides chemical affinity, which played a dominant role over the topography [200]. On the contrary, after DPNS, with the bean-like nanostructures, samples showed a more hydrophobic behavior with a contact angle of 100.7 ± 6.9°. The difference could be related to the decrease in the rust layer and the formation of texture patterns. This increase in the contact angle due to the formation of nanobeans can be explained by the air entrapment supported by the Cassie–Baxter model [200,225].

Surfaces with low contact angles and low Gibbs free energy have been previously correlated with faster apatite nucleation than high contact angle surfaces [226]. However, in the Mg case, the surface wettability effect is combined with other attributes such as surface composition, pH increase, and Mg^{2+} ions release capacity. Moreover, the formation of nanostructures increases the number of efficient areas in contact with the immersion solution (DMEM), increasing the possibility of heterogeneous hydroxyapatite nucleation [189]. In the present work, enhanced mineralization was observed on the DPNS samples after 5 hours of immersion in DMEM (**Figure 4-7**). Even if the DPNS nanotopography had an impact at the beginning of the immersion process, it became less significant as the morphology changed at the early stages of corrosion. As shown in **Figure 4-8**, after 5 hours of immersion, the cross-section micrograph revealed the formation of a continuous dense layer deposited over the DPNS substrate. Then, the deposited rust or CaP layer corresponds to the surface that faces the corrosion process and the material tissue interactions.

The behavior of the DPNS surface is then attributed to the dominant effect of the chemistry change. The Al that accumulated adjacent to the nanostructured layer triggered a reduction of water originated from galvanic corrosion [204,227,228], which resulted in an abrupt rise in pH (release of hydroxyl; OH^- ions). The release of Mg^{2+} and OH^- ions catalyzed the heterogeneous nucleation and growth of CaP phases [162,210,229]. The pH increase was decelerated as the diffusion of water and ions to the surface was, in turn, decelerated by the growth of the protective CaP layer on the surface [230]. Hence, the ICP-OES analysis showed a gradual decrease in the Mg^{2+} released from the DPNS samples. After 48 h of immersion, a slight decrease in pH was detected. This decrease could be caused by the formation of apatites, which, in turn, consumed OH^- from DMEM. This phenomenon was also observed in [231].

In contrast, the poorly crystalline nature of the coating in the pretreated sample contributed to its dissolution in the medium, as confirmed by the ICP-OES analysis, which showed significant differences in the Mg^{2+} release after 7 and 14 d of immersion. Moreover, the corrosion rate was significantly lower after 7 and 14 d of immersion. These Mg^{2+} release values observed in the Ctrl sample have also been described by Cheng et al. [81]. They studied the corrosion and Mg^{2+} ions released using Mg (PMg) microporous scaffolds with a similar pore size (250 µm and 400 µm), reaching around 125 ppm and 260-350 ppm at 7 and 14 days, respectively. In our DPNS samples, the Mg^{2+} released was controlled, reaching similar values at 7 and 14 days (~150-180 ppm), highlighting the effect of DPNS on the ions release process.

The hBM-MSCs were seeded on the preincubated surfaces without extracting the "preincubation" media. At this point, the conditions of the environment represented the maximum static concentration to which cells can be exposed [216]. The initial conditions of the hBM-MSC culture were established considering the regulation of Mg in the human body. The metabolic regulation of Mg ions plays an essential role in the corrosion of Mg systems because the release of Mg^{2+} and OH^- is conditioned by the receiving capacity of the medium [232–234]. The excess of Mg^{2+} released from the implant is supposed to diffuse into the extracellular fluid and then into the blood plasma via the blood vessel network, to be filtered into finally, and excreted by the urine [81,234]. However, Zhang et al. [12] proposed that, when the device is implanted into the bone, the released Mg^{2+} is transported to the periosteal region via Harvensian's canals; thus, the Mg ions accumulate at the fracture site, and the presence of the Mg^{2+} in the fracture stimulates bone healing. Cipriano et al. [216] also demonstrated that the Mg^{2+} concentration and OH^+ at the cell-surface interface did not cause adverse effects on cellular responses.

A higher density of hBM-MSCs was observed on the DPNS samples after 4 h in culture (**Figure 4-12**); moreover, some polygonal cells were observed on these surfaces. Anisotropic cell spreading could be attributed to abrupt changes on the surface topography at this time point [216]. In contrast, all hBM-MSCs in the control samples had only spherical shapes. After 24 h of culture, fluorescence images showed more cells attached to the DPNS samples, while the presence of vinculin protein was higher detected in the immunostaining, which indicated the increased formation of focal adhesion points. This effect was correlated with the stability of the surface. In addition, a greater isotropic cell spreading was observed. At this point, it should be mentioned the challenge of obtaining focused confocal images using fluorescence filters because the oxides on the surfaces reacted with the solutions involved in the staining process (i.e., PBS [139]) that acted as artifacts. The cells seemed to be buried on a corrosion layer built on top of the samples hindering the detection of the cellular presence and its internal structures. This phenomenon was also described in [218]. The formation of this corrosion layer was avoided by dipping the samples in deionized water instead of washing them with PBS after each staining step. Supplementary **Figure B-1**. shows a comparison of fluorescence images taken in both cases using similar confocal microscope settings.

Despite the medium change, which was expected to destabilize the surface by resuming the release of Mg^{2+} and OH^-, cells with well-developed nuclei and widespread and elongated cell shapes were observed on the DPNS samples after 4 d of immersion. The focal adhesion points were also increased, indicating a stronger cell adhesion compared to Ctrl surfaces [235]. Cell metabolism is expected to affect the stability of the surface and has been reported to be beneficial for corrosion resistance [218,235]. Two mechanisms are associated with the interaction of the cells with the corrosion of Mg: first, attached cells decrease the exposed surface area and act as a kinetic barrier against the dissolution of Mg [235]. Second, as proliferation and differentiation are states of high cellular metabolic rate, the cells reduce pyruvate, which, in the presence of hydrogen, forms water, CO_2, and acetic acid, thus causing the downregulation of the pH [218,233].

The flattened and elongated cell morphology of the hBM-MSCs on the DPNS sample and the well-defined focal adhesion points can also be attributed to the osteoblast induction potential of Mg^{2+} together with the augmented surface area caused by the porosity of the sample and the CaP formed on the surface [218]. As mentioned, high-metabolism stages, such as proliferation and differentiation, could benefit corrosion resistance [218]. ALP, as an early indicator of osteoblastic activity, showed a significant increase in mineralization on the DPNS samples compared with the pretreated samples and TCP after 4 and 7 d in culture. Previous reports demonstrated that the addition of Mg^{2+} to the biological environment enhanced the osteogenic expression of hBM-MSCs [236]. However, the osteoblast induction potential of Mg^{2+} is conditioned by the concentration of ions in the medium [233,237]. The increase in ALP expression on the DPNS sample compared with TCP can also be attributed to the increased surface area on the scaffold, which gives the cells a wider space to grow and develop.

The ALP activity and cell morphology confirmed that the DPNS modification enhances osteogenic differentiation on hBM-MSCs directly seeded on the surface of the DPNS scaffold. These results are consistent with the hypothesis that surface stability and topography are more relevant to the cell's behavior than are Mg ions and pH [216]. However, the fold change in the relative expression of the relevant osteogenic genes *ALP*, *OPN*, and *RunX2*, as assessed using RT-PCR, supported the hypothesis of the Mg^{2+} osteogenic potential. Previous studies showed that higher Mg concentrations induced a more relative osteogenic gene expression [218,236]. **Figure 4-11** shows that significantly more Mg ions were released from the Ctrl sample. Subsequently, after 14 d in culture, MC3T3 cells cultured in Ctrl extracts exhibited a significantly higher relative expression of *ALP* compared with TCP and a significantly higher relative expression of *OPN* compared with

DPNS. The relative gene expression in the DPNS sample was mostly comparable to that of the TCP. However, after 14 d in culture, the *OPN* gene was highly significantly expressed in TCP compared with both testing samples; moreover, the relative expression of the *OPN* gene in the Ctrl sample was significantly higher than its relative expression in DPNS. Previous studies suggest that OPN is related to the number of osteoclasts in the environment and acts as a regulator of MC3T3 growth and differentiation [238]. Another study focused on the biodegradation of Mg-phosphate scaffolds (MgP) demonstrated that the pore architecture (such as the presence of nanofeatures and the surface geometry) has a strong impact on bone formation and remodeling process [239].

The modulation of macrophage polarization has been proposed as another mechanism underlying the osteogenic effect of Mg^{2+} [14]. Mg ions mediate the immune response by modulating the secretion of proinflammatory cytokines promoting a pro regeneration phenotype [13,14,240]. In the present work, an initial increase in the secretion of the proinflammatory cytokine TNF-α was observed in the DPNS sample. This effect was probably attributable to the response of the cells to the H_2 bubbles, which cause turbulence and a pH increase, thus rendering the medium hostile for cells [241]. However, both M1 (proinflammatory) and M2 (anti-inflammatory) phenotypes play a role in the fracture healing process [49]. The release of proinflammatory cytokines has been described to stimulate the recruitment of progenitor cells, which then resolve the inflammation and promote the next stage of healing [49,242,243]. After 72 h in culture, the stabilization of the surface and the slight decrease in the pH of the medium (because of cellular functions) render the environment more adequate for cells, as can be noted in the concentration of TNF-α in the DPNS samples, which was comparable to the concentration observed in the TCP samples.

A more notable concentration variation occurred with the secretion of the anti-inflammatory cytokine IL10 after 72 h in culture. The anti-inflammatory response has been reported to start at later stages of inflammation, with the secretion of tissue repair signals [49]. However, both responses, TNF-α and IL10, were increased with time in culture in the DPNS samples. The phenotypes and function of the macrophages change in response to the chemical and physical clues of the environment [14]. In addition to chemistry, the architectural characteristics of the scaffold (i.e., interconnectivity and pore size and shape) are involved in the polarization of macrophages [14,23]. Therefore, different macrophage processes may occur in parallel on the surface of the scaffold, which was also reflected in the high standard deviations obtained.

4.5 Conclusion

DPNS scaffolds showed a significantly lower corrosion rate ($P < 0.01$) compared to the pretreated control samples. The corrosion rate results were dominated by the chemistry change on the surface more than the obtained nanotopography. In addition, DPNS treatment enhanced the apatite formation ability of the scaffolds; hence, the DPNS CaP-rich phases promoted cell spread and the formation of focal adhesion points significantly in hBM-MSC directly seeded on the surfaces. Furthermore, the alkaline phosphatase (ALP) activity of DPNS samples (9.28 $U.L^{-1}$) was significantly higher than the ALP activity of cells seeded on control wells and pretreated samples. Similarly, this material also released active Mg^{2+} ions, which promoted the relative fold expression of the *OPN*, *ALP*, and *RunX2* osteogenic-related genes. Moreover, the immune response of murine macrophages (J774A.1) was also upregulated, reaching lower levels of TNF-α cytokine expression.

5. Effect of DPNS on microarchitected scaffolds

As mentioned in **section 1.3.2**, architected structures have been demonstrated to enable the innovative design of bone biomechanics functionality. The fabrication of complex and topologically ordered Mg architectures is an emerging field. Its development has been focused on optimizing the production constraints, which include the manufacturing or additive manufacturing method and safety concerns due to the Mg's flammable condition **(chapter 2)**. In the present work, diamonds and truncated octahedra were selected as unit cells given their similarity with trabecular bone units **(see section 1.3.2)** to produce topologically ordered Mg scaffolds. However, with the topologically ordered design comes the increase in exposed area. Even though the specific increase in surface area, due to the high porosity, is a significant factor influencing porous Mg's corrosion, the emphasis on the surface evolution and surface protection of predesigned Mg structures has been limited.

In lattice structures, a surface modification method must protect the exposed surface without clogging the pores or compromising the dimensions. However, as studied in **Chapter 2**, the complex geometry condition complicates the applicability of most common surface modification processes used for Mg protection. For instance, surface coatings are constrained by their adhesive properties, and the coating methods require modifications to the structures' geometry (i.e., decrease in strut thickness). Other consequences include uneven coating, peeling off, and delamination.

DPNS is proposed for porous materials since it can control the corrosion dynamics of Mg without the use of a coating or changing the bulk characteristics of the porous material. In that way, irradiating MgAl systems with Ar ions causes an Al supply on the near-surface from the alloy bulk due to the bombardment-enhanced Gibbsian segregation [35]. The observations in **Chapter 3** demonstrate that the Al accumulated can significantly be controlled with the ion fluence and the incidence angle. Furthermore, the development of an Al-enriched layer on the surface has been shown to accelerate the passivation kinetics and induce precipitation of products (i.e., CaP-based phases) that enhance corrosion protection. The precipitation of Ca-phosphate products also induces bioactivity in Mg surfaces (see **section 4.2.5**). However, excessive accumulation of Al leads to the formation of cracks.

Well-ordered nanostructures are formed to express the kinetic processes taking part during the irradiation. However, the conventional use of ion-based surface modification is applied to initially polished or flat materials [244]. In addition to the process parameters (energy, gas species, incidence angle, and ions doses), the conditions of plasma immersion and particle separation around the lattice geometry will alter the resultant surface. When examining surface morphology evolution in the application of energetic particles to surface modify architected lattice structures, the local slope's variation across the struts must be considered. Other phenomena that can influence surface evolution in cross struts are the multi-scale spatio-temporal mechanisms that involve multi-scale surface curvature, i.e., the shape of the salt grains on the as-cast surface, and shadowing (caused by the neighboring structures at the macro scale), and/or energetic particle reflection [244].

In the present chapter, despite Ar energetic ions are incident on the scaffold as a line-of-sight (LOS) beam, the reflected ions can backscatter to inner regions of the complex lattice structures. Hence, various nanotopographies can be generated on non-LOS surfaces, depending on the structure's geometry, energetic particles, and local material surface variations. The author then postulated that the DPNS treatment could be designed together with the architecture of the implant. Therefore, this chapter pretends to understand the DPNS interaction with the 3D microarchitected materials and the role of Al precipitation on the near-surface to provide mechanisms to customize the corrosion and bioactivity of Mg-based implants.

5.1 Materials and methods

5.1.1 Scaffolds fabrication[1]

Uniform cylindrical grids, populated with diamond and truncated octahedron unit cells, were 3D printed via digital light processing to obtain a positive resin template (**Figure 5-1**a). After that, the resin template was immersed in a supersaturated solution of powdered NaCl and deionized water (**Figure 5-1**b). The resin was burned out to obtain a NaCl negative template that was simultaneously sintered. Then, the negative salt template was infiltrated with molten AZ31 (composition: Mg at bal. and Al-3.3% Zn-1.1%) at a temperature of 680 °C. The melting atmosphere was protected from oxidation and ignition with the combination of Ar gas and salt fluxes (KCl, $MgCl_2$, MgO, CaF_2). The Ar gas pressure also assisted the metal infiltration on the salt template. Finally, the NaCl/metal composite was immersed in an ultrasonic bath containing NaOH to reveal the porous structure. Details of the manufacturing process are described in [245]. The samples were exposed to 1-keV Ar^+ ions at an angle of 45° for 5 min to obtain a clean surface. A photographic register of the manufacturing process is shown in **Figure 5-1**.

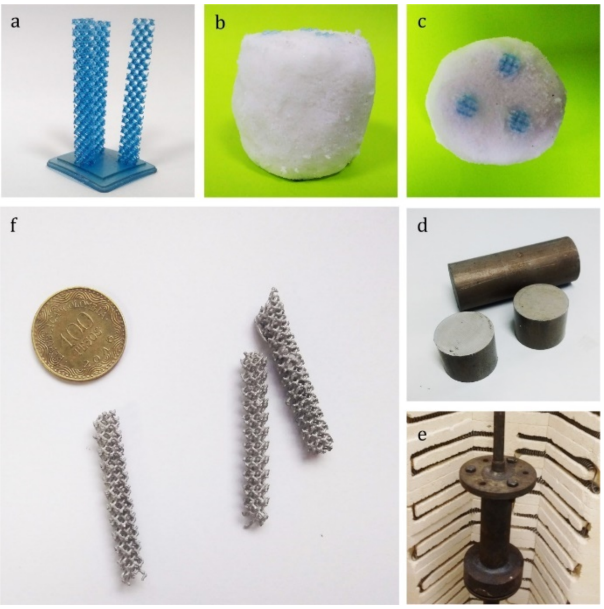

Figure 5-1. Photographic register of the casting process. a) resin templates were 3D printed via digital light processing. b) the resin templated was immersed in a supersaturated salt solution to obtain a salt/resin product. c) the resin was burned out to create a salt negative template. d) shows the cylindrical parts of AZ31 that were used to infiltrate the salt template. e) crucible and set up to melt the Mg parts and infiltrate the salt template.

---

[1] This methodology has contributions of Luisa Fernanda Marulanda Zapata and Oscar David Acevedo Rueda.

5.1.2 Characterization of the as-cast scaffolds.

Surface chemistry and phase composition

The as-cast scaffolds' phase composition was characterized via X-ray diffraction (XRD; Philips X'PERT) with a CuKα source operating at 45 kV and 40 mA over the range of 10–90° (2θ) and a counting time of 2 s per step.

Samples for metallographic analysis were embedded in epoxy resin and sequentially grounded with SiC papers up to 2400 grit and 0.04 µm polycrystalline diamond. The samples were then etched with a solution containing 1ml of acetic acid, 1 ml H_2O, 420 mg picric acid, and 7 ml ethanol for 5 s. Samples were analyzed via scanning electron microscopy (SEM; Hitachi 4700) equipped with energy dispersive spectroscopy (EDS) at an acceleration voltage of 15 kV.

Sample morphology

The pretreated samples' geometric characteristics were evaluated via micro-computed tomography (µ-CT; XRadia µ-CT) at 60 kV voltage and 10-µm resolution. The µ-CT slides were used to estimate the strut's diameter, and then, they were reconstructed using Mimics software to calculate volume and surface area.

Surface topography was evaluated via scanning electron microscopy (SEM; Hitachi 4800). The acceleration voltage was 5 kV. The distribution of elements was calculated with SEM/EDS at an acceleration voltage of 15 kV.

Compression test

Uniaxial compression tests were performed after the standards of mechanical testing of porous and cellular metals (ISO-13314:2011). Cylindrical specimens of 18 mm in diameter and 28 mm in height were used. Three tests per specimen were carried out in a Shimadzu AGX-V with a 10 kN load cell and at a working speed of 22 mm/min. Samples were comprised up to 90% of their original height.

5.1.3 Surface modification via DPNS

Samples of both truncated octahedron and diamond unit cells were exposed to Ar^+ ions. The samples had 6 – 8 mm in diameter and 7 mm in height to be used later in cell cultures and immersion tests. Due to the increase in the porosity, an AZ31 sample holder was fabricated to contain the samples during DPNS mechanically. The orientation of the samples is shown in **Figure 5-2**. The surfaces were then irradiated with a Tectra GenII ion source in IGNIS, operating at room temperature in ultrahigh vacuum (base pressure $<3\times10^{-8}$ Pa). The irradiation parameters were Ar^+ ions with 700 eV energy, 1×10^{17} ions/cm^2 fluence with the ions source directed to the scaffold. This set of conditions were selected due to the results observed in **Chapter 2**, where the match of these parameters and the chemical composition of the bulk sample presented the most mineralized surfaces. With the purpose of the discussion, the samples were identified, as shown in **Table 5-1**.

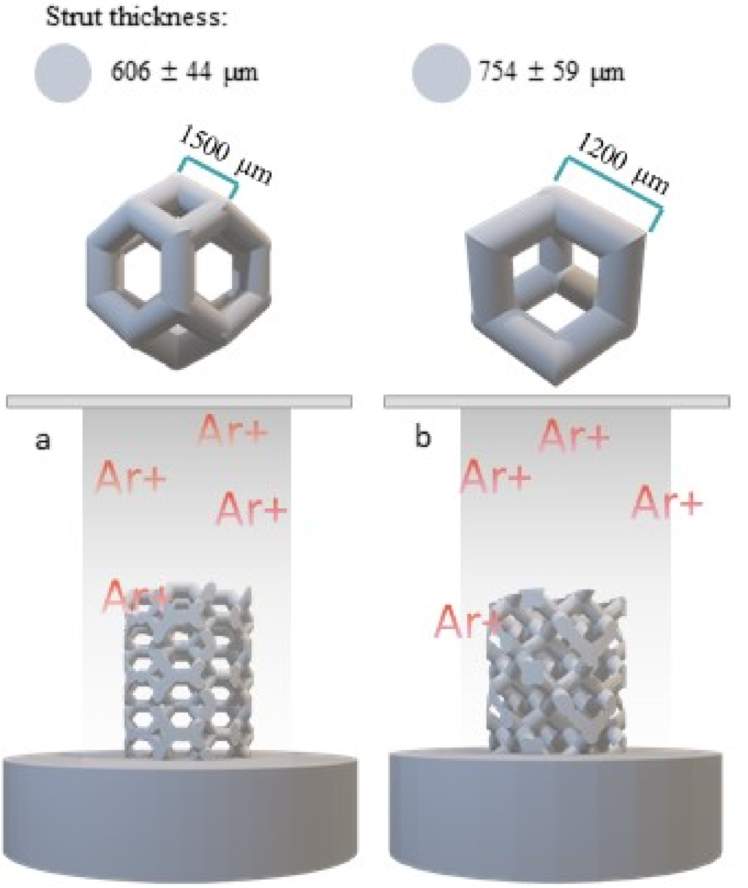

Figure 5-2. Dimensions of the unit cells and orientation of the samples during DPNS. Strut thickness and length of the a) truncated octahedron and b) diamond unit cells followed by the schematic representation of the DPNS. The beam was facing the samples, as is shown in a) and b). The truncated octahedron's squares were normal to the beam, while all the struts on the diamond received oblique irradiation.

Table 5-1 Samples nomenclature.

Nomenclature	Base Unit	Treatment
DiCtrl	Diamond	Pretreated
OTCtrl	Truncated Octahedron	Pretreated
DiDPNS	Diamond	DPNS
OTDPNS	Truncated Octahedron	DPNS

5.1.4 In vitro degradation

The samples were individually immersed in 50 ml of medium. The immersion solution was DMEM at 37 °C. H_2 release was monitored at different time points for seven days via the gas-collecting method [196]. The samples were fixed with a small area embedded in epoxy resin to identify the orientation; then, the surface area was calculated from the micro-CT volume avoiding the part immersed in resin. The pH was measured at the same time points with a pH-meter Thermo Orion 720. Surface topography was evaluated via SEM/EDS, as described above.

The concentration of Mg ions in the corrosion medium was measured via ICP-OES after 48 and 168 hours. A set of samples was removed from the media after 48 and 168 hours to evaluate the geometry and volume changes via µ-CT with 10-µm spatial resolution. For this sample set, the corrosion products were removed with 150 g CrO_3 + 10 g Ag_2CrO_4 in 1 L deionized water in boiling conditions after ASTM G1. Two parameters were considered to analyze the structures' integrity during the immersion time: pore diameter and strut thickness. The pore diameter is defined as the largest spheres' diameter that can be contained within the structure. The strut thickness was calculated from the stack of the µ-CT slides as follows: all images were binarized using the Minimum algorithm from Image J software, and then, the Local Thickness plugin was used to calculate the thickness map. The algorithm behind the Local Thickness plugin calculates the thickness of a point by the Euclidian distance transformation in which the pore centers are the reference points [246,247] Volume viewer plugin was used to visually represent the sample.

5.1.5 Biological behavior

MC3T3-E1, subclone 4 (best described in **section 4.2.5**), were seeded on the surfaces of treated and pretreated samples, at a density of 1×10^5 cells/cm^2. Samples were used as discs of 6 mm in diameter to minimize the movement in the 96-well plates' wells and prevent the material's upside-down. Then, the drops with the cells were placed in the center of the struts. The cell growth medium was α-MEM, supplemented with FBS. Cell morphology was observed under confocal microscopy using fluorescence stains Texas Red®-X phalloidin and DAPI following the procedure described in **section 4.2.5**.

Extracts of the DPNS samples and controls were obtained by immersing the samples on α-MEM supplemented with FBS after ISO 10993-12 (described **section 4.2.5**). MC3T3 cells were seeded in 24-well plates at a density of 5×10^4 cells/cm^2. Cells cultured in alpha-MEM without materials extracts were used as TCP. After four days in culture, differentiation was induced by adding 10 nM dexamethasone, 6 mM ascorbic acid, and 10 mM b-glycerophosphate sodium to all the wells.

After seven days, cells were collected to evaluate osteogenic-related gene expressions via RT-PCR, as described in **section 4.2.5**. The selected genes' quantification was performed with the SYBR green PCR master mix (Invitrogen) with the primers listed in **Table 4-1**. The housekeeping gene Glyceraldehyde 3-phosphate dehydrogenase (GAPDH) was used to normalize the mean cycle threshold (Ct). The mRNA expression levels were compared via the ΔΔCt method, and the results were expressed as fold changes of the target gene expression amount ($2^{-\Delta\Delta CT}$).

5.1.6 Statistics

One-way analysis of variance (ANOVA) was used to estimate statistical significance between groups, followed by Tukey's multiple comparison test. * $p < 0.1$ was considered statistically significant. Data are presented as mean ± standard deviation.

5.2 Results

Diamond and truncated octahedron unit cells were used to populate uniform cylindrical grids. Final struts diameters were 754 ± 59 µm for diamond and 606 ± 44 µm for the truncated octahedron (**Figure 5-1**). Pore sizes were 1.58 mm and 2.15 mm, respectively; then, this set of dimensions results in around 83.4 % and 77.9 % porosities for the truncated octahedron and diamond unit cells, respectively. The samples were consistent in chemistry (95.6 ± 0.01 % Mg, 3.10 ± 0.01 % Al, 0.24 ± 0.01 % Mn, 1.07 ± 0.07 % Zn), which can also be noticed in the SEM micrographs with BSE detectors of the microstructure(**Figure 5-3**), further confirmed with EDS (**Table 5-2**) and XRD analysis (**Figure 5-5**). Both structures contained similar microconstituents, including dark α-Mg and greyish-white second phases (**Figure 5-3**c and d). According to EDS, the chemical composition of the island-like shapes accumulated along the grain boundaries are close to $Mg_{21}(Zn, Al)_{17}$ phase. Intermetallic Al_8Mn_5 was also observed (**Figure 5-3**c and d).

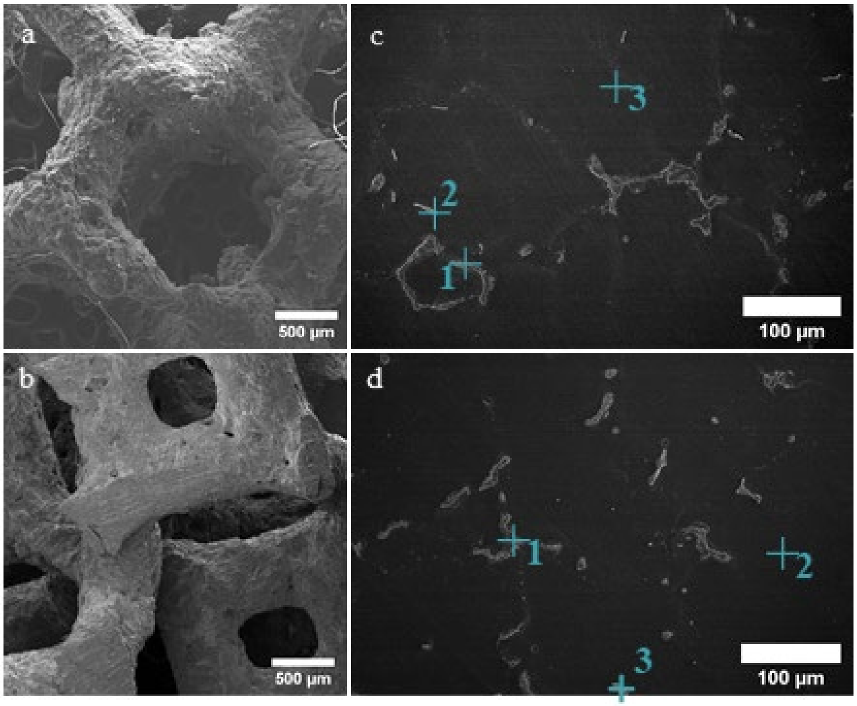

Figure 5-3. Microstructure of the as-cast truncated octahedron and diamond lattice structures. a) and b) SEM micrographs of the diamond and truncated octahedron lattices structures at 30X. Metallographic micrographs of the c) diamond and d) truncated octahedron scaffolds. The dark α-Mg matrix can be observed, followed by the second phase distributed along the grain boundaries. The distribution of elements on the surface shows the $Mg_{21}(Zn, Al)_{17}$ as the dominant second phase (**Table 5-2**).

Table 5-2. Distribution of elements of the as-cast scaffolds in the positions marked in Figure 5-3.

	Diamond			Truncated octahedron		
	①	②	③	①	②	③
Element	At.%			At.%		
C	3.1	9.9	14.9	-	3.1	-
O	1.3	1.7	15.1	4.0	1.3	10.5
Mg	38.7	88.7	8.1	39.3	38.7	51.6
Al	15.2	-	40.6	15.5	-	23.7
Zn	41.6	-	-	41.1	-	-
Mn	-	-	21.2	-	-	14.1

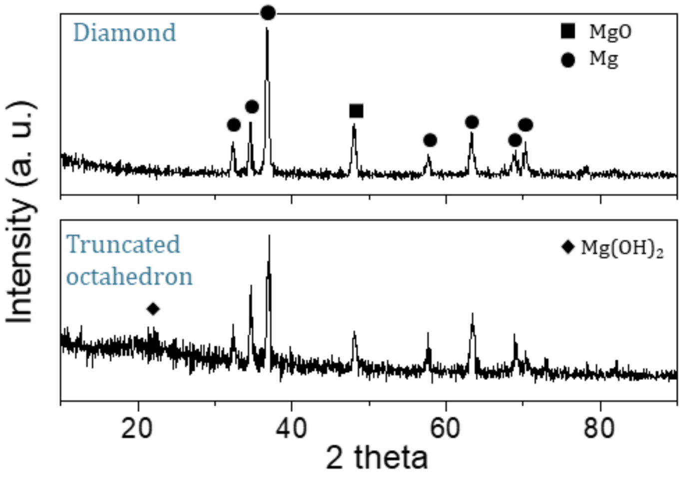

Figure 5-4. XRD analysis of the as-cast diamond and truncated octahedron lattice structures. Similar peaks are observed on the as-cast structures that include Mg and MgO as main products.

5.2.1 Mechanical properties

Although both scaffolds had different unit cells, the compressive behavior was similar. Three replicates of each scaffold were tested in the direction of the infiltration. The stress-strain curves revealed the three distinct stages of the porous structures (**Figure 5-5**): I) elastic zone, II) plateau, and III) densification. Both samples showed stress hardening behavior in the plateau region. However, some stress fluctuations were observed on the truncated octahedron. Compressive mechanical properties are summarized in **Table 5-3**. Despite the similarities, it can be noticed that the diamond lattice structure presented a higher elastic modulus and yield strength.

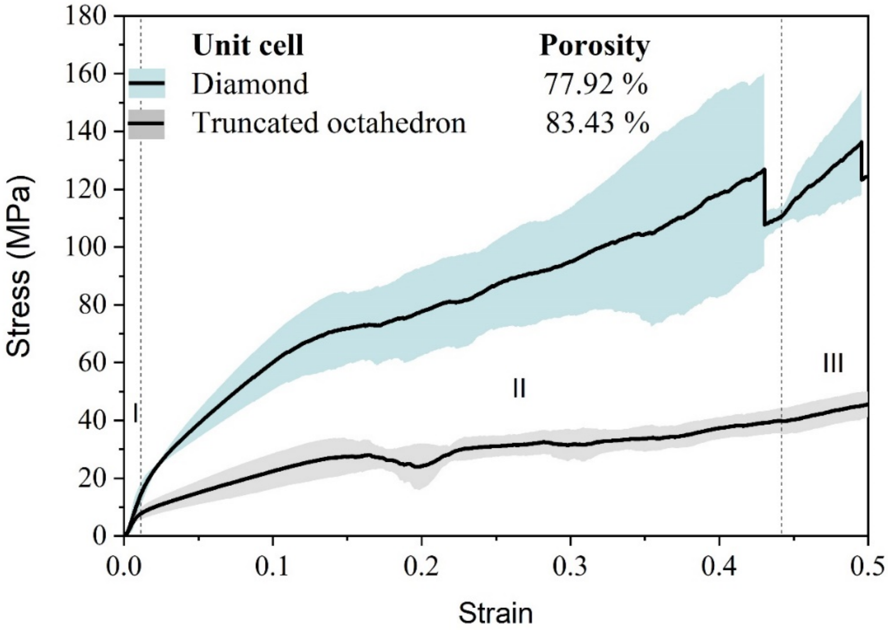

Figure 5-5. Compressive mechanical properties of the diamond and truncated octahedron lattice structures. The samples showed the typical three stages of porous materials under compression: I) elastic zone, II) plateau, and III) densification. Although both samples had similar compressive behavior, it can be noticed that the diamond lattice had higher mechanical properties (Young modulus 1.6 ± 0.4 GPa) than the truncated octahedron (Young modulus 0.9 ± 0.2)

Table 5-3 Samples geometry and mechanical properties

Sample	Strut thickness (μm)	Pore size (μm)	Pore interconnection (μm)	Yield strength (MPa)	Elastic modulus (GPa)
DiCtrl	754 ± 59	1638 ± 1	1474 ± 0.1	26.5 ± 9.4	1.6 ± 0.4
OTCtrl	606 ± 44	2152 ± 1	Square: 526 ± 3.2 Pentagon: 2324 ± 1.3	8.9 ± 2.7	0.9 ± 0.2

5.2.2 Surface evolution after DPNS

Surface topography was evaluated via SEM. Preirradiated structures had differences in the appearance of the surface. OTCtrl revealed the typical platelet-like morphology (**Figure 5-6**a), while the oxide in the DiCtrl showed a continuous layer of oxide clusters (**Figure 5-7**b). After DPNS, distinct topographies were observed on the surfaces. Nanostructures were identified to be grouped onto regions of behavior delimited by the strut exposure (its location on the unit cell) and the micro surface roughening guided by the sintering process's texture.

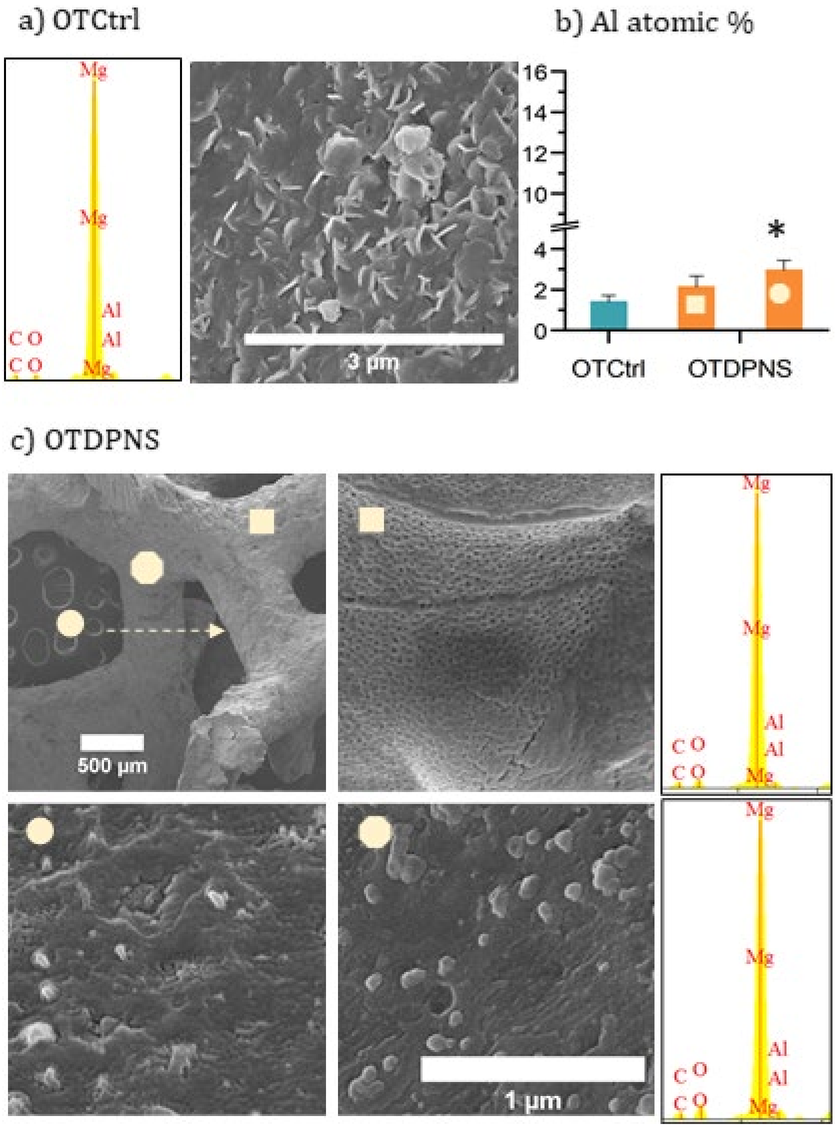

Figure 5-6. Surface topography and distribution of elements via EDS at different locations of the OTCtrl and OTDPNS samples. a) OTCtrl SEM/EDS analysis. b) comparison of the Al accumulated on the surface before and after DPNS. A significant Al increase (* $p < 0.1$) is observed on the struts that form the square on the OTDPNS sample. c) SEM/EDS of three different locations of the OTDPNS sample.

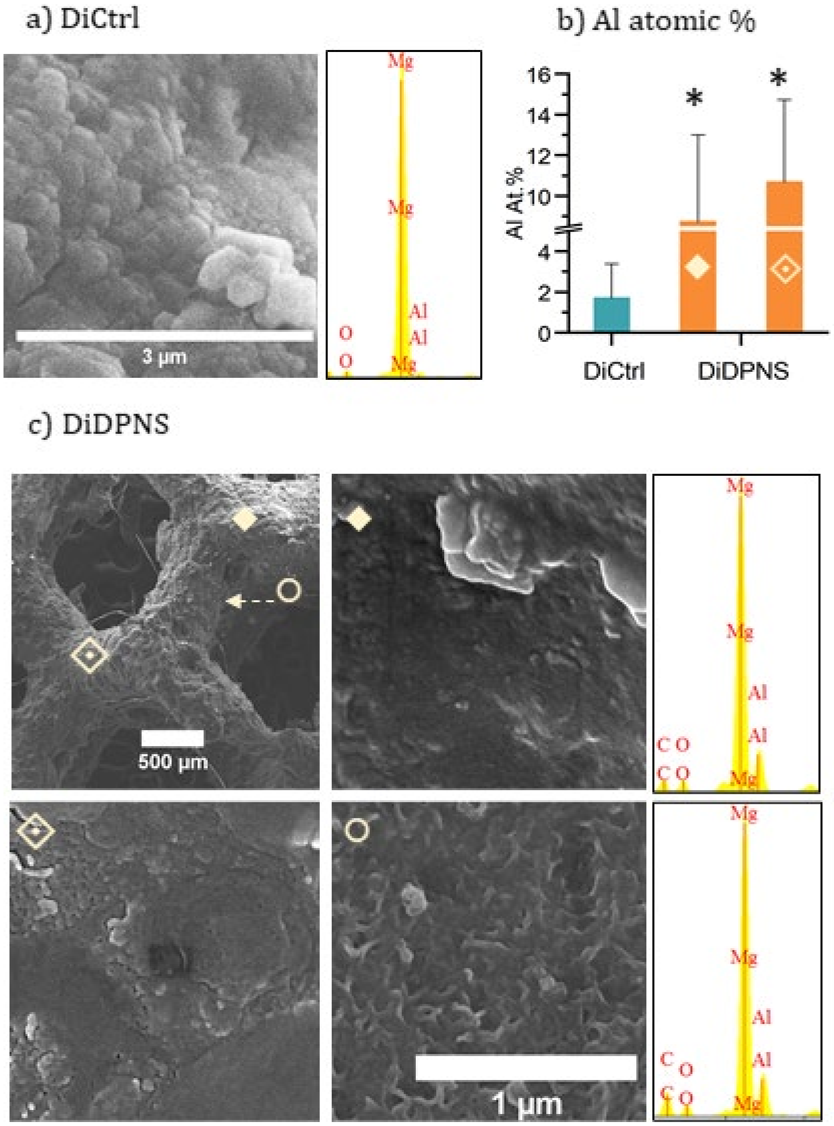

Figure 5-7. Surface topography and distribution of elements via EDS at different locations of the DiCtrl and DiDPNS samples. a) DiCtrl SEM/EDS analysis. b) comparison of the Al accumulated on the surface before and after DPNS. A significant Al increase (* $p < 0.1$) is observed on the two evaluated locations on the DiDPNS sample. c) SEM/EDS of three different locations of the DiDPNS sample.

Figure 5-6c and **Figure 5-7c** present the surface transformation after the DPNS concerning the local incidence of the ions. In DiDPNS, the top surface showed nanobeans formation. However, the nanobeans started disappearing when expanding across the cross struts, where the surface presented mixed regions of smooth spots and nanobeans (**Figure 5-7**c). The back surface seems that there were still platelet-like morphology regions similar to the platelets in the OTCtrl before irradiation (**Figure 5-6**a). However, no evident nanostructures formation was noticed.

In the truncated octahedron structures (OTDPNS), the square face was directed onto the beam; this top surface showed nanopores-like assemblies delimited by the barriers formed during the sintering process. In the cross struts, nanopillars and spots of nanobeans assemblies were mixed. The OTDPNS surface seems more modified than the DiDPNS, considering the formation of the nanostructures. However, the EDS results showed an increased signal of Al on the DiDPNS samples after DPNS (**Figure 5-6**b and **Figure 5-7**b).

5.2.3 Chemistry after DPNS

Treated and no treated samples were analyzed via EDS (**Figure 5-6** and **Figure 5-7**). The surface of no treated samples consists mainly of Mg (71.8 ± 7.1 at. %) with small traces of other elements: C 21.0 ± 6.5 at. %, O 4.9 ± 1.4 at. %, and Al 1.4 ± 0.3 %. The chemistry was constant within the two preirradiated structures in all the struts.

Consistent with the SEM observations, the distribution of elements after DPNS depends on the foam's location. Two locations were analyzed for the truncated octahedron and diamond lattice structures. The correspondent EDS and locations are shown in **Figure 5-6**c and **Figure 5-7**c; a comparison of the Al accumulation on the surface is shown in **Figure 5-6**b and **Figure 5-7**b. A slight increase in the Al concentration (2.1 ± 0.5 at. %) was observed on the OTDPNS sample in the squares' struts normal to the beam. Instead, the diagonal strut showed a significant increase in the Al content on the surface (2.9 ± 0.5 at. %; $p < 0.1$). The modified diamond lattice showed more drastic changes in both analyzed struts; although both locations showed a significant increase ($p < 0.1$) on the Al content compared to the control, the diagonal strut presented even higher Al accumulation (10.1 ± 4.1 at. %).

5.2.4 Corrosion resistance

For all the samples, hydrogen gas evolved rapidly at the early time points. Then, despite the alloy content and the microstructure's consistency, differences were spotted in the corrosion rate of OTCtrl and DiCtrl samples. It can be observed from **Figure 5-8**a and **8**b that the hydrogen evolution started with a similar rate, and, after 24 hours of immersion, the corrosion of the DiCtrl began to differentiate and increase. At the end of the testing time (7 days), it was a difference of 32.3 ± 5.7% between the pretreated samples.

Details of the corrosion process were observed in the μ-CT scans used to identify corrosion patterns within the unit cells. **Figure 5-9** shows the evolution of the unit cells with the time of immersion in DMEM. After the first 48 hours, there were no significant differences in the samples' strut thickness and pore size. The truncated octahedron structure preserved its integrity, as shown in the histogram of struts thickness (**Figure 5-10**), in which there was a similar distribution for the entire testing time. However, after seven days, data shifted to lower values (**Figure 5-10**), and some signals of corrosion were visible in the struts (**Figure 5-9**). Moreover, the struts higher than 700 μm disappeared from the histogram. This behavior can be correlated with localized corrosion and the loss of single struts instead of a homogeneous dissolution of the material.

In the DiCtrl structure, after 48 hours of immersion, the struts' size has a similar distribution compared to the pre immersed samples (**Figure 5-10**a and **10**b). After seven days, the loss of single struts made it hard to identify differentiated corrosion mechanisms; common behaviors can be highlighted: the corrosion of the struts started on the specimens' periphery. Moreover, the higher magnification views of the μ-CT volumes showed severe localized corrosion in the form of pits. Corrosion began at weak points and promoted the propagation of holes and apparently detachment of material; then, in **Figure 5-9**, single corroded struts were visible, showing decreased strut size (turning in violet color). The exposed surfaces continued reacting with the corrosion medium, and after seven days of immersion, more neighbor struts were visibly corroded.

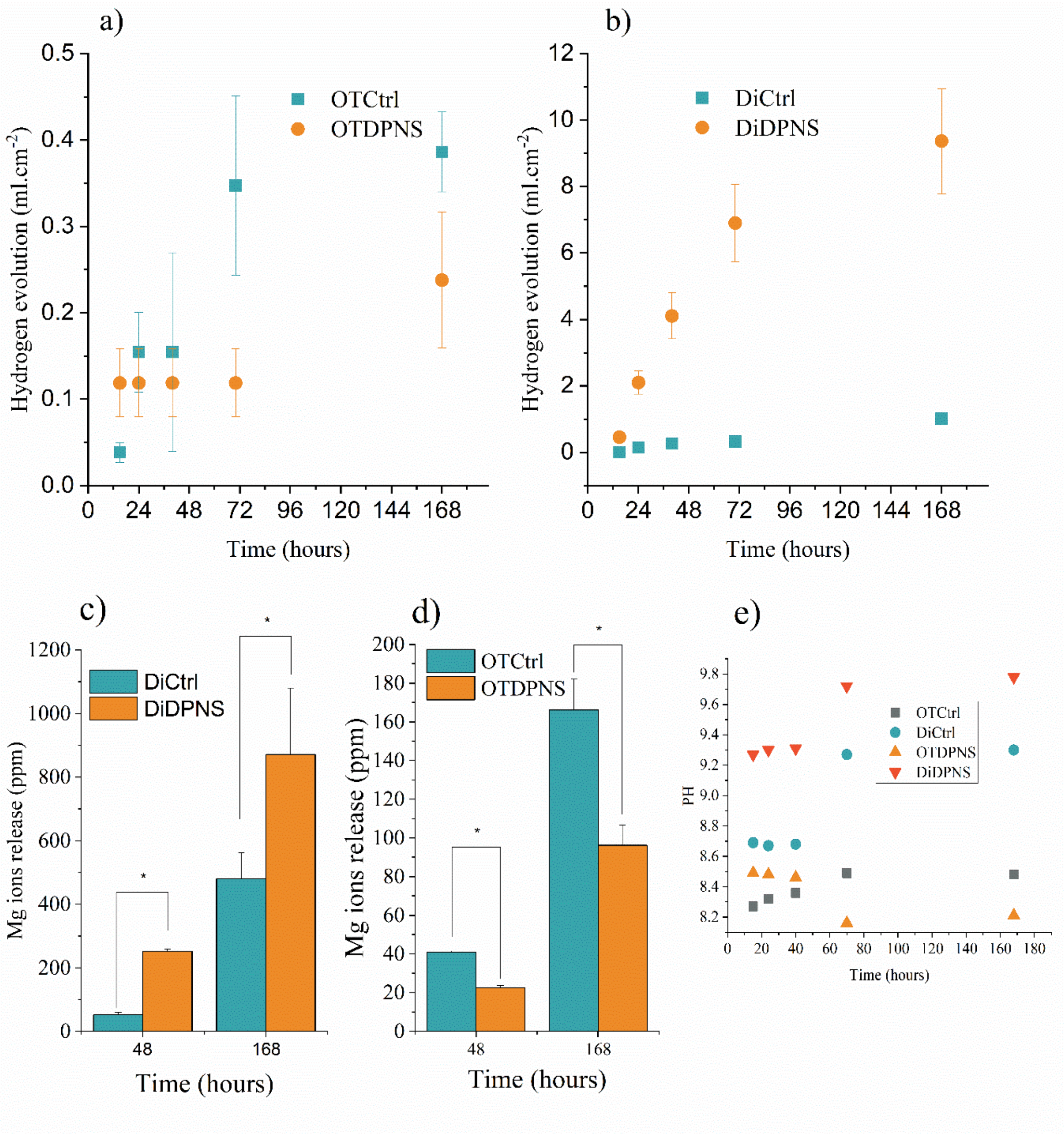

Figure 5-8. Immersion test of DPNS treated and no treated samples. a) hydrogen evolution measured via the gas collecting method of OTDPNS and OTCtrl samples. It can be noticed that the corrosion behavior of the truncated octahedron samples changed with the DPNS treatment. b) DiCtrl and DiDPNS samples. The dissolution of Mg was significantly decreased in the truncated octahedron samples. Contrarily, the corrosion of the diamond lattice samples was significantly accelerated with the DPNS treatment. c) and d) show the Mg ions release (via ICP-OES) after 48 and 168 hours. * represents significant differences ($p < 0.1$). e) pH changes for all the samples.

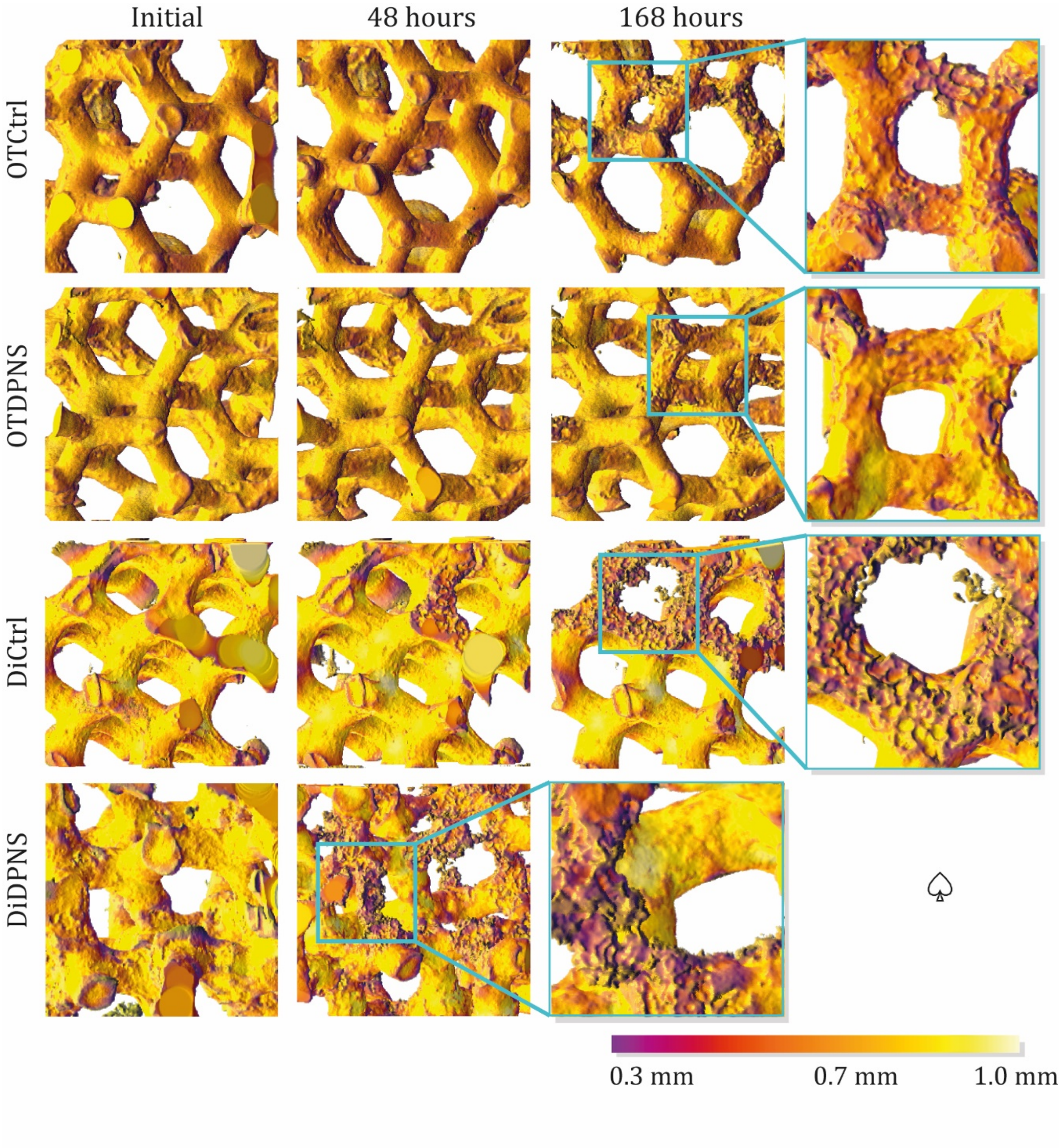

Figure 5-9. Volumetric representations that show the scaffold's evolution with the time of immersion in DMEM (48 and 168 hours). The samples are colored depending on the local strut thickness, starting at violet (0.3 mm) to white (1.0 mm). The symbol u indicates that the sample was entirely dissolved.

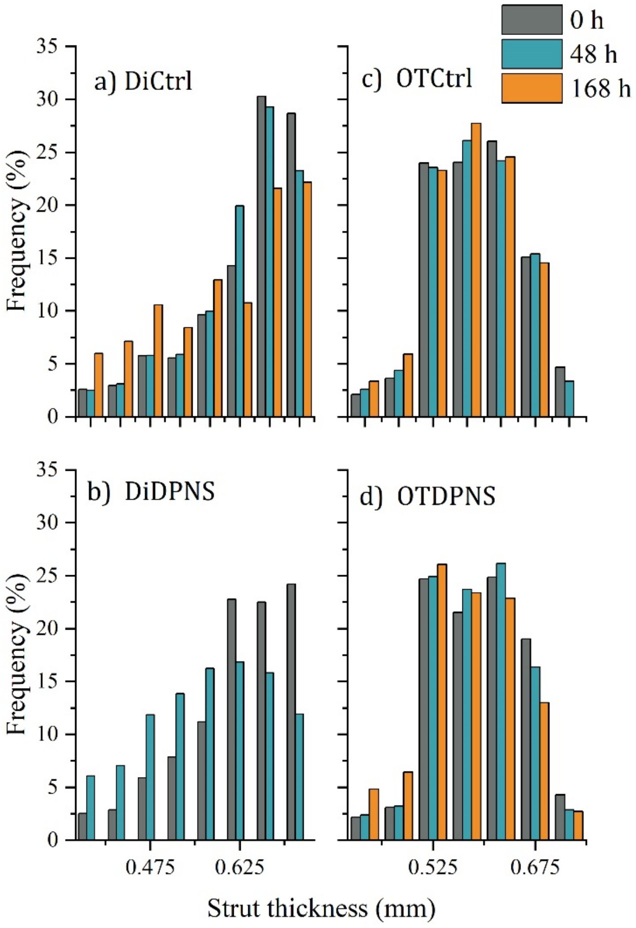

Figure 5-10. Histogram of strut thickness. The data was calculated from the µ-CT stacks before and after DPNS and after 48 h and 168 h of immersion.

After DPNS, two contrast behaviors were observed: first, the hydrogen evolution of the DiDPNS sample was dramatically accelerated. Meanwhile, the hydrogen evolution of the OTDPNS was decreased (**Figure 5-8**a). The hydrogen release data difference turned more drastic than the hydrogen release in the following times of immersion. The ICP-OES data showed a significant decrease ($p < 0.1$) of the Mg release after 48 and 168 hours of immersion **Figure 5-8**c. Details of the corrosion process were examined in the µ-CT scans. No significant corrosion signals were noticed on the OTDPNS sample after 48 hours of immersion, and the strut size remained constant. However, after 168 hours, the sample developed the corrosion characteristic microtopography (**Figure 5-9**). The DPNS treatment caused a change in the corrosion mechanism, and, contrary to the localized group of pits on the pretreated samples, it was a less severe formation of pits on the OTDPNS unit cells. The pits' depth was less pronounced, and the pits coalesce faster instead of going more in-depth on the strut. After DPNS, the DiDPNS samples corroded rapidly. The strut thickness was highly degraded after 48 hours of immersion, and consequently, the strut diameter data for DiDPNS shifted to lower values. Then, the sample was dissolved entirely on day seventh.

The SEM micrographs in **Figure 5-11** present the surface transformation after 24 hours of immersion. The corrosion products deposited on the surface were also analyzed via EDS. Naked samples revealed cracked surfaces; however, cracks were more prominent in the DiCtrl samples. The DiCtrl samples had a degradation layer composed mainly of a network of cracks and deposited products. Only Mg and O were detected on the surface. The OTCtrl sample had a similar appearance with the network of cracks and the deposition of semisphere products. However, in addition to Mg and O, Ca and P were deposited on the surfaces.

After DPNS, the diamond lattice structure showed a continued network of cracks all over the sample. However, the cracks were smaller, more continuous, and less pronounced. This behavior reflects the corrosion mechanism's change from localized corrosion dominated by defects in the structure to continued corrosion on the surface due to galvanic nano sites' accumulation. The appearance of the surface was similar in both the normal and oblique struts. A slight increase of Ca and P was observed in both areas. On the contrary, in the OTDPNS, there was a lower propagation of cracks, and the foam's location differentiated the corrosion appearance. The top surface was slightly modified, while the cross struts revealed the accumulation of semispheres. Again, a slight deposition of Ca and P was detected on the surface.

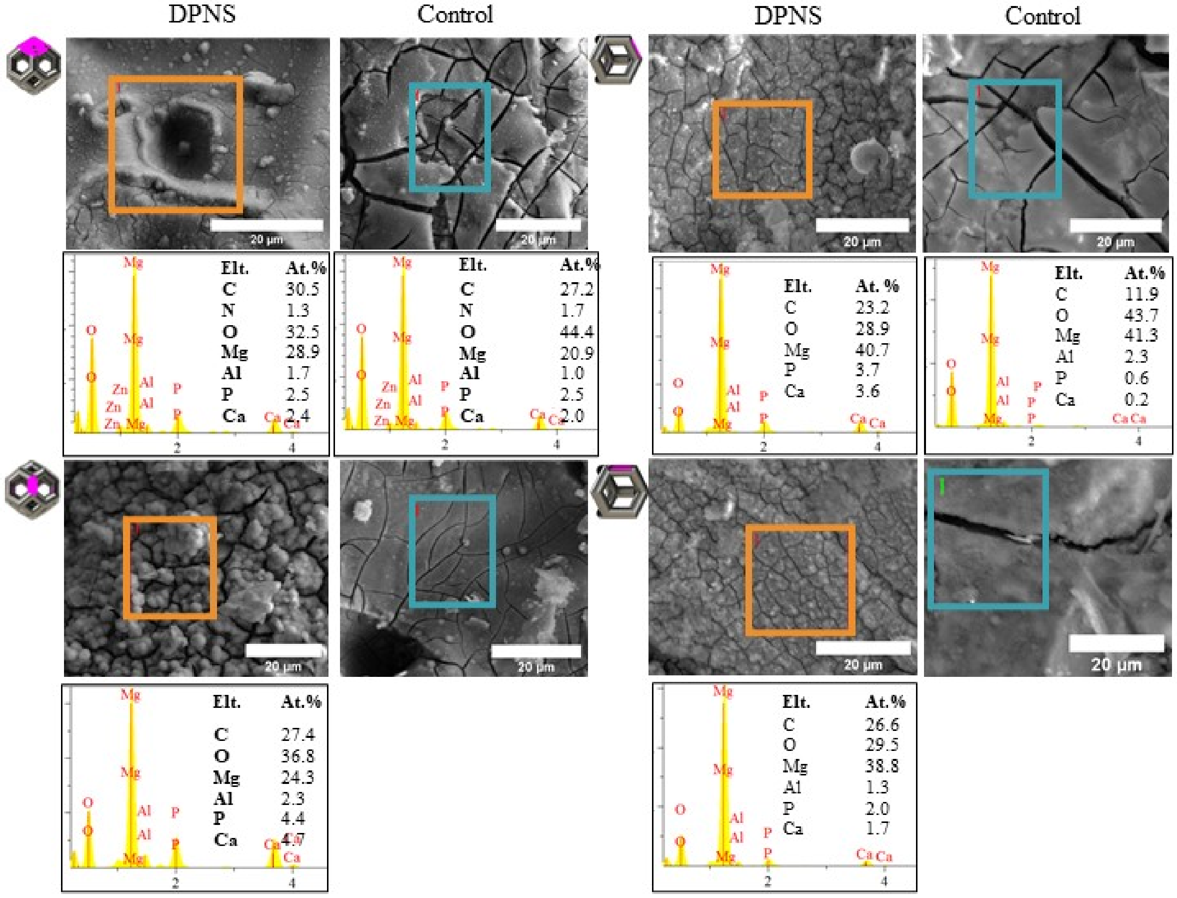

Elt.	At.%
C	30.5
N	1.3
O	32.5
Mg	28.9
Al	1.7
P	2.5
Ca	2.4

Elt.	At.%
C	27.2
N	1.7
O	44.4
Mg	20.9
Al	1.0
P	2.5
Ca	2.0

Elt.	At. %
C	23.2
O	28.9
Mg	40.7
P	3.7
Ca	3.6

Elt.	At.%
C	11.9
O	43.7
Mg	41.3
Al	2.3
P	0.6
Ca	0.2

Elt.	At.%
C	27.4
O	36.8
Mg	24.3
Al	2.3
P	4.4
Ca	4.7

Elt.	At.%
C	26.6
O	29.5
Mg	38.8
Al	1.3
P	2.0
Ca	1.7

Figure 5-11. Surface morphology and chemistry after 24 hours of immersion in DMEM. OTDPNS has less evolution of cracks, and the chemistry depended on the location. Higher Ca and P atomic percents were observed in the oblique strut. DiDPNS has smaller cracks than the DiCtrl, and Ca, and P were also deposited on the surface

5.2.5 Bioactivity

MC3T3 cells were seeded on each sample, taking into account the estimated surface area. The strut's rounded nature made it difficult to quantify the attached nuclei; then, Texas Red®-X phalloidin and DAPI images were used as a qualitative reference for the cell's spread and adhesion. More cells are attached to both DPNS samples after 24 hours of in culture compared to the controls. Moreover, after seven days in culture, cells were still attached to both DPNS surfaces **(Figure 5-12)**. Contrary to the behavior observed in the immersion test, the samples used in cell cultures were not wholly dissolved after seven days of immersion. This result could indicate that the corrosion mechanism changed in the presence of cells.

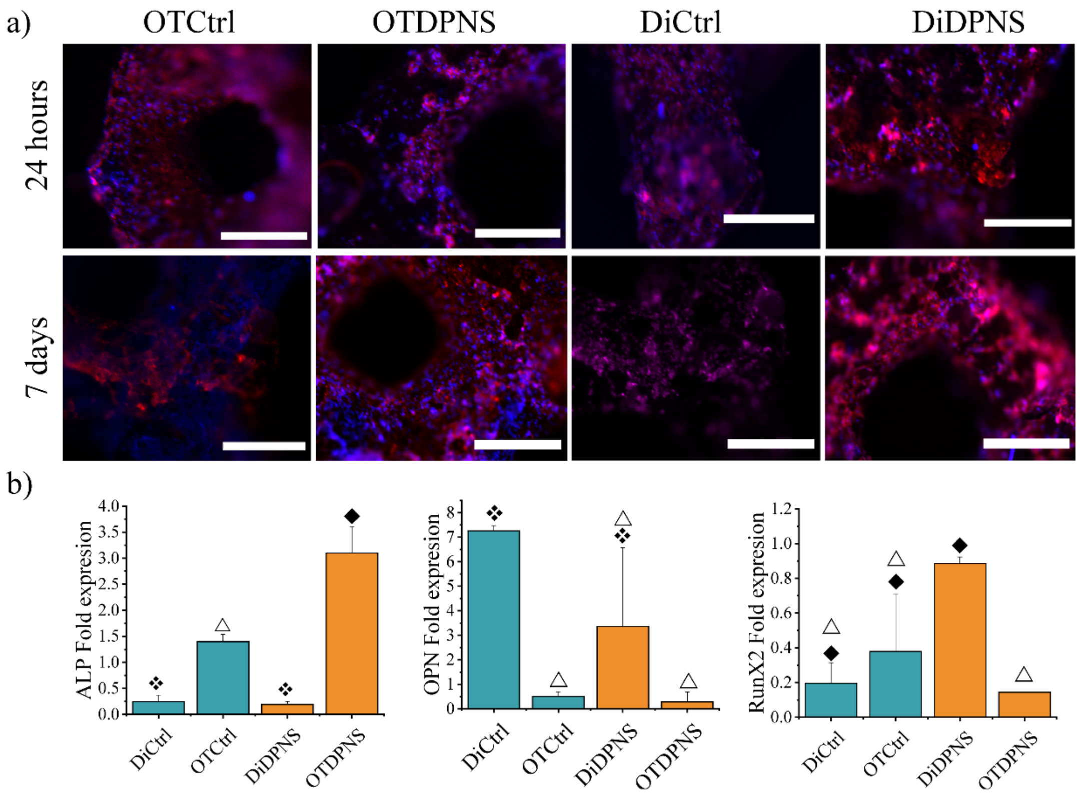

Means that do not share a symbol are significantly different ($p < 0.05$)

Figure 5-12. The biological behavior of pretreated and DPNS samples. a) fluorescence images of the MC3T3 cells seeded on the pretreated and DPNS samples after 24 hours and 7 days in culture. Red color represents phalloidin, and blue color stained nuclei with DAPI. Scale bars represent 500 µm. b) shows the fold expression of the osteogenic related genes ALP, OPN, and Runx2, of MC3T3 cells seeded in the materials' extracts. Means that do not share a symbol are significantly different ($p < 0.01$)

The expression of genes associated with osteoblastic differentiation was analyzed in MC3T3.E1 cells cultures in the material's extracts via RT-PCR after seven days in culture. The ALP levels, OPN, and RunX2 showed the following characteristics: OTCtrl presented significantly higher ALP expression than DiCtrl. Moreover, ALP was significantly increased in the truncated octahedron scaffold treated with DPNS (OTDPNS). Contrarily, the DiDPNS fold expression of ALP was similar to the DiCtrl. In contrast, the OPN fold expression was significantly different in DiCtrl samples compared to the truncated octahedrons. There were no significant differences in the OPN fold expression in both diamond samples. Meanwhile, the OTCtrl and OTDPNS had a low and similar OPN fold expression. There were no significant differences between pretreated and DPNS samples in the fold expression of RunX2. The highest RunX2 expression was in the DiDPNS sample, which was significantly higher than the OTDPNS.

5.3 Discussion

5.3.1 Analysis of the structures

Truncated octahedron and diamond lattice structures were successfully fabricated via infiltration casting. The employed constraints for the design of the scaffolds were pore interconnections with high vascularization potential between 500 and 900 µm (see section 1.3.1), with a minimum strut thickness of 200 µm, considering the manufacturing restrictions. The truncated octahedron unit cells were on the limit of the constraints since the manufacturing process could clog the polyhedron's square face, hindering a larger strut size. Then, the diamond-lattice was designed to contain a similar number of unit cells per volume fraction.

Afterward, the topologically ordered Mg-based scaffolds were fabricated. The alloy composition and the microstructure achieved were similar in the two structures, which can be related to the manufacturing process's replicability. In both samples, the chemical composition of the dominant second phase was not equivalent to the β-$Mg_{17}Al_{12}$ phase, which has been widely reported as the governing second phase in AZxx systems [248,249]. Instead, the island shapes accumulated along the grain boundaries were close to $Mg_{21}(Zn, Al)_{17}$. This phase has been reported for AZ31 and AZ64 alloys [248,250]. Wu et al.[248] described that the formation of the dominant microconstituents in AZxx systems is mainly related to the Zn/Al ratio. β-$Mg_{17}Al_{12}$ is principally formed when the ratio is less than 0.35; on the contrary, when the ratio is higher, $Mg_{21}(Zn, Al)_{17}$ is formed by the reaction $L + Mg_{17}Al_{12} \rightarrow \alpha\text{-}Mg + Mg_{21}(Zn, Al)_{17}$.

The stress-strain curve (**Figure 5-5**) of both lattice structures had the three stages of the typical compression behavior of porous solids: linear elastic deformation, plastic deformation, and densification. The initial loading appeared to be elastic, but the initial curve was not straight. As described by Ashby et al. [251], the slope of the initial loading is lower than the actual modulus because some cells yield at very low loads. Thus, instead of the elastic module, the unloading module describes better the behavior of the structures. Future work must consider dynamic mechanical testing of the material to describe the structure's behavior better. Despite both structures exhibited bending-dominated or stretch-dominated behavior, the diamond lattice structure had better mechanical properties. This behavior could be attributed to the nature of the porous structures. In porous metals, compressive strength decreases with increasing cell size. Moreover, it was a difference of ~150 µm in the strut thickness, and it has been established that the decrease in the strut thickness increases the buckling behavior [93]. However, the Young moduli of both structures were between the range of the cancellous bone (0.3–5 GPa) [5].

5.3.2 Corrosion behavior

The corrosion behavior of Mg alloys is influenced by several factors: alloying, microstructure, and the surrounding environment [252]. The current trend on the fabrication of topologically ordered materials introduces the architectural parameters as new corrosion triggers [93]. Accordingly, despite the microstructural similarities between diamond and truncated octahedron lattice structures, the corrosion properties were significantly different for both sample sets. After seven days of immersion, less hydrogen volume was collected from the as-cast truncated octahedron lattice structure than the as-cast diamond-lattice (**Figure 5-8**). There was a sharp increase in truncated octahedron's hydrogen evolution at the initial stage of corrosion compared to diamond's. This effect can be explained by the truncated octahedron scaffold's larger surface area (26.5% larger) than the diamond lattice structure in contact with DMEM (3.2 ±1.2 cm^2). The increased surface area is likely to accelerate passivation kinetics and reduce the micro galvanic couplings' intensity by forming less soluble precipitates on the surface. Then, the material corrosion resulted in the release of Mg^{2+} and reduced H_2O, which caused H_2 and OH^- release into the DMEM. Higher hydrogen evolution is related to the formation of a higher alkaline environment, which favors the deposition of protective Ca and P. Moreover, the small pore interconnections of the truncated octahedron samples could be following the reasoning of the corrosion mechanism schematically shown in **Figure 2-2b.** Then, the small pore interconnections limit the diffusion of ions at the center of the scaffold.

On the contrary, the rust film formed in the diamond structure allowed the sustained ions interchange (**Figure 2-2**a). In a porous structure, the reaction conditions during the corrosion process can quickly and locally change. Then the morphology of the precipitation varies with the location of the scaffold [16,156]. The micro and macrostructure's local variations acted as seeds for the corrosion to start [136]. In the porous structures evaluated in the present report, the corrosion attack started at single struts at the outer layers to further propagate toward the center of the struts (**Figure 5-9**). Then, the DMEM continued eroding the materials until the corrosion regions merged, weakening the entire structure when increasing the immersion time. As mentioned in **section 2.2.2**, the sample-medium-volume-to-surface-area ratio influences the corrosion behavior of the samples, and the ASTM standards recommendation of a sample-medium-volume-to-surface-area ratio of

0.2–0.4 ml mm^{-2} results in a small ratio for Mg since the samples' corrosion is conditioned by the ions receiving capacity of the media. The ideal sample-medium-volume-to-surface-area ratio for porous Mg is debatable due to the differences in the testing conditions (see **Table 2-1** in **section 2.2.1**). The truncated octahedron and diamond lattice structures of this thesis, with similar sample sizes, were immersed in 50 ml of DMEM, representing a higher medium-volume-to-sample-area ratio for the diamond lattice structures.

5.3.3 Surface evolution after DPNS

The nanostructures are an expression of different kinetic processes caused by the irradiation. When ions driven from a low energy source are used to bombard materials, the surface usually develops a periodic pattern. Hence, the pattern's nature depends on the collision conditions (i.e., crystal orientation, the chemistry of the surface, and irradiation parameters). Discussions about ion beams' effects on surfaces primarily focus on the evolution of initially polished or flat materials [244]. This work presents evidence of irradiation of complex structures; then, as seen in **Figure 5-6** and **Figure 5-7**as the beam moves across the structure, different parts are irradiated at varied angles, which considerably fluctuates the surface topography. The incidence angle significantly influences the modification when Ar ions are used to bombard Mg (see **3.4.1**). Moreover, the non-LOS surfaces were surface modified after DPNS.

There is no uniform pattern over the structures. Hence, consistent with the results in **chapter 3**, normal struts (i.e., the squares normal to the beam in the truncated octahedron) were less modified than the surfaces receiving oblique irradiation (**Figure 5-6** and **Figure 5-7**). At angles of the surface where the ion beam impacts near-normal incidence, the morphology was smooth; then, as the beam approached more grazing incidence, the surface developed ripples morphology. Nanopillars were formed and growing in size when increasing the struts' slope. Diamond lattice structures received mostly oblique irradiation; then, the surfaces had more evident changes, including higher accumulation of Al.

Mg does not easily form a passive film, and cracks appeared on the naked samples (**Figure 5-11**). Then, pits became evident in the µ-CT volumes (**Figure 5-9**). The increase of Al on the surface (due to DPNS) accelerated the corrosion kinetics in both DiDPNS and OTDPNS. The increase in pH speeded up the CaP deposition [162]. The deposition of corrosion products protected the OTDPNS sample from further corrosion. Then, the evolution of H_2 and the dissolution of Mg decreased

(**Figure 5-8**a). A lower propagation of cracks was also observed in the OTDPNS sample than its pretreated analogous.

In the diamond-lattice structures, the passivation kinetics process was also accelerated; however, the excessive accumulation of Al produced more intensive corrosion processes and augmented the Mg dissolution due to the elevated increase in galvanic sites [29,212]. Then, the formation of surface microcracks deteriorated the corrosion products [33,215]. Contrary to the DiCtrl sample, which formed more expanded cracks, the DiDPNS developed a continuous network of small cracks. This event can be correlated with the formation of galvanic sites at the nanoscale. In the DiDPNS sample, the DPNS process created and homogenization effect, then the samples had similar chemistry and morphology after immersion in DMEM. Then, a lower accumulation of Al on the surface would decrease the diamond lattice structure corrosion. These results raise the hypothesis that less energy is required to control the corrosion of diamond lattice structures, as will be studied in the next chapter.

5.3.4 Biological behavior

Several authors have reported the sensitivity of the cell proliferation and differentiation activities to the 2D and 3D architecture of the implants. The design of scaffolds considering the cell aspects is described in **section 1.3.1**. Some general trends are that the cells expand and proliferate more in struts that are set apart. However, pores with more corners promote cell differentiation. The MC3T3 cells' behavior in the present work was different between analogous geometries, suggesting independence of the cell's conduct and geometry of the pore. Despite a similar quantity of cells attached to the surface at the early stages of the assay, the adhesion and proliferation of cells were enhanced with the DPNS treatment, as observed at 7 d of cell culture (**Figure 5-12**). Then the cells remained on the surface after seven days of immersion. This behavior can be explained with Ca and P's preferential deposition on the DPNS surfaces [189]. The increase in the apatite nucleation ability has been described as a sign of osteointegration potential [189]. Contrarily to the immersion test, the DiDPNS samples did not completely dissolve during the cell culture assays. It is then suggested that the corrosion mechanism of the sample has changed with the cells adhered to the surface, acting as a kinetic barrier that blocked the ions interchange on the surface [235].

The expression of osteogenic-related genes in the materials' extracts can be correlated with the Mg ions release and the Mg^{2+} osteogenic potential. The ALP, which is an early osteogenic marker, was significantly higher expressed in the OTDPNS sample. RunX2 gene expression was similar for the samples having the highest expression in the DiDPNS samples. The results are coincident with the statement that the osteoblast induction potential of Mg^{2+} is conditioned by the concentration of Mg ions in the medium (see **section 4.4**). Then, the OPN fold expression was higher in the DiDPNS samples. It has also been suggested that OPN fold expression is related to the number of osteoclasts in the environment [238].

5.3.5 Conclusions

Two geometries were treated with DPNS, truncated octahedron, and diamond lattice structures. The results were highly conditioned on how the ions locally hit the surface. In the truncated octahedron case, the deposition of Ca-phosphate products protected truncated octahedron samples from further corrosion. However, in the diamond lattice structure, a large increase in the Al accumulated on the near-surface accelerated Mg's dissolution due to the excessive increase in nanogalvanic sites. In both DPNS samples, the cells spread, and attachment was increased after the DPNS treatment.

6. In vivo response of DPNS modified Mg-based scaffolds

Biodegradation control, mechanical stability, and strength are vital characteristics of Mg scaffolds during the bone healing process. The role of these materials is to clamp together two healthy parts of the tissue [145]. As seen in (**Figure 5-5**, page 106), diamond lattice structures have superior mechanical properties to truncated octahedra. The structure with diamond unit cells becomes more convenient for the support requirements during the bone replacing period. However, this structure's corrosion must be controlled to sustain the mechanical advantages during the healing time. A schematic representation of the biodegradable metal supporting function during bone healing is shown in **Figure 6-1**.

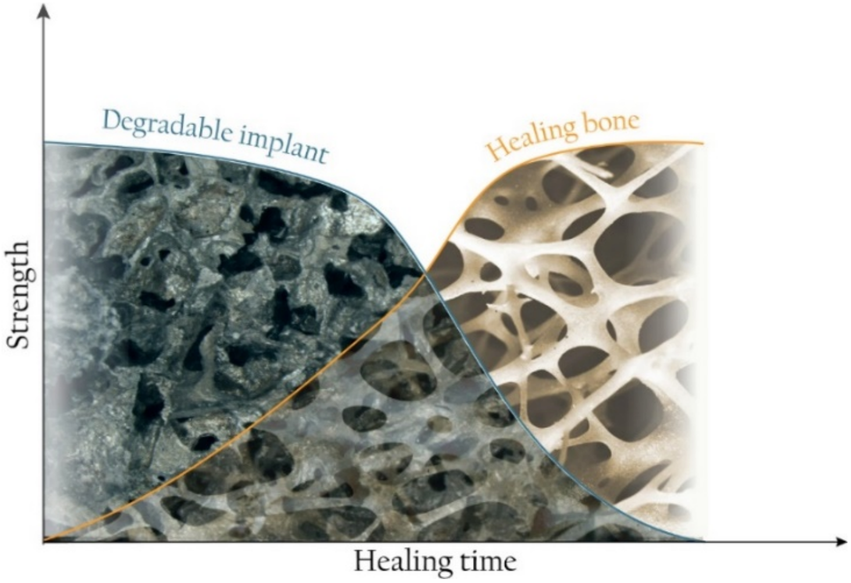

Figure 6-1 Biodegradable implant support function during bone healing. The biodegradable porous metal is expected to provide strength and be integrated with the tissue and bioresorb after fulfilling the supporting functions.

The diamond lattice structure has more surfaces exposed to oblique irradiation than the truncated octahedron because of the assembly's nature. As demonstrated in **section 3.4.4**, the incidence angle significantly affects the DPNS outcome when irradiating AZXX systems. It is then hypothesized that less energy is required to produce a more regulated Al supply on the diamond surface, enhancing the apatite formation ability of these samples and decreasing the corrosion rate.

The apatite formation ability enhanced by DPNS is expected to enhance the in vivo biocompatibility of the material. However, the relation of the corrosion mechanism of Mg systems in vitro and in vivo is still speculative. In the in vitro conditions, as described in **section 2.2.1**, a concentration of Cl^- ions higher than 30 mM accelerates pit corrosion by transforming $Mg(OH)_2$ into soluble $MgCl_2$. Hence, the concentration of Cl^- ions presented in the DMEM accelerates the samples' pit formation. New factors, including the concentration of ions, oxygen affinity, local pH, and the presence of proteins, are associated with the corrosion rate of Mg implants in vivo [177]. These factors are, in turn, associated with the implantation location because of the water content, the nature of the electrolytes, the blood vessels, and the level of blood flow. For instance, implants located under the periosteum exhibited a higher volume loss than Mg implants inserted near the cortical bone [253]. Hence, the apatite formation ability of the DPNS sample to form denser oxide products is expected to reduce the in vitro and in vivo corrosion rate, as the solubility of CaP phases in the body fluid is relatively low. The corrosion reaction is then inhibited by forming a protective barrier on the surface [254],[255].

6.1 Methodology

6.1.1 DPNS

The samples, fabricated as described in **section 5.1.1**, were fixed to an AZ31 sample holder, as shown in **Figure 6-2a**. The Ar^+ irradiation was conducted with the orientation shown in **Figure 6-2**b. After that, the sample was rotated upside down (**Figure 6-2**c), and the irradiation conditions were again applied to the surface. As mentioned, less energy was used to produce a controlled accumulation of Al on the surface. The samples were irradiated in IGNIS operating at room temperature in ultrahigh vacuum (base pressure $<3\times10^{-8}$ Pa). The irradiation parameters were Ar^+ ions with 400 eV energy and 1×10^{17} ions/cm^2 fluence.

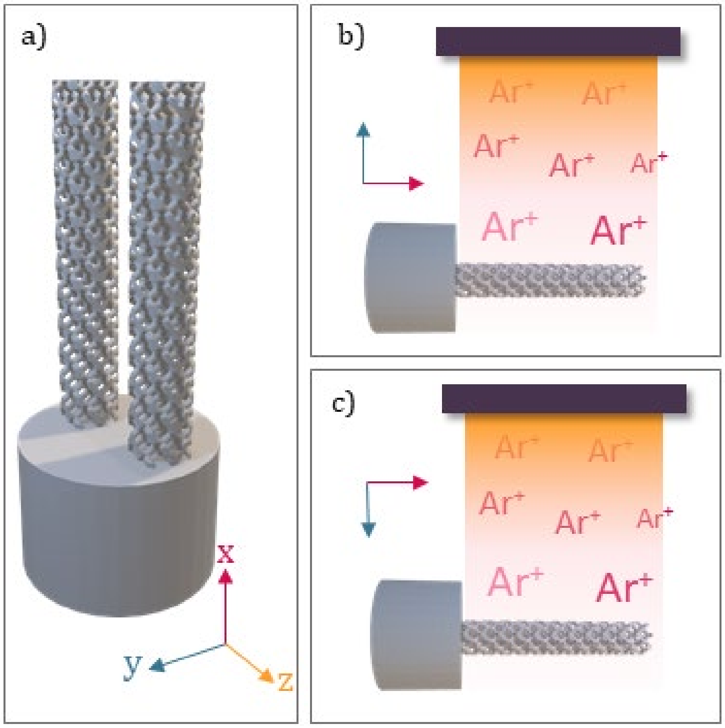

Figure 6-2. Schematic representation of the DPNS process. a) the location of the diamond structures on the AZ31 sample holder. b) initial orientation of the samples. c) orientation of the samples after rotation.

6.1.2 In vitro degradation

The samples were immersed in DMEM, as described in **section 5.1.4**. The concentration of Mg ions in the corrosion medium was analyzed via ICP-OES after 2, 7, and 14 days. The samples were observed before and after removing the corrosion products with 150 g CrO_3 + 10 g Ag_2CrO_4 in 1 L deionized water in boiling conditions.

Surface topography and distribution of elements of the different stages (DPNS and immersion) were evaluated via SEM/EDS. After DPNS, measurements were conducted as described in **5.1.2**. After immersion, the SEM/EDS analyses were conducted in FE-SEM (JEOL FE-JSM-7100F) equipped with EDS (Oxford 51-XMX1178). The samples were covered with Au/Pt.

6.1.3 Evaluation of in vitro bioactivity

The in vitro bioactivity was evaluated following the procedure described in **section 5.1.5**. Briefly, MC3T3-E1, subclone 4 were seeded on the surfaces with α-MEM supplemented with FBS as the growth medium. The cell morphology was observed under confocal microscopy using fluorescence stains.

6.1.4 In vivo degradation

The ethics committee of the *Universidad Nacional de Colombia* (*Comité para el Cuidado y Uso de los Animales* – CICUA) approved the protocols for animal experiments. The ethics committee approval is shown in **Appendix C**. The experiments were carried out in the *Corporación para Investigaciones Biológicas* (CIB), Medellín, Colombia.

Surgical procedure

Wistar rats (12 weeks old weighing 200 ± 24 g) were used to evaluate the scaffolds' in-vivo biodegradation and compatibility. The procedure was carried out aseptically and under local anesthesia, giving the rats an intramuscular injection of ketamine/xylazine mixture, 100 mg kg $^{-1}$ and 10 mg kg^{-1}, respectively. Each rat was placed in ventral ulna position, and an incision of approximately 1 cm in length was made in the skin. Through this incision, the piece of material was implanted under the rats' back skin in the proximal and distal locations schematically shown in **Figure 6-3,** where a) is "proximal" and b) is "distal." A photographic register of the implantation process is shown in Appendix D, **Figure D-1**. The skin incision was closed using an absorbable synthetic suture Monocryl*Plus (Ethicon). After 1, 4, and 8 weeks the animals were sacrificed using a CO_2 chamber.

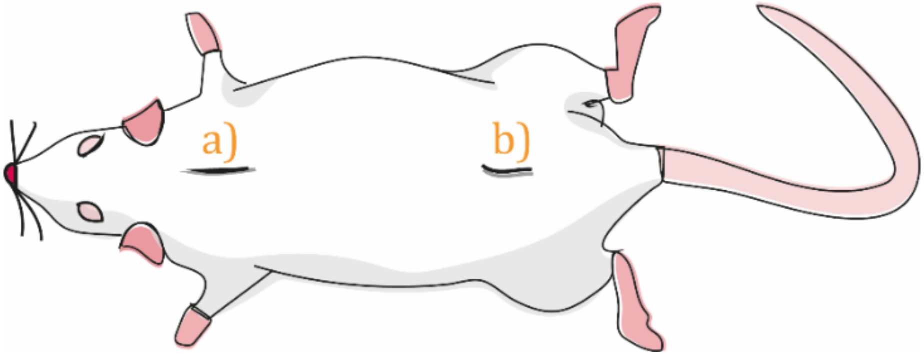

Figure 6-3. Schematic representation of the incisions for the implantation of the scaffolds. The implants were placed under the rats' skin at a) proximal and b) distal locations.

The biodegradation of the pre-treated scaffold (n = 5) and the DPNS scaffold (n = 5) were evaluated via mass loss after four weeks of implantation. The samples were weighed before and after being implanted and extracted. The corrosion products of the removed implants were eliminated by immersing each piece in a cleaning solution containing 150 g CrO_3 + 10 g Ag_2CrO_4 in 1 L in boiling conditions. Then, the corrosion rate was calculated following **Equation 2.8**. The details of the corrosion mechanism were analyzed with SEM, equipped with EDS. The diameter of the struts was measured from stereomicrographs of the explanted samples after the removal of the corrosion products; ten random locations were measured on each explanted material.

The procedure described above was repeated after 1, 4, and 8 weeks to elucidate the in vivo corrosion mechanism of the DPNS samples. The samples were implanted at distal (n = 5) and proximal (n = 5) locations.

6.2 Results and discussion

6.2.1 DPNS and in vitro characterization

Two different morphologies were observed on the irradiated samples, consisting of a surface with a nanoripples formation and a second surface with nanodots' formation (**Figure 6-4**a and b, respectively). The diamond structure in the present chapter, modified with lower energy (400 eV), presented comparatively smoother surfaces than the DiDPNS structures in **section 5.2.2**, irradiated with higher energy (700 eV). Moreover, an Al supply (2.3 ±0.7 wt.%) in the near-surface was again observed in the diamond structures irradiated with 400 eV (**Figure 6-4**c and d); However, the Al accumulation was lower than the 700 eV diamond case (**Figure 5-7**). As explained in **Chapter 3**, the energy parameter alone does not significantly affect the DPNS results in Mg systems; however, energy and fluence interaction significantly influences the DPNS outcome.

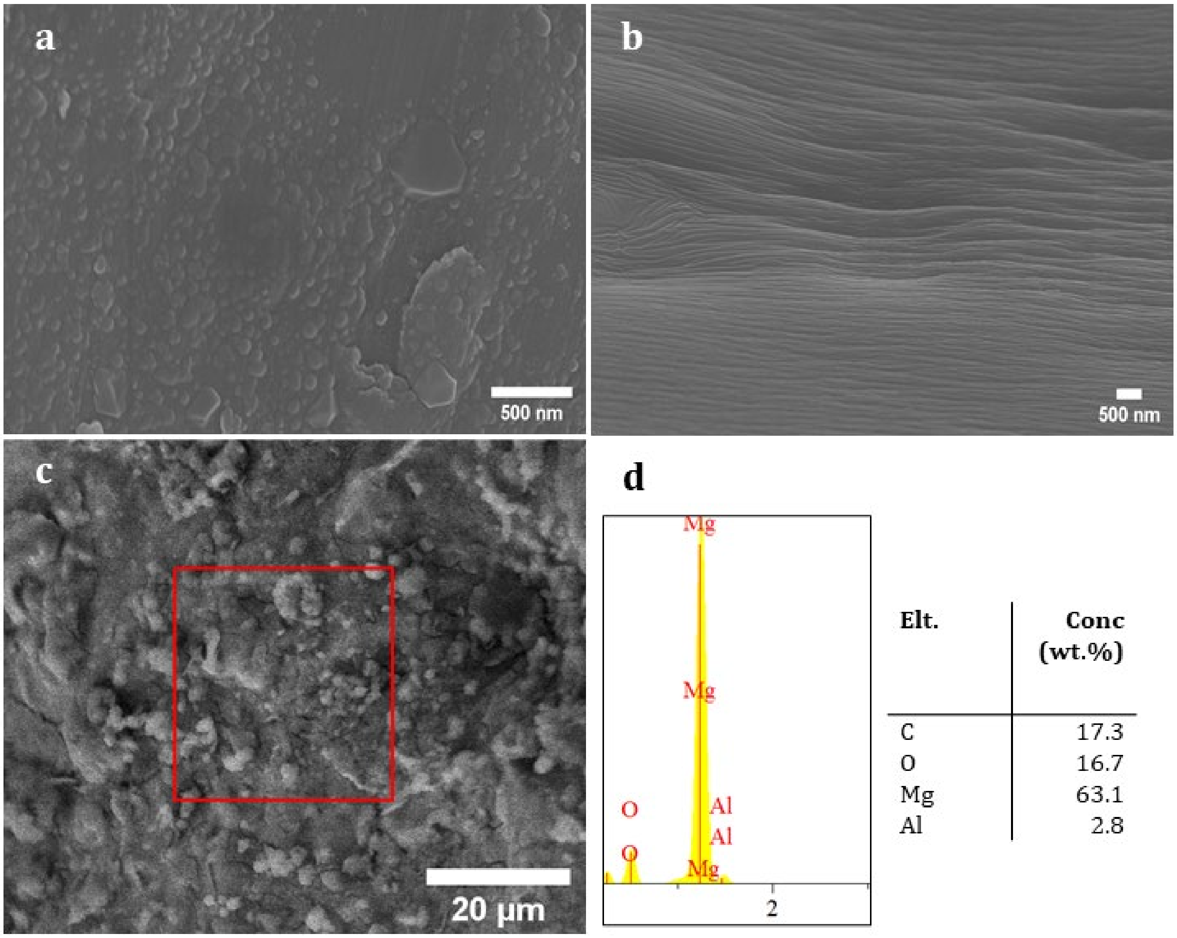

Elt.	Conc (wt.%)
C	17.3
O	16.7
Mg	63.1
Al	2.8

Figure 6-4. SEM micrographs and SEM/EDS analysis of the diamond samples irradiated with 400 eV. a) and b) SEM micrographs of the nanostructures formed on the 400-eV irradiated sample surface. c) a lower magnification micrograph showing the area of the EDS analysis in d)

Moreover, in the course of this thesis, smooth nanotopographies have been observed on surfaces that face the beam near-normal incidence, in turn, associated with a slight accumulation of Al on the surface more convenient for the degradation control (**Figure 4-17**). The new observed surfaces (in diamond-DPNS with 400 eV energy) and the chemistry change may result from the synchronic effect of the decrease in energy and the sample rotation. However, confirming the exact incidence angle of the beam on the sample's surface is challenging due to the complexity of the geometry.

After two days of immersion in DMEM, the Mg ions collected from the DPNS materials' degradation were significantly higher than the control (**Figure 6-5**a). After seven days, the release of Mg ions was suppressed on the DPNS samples while continued in the controls. At this time point, the accumulation of CaP products, with a Ca:P ratio of 1.44 ± 0.04, was observed in the SEM/EDS analysis (**Figure 6-5**b and c). At the end of the testing time (14 d), the accumulation of ions released from the control sample was significantly higher (**p ‹0.01) than the ions released from the DPNS samples (**Figure 6-5**a). The scaffolds' bioactivity was enhanced after the DPNS treatment, and consequently, more MC3T3 cell nuclei were attached to that surface (**Figure 6-6**).

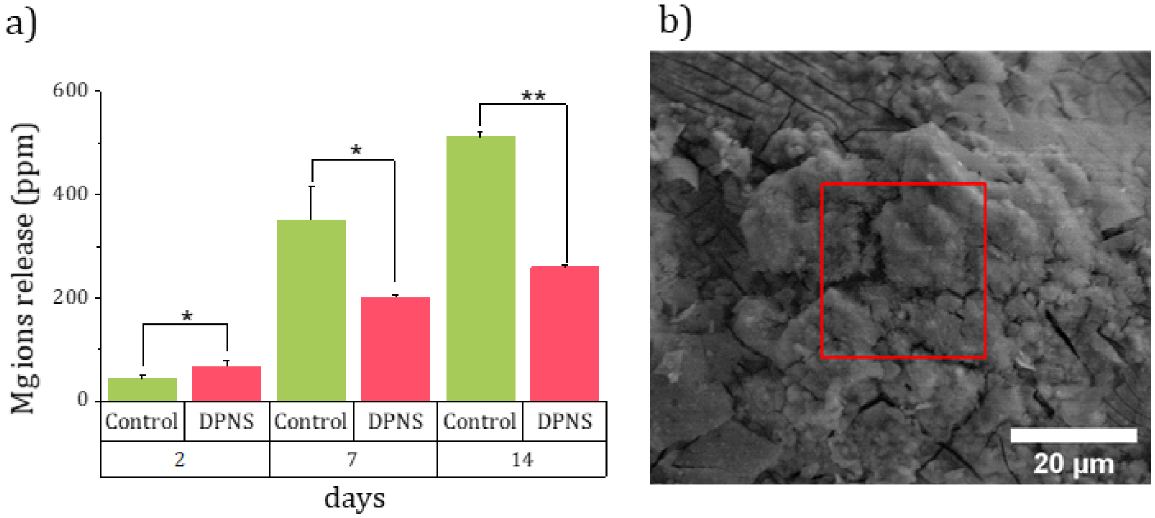

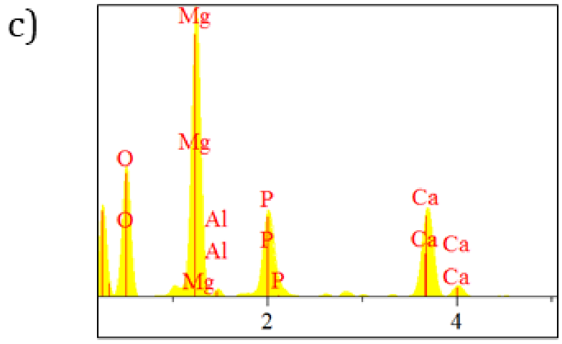

Elt.	Conc (wt.%)
C	26.1
O	32.1
Mg	20.7
Al	0.5
P	8.2
Ca	12.3

Figure 6-5. In vitro corrosion of the diamond samples irradiated with 400 eV energy. a) Mg ions released after 2, 7, and 14 days of immersion, *p ‹0.05 and **p ‹0.01. b) SEM micrograph after 7 days of immersion. The red square shows the location of the EDS analysis in c).

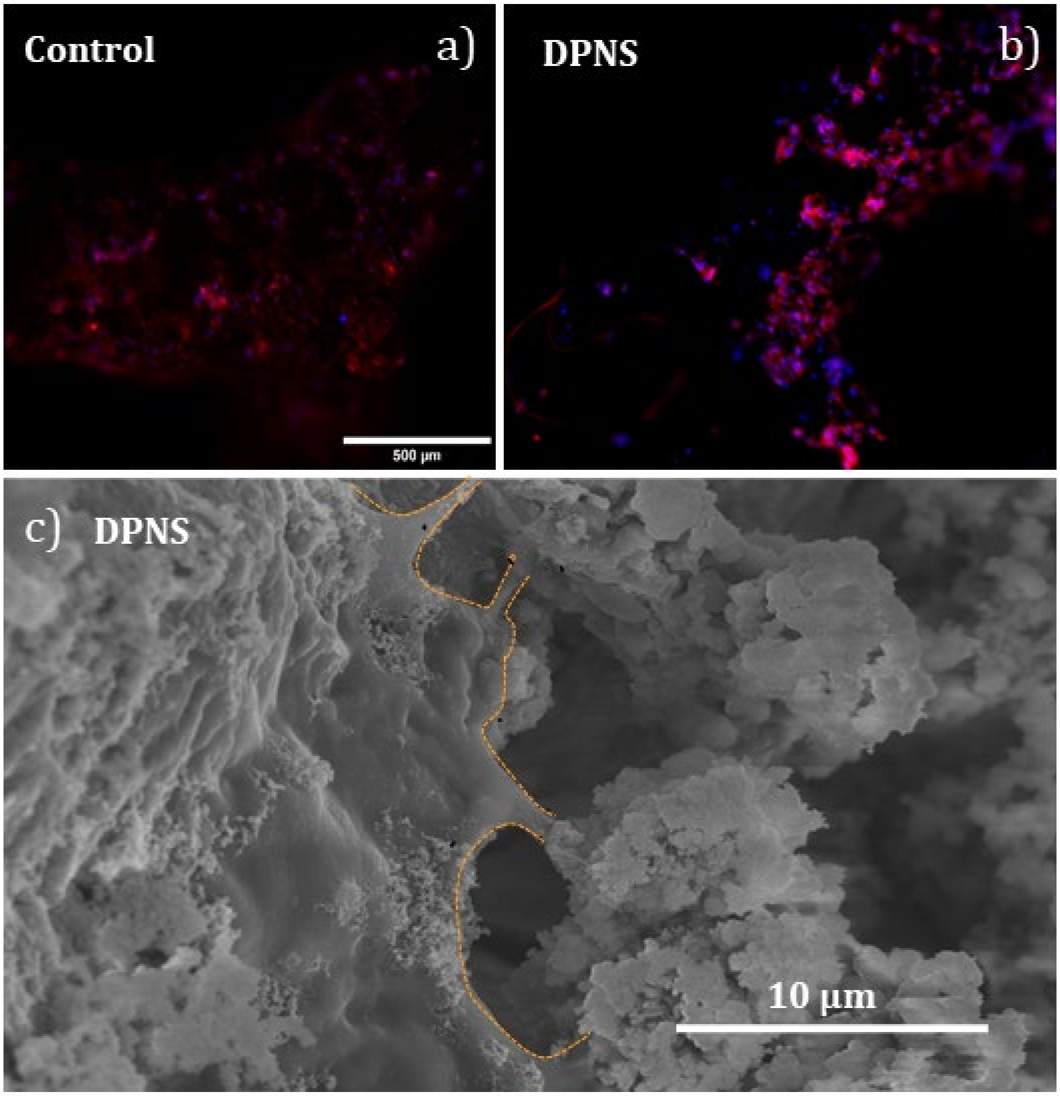

Figure 6-6. In vitro biological behavior of the control and diamond sample irradiated with 400 eV energy. a) is the fluorescence micrograph of MC3T3 cells stained with Actin and DAPI (blue and red respectively. B) fluorescence micrographs of the MC3T3 in the DPNS sample. c) SEM micrograph of the cells adhered to the DPNS surface. Cells contour is marked with the dashed lines.

6.2.2 In vivo characterization

Control and DPNS materials were compared by implanting the samples under the rat's skins for 4 weeks. **Figure 6-7** shows representative macroscopic pictures of both samples. In the DPNS case (**Figure 6-7**b), the image revealed healthy tissue with H_2 bubbles formation (blue arrow), and the scaffold was evident under the skin (violet arrow). On the contrary, the control samples were dissolved entirely. The only trace of the implant was a small "pigment" on the tissue (**Figure 6-7**a, yellow arrow). Miura et al. [253] described that the corrosion of Mg implanted in Wistar rats depended on the thickness of a fibrous tissue that encapsulates the implant. According to this rationale, a thicker capsule was formed around the DPNS sample in the present work. However, further experiments, such as µ-CT scans, are required to support this suggestion.

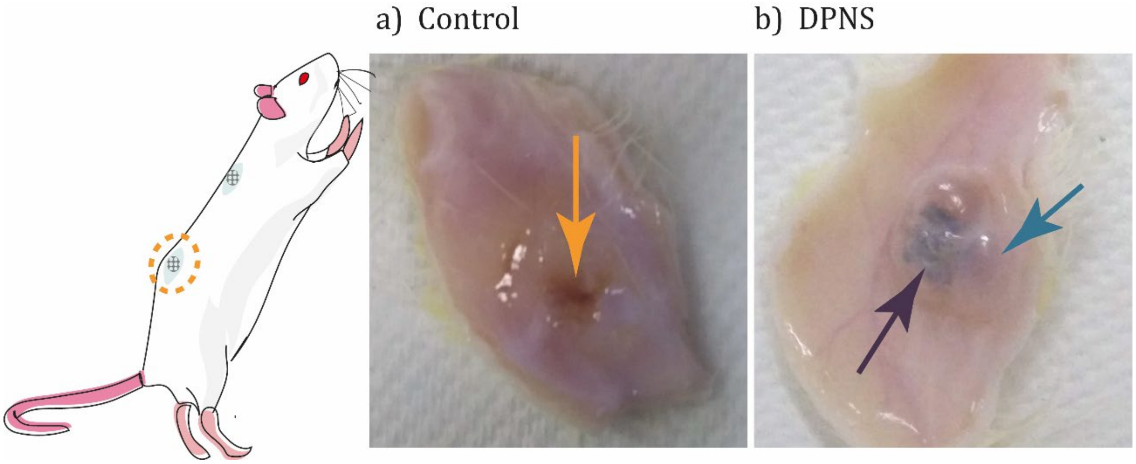

Figure 6-7. Retrieved tissue after 4 weeks of implantation. a) control, the yellow arrow is signaling a small pigmented zone after the complete dissolution of the implant. b) DPNS, the violet arrow is showing the implant visible under the skin. The Blue arrow is showing the formation of gas bubbles under the tissue.

Macroscopic observations of the DPNS samples on the implanted zones showed signs of well-tolerated places with minor reactions in all surgical wounds (**Figure 6-8**). Gas pockets, formed as the result of the hydrogen evolved during the dissolution of Mg, were visible from the first week of implantation (**Figure 6-8**a). However, the gas pockets were decreasing in size with the implantation time progression (**Figure 6-8**c). At weeks 4 and 8, the accumulated gas was evidently dissolved, and the tissue sections revealed healthy segments without redness or swelling. There were no significant differences in the corrosion rates in both proximal and distal locations (**Figure 6-9**a). Moreover, despite the gas pocket dissolution, there were no significant differences in the corrosion rates after 1, 4, and 8 weeks of implantation (**Figure 6-9**b).

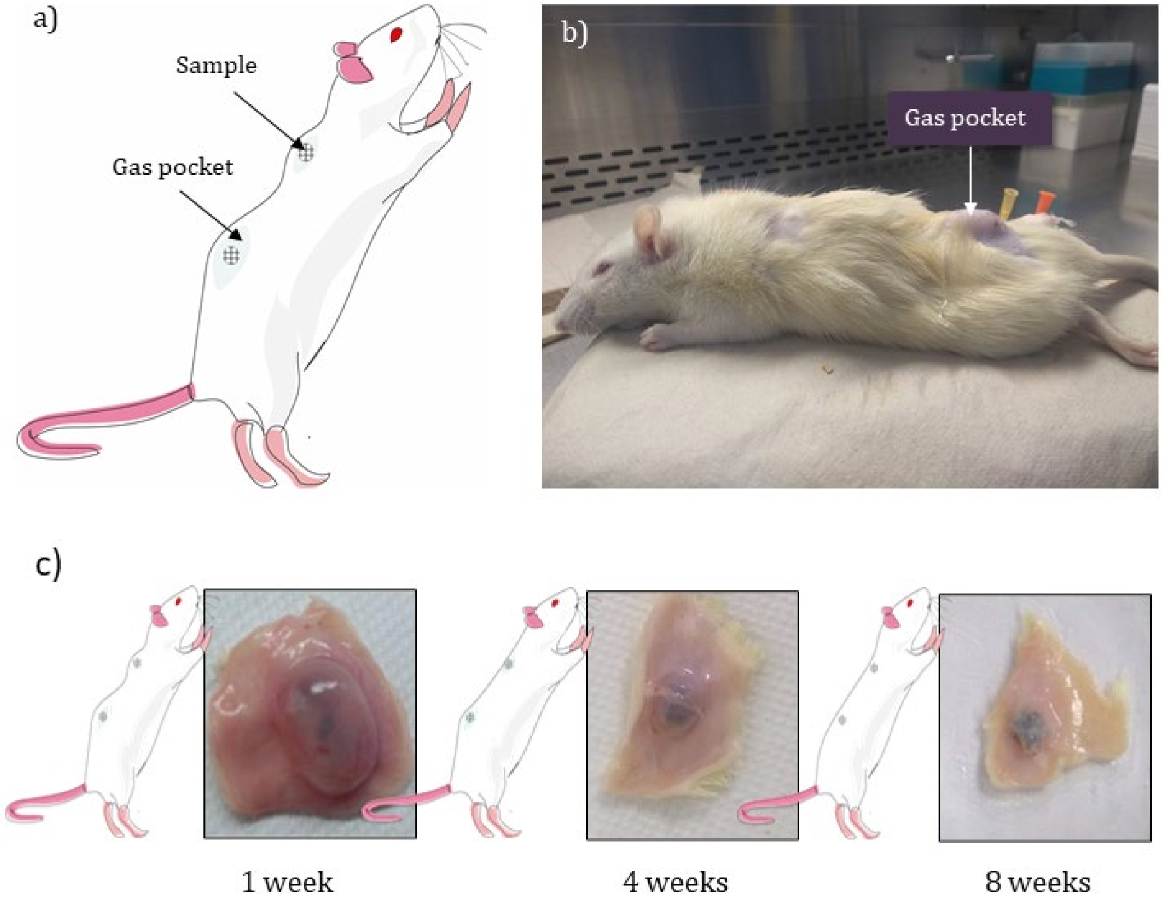

Figure 6-8. Macroscopic evaluation of the DPNS implants during the implantation time. a) schematic representation of the gas pockets formation around the implant. b) photograph of the rat after 1 week of implantation. c) tissue samples retrieved from the implantation site showing the dissolution of the gas pockets during the time.

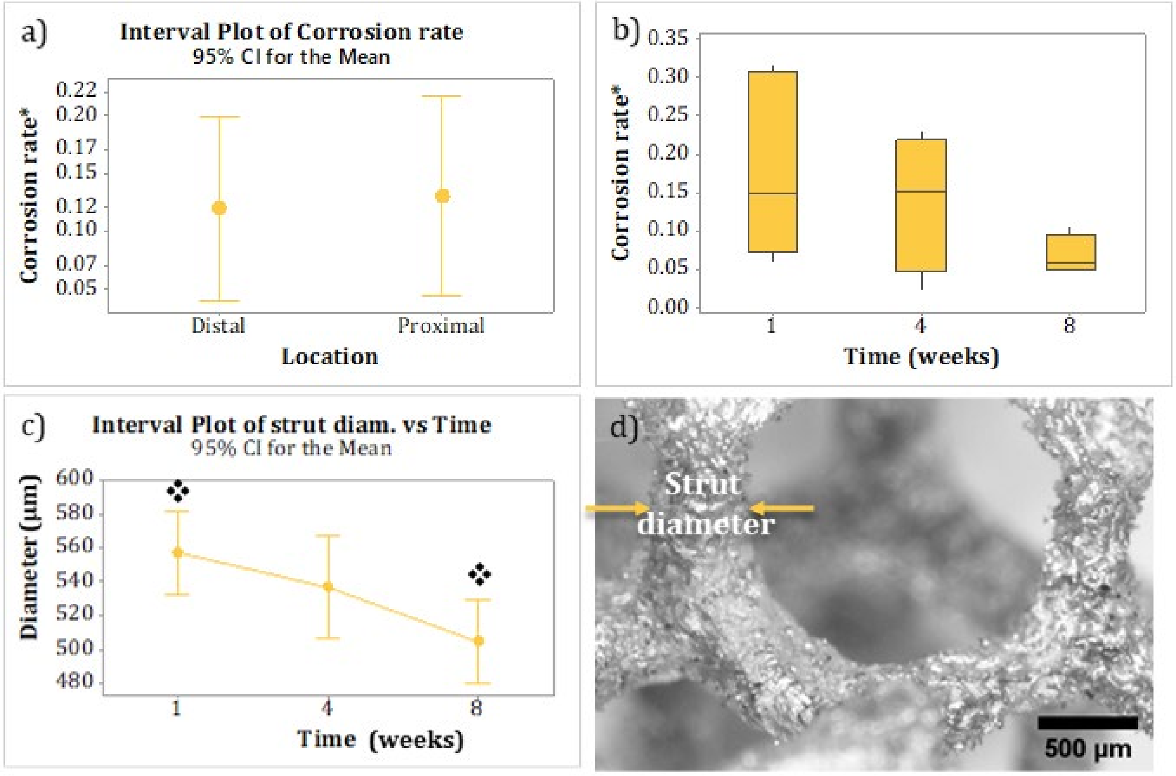

Figure 6-9. In vivo corrosion of the diamond samples irradiated with 400 eV. a) interval plot of the corrosion rate in both distal and proximal locations. b) box plot of the corrosion rate at the different extraction times. * the corrosion rate units are mg.cm^{-2}.d^{-1}. c) interval plot of the strut diameter vs. time after 1, 4, and 8 weeks of implantation. There are significant differences in the strut diameter between weeks 1 and 8 (❖$p < 0.05$). d) stereomicrograph of a sample after 4 weeks of immersion showing the mechanism of strut diameter measuring.

As mentioned before, the corrosion of Mg systems is dependent on the equilibrium concentration of ions in the aqueous environment [177]. This statement suggests that in the in vivo conditions, the corrosion of Mg is accelerated since the dynamic nature of electrolytes flow avoids reaching that equilibrium concentration [256]. However, differences in the corrosion mechanisms of Mg systems in vitro and in vivo are still speculative. The in vitro case, which principally consists of pit formation due to the Cl^- attack, has been demonstrated to change with vivo conditions. New passivated zones appear due to the growth of tissue on the implant surface [257]. Moreover, as observed above (**Figure 6-8**) and noticed in other in vivo Mg studies [253,258–260], in the first stages of the corrosion process, the hydrogen gas accumulated creates a subcutaneous gas pocket due to the low diffusion coefficient of hydrogen in the tissues. This accumulation of H_2 is dependent on the water content and blood flow in the zone [257]. For instance, the blood flow (18.9 ± 1.4 ml/min/100 g) and water content (65.1 ± 0.7 %) in rat's skin are higher than the blood flow and water content in other tissues such as bone (blood flow: 2.3 ± 2.0 ml/min/100 g; water content: 44.6 ± 1.7 %) [253]. A reported isometric exercise increased, femoral blood flow in humans is 4.2 ± 1.2 mL/min/100 g [261]; however, comparisons between human and rat models are still dependent on specific metabolic aspects.

After removing the corrosion products with CrO_3, the formation of corrosion pits was evident in the DPNS in vitro sample (**Figure 6-10**a). The corrosion topography consists of lines, like rivers. On the other hand, after the first week of implantation, the explanted scaffold's morphology showed a different rough topography with the formation of holes. The holes in the explanted scaffold were deeper and smaller in width than the in vitro samples. Walker et al. [262] reported that the in vitro corrosion of Mg is higher than in the in vivo environment, possibly due to the higher concentration of Cl^- ions on the in vitro solution. Moreover, the presence of proteins on the Mg surface in vivo protects the sample from further corrosion [263,264].

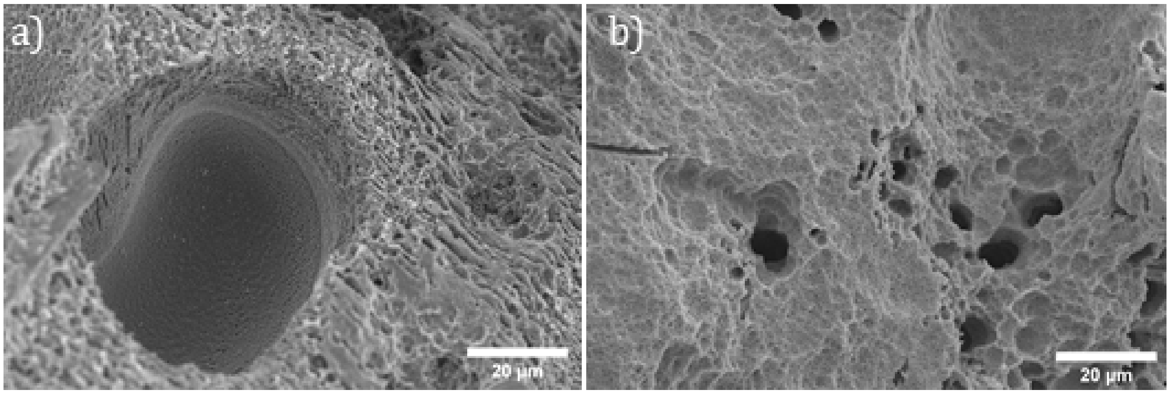

Figure 6-10. Corrosion morphology of in vitro and in vivo samples after 1 week of implantation. a) in vitro sample. b) in vivo sample. The corrosion products were removed with the CrO3-based solution.

The morphology in the in vivo samples (after removing the corrosion products) was constant during the whole implantation period (8 weeks; **Figure 6-11**), which was also consistent with the steadiness of the corrosion rate (**Figure 6-9**a). The struts diameter was conserved during weeks 1 and 4. However, there were significant differences in the strut's diameter between week 1 and 8 **Figure 6-9**c.

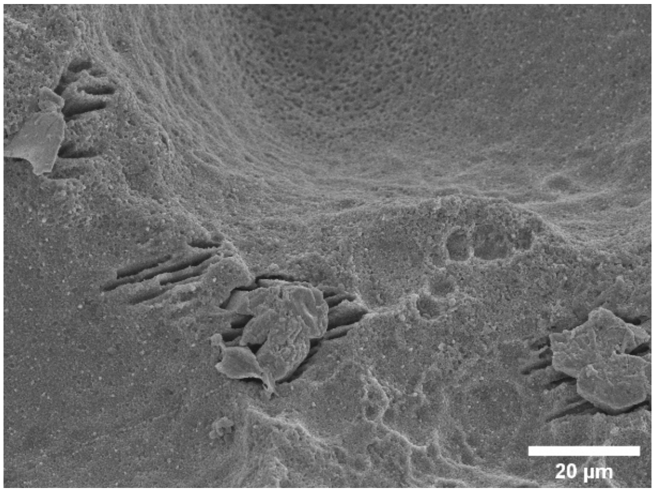

Figure 6-11. Corrosion morphology of in vivo samples after 8 weeks of implantation.

SEM morphology of the retrieved implants is observed in the EDS micrographs in **Figure 6-12**a, b, and d. The EDS analysis showed increasing Ca and P signals. An additional peak correspondent to K was observed in the samples at 4 weeks. The presence of K was new for the corrosion behavior of the Mg-based implants observed during the development of this thesis. However, K deposition has been noticed in other in vivo studies [265]. At higher magnification, the corrosion products of the extracted implants revealed dendritic crystals that were similar to the corrosion products in [265]. The increasing signal of Ca and P could be analyzed as a descriptor of the deposition of a protective layer of corrosion products, which can also be noticed in decreasing the Mg concentration.

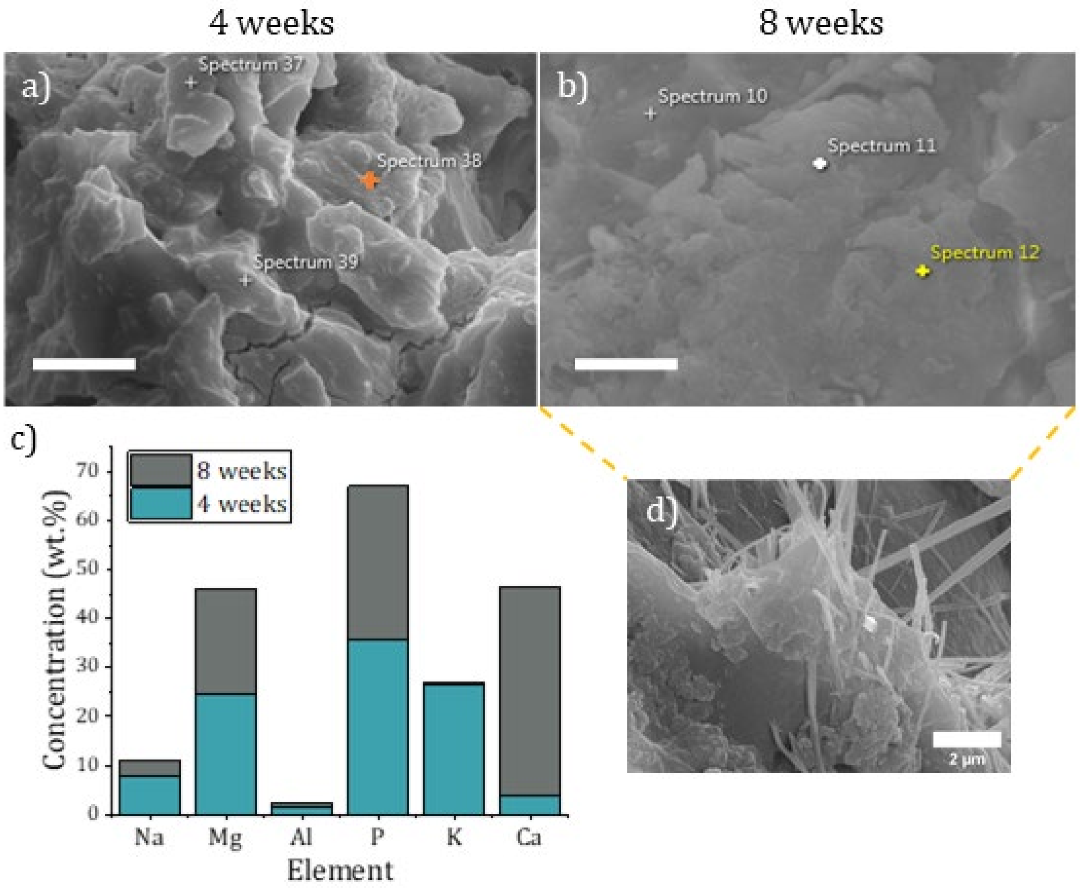

Figure 6-12. SEM/EDS analysis of the as-explanted DPNS sample. a) SEM after 4 weeks of implantation. b) 8 weeks of implantation with a higher magnification view in d). Scale bar in a) and b) represents 10 µm. c) shows the distribution of elements on the surface after 4 and 8 weeks.

6.3 Conclusions

The decrease of the applied energy on the structure with diamond unit cells caused a controlled accumulation of Al that was convenient to increase the apatite nucleation ability of the DPNS-foams. The samples were tested for corrosion resistance and biocompatibility in vivo and in vitro. The release of Mg ions after two weeks of immersion was highly significantly decreased in the DPNS sample. Moreover, higher cell density was observed on the DPNS surface. In the in vivo outcome, the control samples were wholly dissolved after 4 weeks of implantation. Meanwhile, the in vivo corrosion rate was consistent without significant differences during the entire implantation period. Hydrogen gas pockets were observed in the initial stages of the implantation; however, the hydrogen accumulation was safely dissolved during the time. Then, DPNS treatment enhanced the stability of the in vivo samples after 8 weeks of immersion.

7. Conclusions and future perspectives

7.1 Conclusions

- Mg degradation involves mostly localized corrosion boosted by the pores' clogging and the strut loss due to the accumulation of corrosion products. The current protection mechanisms consist of conversion coatings, including chemical conversion and deposition of ceramic, polymeric, and hybrid coatings. These coatings are hindered by their volume, which compromises the bulk properties of the material and their adhesion properties that can cause delamination. Moreover, some conversion methods, such as MAO, require the dissolution of the bulk material leading to a reduction in the strut thickness. Hence, the protection mechanism must consider the samples' geometry to balance corrosion protection and open porosity.

- An open-porous Mg-based scaffold for bone tissue engineering has been obtained and surface-modified to enhance corrosion resistance and biocompatibility. The modification method is limited to the first nanometers of the surface, avoiding changes in the bulk properties of the material.

- DPNS was proposed as the surface modification method since the exposure of AZ31 samples to low-energy Ar^+ irradiation causes Al supply on the near-surface due to the ion-enhanced Gibbsian segregation. The interaction of the Ar ions bombardment with the AZ31 surface was studied under different DPNS conditions. The results showed that minor changes in Fluence, Incidence angle, and the interaction of Energy and Fluence, can control the accumulation of Al on the near-surface in the form of Al-rich nanoclusters. Hence, nanogalvinc sites are created; and the fine-tuning of them can control the CaP deposition when immersing the samples in physiological environments. From this basis, a surface modification method was designed to enhance the apatite formation ability of the scaffolds to improve the corrosion rate and bioactivity. This finding also introduces information on the understanding of Al's role in modulating surface properties on AZxx systems.

- The apatite formation ability was conditioned to the Al accumulated on the near-surface, which permitted surfaces for different biological purposes by tailoring the CaP ratio.
- Information about the role of well-ordered topography is introduced for porous Mg at the nanoscale level. Nanostructures are formed on the immediate surface due to the kinetic processes occurring during the Ar^+ ions irradiation. Despite the dominant effect of the Al-accumulated, the creation of the nanostructures leads to the development of a temporary hydrophobic surface associated with faster apatite deposition. However, the importance of the surface nanotopography is limited to the initial stages of immersion since the nanostructures are rapidly replaced by the rust layer deposited on the DPNS sample when immersed in aqueous environments.
- Traditional ion irradiation studies have been applied to initially flat surfaces. In the present thesis, complex porous structures were treated with Ar^+ ions. In topologically ordered structures, the DPNS outcome is highly conditioned on how the ions locally hit the surface. Surfaces that were facing the beam with near-normal incidence presented lower modification than surfaces in oblique irradiation. Then, DPNS modification can be designed, taking into account the geometry of the material.
- DPNS samples presented higher biocompatibility regarding enhanced surfaces for cell adhesion and proliferation. The transformation of the DPNS-surfaces in the physiological fluid also motivated a greater isotropic cell spreading with the formation of focal adhesion points, demonstrating a more stable environment for the cells to grow.
- Replacing the PBS in the fluorescence staining processes with quick dips in deionized water improved the observability of cells adhered to Mg samples under a confocal microscope by avoiding the formation of corrosion layers during the staining protocol.
- DPNS improved in vitro and in vivo corrosion resistance of the Mg scaffolds. For instance, control samples were wholly dissolved after 4 weeks of implantation under the back skin of Wistar rats. On the contrary, in the DPNS samples, the in vivo corrosion rate was constant during the entire implantation period. Hydrogen gas pockets were observed in the initial stages of the implantation, and the accumulated gas was safely dissolved with time.

Healthy tissue with no noticeable reaction was observed after 8 weeks of in vivo implantation.

- The experimental set-ups were far from representing the in vivo environment, starting with the static conditions testing. However, the apatite formation ability enhanced by the DPNS treatment was in good agreement with the in vivo biocompatibility of the material.

7.2 Future perspectives

- Extrapolating the Mg as clinical orthopedic material requires continuous research on the development of manufacturing methods that produce high purity Mg-based alloys. High purity alloys would allow greater precision in the modification via DPNS.
- The in vitro characterization still has limitations in terms of representing the in vivo environment and corrosion mechanism. The differences between in vitro and in vivo environments are noticeable but still speculative. The in vitro corrosion and biocompatibility testing in the present thesis were performed in static conditions, which is a limitation of the work since body fluid and cell metabolism products influence the degradation outcome. Future studies should consider developing complex environments, such as bioreactors, to better simulate the in vivo environments.
- In the present thesis, considerable advances have been made in the short-term control of porous Mg corrosion in the in vivo environment. The samples presented geometrical stability and steady degradation during the time. Therefore, future work should consider evaluating the behavior of these materials in an in vivo bone model to determine the tissue growth, angiogenesis, and stability of the mechanical properties.

A. Appendix: supplementary material for chapter 3.

Introduction

A 2^3 full factorial design was applied to find the levels of energy, fluence, and incidence angle that optimized the CaP ratio and minimized the H_2 evolution rate of Mg scaffolds treated with directed plasma nanosynthesis (DPNS) and immersed in Dulbecco's modified Eagles' medium. The levels of energy, fluence, and incidence angle were independent variables. The base designs consisted of three factors, eight combinations, and two replicates for 16 runs. Discussion about the results is described in the main text of **chapter 3**.

Methods

With factorial design 2^3, three factors are studied at two levels each. It consists of eight ($2^3 = 2 \times 2 \times 2 = 8$) different treatments. This factorial design usually considers seven effects (2^3-1= 7), including the triple interaction of the main effects (ABC) (Montgomery, 2020). However, in the present work, 2^3 factorial design was used to study six effects on the H2 evolution rate and Ca-phosphate ratio: the main effects A (energy), B (fluence), C (angle), and three double interactions AB, AC, BC. The factorial designs for H_2 evolution rate and CaP ratio are given in **Table A.1** and **Table A.2**. The runs were performed in random order. Minitab software was used for data analysis.

Table A.1. Experimental setup. The 2^3 factorial design for H_2 evolution rate

StdOrder	RunOrder	Energy (eV)	Fluence (cm^{-2})	Angle (deg.)	H_2 evolution rate ($ml/cm^{-2}/h$)
1	5	400	1×10^{17}	0	0.039
2	3	700	1×10^{17}	0	0.027
3	7	400	1×10^{18}	0	0.049
4	4	700	1×10^{18}	0	0.049
5	8	400	1×10^{17}	60	0.054
6	6	700	1×10^{17}	60	0.027
7	2	400	1×10^{18}	60	0.062
8	1	700	1×10^{18}	60	0.073
9	16	400	1×10^{17}	0	0.037
10	9	700	1×10^{17}	0	0.020
11	15	400	1×10^{18}	0	0.032
12	11	700	1×10^{18}	0	0.039
13	10	400	1×10^{17}	60	0.052
14	12	700	1×10^{17}	60	0.029
15	14	400	1×10^{18}	60	0.060
16	13	700	1×10^{18}	60	0.105

Table A.2. Experimental setup. The 2^3 -factorial design for CaP

StdOrder	RunOrder	Energy (eV)	Fluence (cm-2)	Angle (deg.)	Ca:P
1	13	400	$1{\times}10^{17}$	60	0.735
2	10	700	$1{\times}10^{17}$	0	1.404
3	9	400	$1{\times}10^{17}$	0	1.038
4	16	700	$1{\times}10^{18}$	60	0.000
5	14	700	$1{\times}10^{17}$	60	1.040
6	12	700	$1{\times}10^{18}$	0	0.000
7	11	400	$1{\times}10^{18}$	0	0.000
8	15	400	$1{\times}10^{18}$	60	0.390
9	1	400	$1{\times}10^{17}$	0	1.052
10	2	700	$1{\times}10^{17}$	0	1.866
11	7	400	$1{\times}10^{18}$	60	0.441
12	6	700	$1{\times}10^{17}$	60	0.655
13	4	700	$1{\times}10^{18}$	0	0.000
14	5	400	$1{\times}10^{17}$	60	0.958
15	8	700	$1{\times}10^{18}$	60	0.000
16	3	400	$1{\times}10^{18}$	0	0.481

Residuals plots were used to determine whether the model met the assumptions of the analysis: residues are distributed normal, independent, and with constant variance. Analysis of variance (ANOVA) was used to study the incidence of the effects and interactions on the responses at $p < 0.5$. Pareto's charts of standardized effects and main effects plots were used for the practical interpretation of the data.

Results

From the residuals plot in **Figure A.1**, one data point was identified to have a large residual. This point is marked with an orange square in **Figure A.1a**. Because unusual data can have a strong influence on the results, the atypical data was particularly analyzed. However, in this case, it is not a risky situation that could affect the conclusions of the ANOVA based on clearly small p-values. Also, the dispersion occurs just at the point where the H_2 evolution rate was the fastest, which reinforces the conclusions obtained. The data was in good agreement with the high corrosion rate of the samples irradiated with 700 eV energy, 1×10^{18} cm^{-2} fluence, and 60 ° incidence angle. From **Figure A.1b**, since the points adhere to the visually placed line, it is concluded that there are no violations of the normality assumption. Finally, it is not an apparent tendency of the points in **Figure A.1c**; then, it is concluded that there is no problem with the declaration of independence. The same analysis was applied to the plots. **Figure A.1d**, e, and c related to the Ca-phosphate ratio, and it was confirmed that the residues met the assumptions for the analysis.

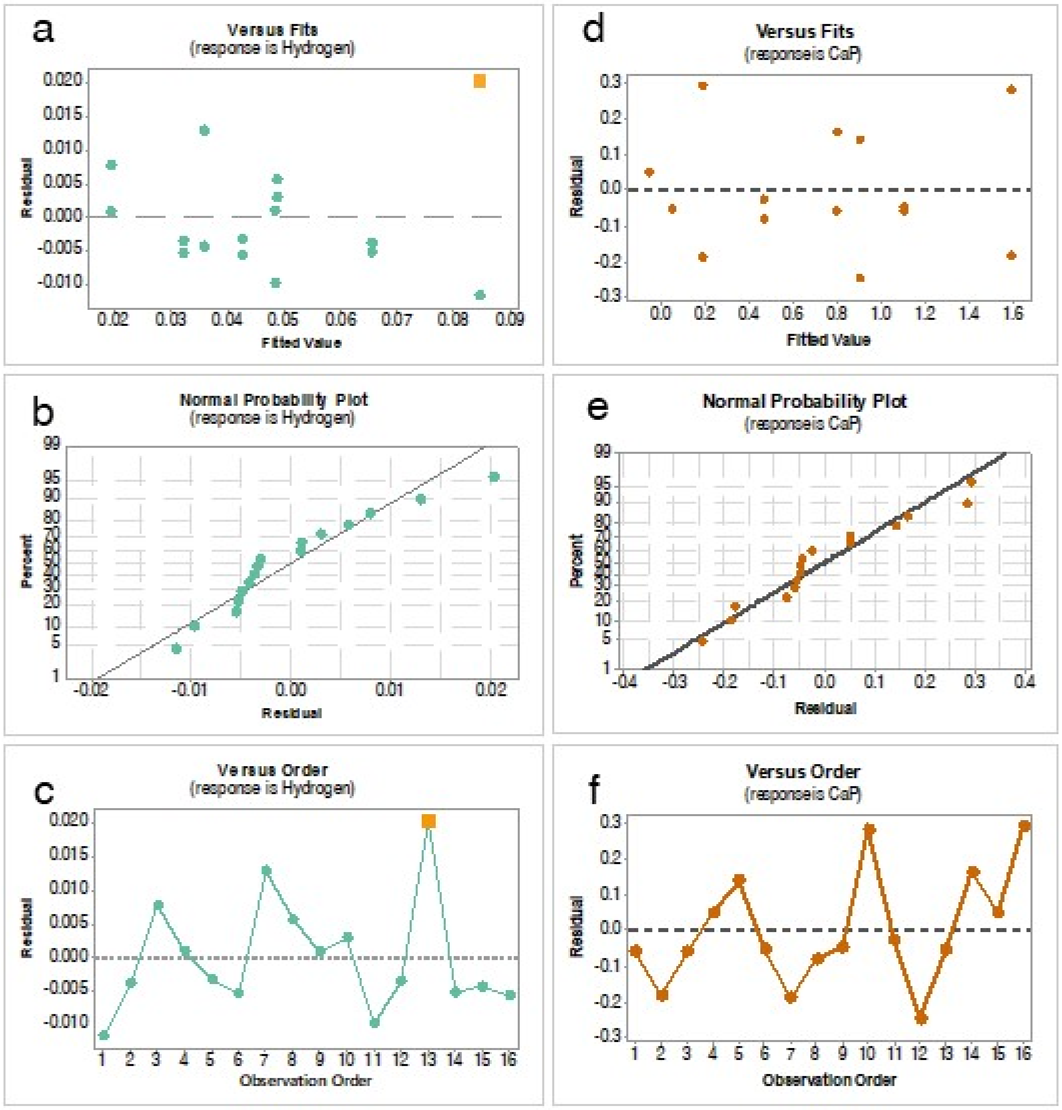

Figure A.1. Left residual plots for H_2 evolution rate: a) Residuals vs. Fitted Values: residuals are on the y-axis and fitted values (estimated responses) on the x-axis. The plot was used to look for non-linearity, unequal error variances, and outliers. An outlier was identified at 0.024. b) Normal probability plot. c) Residuals vs. order of data plot used to verify the assumption of the independence of the residues. On the right residual plots for CaP were d) Residuals vs. Fitted Values, e) Normal probability plot, and f) Residuals vs. order of data plot. All the assumptions for the CaP analysis were met.

Table A.3. ANOVA for H_2 evolution rate

Source	DF	Adj SS	Adj MS	F-Value	P-Value
Energy	1	0.000	0.000	0.148	0.709
Fluence	1	0.002	0.002	17.852	0.002
Angle	1	0.002	0.002	15.400	0.003
Energy*Fluence	1	0.001	0.001	10.943	0.009
Energy*Angle	1	0.000	0.000	0.369	0.559
Fluence*Angle	1	0.001	0.001	4.651	0.059
Error	9	0.001	0.000		
Total	15	0.007			

DF = Degrees of freedom

Adj SS = Adjustment to the sum of squares.

Adj MS = Adjusted mean squares.

R-sq	R-sq(adj)
84.58%	74.30%

ANOVA results for H_2 release are summarized in **Tables A.3**. From p-values, fluence and angle significantly affect the H_2 release. Also, Energy × Fluence and Fluence × Angle p-values indicate some interaction for these effects. Pareto's chart of standardized effects (**Figure 3-13**, page 63) was used for the practical interpretation of this experiment since this graph reveals the absolute value of the magnitude of the effects. Each bar corresponds to a standardized effect: T-statistics that test the null hypothesis that the effect is 0 are considered standardized effects and are calculated by dividing the estimated effect by its standard error (Montgomery, 2020).

A dotted line was also plotted to determine which effect was statistically significant. Bars that cross the dotted line are significant for the response. For the H_2 evolution rate, the response was more influenced by the incidence angle, followed by the fluence, and the interaction of fluence × angle. From the interactions plot, it can be observed that less fluence was required to produce a protective effect on the surface when energy was increased. On the contrary, an increase in the incidence angle was always detrimental to the response.

ANOVA for the Ca-phosphate ratio is shown in **Table A.4**. Again, fluence and angle influence the response for the Ca-phosphate ratio. Energy, by itself, does not influence the response. Also, the interaction of energy × fluence, energy× angle, and fluence × angle affects the response. From Pareto's chart (**Figure 3-13**), fluence is the effect that has more influence on the Ca-phosphate ratio formation, followed by the interaction of energy × fluence.

Table A.4. ANOVA for CaP ratio

Source	DF	Adj SS	Adj MS	F-Value	P-Value
Energy	1	0.001	0.001	0.03	0.876
Fluence	1	3.456	3.456	85.08	0.000
Angle	1	0.164	0.164	4.05	0.075
Energy*Fluence	1	0.389	0.389	9.57	0.013
Energy*Angle	1	0.146	0.146	3.59	0.091
Fluence*Angle	1	0.337	0.337	8.30	0.018
Error	9	0.366	0.041		
Lack-of-fit	1	0.043	0.043	1.06	0.333
Pure error	8	0.323	0.040		
Total	15	4.859			

DF = Degrees of freedom

Adj SS = Adjustment to the sum of squares.

Adj MS = Adjusted mean squares.

R-sq	R-sq(adj)
92.48%	87.46%

Reference

Montgomery DC (2020) The 2k Factorial Design. In Des. Anal. Exp., 212–241 10th ed. John Wiley & Sons.

B. Appendix: supplementary figure for chapter 4

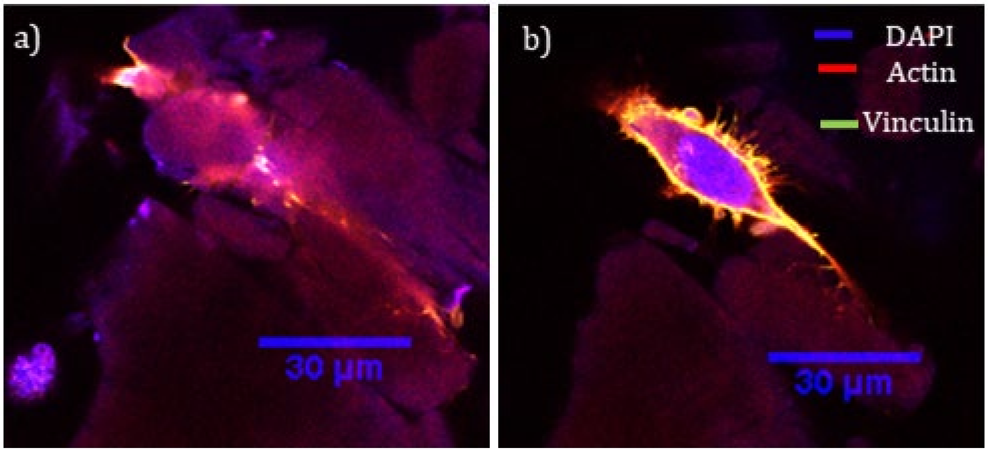

Figure B.1. Comparison of fluorescence images using similar confocal microscope settings and different staining processes. a) sample was stained after the traditional protocol following each staining step (fixation, permeabilization, and staining) with PBS washes. The cell was buried in a corrosion layer formed during the staining process. b) sample was stained with quick dips in deionized water after each staining step. The cell structures were more evident after avoiding the formation of corrosion layers during the staining process.

C. Appendix: ethics committee approval

Dirección de Investigación y Extensión
Vicerrectoría de Sede
Sede Medellín

UNIVERSIDAD
NACIONAL
DE COLOMBIA

Comité para el Cuidado y Uso de los Animales – CICUA

Medellín, 15 de noviembre de 2019 **[CICUA-054-19]**

Investigador
JUAN FERNANDO RAMÍREZ PATIÑO
Departamento de Ingeniería Mecánica
Facultad de Minas
La Sede

Asunto: Aval ético

Cordial saludo:

El Comité para el Cuidado y Uso de los Animales - CICUA de la Universidad Nacional de Colombia Sede Medellín, constituido mediante el Acuerdo 010 de 2016 del Consejo de Sede, tomó en consideración el componente ético involucrado en la propuesta ***"RESISTENCIA A LA CORROSIÓN Y SU ASOCIACIÓN CON LA RESPUESTA DEL TEJIDO CIRCUNDANTE EN RATAS DE MG POROSO MODIFICADO POR NANOSÍNTESIS DE PLASMA DIRECTO"***.

Al respecto, el Comité ha decidido **OTORGAR EL AVAL ÉTICO** para desarrollar el proyecto presentado para ***"Tesis de Doctorado"***, bajo las siguientes consideraciones:

- **(i)** El aval sólo aplica para el desarrollo del proyecto de investigación que implica experimentación con animales no humanos;
- **(ii)** El Investigador Principal debe tramitar y obtener ante las entidades competentes, los permisos que se llegasen a requerir para el desarrollo de la propuesta y remitir copia de los mismos a este comité, antes de iniciar la ejecución del proyecto; y
- **(iii)** Acatar las disposiciones establecidas en la Ley 1774 de 2016 y en el Decreto 2113 del 15 de diciembre de 2017 emitido por el Ministerio de Agricultura.

Asimismo, el Comité decide que el investigador deberá ser garante en cuanto al cumplimiento de las normas establecidas para este tipo de investigación.

Atentamente,

Albeiro López Herrera

ALBEIRO LÓPEZ HERRERA
Presidente

[Página **1** de 1]
Elaboró: DAPP

Carrera 65 Nro. 59A – 110
Bloque 41 – Oficina 221
Teléfono: 430 9575
Medellín, Colombia
cetica_med@unal.edu.co

Proyecto
cultural y colectivo
de nación

D. Appendix: supplementary figure for Chapter 6

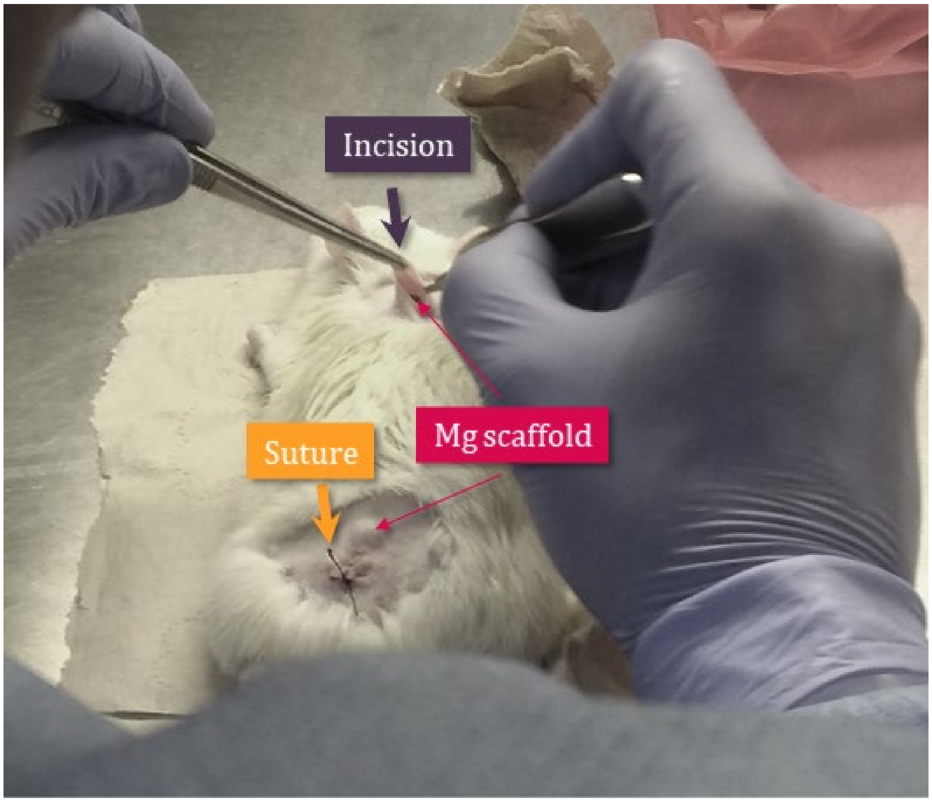

Figure D.1. Photograph of the in vivo implantation process. The implants were inserted under the skin through two incisions of ~1 cm, in proximal and distal locations. Then, the incision was sutured with a synthetic absorbable suture.

References

[1] E. Roddy, M.R. DeBaun, A. Daoud-Gray, Y.P. Yang, M.J. Gardner, Treatment of critical-sized bone defects: clinical and tissue engineering perspectives, Eur. J. Orthop. Surg. Traumatol. 28 (2018) 351–362. https://doi.org/10.1007/s00590-017-2063-0.

[2] S. van Gaalen, M. Kruyt, G. Meijer, A. Mistry, A. Mikos, J. van den Beucken, J. Jansen, K. de Groot, R. Cancedda, C. Olivo, M. Yaszemski, W. Dhert, Chapter 19 - Tissue engineering of bone, in: Academic Press, Burlington, 2008: pp. 559–610. http://www.sciencedirect.com/science/article/pii/B9780123708694000197 (accessed February 9, 2016).

[3] T.X. Song, Y.L. Hu, Z.M. He, Y. Cui, Q. Ding, Z.Y. Qiu, Clinical applications of the mineralized collagen, in: Miner. Collagen Bone Graft Substitutes, Elsevier, 2019: pp. 167–232. https://doi.org/10.1016/B978-0-08-102717-2.00005-9.

[4] W. Wang, K.W.K. Yeung, Bone grafts and biomaterials substitutes for bone defect repair: A review, (2017). https://doi.org/10.1016/j.bioactmat.2017.05.007.

[5] S. Wu, X. Liu, K.W.K.K. Yeung, C. Liu, X. Yang, Biomimetic porous scaffolds for bone tissue engineering, Mater. Sci. Eng. R Reports. 80 (2014) 1–36. https://doi.org/10.1016/j.mser.2014.04.001.

[6] A. Nauth, E. Schemitsch, B. Norris, Z. Nollin, J.T. Watson, Critical-Size Bone Defects, J. Orthop. Trauma. 32 (2018) S7–S11. https://doi.org/10.1097/BOT.0000000000001115.

[7] S.K. Jaganathan, M. Prasath Mani, M. Ayyar, R. Rathanasamy, Biomimetic electrospun polyurethane matrix composites with tailor made properties for bone tissue engineering scaffolds, Polym. Test. 78 (2019) 105955. https://doi.org/10.1016/j.polymertesting.2019.105955.

[8] H. Zhou, S.B. Bhaduri, 3D printing in the research and development of medical devices, in: Biomater. Transl. Med. A Biomater. Approach, Elsevier, 2018: pp. 269–289. https://doi.org/10.1016/B978-0-12-813477-1.00012-8.

[9] A.H. Yusop, A.A. Bakir, N.A. Shaharom, M.R. Abdul Kadir, H. Hermawan, Porous Biodegradable Metals for Hard Tissue Scaffolds: A Review, Int. J. Biomater. 2012 (2012) 1–10. https://doi.org/10.1155/2012/641430.

[10] H. Ding, H. Pan, X. Xu, R. Tang, Toward a Detailed Understanding of Magnesium Ions on Hydroxyapatite Crystallization Inhibition, Cryst. Growth Des. 14 (2014) 763–769. https://doi.org/10.1021/cg401619s.

[11] E. O'Neill, G. Awale, L. Daneshmandi, O. Umerah, K.W.-H. Lo, The roles of ions on bone regeneration, Drug Discov. Today. 23 (2018) 879–890. https://doi.org/10.1016/J.DRUDIS.2018.01.049.

[12] Y. Zhang, J. Xu, Y.C. Ruan, M.K. Yu, M. O'Laughlin, H. Wise, D. Chen, L. Tian, D. Shi, J. Wang, S. Chen, J.Q. Feng, D.H.K. Chow, X. Xie, L. Zheng, L. Huang, S. Huang, K. Leung, N. Lu, L. Zhao, H. Li, D. Zhao, X. Guo, K. Chan, F. Witte, H.C. Chan, Y. Zheng, L. Qin, Implant-derived magnesium induces local neuronal production of CGRP to improve bone-fracture healing in rats, Nat. Med. 22 (2016) 1160–1169. https://doi.org/10.1038/nm.4162.

[13] M. Wang, Y. Yu, K. Dai, Z. Ma, Y. Liu, J. Wang, C. Liu, Improved osteogenesis and angiogenesis of magnesium-doped calcium phosphate cement: Via macrophage immunomodulation, Biomater. Sci. 4 (2016) 1574–1583. https://doi.org/10.1039/c6bm00290k.

[14] B. Li, H. Cao, Y. Zhao, M. Cheng, H. Qin, T. Cheng, Y. Hu, X. Zhang, X. Liu, In vitro and in vivo responses of macrophages to magnesium-doped titanium, Sci. Rep. 7 (2017) 1–12. https://doi.org/10.1038/srep42707.

[15] T.L. Nguyen, M.P. Staiger, G.J. Dias, T.B.F. Woodfield, A Novel Manufacturing Route for Fabrication of Topologically-Ordered Porous Magnesium Scaffolds, Adv. Eng. Mater. 13 (2011) 872–881.

https://doi.org/10.1002/adem.201100029.

[16] G. Jia, C. Chen, J. Zhang, Y. Wang, R. Yue, B.J.C. Luthringer - Feyerabend, R. Willumeit-Roemer, H. Zhang, M. Xiong, H. Huang, G. Yuan, F. Feyerabend, In vitro degradation behavior of Mg scaffolds with three-dimensional interconnected porous structures for bone tissue engineering, Corros. Sci. 144 (2018) 301–312. https://doi.org/10.1016/j.corsci.2018.09.001.

[17] Y. Wang, P. Fu, N. Wang, L. Peng, B. Kang, H. Zeng, G. Yuan, W. Ding, Challenges and Solutions for the Additive Manufacturing of Biodegradable Magnesium Implants, Engineering. (2020). https://doi.org/10.1016/j.eng.2020.02.015.

[18] J. M.Rúa, A.A. Zuleta, J. Ramírez, P. Fernández-Morales, Micro-arc oxidation coating on porous magnesium foam and its potential biomedical applications, Surf. Coatings Technol. 360 (2019) 213–221. https://doi.org/10.1016/j.surfcoat.2018.12.106.

[19] S. Julmi, A.-K. Krüger, A.-C. Waselau, A. Meyer-Lindenberg, P. Wriggers, C. Klose, H.J. Maier, Processing and coating of open-pored absorbable magnesium-based bone implants, Mater. Sci. Eng. C. 98 (2019) 1073–1086. https://doi.org/10.1016/j.msec.2018.12.125.

[20] S. Weiner, H.D. Wagner, The material bone: Structure-mechanical function relations, Annu. Rev. Mater. Sci. 28 (1998) 271–298.

[21] M. Yazdimamaghani, M. Razavi, D. Vashaee, L. Tayebi, Microstructural and mechanical study of PCL coated Mg scaffolds, Surf. Eng. 30 (2014) 920–926. https://doi.org/10.1179/1743294414Y.0000000307.

[22] M. Yazdimamaghani, M. Razavi, D. Vashaee, L. Tayebi, Surface modification of biodegradable porous Mg bone scaffold using polycaprolactone/bioactive glass composite, Mater. Sci. Eng. C. 49 (2015) 436–444. https://doi.org/10.1016/j.msec.2015.01.041.

[23] Z. Chen, X. Mao, L. Tan, T. Friis, C. Wu, R. Crawford, Y. Xiao, Osteoimmunomodulatory properties of magnesium scaffolds coated with β-tricalcium phosphate, Biomaterials. 35 (2014) 8553–8565. https://doi.org/10.1016/j.biomaterials.2014.06.038.

[24] Z.Z. Yin, W.C. Qi, R.C. Zeng, X.B. Chen, C.D. Gu, S.K. Guan, Y.F. Zheng, Advances in coatings on biodegradable magnesium alloys, J. Magnes. Alloy. 8 (2020) 42–65. https://doi.org/10.1016/j.jma.2019.09.008.

[25] R.C. Zeng, L.Y. Cui, K. Jiang, R. Liu, B.D. Zhao, Y.F. Zheng, In Vitro Corrosion and Cytocompatibility of a Microarc Oxidation Coating and Poly(l -lactic acid) Composite Coating on Mg-1Li-1Ca Alloy for Orthopedic Implants, ACS Appl. Mater. Interfaces. 8 (2016) 10014–10028. https://doi.org/10.1021/acsami.6b00527.

[26] F. Czerwinski, ed., Magnesium Alloys - Corrosion and Surface Treatments, InTech, 2011. http://www.intechopen.com/books/magnesium-alloys-corrosion-and-surface-treatments (accessed November 3, 2014).

[27] G. Zhang, L. Wu, A. Tang, Y. Ma, G.-L. Song, D. Zheng, B. Jiang, A. Atrens, F. Pan, Active corrosion protection by a smart coating based on a MgAl-layered double hydroxide on a cerium-modified plasma electrolytic oxidation coating on Mg alloy AZ31, Corros. Sci. 139 (2018) 370–382. https://doi.org/10.1016/J.CORSCI.2018.05.010.

[28] J. Liao, M. Hotta, Corrosion products of field-exposed Mg-Al series magnesium alloys, Corros. Sci. 112 (2016) 276–288. https://doi.org/10.1016/j.corsci.2016.07.023.

[29] G. Wu, R. Xu, K. Feng, S. Wu, Z. Wu, G. Sun, G. Zheng, G. Li, P.K. Chu, Retardation of surface corrosion of biodegradable magnesium-based materials by aluminum ion implantation, Appl. Surf. Sci. 258 (2012) 7651–7657. https://doi.org/10.1016/j.apsusc.2012.04.112.

[30] M.C. Delgado, F.R. García-Galvan, I. Llorente, P. Pérez, P. Adeva, S. Feliu, Influence of aluminium enrichment in the near-surface region of commercial twin-roll cast AZ31 alloys on their corrosion behaviour, Corros. Sci. 123 (2017) 182–196. https://doi.org/10.1016/J.CORSCI.2017.04.027.

[31] M.K. Lei, P. Li, H.G. Yang, X.M. Zhu, Wear and corrosion resistance of Al ion implanted AZ31 magnesium alloy, Surf. Coatings Technol. 201 (2007) 5182–5185. https://doi.org/10.1016/J.SURFCOAT.2006.07.091.

[32] D. Dubé, M. Fiset, A. Couture, I. Nakatsugawa, Characterization and performance of laser melted AZ91D and AM60B, Mater. Sci. Eng. A. 299 (2001) 38–45. https://doi.org/10.1016/S0921-5093(00)01414-3.

[33] S. Hao, M. Li, Producing nano-grained and Al-enriched surface microstructure on AZ91 magnesium alloy by high current pulsed electron beam treatment, Nucl. Instruments Methods Phys. Res. Sect. B Beam Interact. with Mater. Atoms. 375 (2016) 1–4. https://doi.org/10.1016/j.nimb.2016.03.035.

[34] A. Pardo, M.C. Merino, A.E. Coy, F. Viejo, R. Arrabal, S. Feliú, Influence of microstructure and composition on the corrosion behaviour of Mg/Al alloys in chloride media, Electrochim. Acta. 53 (2008) 7890–7902. https://doi.org/10.1016/J.ELECTACTA.2008.06.001.

[35] F. Reichel, L.P.H. Jeurgens, E.J. Mittemeijer, Modeling compositional changes in binary solid solutions under ion bombardment: Application to the Ar+ bombardment of MgAl alloys, Phys. Rev. B - Condens. Matter Mater. Phys. 73 (2006). https://doi.org/10.1103/PhysRevB.73.024103.

[36] H.C. Xiu-Mei Wang, Zhi-Ye Qiu, Mineralized Collagen Bone Graft Substitutes, Woodhead Publishing, 2019. https://books.google.com.co/books?id=f2WTDwAAQBAJ&pg=PA167&lpg=PA167&dq=bone+grafting+world+statistics&source=bl&ots=oEDeBHR4dg&sig=ACfU3U2k5KXjAJY5y8OpX6MVpIkBqnxHsw&hl=es&sa=X&ved=2ahUKEwjUjYXG56rqAhVKSN8KHfnaDbk4FBDoATAAegQICxAB#v=onepage&q=bone grafti (accessed June 30, 2020).

[37] M.A. Yánez Contreras, C.D. Maldonado Pedroza, K.P. Del Risco Serje, Labor force participation of people aged 60 years old and above in Colombia, Rev. Econ. Del Caribe. (2016) 39–63. https://doi.org/10.14482/ecoca.17.8004.

[38] R. Aziziyeh, M. Amin, M. Habib, J. Garcia Perlaza, K. Szafranski, R.K. McTavish, T. Disher, A. Lüdke, C. Cameron, The burden of osteoporosis in four Latin American countries: Brazil, Mexico, Colombia, and Argentina, J. Med. Econ. 22 (2019) 638–644. https://doi.org/10.1080/13696998.2019.1590843.

[39] Instituto Nacional De Salud, Informe anual red de donación y trasplantes, 2018. https://www.ins.gov.co/Direcciones/RedesSaludPublica/DonacionOrganosYTejidos/Estadisticas/Informe-Anual-Red-Donacion-Trasplantes-2018.pdf.

[40] W.M. Baldwin, C.P. Larsen, R.L. Fairchild, Innate immune responses to transplants: A significant variable with cadaver donors, Immunity. 14 (2001) 369–376. https://doi.org/10.1016/S1074-7613(01)00117-0.

[41] R.A. Navarro, N.C. Reddy, J.M. Weiss, A.J. Yates, F.H. Fu, M. McKee, E.S. Lederman, Orthopaedic Systems Response to and Return from the COVID-19 Pandemic: Lessons for Future Crisis Management, J. Bone Jt. Surg. - Am. Vol. 102 (2020) E75. https://doi.org/10.2106/JBJS.20.00709.

[42] B. Fiani, R. Jenkins, I. Siddiqi, A. Khan, A. Taylor, Socioeconomic Impact of COVID-19 on Spinal Instrumentation Companies in the Era of Decreased Elective Surgery, Cureus. 12 (2020). https://doi.org/10.7759/cureus.9776.

[43] S. Von Euw, Y. Wang, G. Laurent, C. Drouet, F. Babonneau, N. Nassif, T. Azaïs, Bone mineral: new insights into its chemical composition, Sci. Rep. 9 (2019) 1–11. https://doi.org/10.1038/s41598-019-44620-6.

[44] J.L. Shaker, L. Deftos, Calcium and Phosphate Homeostasis, in: Endocr. Reprod. Physiol., Elsevier, 2013: pp. 77-e1. https://doi.org/10.1016/b978-0-323-08704-9.00004-x.

[45] J.D. Black, B.J. Tadros, Bone structure: from cortical to calcium, Orthop. Trauma. 34 (2020) 113–119. https://doi.org/10.1016/j.mporth.2020.03.002.

[46] J.Y. Rho, L. Kuhn-Spearing, P. Zioupos, Mechanical properties and the hierarchical structure of bone, Med. Eng. Phys. 20 (1998) 92–102. https://doi.org/10.1016/S1350-4533(98)00007-1.

[47] F.M. Vanhoenacker, A.L. Baert, C. Faletti, M. Maas, J.L.M.A. Gielen, Imaging of Orthopedic Sports Injuries, Springer Berlin Heidelberg, 2007. https://books.google.com.co/books?id=BjWq_4WqRFEC.

[48] R. Oftadeh, M. Perez-Viloria, J.C. Villa-Camacho, A. Vaziri, A. Nazarian, Biomechanics and Mechanobiology of Trabecular Bone: A Review, J. Biomech. Eng. 137 (2015). https://doi.org/10.1115/1.4029176.

[49] G.S. Baht, L. Vi, B.A. Alman, The Role of the Immune Cells in Fracture Healing, Curr. Osteoporos. Rep. 16 (2018) 138–145. https://doi.org/10.1007/s11914-018-0423-2.

[50] T. Ono, H. Takayanagi, Osteoimmunology in Bone Fracture Healing, Curr. Osteoporos. Rep. 15 (2017) 367–375. https://doi.org/10.1007/s11914-017-0381-0.

[51] A. Dorronsoro, I. Ferrin, J.M. Salcedo, E. Jakobsson, J. Fernández-Rueda, V. Lang, P. Sepulveda, K. Fechter, D. Pennington, C. Trigueros, Human mesenchymal stromal cells modulate T-cell responses through TNF-α-

mediated activation of NF-κB, Eur. J. Immunol. 44 (2014) 480–488. https://doi.org/10.1002/eji.201343668.

[52] T.A. Einhorn, Bone Regeneration and Repair, J. Bone Jt. Surg. 88 (2006) 469–470. https://doi.org/10.2106/00004623-200602000-00050.

[53] L.J. Kidd, A.S. Stephens, J.S. Kuliwaba, N.L. Fazzalari, A.C.K. Wu, M.R. Forwood, Temporal pattern of gene expression and histology of stress fracture healing, Bone. 46 (2010) 369–378. https://doi.org/10.1016/j.bone.2009.10.009.

[54] N.A. Sims, T.J. Martin, The osteoblast lineage: Its actions and communication mechanisms, in: Princ. Bone Biol., Elsevier, 2019: pp. 89–110. https://doi.org/10.1016/B978-0-12-814841-9.00004-X.

[55] G.K.K. and A.E. Javad Parvizi, High Yield Orthopaedics, Elsevier, 2010. https://doi.org/10.1016/c2009-0-32243-6.

[56] T.A. Franz-Odendaal, B.K. Hall, P.E. Witten, Buried alive: How osteoblasts become osteocytes, Dev. Dyn. 235 (2006) 176–190. https://doi.org/10.1002/dvdy.20603.

[57] M.H.V. Choy, R.M.Y. Wong, S.K.H. Chow, M.C. Li, Y.N. Chim, T.K. Li, W.T. Ho, J.C.Y. Cheng, W.H. Cheung, How much do we know about the role of osteocytes in different phases of fracture healing? A systematic review, J. Orthop. Transl. 21 (2020) 111–121. https://doi.org/10.1016/j.jot.2019.07.005.

[58] B.M. Willie, E.A. Zimmermann, I. Vitienes, R.P. Main, S. V. Komarova, Bone adaptation: Safety factors and load predictability in shaping skeletal form, Bone. 131 (2020) 115114. https://doi.org/10.1016/j.bone.2019.115114.

[59] J.H. Kim, D. Kim, M.G. Lee, Mechanics of Cellular Materials and its Applications, in: Multiscale Simulations Mech. Biol. Mater., John Wiley and Sons, 2013: pp. 411–434. https://doi.org/10.1002/9781118402955.ch22.

[60] L.J. Gibson, The mechanical behaviour of cancellous bone, J. Biomech. 18 (1985) 317–328. https://doi.org/10.1016/0021-9290(85)90287-8.

[61] A. Nouri, Deakin University, Deakin University, Novel metal structures through powder metallurgy for biomedical applications, 2008.

[62] T.S. Keller, Predicting the compressive mechanical behavior of bone, J. Biomech. 27 (1994) 1159–1168. https://doi.org/10.1016/0021-9290(94)90056-6.

[63] J.D. Silva-Henao, R.J. Rueda Esteban, A. Marañon-Leon, J.P. Casas-Rodríguez, Post-yield mechanical properties of bovine trabecular bone – Relationships with bone volume fraction and strain rate, Eng. Fract. Mech. 233 (2020) 107053. https://doi.org/10.1016/j.engfracmech.2020.107053.

[64] H. Leng, M.J. Reyes, X.N. Dong, X. Wang, Effect of age on mechanical properties of the collagen phase in different orientations of human cortical bone, Bone. 55 (2013) 288–291. https://doi.org/10.1016/j.bone.2013.04.006.

[65] L.J. Gibson, M.F. Ashby, Cellular Solids: Structure and Properties, Cambridge University Press, 1999. http://books.google.com.co/books?id=IySUr5sn4N8C.

[66] N. Fratzl-Zelman, A.P. Roschger, A.A. Gourrier, A.M. Weber, A.B.M. Misof, A.N. Loveridge, A.J. Reeve, A.K. Klaushofer, A.P. Fratzl, Á.P. Roschger, Á.B.M. Misof, Á.K. Klaushofer, A. Gourrier, Á.M. Weber, Á.P. Fratzl, M. Weber, E. Schmid, N. Loveridge, Á.J. Reeve, Combination of Nanoindentation and Quantitative Backscattered Electron Imaging Revealed Altered Bone Material Properties Associated with Femoral Neck Fragility, Calcif Tissue Int. 85 (2009) 335–343. https://doi.org/10.1007/s00223-009-9289-8.

[67] M.A.K.L. and W.S. M. A. Wettergreen, B. S. Bucklen, CAD Assembly Process for Bone Replacement Scaffolds in Computer-Aided Tissue Engineering, in: Virtual Prototyp. Bio Manuf. Med. Appl., 2008: pp. 87–112.

[68] R. Dimitriou, E. Tsiridis, P. V. Giannoudis, Current concepts of molecular aspects of bone healing, Injury. 36 (2005) 1392–1404. https://doi.org/10.1016/j.injury.2005.07.019.

[69] C.W. Schlickewei, H. Kleinertz, D.M. Thiesen, K. Mader, M. Priemel, K.H. Frosch, J. Keller, Current and future concepts for the treatment of impaired fracture healing, Int. J. Mol. Sci. 20 (2019). https://doi.org/10.3390/ijms20225805.

[70] F. Barrère, C.A. van Blitterswijk, K. de Groot, Bone regeneration: Molecular and cellular interactions with calcium phosphate ceramics, Int. J. Nanomedicine. 1 (2006) 317–332.

[71] R. Langer, J.P. Vacanti, Tissue Engineering, n.d. http://science.sciencemag.org/ (accessed June 13, 2020).

[72] K. Alvarez, H. Nakajima, Metallic scaffolds for bone regeneration, Materials (Basel). 2 (2009) 790–832. https://doi.org/10.3390/ma2030790.

[73] N. Abbasi, S. Hamlet, R.M. Love, N.T. Nguyen, Porous scaffolds for bone regeneration, J. Sci. Adv. Mater. Devices. 5 (2020) 1–9. https://doi.org/10.1016/j.jsamd.2020.01.007.

[74] K.A. Hing, Bioceramic bone graft substitutes: Influence of porosity and chemistry, Int. J. Appl. Ceram. Technol. 2 (2005) 184–199. https://doi.org/10.1111/j.1744-7402.2005.02020.x.

[75] X. Xiao, W. Wang, D. Liu, H. Zhang, P. Gao, L. Geng, Y. Yuan, J. Lu, Z. Wang, The promotion of angiogenesis induced by three-dimensional porous beta-tricalcium phosphate scaffold with different interconnection sizes via activation of PI3K/Akt pathways, Sci. Rep. 5 (2015) 1–11. https://doi.org/10.1038/srep09409.

[76] C.M. Murphy, F.J. O'Brien, Understanding the effect of mean pore size on cell activity in collagen-glycosaminoglycan scaffolds, Cell Adhes. Migr. 4 (2010) 377–381. https://doi.org/10.4161/cam.4.3.11747.

[77] L. Chu, G. Jiang, X.-L. Hu, T.D. James, X.-P. He, Y. Li, T. Tang, Biodegradable macroporous scaffold with nano-crystal surface microstructure for highly effective osteogenesis and vascularization, J. Mater. Chem. B. 6 (2018) 1658–1667. https://doi.org/10.1039/C7TB03353B.

[78] Z. Chen, X. Yan, S. Yin, L. Liu, X. Liu, G. Zhao, W. Ma, W. Qi, Z. Ren, H. Liao, M. Liu, D. Cai, H. Fang, Influence of the pore size and porosity of selective laser melted Ti6Al4V ELI porous scaffold on cell proliferation, osteogenesis and bone ingrowth, Mater. Sci. Eng. C. 106 (2020) 110289. https://doi.org/10.1016/j.msec.2019.110289.

[79] P. Ouyang, H. Dong, X. He, X. Cai, Y. Wang, J. Li, H. Li, Z. Jin, Hydromechanical mechanism behind the effect of pore size of porous titanium scaffolds on osteoblast response and bone ingrowth, Mater. Des. 183 (2019) 108151. https://doi.org/10.1016/j.matdes.2019.108151.

[80] S. Ray, U. Thormann, M. Eichelroth, M. Budak, C. Biehl, M. Rupp, U. Sommer, T. El Khassawna, F.I. Alagboso, M. Kampschulte, M. Rohnke, A. Henß, K. Peppler, V. Linke, P. Quadbeck, A. Voigt, F. Stenger, D. Karl, R. Schnettler, C. Heiss, K.S. Lips, V. Alt, Strontium and bisphosphonate coated iron foam scaffolds for osteoporotic fracture defect healing, Biomaterials. 157 (2018) 1–16. https://doi.org/10.1016/j.biomaterials.2017.11.049.

[81] M.Q. Cheng, T. Wahafu, G.F. Jiang, W. Liu, Y.Q. Qiao, X.C. Peng, T. Cheng, X.L. Zhang, G. He, X.Y. Liu, A novel open-porous magnesium scaffold with controllable microstructures and properties for bone regeneration, Sci. Rep. 6 (2016) 24134. https://doi.org/10.1038/srep24134.

[82] M.H. Kang, H. Lee, T.S. Jang, Y.J. Seong, H.E. Kim, Y.H. Koh, J. Song, H. Do Jung, Biomimetic porous Mg with tunable mechanical properties and biodegradation rates for bone regeneration, Acta Materialia Inc., 2019. https://doi.org/10.1016/j.actbio.2018.11.045.

[83] E. Dayaghi, H.R. Bakhsheshi-Rad, E. Hamzah, A. Akhavan-Farid, A.F. Ismail, M. Aziz, E. Abdolahi, Magnesium-zinc scaffold loaded with tetracycline for tissue engineering application: In vitro cell biology and antibacterial activity assessment, Mater. Sci. Eng. C. 102 (2019) 53–65. https://doi.org/10.1016/j.msec.2019.04.010.

[84] N. Taniguchi, S. Fujibayashi, M. Takemoto, K. Sasaki, B. Otsuki, T. Nakamura, T. Matsushita, T. Kokubo, S. Matsuda, Effect of pore size on bone ingrowth into porous titanium implants fabricated by additive manufacturing: An in vivo experiment, Mater. Sci. Eng. C. 59 (2016) 690–701. https://doi.org/10.1016/j.msec.2015.10.069.

[85] S. Kujala, J. Ryhänen, A. Danilov, J. Tuukkanen, Effect of porosity on the osteointegration and bone ingrowth of a weight-bearing nickel–titanium bone graft substitute, Biomaterials. 24 (2003) 4691–4697. https://doi.org/10.1016/S0142-9612(03)00359-4.

[86] S. Limmahakhun, A. Oloyede, K. Sitthiseripratip, Y. Xiao, C. Yan, 3D-printed cellular structures for bone biomimetic implants, Addit. Manuf. 15 (2017) 93–101. https://doi.org/10.1016/j.addma.2017.03.010.

[87] C.M. Murphy, M.G. Haugh, F.J. O'Brien, The effect of mean pore size on cell attachment, proliferation and migration in collagen–glycosaminoglycan scaffolds for bone tissue engineering, Biomaterials. 31 (2010) 461–466. https://doi.org/10.1016/j.biomaterials.2009.09.063.

[88] B.B. Mandal, S.C. Kundu, Osteogenic and adipogenic differentiation of rat bone marrow cells on non-mulberry and mulberry silk gland fibroin 3D scaffolds, Biomaterials. 30 (2009) 5019–5030. https://doi.org/10.1016/j.biomaterials.2009.05.064.

[89] Y. Kuboki, Q. Jin, H. Takita, Geometry of carriers controlling phenotypic expression in BMP-induced osteogenesis and chondrogenesis., J. Bone Joint Surg. Am. 83 A Suppl 1 (2001). https://doi.org/10.2106/00004623-200100002-00005.

[90] T. Lou, X. Wang, G. Song, Z. Gu, Z. Yang, Structure and properties of PLLA/β-TCP nanocomposite scaffolds for bone tissue engineering, J. Mater. Sci. Mater. Med. 26 (2015) 34. https://doi.org/10.1007/s10856-014-5366-2.

[91] S. Pina, R.F. Canadas, G. Jiménez, M. Perán, J.A. Marchal, R.L. Reis, J.M. Oliveira, Biofunctional Ionic-Doped Calcium Phosphates: Silk Fibroin Composites for Bone Tissue Engineering Scaffolding, Cells Tissues Organs. 204 (2017) 150–163. https://doi.org/10.1159/000469703.

[92] M. Mauri, T. Elli, G. Caviglia, G. Uboldi, M. Azzi, RAWGraphs: A Visualisation Platform to Create Open Outputs, in: Proc. 12th Biannu. Conf. Ital. SIGCHI Chapter - CHItaly '17, ACM Press, New York, New York, USA, 2017: pp. 1–5. https://doi.org/10.1145/3125571.3125585.

[93] T. Maconachie, M. Leary, B. Lozanovski, X. Zhang, M. Qian, O. Faruque, M. Brandt, SLM lattice structures: Properties, performance, applications and challenges, Mater. Des. 183 (2019) 108137. https://doi.org/10.1016/j.matdes.2019.108137.

[94] C. Yan, L. Hao, A. Hussein, P. Young, D. Raymont, Advanced lightweight 316L stainless steel cellular lattice structures fabricated via selective laser melting, Mater. Des. 55 (2014) 533–541. https://doi.org/10.1016/j.matdes.2013.10.027.

[95] B.S. Bucklen, W.A. Wettergreen, E. Yuksel, M.A.K. Liebschner, Bone-derived CAD library for assembly of scaffolds in computer-aided tissue engineering, Virtual Phys. Prototyp. 3 (2008) 13–23. https://doi.org/10.1080/17452750801911352.

[96] M.A. Wettergreen, B.S. Bucklen, B. Starly, E. Yuksel, W. Sun, M.A.K. Liebschner, Creation of a unit block library of architectures for use in assembled scaffold engineering, Comput. Des. 37 (2005) 1141–1149. https://doi.org/10.1016/j.cad.2005.02.005.

[97] C.K. Chua, K.F. Leong, C.M. Cheah, S.W. Chua, Development of a Tissue Engineering Scaffold Structure Library for Rapid Prototyping. Part 1: Investigation and Classification, Int J Adv Manuf Technol. 21 (2003) 291–301. https://link.springer.com/content/pdf/10.1007%2Fs001700300034.pdf (accessed August 9, 2017).

[98] C.K. Chua, K.F. Leong, C.M. Cheah, S.W. Chua, Development of a Tissue Engineering Scaffold Structure Library for Rapid Prototyping. Part 2: Parametric Library and Assembly Program, 2003.

[99] N. Chantarapanich, P. Puttawibul, S. Sucharitpwatskul, P. Jeamwatthanachai, S. Inglam, K. Sitthiseripratip, Scaffold Library for Tissue Engineering: A Geometric Evaluation, Comput. Math. Methods Med. 2012 (2012) 1–14. https://doi.org/10.1155/2012/407805.

[100] M.J. Wenninger, Polyhedron models, Cambridge University Press, 2015. https://doi.org/10.1017/CBO9780511569746.

[101] J. Wieding, A. Wolf, R. Bader, Numerical optimization of open-porous bone scaffold structures to match the elastic properties of human cortical bone, J. Mech. Behav. Biomed. Mater. 37 (2014) 56–68. https://doi.org/10.1016/j.jmbbm.2014.05.002.

[102] G. Bini, F. Bini, R. Bedini, A. Marinozzi, F. Marinozzi, A topological look at human trabecular bone tissue, Math. Biosci. 288 (2017) 159–165. https://doi.org/10.1016/j.mbs.2017.03.009.

[103] V.M. Posada, C. Orozco, J. Ramírez, P. Fernandez-Morales, Human bone inspired design of an Mg alloy-based foam, 2018. https://doi.org/10.4028/www.scientific.net/MSF.933.291.

[104] L.J. Gibson, Biomechanics of cellular solids, J. Biomech. 38 (2005) 377–399. https://doi.org/10.1016/j.jbiomech.2004.09.027.

[105] P.K. Zysset, M.S. Ominsky, S.A. Goldstein, A novel 3D microstructural model for trabecular bone: I. The relationship between fabric and elasticity, Comput. Methods Biomech. Biomed. Engin. 1 (1998) 321–331. https://doi.org/10.1080/01495739808936710.

[106] S.M. Ahmadi, G. Campoli, S. Amin Yavari, B. Sajadi, R. Wauthle, J. Schrooten, H. Weinans, A.A. Zadpoor, Mechanical behavior of regular open-cell porous biomaterials made of diamond lattice unit cells, J. Mech. Behav.

Biomed. Mater. 34 (2014) 106–115. https://doi.org/10.1016/j.jmbbm.2014.02.003.

[107] P. Heinl, L. Müller, C. Körner, R.F. Singer, F.A. Müller, Cellular Ti–6Al–4V structures with interconnected macro porosity for bone implants fabricated by selective electron beam melting, Acta Biomater. 4 (2008) 1536–1544. https://doi.org/10.1016/j.actbio.2008.03.013.

[108] N. Reznikov, H. Chase, Y. Ben Zvi, V. Tarle, M. Singer, V. Brumfeld, R. Shahar, S. Weiner, Inter-trabecular angle: A parameter of trabecular bone architecture in the human proximal femur that reveals underlying topological motifs, Acta Biomater. 44 (2016) 65–72. https://doi.org/10.1016/j.actbio.2016.08.040.

[109] A. Ataee, Y. Li, D. Fraser, G. Song, C. Wen, Anisotropic Ti-6Al-4V gyroid scaffolds manufactured by electron beam melting (EBM) for bone implant applications, Mater. Des. 137 (2018) 345–354. https://doi.org/10.1016/j.matdes.2017.10.040.

[110] A.A. Zadpoor, Bone tissue regeneration: the role of scaffold geometry, Biomater. Sci. 3 (2015) 231–245. https://doi.org/10.1039/C4BM00291A.

[111] Y. Qin, P. Wen, H. Guo, D. Xia, Y. Zheng, L. Jauer, R. Poprawe, M. Voshage, J.H. Schleifenbaum, Additive manufacturing of biodegradable metals: Current research status and future perspectives, Acta Biomater. 98 (2019) 3–22. https://doi.org/10.1016/j.actbio.2019.04.046.

[112] R. Karunakaran, S. Ortgies, A. Tamayol, F. Bobaru, M.P. Sealy, Additive manufacturing of magnesium alloys, Bioact. Mater. 5 (2020) 44–54. https://doi.org/10.1016/j.bioactmat.2019.12.004.

[113] M. Joner, P. Ruppelt, P. Zumstein, C. Lapointe-Corriveau, G. Leclerc, A. Bulin, M.I. Castellanos, E. Wittchow, M. Haude, R. Waksman, Preclinical evaluation of degradation kinetics and elemental mapping of first- and second-generation bioresorbable magnesium scaffolds, EuroIntervention. 14 (2018) e1040–e1048. https://doi.org/10.4244/eij-d-17-00708.

[114] R. Biber, J. Pauser, M. Geßlein, H.J. Bail, Magnesium-Based Absorbable Metal Screws for Intra-Articular Fracture Fixation., Case Rep. Orthop. 2016 (2016) 9673174. https://doi.org/10.1155/2016/9673174.

[115] U&i Corporation - Driving beyond the innovations, (n.d.). http://www.youic.com/sub02/list.php?ca_id=10 (accessed October 25, 2020).

[116] G. Papanikolaou, K. Pantopoulos, Iron metabolism and toxicity, Toxicol. Appl. Pharmacol. 202 (2005) 199–211. https://doi.org/10.1016/j.taap.2004.06.021.

[117] P. Sharma, P.M. Pandey, Corrosion behaviour of the porous iron scaffold in simulated body fluid for biodegradable implant application, Mater. Sci. Eng. C. 99 (2019) 838–852. https://doi.org/10.1016/j.msec.2019.01.114.

[118] D. Carluccio, C. Xu, J. Venezuela, Y. Cao, D. Kent, M. Bermingham, A.G. Demir, B. Previtali, Q. Ye, M. Dargusch, Additively manufactured iron-manganese for biodegradable porous load-bearing bone scaffold applications, Acta Biomater. 103 (2020) 346–360. https://doi.org/10.1016/j.actbio.2019.12.018.

[119] P. Sharma, P.M. Pandey, A novel manufacturing route for the fabrication of topologically-ordered open-cell porous iron scaffold, Mater. Lett. 222 (2018) 160–163. https://doi.org/10.1016/J.MATLET.2018.03.206.

[120] R. Alavi, A. Trenggono, S. Champagne, H. Hermawan, Investigation on Mechanical Behavior of Biodegradable Iron Foams under Different Compression Test Conditions, Metals (Basel). 7 (2017) 202. https://doi.org/10.3390/met7060202.

[121] I. Cockerill, Y. Su, S. Sinha, Y.X. Qin, Y. Zheng, M.L. Young, D. Zhu, Porous zinc scaffolds for bone tissue engineering applications: A novel additive manufacturing and casting approach, Mater. Sci. Eng. C. 110 (2020) 110738. https://doi.org/10.1016/j.msec.2020.110738.

[122] J. Nriagu, Zinc deficiency in human health, in: Encycl. Environ. Heal., Elsevier, 2019: pp. 489–499. https://doi.org/10.1016/B978-0-12-409548-9.11433-2.

[123] P.K. Bowen, E.R. Shearier, S. Zhao, R.J. Guillory, F. Zhao, J. Goldman, J.W. Drelich, Biodegradable Metals for Cardiovascular Stents: From Clinical Concerns to Recent Zn-Alloys, Adv. Healthc. Mater. 5 (2016) 1121–1140. https://doi.org/10.1002/adhm.201501019.

[124] J. Venezuela, M.S. Dargusch, The influence of alloying and fabrication techniques on the mechanical properties, biodegradability and biocompatibility of zinc: A comprehensive review, Acta Biomater. 87 (2019) 1–40.

https://doi.org/10.1016/j.actbio.2019.01.035.

[125] S.M. Glasdam, S. Glasdam, G.H. Peters, The Importance of Magnesium in the Human Body: A Systematic Literature Review, in: Adv. Clin. Chem., Academic Press Inc., 2016: pp. 169–193. https://doi.org/10.1016/bs.acc.2015.10.002.

[126] N.-E.L. Saris, E. Mervaala, H. Karppanen, J.A. Khawaja, A. Lewenstam, Magnesium: An update on physiological, clinical and analytical aspects, Clin. Chim. Acta. 294 (2000) 1–26. https://doi.org/10.1016/S0009-8981(99)00258-2.

[127] J.-L. Wang, J.-K. Xu, C. Hopkins, D. Ho-Kiu Chow, L. Qin, Biodegradable Magnesium-Based Implants in Orthopedics-A General Review and Perspectives, (2020). https://doi.org/10.1002/advs.201902443.

[128] S. Castiglioni, A. Cazzaniga, W. Albisetti, J.A.M. Maier, Magnesium and Osteoporosis: Current State of Knowledge and Future Research Directions, Nutrients. 5 (2013) 3022–3033. https://doi.org/10.3390/nu5083022.

[129] R.K. Rude, H.E. Gruber, Magnesium deficiency and osteoporosis: Animal and human observations, J. Nutr. Biochem. 15 (2004) 710–716. https://doi.org/10.1016/j.jnutbio.2004.08.001.

[130] T.A. Grünewald, H. Rennhofer, B. Hesse, M. Burghammer, S.E. Stanzl-Tschegg, M. Cotte, J.F. Löffler, A.M. Weinberg, H.C. Lichtenegger, Magnesium from bioresorbable implants: Distribution and impact on the nano- and mineral structure of bone, Biomaterials. 76 (2016) 250–260. https://doi.org/10.1016/j.biomaterials.2015.10.054.

[131] J. Wang, J. Xu, B. Song, D.H. Chow, P. Shu-hang Yung, L. Qin, Magnesium (Mg) based interference screws developed for promoting tendon graft incorporation in bone tunnel in rabbits, Acta Biomater. 63 (2017) 393–410. https://doi.org/10.1016/j.actbio.2017.09.018.

[132] M. Yazdimamaghani, M. Razavi, D. Vashaee, K. Moharamzadeh, A.R. Boccaccini, L. Tayebi, Porous magnesium-based scaffolds for tissue engineering, Mater. Sci. Eng. C. 71 (2017) 1253–1266. https://doi.org/10.1016/j.msec.2016.11.027.

[133] Y. Yan, Y. Kang, D. Li, K. Yu, T. Xiao, Q. Wang, Y. Deng, H. Fang, D. Jiang, Y. Zhang, Microstructure, Mechanical Properties and Corrosion Behavior of Porous Mg-6 wt.% Zn Scaffolds for Bone Tissue Engineering, J. Mater. Eng. Perform. 27 (2018) 970–984. https://doi.org/10.1007/s11665-018-3189-x.

[134] Z.S. Seyedraoufi, S. Mirdamadi, Synthesis, microstructure and mechanical properties of porous Mg□Zn scaffolds, J. Mech. Behav. Biomed. Mater. 21 (2013) 1–8. https://doi.org/10.1016/j.jmbbm.2013.01.023.

[135] X.N. Gu, W.R. Zhou, Y.F. Zheng, Y. Liu, Y.X. Li, Degradation and cytotoxicity of lotus-type porous pure magnesium as potential tissue engineering scaffold material, Mater. Lett. 64 (2010) 1871–1874. https://doi.org/10.1016/j.matlet.2010.06.015.

[136] Y. Li, J. Zhou, P. Pavanram, M.A. Leeflang, L.I. Fockaert, B. Pouran, N. Tümer, K.-U. Schröder, J.M.C. Mol, H. Weinans, H. Jahr, A.A. Zadpoor, Additively manufactured biodegradable porous magnesium, Acta Biomater. 67 (2018) 378–392. https://doi.org/10.1016/j.actbio.2017.12.008.

[137] M.P. Staiger, I. Kolbeinsson, N.T. Kirkland, T. Nguyen, G. Dias, T.B.F. Woodfield, Synthesis of topologically-ordered open-cell porous magnesium, Mater. Lett. 64 (2010) 2572–2574. https://doi.org/10.1016/j.matlet.2010.08.049.

[138] X.X. Wang, Z. Li, Y. Huang, K. Wang, X.X. Wang, F. Han, Processing of magnesium foams by weakly corrosive and highly flexible space holder materials, Mater. Des. 64 (2014) 324–329. https://doi.org/10.1016/j.matdes.2014.07.049.

[139] S. Dutta, K. Bavya Devi, M. Roy, Processing and degradation behavior of porous magnesium scaffold for biomedical applications, Adv. Powder Technol. 28 (2017) 3204–3212. https://doi.org/10.1016/J.APT.2017.09.024.

[140] D. YANG, C. SEO, B.-Y. HUR, D. YANG, C. SEO, B.-Y. HUR, Mg Alloy Foam Fabrication via Melt Foaming Method, 材料科学与技术. 24 (2009) 302–304. https://www.jmst.org/CN/abstract/abstract8161.shtml (accessed October 27, 2020).

[141] V.M. Posada, J.F. Ramirez, J.P. Allain, A.S. Shetty, P. Fernández-Morales, Synthesis and properties of Mg-based foams by infiltration casting without protective cover gas, J. Mater. Eng. Perform. (2020). https://doi.org/10.1007/s11665-020-04566-7.

[142] M. Ali, M. Elsherif, A.E. Salih, A. Ul-Hamid, M.A. Hussein, S. Park, A.K. Yetisen, H. Butt, Surface modification and cytotoxicity of Mg-based bio-alloys: An overview of recent advances, J. Alloys Compd. 825 (2020) 154140. https://doi.org/10.1016/j.jallcom.2020.154140.

[143] N. Sezer, Z. Evis, S.M. Kayhan, A. Tahmasebifar, M. Koç, Review of magnesium-based biomaterials and their applications, J. Magnes. Alloy. 6 (2018) 23–43. https://doi.org/10.1016/J.JMA.2018.02.003.

[144] N. Sezer, Z. Evis, M. Koç, Additive manufacturing of biodegradable magnesium implants and scaffolds: Review of the recent advances and research trends, J. Magnes. Alloy. (2020). https://doi.org/10.1016/j.jma.2020.09.014.

[145] J. Chen, L. Tan, X. Yu, I.P. Etim, M. Ibrahim, K. Yang, Mechanical properties of magnesium alloys for medical application: A review, J. Mech. Behav. Biomed. Mater. 87 (2018) 68–79. https://doi.org/10.1016/J.JMBBM.2018.07.022.

[146] R.B. Heimann, Magnesium alloys for biomedical application: Advanced corrosion control through surface coating, Surf. Coatings Technol. (2020) 126521. https://doi.org/10.1016/j.surfcoat.2020.126521.

[147] S. Heise, S. Virtanen, A.R. Boccaccini, Tackling Mg alloy corrosion by natural polymer coatings-A review, J. Biomed. Mater. Res. Part A. 104 (2016) 2628–2641. https://doi.org/10.1002/jbm.a.35776.

[148] V. Hernández-Montes, C.P. Betancur-Henao, J.F. Santa-Marín, Titanium dioxide coatings on magnesium alloys for biomaterials: A review, DYNA. 84 (2017) 261–270. https://doi.org/10.15446/dyna.v84n200.59664.

[149] Y. Ding, C. Wen, P. Hodgson, Y. Li, Effects of alloying elements on the corrosion behavior and biocompatibility of biodegradable magnesium alloys: a review, J. Mater. Chem. B. 2 (2014) 1912–1933. https://doi.org/10.1039/C3TB21746A.

[150] M. Esmaily, J.E. Svensson, S. Fajardo, N. Birbilis, G.S. Frankel, S. Virtanen, R. Arrabal, S. Thomas, L.G. Johansson, Fundamentals and advances in magnesium alloy corrosion, Prog. Mater. Sci. 89 (2017) 92–193. https://doi.org/10.1016/J.PMATSCI.2017.04.011.

[151] F. Cao, G.-L. Song, A. Atrens, Corrosion and passivation of magnesium alloys, Corros. Sci. 111 (2016) 835–845. https://doi.org/10.1016/J.CORSCI.2016.05.041.

[152] D. Zhao, F. Witte, F. Lu, J. Wang, J. Li, L. Qin, Current status on clinical applications of magnesium-based orthopaedic implants: A review from clinical translational perspective, Biomaterials. (2016). https://doi.org/10.1016/j.biomaterials.2016.10.017.

[153] N. Jasmawati, S. Fatihhi, A. Putra, A. Syahrom, M. Harun, A. Öchsner, M. Abdul Kadir, Mg-based porous metals as cancellous bone analogous material: A review, Proc. Inst. Mech. Eng. Part L J. Mater. Des. Appl. 231 (2017) 544–556. https://doi.org/10.1177/1464420715624449.

[154] A. Vahidgolpayegani, C. Wen, P. Hodgson, Y. Li, Production methods and characterization of porous Mg and Mg alloys for biomedical applications, Met. Foam Bone. (2017) 25–82. https://doi.org/10.1016/B978-0-08-101289-5.00002-0.

[155] Y. Liu, B. Rath, M. Tingart, J. Eschweiler, Role of implants surface modification in osseointegration: A systematic review, J. Biomed. Mater. Res. Part A. 108 (2020) 470–484. https://doi.org/10.1002/jbm.a.36829.

[156] R. Walter, M.B. Kannan, Y. He, A. Sandham, Effect of surface roughness on the in vitro degradation behaviour of a biodegradable magnesium-based alloy, Appl. Surf. Sci. 279 (2013) 343–348. https://doi.org/10.1016/j.apsusc.2013.04.096.

[157] S. Virtanen, Biodegradable Mg and Mg alloys: Corrosion and biocompatibility, in: Mater. Sci. Eng. B Solid-State Mater. Adv. Technol., Elsevier, 2011: pp. 1600–1608. https://doi.org/10.1016/j.mseb.2011.05.028.

[158] X.-N. Gu, S.-S. Li, X.-M. Li, Y.-B. Fan, Magnesium based degradable biomaterials: A review, Front. Mater. Sci. 8 (2014) 200–218. https://doi.org/10.1007/s11706-014-0253-9.

[159] F. Peng, D. Wang, D. Zhang, B. Yan, H. Cao, Y. Qiao, X. Liu, PEO/Mg–Zn–Al LDH Composite Coating on Mg Alloy as a Zn/Mg Ion-Release Platform with Multifunctions: Enhanced Corrosion Resistance, Osteogenic, and Antibacterial Activities, ACS Biomater. Sci. Eng. 4 (2018) 4112–4121. https://doi.org/10.1021/acsbiomaterials.8b01184.

[160] Y. Xin, T. Hu, P.K. Chu, In vitro studies of biomedical magnesium alloys in a simulated physiological environment:

A review, Acta Biomater. 7 (2011) 1452–1459. https://doi.org/10.1016/j.actbio.2010.12.004.

[161] R. ZENG, J. ZHANG, W. HUANG, W. DIETZEL, K.U. KAINER, C. BLAWERT, W. KE, Review of studies on corrosion of magnesium alloys, Trans. Nonferrous Met. Soc. China. 16 (2006) s763–s771. https://doi.org/10.1016/S1003-6326(06)60297-5.

[162] J.E. Gray-Munro, M. Strong, The mechanism of deposition of calcium phosphate coatings from solution onto magnesium alloy AZ31, J. Biomed. Mater. Res. Part A. 90A (2009) 339–350. https://doi.org/10.1002/jbm.a.32107.

[163] Z. Wen, C. Wu, C. Dai, F. Yang, Corrosion behaviors of Mg and its alloys with different Al contents in a modified simulated body fluid, J. Alloys Compd. 488 (2009) 392–399. https://doi.org/10.1016/j.jallcom.2009.08.147.

[164] D. Mei, S. V. Lamaka, X. Lu, M.L. Zheludkevich, Selecting medium for corrosion testing of bioabsorbable magnesium and other metals – A critical review, Corros. Sci. 171 (2020) 108722. https://doi.org/10.1016/j.corsci.2020.108722.

[165] W.D. Mueller, M. Lucia Nascimento, M.F. Lorenzo De Mele, Critical discussion of the results from different corrosion studies of Mg and Mg alloys for biomaterial applications, Acta Biomater. 6 (2010) 1749–1755. https://doi.org/10.1016/j.actbio.2009.12.048.

[166] C. Schille, M. Braun, H.P. Wendel, L. Scheideler, N. Hort, H.P. Reichel, E. Schweizer, J. Geis-Gerstorfer, Corrosion of experimental magnesium alloys in blood and PBS: A gravimetric and microscopic evaluation, in: Mater. Sci. Eng. B Solid-State Mater. Adv. Technol., Elsevier, 2011: pp. 1797–1801. https://doi.org/10.1016/j.mseb.2011.04.007.

[167] A. Carangelo, A. Acquesta, T. Monetta, Durability of AZ31 magnesium biodegradable alloys polydopamine aided. Part 2: Ageing in Hank's solution, J. Magnes. Alloy. 7 (2019) 218–226. https://doi.org/10.1016/J.JMA.2019.04.003.

[168] V. Wagener, S. Virtanen, Protective layer formation on magnesium in cell culture medium, Mater. Sci. Eng. C. 63 (2016) 341–351. https://doi.org/10.1016/j.msec.2016.03.003.

[169] M. Yazdimamaghani, M. Razavi, D. Vashaee, L. Tayebi, Development and degradation behavior of magnesium scaffolds coated with polycaprolactone for bone tissue engineering, Mater. Lett. 132 (2014) 106–110. https://doi.org/10.1016/j.matlet.2014.06.036.

[170] M.-H.H. Kang, H. Lee, T.-S.S. Jang, Y.-J.J. Seong, H.-E.E. Kim, Y.-H.H. Koh, J. Song, H.-D. Do Jung, Biomimetic porous Mg with tunable mechanical properties and biodegradation rates for bone regeneration, Acta Biomater. 84 (2019) 453–467. https://doi.org/10.1016/j.actbio.2018.11.045.

[171] X. Lu, Y. Leng, Theoretical analysis of calcium phosphate precipitation in simulated body fluid, Biomaterials. 26 (2005) 1097–1108. https://doi.org/10.1016/j.biomaterials.2004.05.034.

[172] H. Zhuang, Y. Han, A. Feng, Preparation, mechanical properties and in vitro biodegradation of porous magnesium scaffolds, Mater. Sci. Eng. C. 28 (2008) 1462–1466. https://doi.org/10.1016/j.msec.2008.04.001.

[173] A.P. Md Saad, R.A. Abdul Rahim, M.N. Harun, H. Basri, J. Abdullah, M.R. Abdul Kadir, A. Syahrom, The influence of flow rates on the dynamic degradation behaviour of porous magnesium under a simulated environment of human cancellous bone, Mater. Des. 122 (2017) 268–279. https://doi.org/10.1016/j.matdes.2017.03.029.

[174] Y. Li, H. Jahr, X.-Y. Zhang, M.A. Leeflang, W. Li, B. Pouran, F.D. Tichelaar, H. Weinans, J. Zhou, A.A. Zadpoor, Biodegradation-affected fatigue behavior of additively manufactured porous magnesium, Addit. Manuf. 28 (2019) 299–311. https://doi.org/10.1016/j.addma.2019.05.013.

[175] W.C. Kim, K.H. Han, J.G. Kim, S.J. Yang, H.K. Seok, H.S. Han, Y.Y. Kim, Effect of surface area on corrosion properties of magnesium for biomaterials, Met. Mater. Int. 19 (2013) 1131–1137. https://doi.org/10.1007/s12540-013-5032-0.

[176] A.P. Md Saad, N. Jasmawati, M.N. Harun, M.R. Abdul Kadir, H. Nur, H. Hermawan, A. Syahrom, Dynamic degradation of porous magnesium under a simulated environment of human cancellous bone, Corros. Sci. 112 (2016) 495–506. https://doi.org/10.1016/j.corsci.2016.08.017.

[177] N.T. Kirkland, N. Birbilis, M.P. Staiger, Assessing the corrosion of biodegradable magnesium implants: A critical review of current methodologies and their limitations, Acta Biomater. 8 (2012) 925–936. https://doi.org/10.1016/j.actbio.2011.11.014.

[178] S. Singh, P. Vashisth, A. Shrivastav, N. Bhatnagar, Synthesis and characterization of a novel open cellular Mg-based scaffold for tissue engineering application, J. Mech. Behav. Biomed. Mater. 94 (2019) 54–62. https://doi.org/10.1016/j.jmbbm.2019.02.010.

[179] W. Yu, H. Zhao, Z. Ding, Z. Zhang, B. Sun, J. Shen, S. Chen, B. Zhang, K. Yang, M. Liu, D. Chen, Y. He, In vitro and in vivo evaluation of MgF2 coated AZ31 magnesium alloy porous scaffolds for bone regeneration, Colloids Surfaces B Biointerfaces. 149 (2017) 330–340. https://doi.org/10.1016/j.colsurfb.2016.10.037.

[180] R.M. Twyman, ATOMIC EMISSION SPECTROMETRY | Principles and Instrumentation, in: Encycl. Anal. Sci., Elsevier, 2005: pp. 190–198. https://doi.org/10.1016/B0-12-369397-7/00029-7.

[181] Z.S.S. Seyedraoufi, S. Mirdamadi, Effects of pulse electrodeposition parameters and alkali treatment on the properties of nano hydroxyapatite coating on porous Mg–Zn scaffold for bone tissue engineering application, Mater. Chem. Phys. 148 (2014) 519–527. https://doi.org/10.1016/j.matchemphys.2014.06.067.

[182] S. Toghyani, M. Khodaei, M. Razavi, Magnesium scaffolds with two novel biomimetic designs and MgF2 coating for bone tissue engineering, Surf. Coatings Technol. 395 (2020) 125929. https://doi.org/10.1016/j.surfcoat.2020.125929.

[183] G. Jiang, G. He, A new approach to the fabrication of porous magnesium with well-controlled 3D pore structure for orthopedic applications, Mater. Sci. Eng. C. 43 (2014) 317–320. https://doi.org/10.1016/j.msec.2014.07.033.

[184] F.-W. Bach, D. Bormann, R. Kucharski, A. Meyer-Lindenberg, Magnesium sponges as a bioabsorbable material – attributes and challenges, Int. J. Mater. Res. 98 (2007) 609–612. https://doi.org/10.3139/146.101514.

[185] S. Jiang, S. Cai, Y. Lin, X. Bao, R. Ling, D. Xie, J. Sun, J. Wei, G. Xu, Effect of alkali/acid pretreatment on the topography and corrosion resistance of as-deposited CaP coating on magnesium alloys, J. Alloys Compd. 793 (2019) 202–211. https://doi.org/10.1016/J.JALLCOM.2019.04.198.

[186] M. Diez, M.H. Kang, S.M. Kim, H.E. Kim, J. Song, Hydroxyapatite (HA)/poly-l-lactic acid (PLLA) dual coating on magnesium alloy under deformation for biomedical applications, J. Mater. Sci. Mater. Med. 27 (2016) 1–9. https://doi.org/10.1007/s10856-015-5643-8.

[187] M.-H. Kang, H.-D. Jung, S.-W. Kim, S.-M. Lee, H.-E. Kim, Y. Estrin, Y.-H. Koh, Production and bio-corrosion resistance of porous magnesium with hydroxyapatite coating for biomedical applications, Mater. Lett. 108 (2013) 122–124. https://doi.org/10.1016/j.matlet.2013.06.096.

[188] G. Barati Darband, M. Aliofkhazraei, P. Hamghalam, N. Valizade, Plasma electrolytic oxidation of magnesium and its alloys: Mechanism, properties and applications, J. Magnes. Alloy. 5 (2017) 74–132. https://doi.org/10.1016/j.jma.2017.02.004.

[189] R. Chaharmahali, A. Fattah-alhosseini, K. Babaei, Surface characterization and corrosion behavior of calcium phosphate (Ca-P) base composite layer on Mg and its alloys using plasma electrolytic oxidation (PEO): A review, J. Magnes. Alloy. (2020). https://doi.org/10.1016/j.jma.2020.07.004.

[190] A. Kopp, T. Derra, M. Müther, L. Jauer, J.H. Schleifenbaum, M. Voshage, O. Jung, R. Smeets, N. Kröger, Influence of design and postprocessing parameters on the degradation behavior and mechanical properties of additively manufactured magnesium scaffolds, Acta Biomater. 98 (2019) 23–35. https://doi.org/10.1016/j.actbio.2019.04.012.

[191] T. Yuan, J. Yu, J. Cao, F. Gao, Y. Zhu, Y. Cheng, W. Cui, Fabrication of a Delaying Biodegradable Magnesium Alloy-Based Esophageal Stent via Coating Elastic Polymer, Materials (Basel). 9 (2016) 384. https://doi.org/10.3390/ma9050384.

[192] P. Shi, B. Niu, S. E, Y. Chen, Q. Li, Preparation and characterization of PLA coating and PLA/MAO composite coatings on AZ31 magnesium alloy for improvement of corrosion resistance, Surf. Coatings Technol. 262 (2015) 26–32. https://doi.org/10.1016/j.surfcoat.2014.11.069.

[193] M. Yazdimamaghani, M. Razavi, D. Vashaee, V.R. Pothineni, S. Assefa, G.A. Köhler, J. Rajadas, L. Tayebi, In vitro analysis of Mg scaffolds coated with polymer/hydrogel/ceramic composite layers, Surf. Coatings Technol. 301 (2016) 126–132. https://doi.org/10.1016/j.surfcoat.2016.01.017.

[194] V.M. Posada, A. Civantos, J. Ramírez, P. Fernández-Morales, J.P. Allain, Tailoring adaptive bioresorbable Mg-based scaffolds with directed plasma nanosynthesis for enhanced osseointegration and tunable resorption, Appl. Surf. Sci. 550 (2021) 149388. https://doi.org/10.1016/j.apsusc.2021.149388.

[195] N. Angrisani, J. Reifenrath, F. Zimmermann, R. Eifler, A. Meyer-Lindenberg, K. Vano-Herrera, C. Vogt, Biocompatibility and degradation of LAE442-based magnesium alloys after implantation of up to 3.5 years in a rabbit model, Acta Biomater. 44 (2016) 355–365. https://doi.org/10.1016/J.ACTBIO.2016.08.002.

[196] G. Song, A. Atrens, D. StJohn, An Hydrogen Evolution Method for the Estimation of the Corrosion Rate of Magnesium Alloys, Magnes. Technol. 2001. (2013) 254–262. https://doi.org/10.1002/9781118805497.ch44.

[197] H. Saleh, T. Weling, J. Seidel, M. Schmidtchen, R. Kawalla, F.O.R.L. Mertens, H.-P. Vogt, An XPS Study of Native Oxide and Isothermal Oxidation Kinetics at 300 °C of AZ31 Twin Roll Cast Magnesium Alloy, Oxid. Met. 81 (2014) 529–548. https://doi.org/10.1007/s11085-013-9466-z.

[198] G. Wu, K. Dash, M.L. Galano, K.A.Q. O'Reilly, Oxidation studies of Al alloys: Part II Al-Mg alloy, Corros. Sci. 155 (2019) 97–108. https://doi.org/10.1016/j.corsci.2019.04.018.

[199] B. Wang, P. Huang, C. Ou, K. Li, B. Yan, W. Lu, In Vitro Corrosion and Cytocompatibility of ZK60 Magnesium Alloy Coated with Hydroxyapatite by a Simple Chemical Conversion Process for Orthopedic Applications, Int. J. Mol. Sci. 14 (2013) 23614–23628. https://doi.org/10.3390/ijms141223614.

[200] A. Gökhan Demir, V. Furlan, N. Lecis, B. Previtali, Laser surface structuring of AZ31 Mg alloy for controlled wettability, Biointerphases. 9 (2014) 029009. https://doi.org/10.1116/1.4868240.

[201] Ri-Sheng Li, Influence of bombardment-induced Gibbsian segregation on alloy sputtering, Nucl. Instruments Methods Phys. Res. Sect. B Beam Interact. with Mater. Atoms. 82 (1993) 283–290. https://doi.org/10.1016/0168-583X(93)96030-G.

[202] S. Mathieu, C. Rapin, J. Hazan, P. Steinmetz, Corrosion behaviour of high pressure die-cast and semi-solid cast AZ91D alloys, Corros. Sci. 44 (2002) 2737–2756. https://doi.org/10.1016/S0010-938X(02)00075-6.

[203] B. Gao, S. Hao, J. Zou, T. Grosdidier, L. Jiang, J. Zhou, C. Dong, High current pulsed electron beam treatment of AZ31 Mg alloy, J. Vac. Sci. Technol. A Vacuum, Surfaces, Film. 23 (2005) 1548–1553. https://doi.org/10.1116/1.2049299.

[204] G. Bo, H. Yi, Z. Wenfeng, T. Ganfeng, Surface Modification of Mg Alloys AZ31 and ZK60-1Y by High Current Pulsed Electron Beam, Spec. Issues Magnes. Alloy. (2011). https://doi.org/10.5772/16808.

[205] G.T. Bo Gao a, Shengzhi Hao, Jianxin Zou, Wenyuan Wu, C.D. B, Effect of high current pulsed electron beam treatment on surface microstructure and wear and corrosion resistance of an AZ91HP magnesium alloy, Surf. Coatings Technol. 201 (2007) 6297–6303. https://doi.org/10.1016/J.SURFCOAT.2006.11.036.

[206] X. Zhang, K. Zhang, J. Zou, P. Yan, L. Song, Y. Liu, Surface microstructure modifications and in-vitro corrosion resistance improvement of a WE43 Mg alloy treated by pulsed electron beams, Vacuum. 173 (2020) 109132. https://doi.org/10.1016/j.vacuum.2019.109132.

[207] S. Feliu, A. Pardo, M.C. Merino, A.E. Coy, F. Viejo, R. Arrabal, Correlation between the surface chemistry and the atmospheric corrosion of AZ31, AZ80 and AZ91D magnesium alloys, Appl. Surf. Sci. 255 (2009) 4102–4108. https://doi.org/10.1016/J.APSUSC.2008.10.095.

[208] W.J.E.M. Habraken, J. Tao, L.J. Brylka, H. Friedrich, L. Bertinetti, A.S. Schenk, A. Verch, V. Dmitrovic, P.H.H. Bomans, P.M. Frederik, J. Laven, P. van der Schoot, B. Aichmayer, G. de With, J.J. DeYoreo, N.A.J.M. Sommerdijk, Ion-association complexes unite classical and non-classical theories for the biomimetic nucleation of calcium phosphate, Nat. Commun. 4 (2013) 1507. https://doi.org/10.1038/ncomms2490.

[209] G.S. Frankel, A. Samaniego, N. Birbilis, Evolution of hydrogen at dissolving magnesium surfaces, Corros. Sci. 70 (2013) 104–111. https://doi.org/10.1016/J.CORSCI.2013.01.017.

[210] F. Barrere, C.. van Blitterswijk, K. de Groot, P. Layrolle, Nucleation of biomimetic Ca–P coatings on Ti6Al4V from a SBF×5 solution: influence of magnesium, Biomaterials. 23 (2002) 2211–2220. https://doi.org/10.1016/S0142-9612(01)00354-4.

[211] M. Tomozawa, S. Hiromoto, Growth mechanism of hydroxyapatite-coatings formed on pure magnesium and corrosion behavior of the coated magnesium, Appl. Surf. Sci. 257 (2011) 8253–8257. https://doi.org/10.1016/j.apsusc.2011.04.087.

[212] S. Feliu, I. Llorente, Corrosion product layers on magnesium alloys AZ31 and AZ61: Surface chemistry and protective ability, Appl. Surf. Sci. 347 (2015) 736–746. https://doi.org/10.1016/J.APSUSC.2015.04.189.

[213] Y.F. Zhang, B. Hinton, G. Wallace, X. Liu, M. Forsyth, On corrosion behaviour of magnesium alloy AZ31 in simulated body fluids and influence of ionic liquid pretreatments, Corros. Eng. Sci. Technol. 47 (2012) 374–382. https://doi.org/10.1179/1743278212Y.0000000032.

[214] T.L. Nguyen, A. Blanquet, M.P. Staiger, G.J. Dias, T.B.F. Woodfield, On the role of surface roughness in the corrosion of pure magnesium in vitro, J. Biomed. Mater. Res. - Part B Appl. Biomater. 100 (2012) 1310–1318. https://doi.org/10.1002/jbm.b.32697.

[215] R.B. Alvarez, H.J. Martin, M.F. Horstemeyer, M.Q. Chandler, N. Williams, P.T. Wang, A. Ruiz, Corrosion relationships as a function of time and surface roughness on a structural AE44 magnesium alloy, Corros. Sci. 52 (2010) 1635–1648. https://doi.org/10.1016/j.corsci.2010.01.018.

[216] A.F. Cipriano, A. Sallee, R.-G.G. Guan, Z.-Y.Y. Zhao, M. Tayoba, J. Sanchez, H. Liu, Investigation of magnesium–zinc–calcium alloys and bone marrow derived mesenchymal stem cell response in direct culture, Acta Biomater. 12 (2015) 298–321. https://doi.org/10.1016/j.actbio.2014.10.018.

[217] J. Fischer, M.H. Prosenc, M. Wolff, N. Hort, R. Willumeit, F. Feyerabend, Interference of magnesium corrosion with tetrazolium-based cytotoxicity assays☆, Acta Biomater. 6 (2010) 1813–1823. https://doi.org/10.1016/j.actbio.2009.10.020.

[218] A. Burmester, R. Willumeit-Römer, F. Feyerabend, R. Willumeit-Römer, F. Feyerabend, Behavior of bone cells in contact with magnesium implant material, J. Biomed. Mater. Res. - Part B Appl. Biomater. 105 (2017) 165–179. https://doi.org/10.1002/jbm.b.33542.

[219] R. Xin, B. Li, L. Li, Q. Liu, Influence of texture on corrosion rate of AZ31 Mg alloy in 3.5 wt.% NaCl, Mater. Des. 32 (2011) 4548–4552. https://doi.org/10.1016/J.MATDES.2011.04.031.

[220] J. Fischer, D. Pröfrock, N. Hort, R. Willumeit, F. Feyerabend, Improved cytotoxicity testing of magnesium materials, Mater. Sci. Eng. B Solid-State Mater. Adv. Technol. 176 (2011) 830–834. https://doi.org/10.1016/j.mseb.2011.04.008.

[221] D.-T. Chou, D. Hong, P. Saha, J. Ferrero, B. Lee, Z. Tan, Z. Dong, P.N. Kumta, In vitro and in vivo corrosion, cytocompatibility and mechanical properties of biodegradable Mg–Y–Ca–Zr alloys as implant materials, Acta Biomater. 9 (2013) 8518–8533. https://doi.org/10.1016/j.actbio.2013.06.025.

[222] R. Willumeit, A. Möhring, F. Feyerabend, Optimization of Cell Adhesion on Mg Based Implant Materials by Pre-Incubation under Cell Culture Conditions, Int. J. Mol. Sci. 15 (2014) 7639–7650. https://doi.org/10.3390/ijms15057639.

[223] E. Ferna Â Ndez, F.J. Gil, M.P. Ginebra, F.C.M. Driessens, J.A. Planell, S.M. Best, Calcium phosphate bone cements for clinical applications Part II: Precipitate formation during setting reactions, J. Mater. Sci. Mater. Med. 10 (1999) 177–183. https://doi.org/10.1023/A:1008989525461.

[224] M. Gawlik, B. Wiese, V. Desharnais, T. Ebel, R. Willumeit-Römer, M.M. Gawlik, B. Wiese, V. Desharnais, T. Ebel, R. Willumeit-Römer, The Effect of Surface Treatments on the Degradation of Biomedical Mg Alloys—A Review Paper, Materials (Basel). 11 (2018) 2561. https://doi.org/10.3390/ma11122561.

[225] X. Zhang, G. Wu, X. Peng, L. Li, H. Feng, B. Gao, K. Huo, P.K. Chu, Mitigation of Corrosion on Magnesium Alloy by Predesigned Surface Corrosion, Sci. Rep. 5 (2015) 17399. https://doi.org/10.1038/srep17399.

[226] K. DAS, S. BOSE, A. BANDYOPADHYAY, Surface modifications and cell–materials interactions with anodized Ti, Acta Biomater. 3 (2007) 573–585. https://doi.org/10.1016/j.actbio.2006.12.003.

[227] A. Pardo, M.C. Merino, A.E. Coy, R. Arrabal, F. Viejo, E. Matykina, Corrosion behaviour of magnesium/aluminium alloys in 3.5 wt.% NaCl, Corros. Sci. 50 (2008) 823–834. https://doi.org/10.1016/j.corsci.2007.11.005.

[228] B. Carlson, J. Jones, The Metallurgical Aspects of the Corrosion Behaviour of Cast Mg--Al Alloys, Light Met. Process. Appl. (1993) 833–847.

[229] Y. Lu, P. Wan, B. Zhang, L. Tan, K. Yang, J. Lin, Research on the corrosion resistance and formation of double-layer calcium phosphate coating on AZ31 obtained at varied temperatures, Mater. Sci. Eng. C. 43 (2014) 264–271. https://doi.org/10.1016/j.msec.2014.06.039.

[230] S.-H. Kwon, T.-J. Lee, J. Park, J.-E. Hwang, M. Jin, H.-K. Jang, N.S. Hwang, B.-S. Kim, Modulation of BMP-2-

induced chondrogenic versus osteogenic differentiation of human mesenchymal stem cells by cell-specific extracellular matrices, Tissue Eng. Part A. 19 (2013) 49–58. https://doi.org/10.1089/ten.TEA.2012.0245.

[231] F. Geng, L.L. Tan, X.X. Jin, J.Y. Yang, K. Yang, The preparation, cytocompatibility, and in vitro biodegradation study of pure β-TCP on magnesium, J. Mater. Sci. Mater. Med. 20 (2009) 1149–1157. https://doi.org/10.1007/s10856-008-3669-x.

[232] R. Harrison, D. Maradze, S. Lyons, Y. Zheng, Y. Liu, Corrosion of magnesium and magnesium–calcium alloy in biologically-simulated environment, Prog. Nat. Sci. Mater. Int. 24 (2014) 539–546. https://doi.org/10.1016/J.PNSC.2014.08.010.

[233] N.A. Agha, R. Willumeit-Römer, D. Laipple, B. Luthringer, F. Feyerabend, The Degradation Interface of Magnesium Based Alloys in Direct Contact with Human Primary Osteoblast Cells, PLoS One. 11 (2016) e0157874. https://doi.org/10.1371/journal.pone.0157874.

[234] A. Yamamoto, S. Hiromoto, Effect of inorganic salts, amino acids and proteins on the degradation of pure magnesium in vitro, Mater. Sci. Eng. C. 29 (2009) 1559–1568. https://doi.org/10.1016/j.msec.2008.12.015.

[235] F. Seuss, S. Seuss, M.C. Turhan, B. Fabry, S. Virtanen, Corrosion of Mg alloy AZ91D in the presence of living cells, J. Biomed. Mater. Res. - Part B Appl. Biomater. 99B (2011) 276–281. https://doi.org/10.1002/jbm.b.31896.

[236] S. Yoshizawa, A. Brown, A. Barchowsky, C. Sfeir, Magnesium ion stimulation of bone marrow stromal cells enhances osteogenic activity, simulating the effect of magnesium alloy degradation, Acta Biomater. 10 (2014) 2834–2842. https://doi.org/10.1016/j.actbio.2014.02.002.

[237] R.W. Li, N.T. Kirkland, J. Truong, J. Wang, P.N. Smith, N. Birbilis, D.R. Nisbet, The influence of biodegradable magnesium alloys on the osteogenic differentiation of human mesenchymal stem cells, J. Biomed. Mater. Res. Part A. 102 (2014) n/a-n/a. https://doi.org/10.1002/jbm.a.35111.

[238] W. Huang, B. Carlsen, G. Rudkin, M. Berry, K. Ishida, D.T. Yamaguchi, T.A. Miller, Osteopontin is a negative regulator of proliferation and differentiation in MC3T3-E1 pre-osteoblastic cells, Bone. 34 (2004) 799–808. https://doi.org/10.1016/j.bone.2003.11.027.

[239] J.-A. Kim, J. Lim, R. Naren, H. Yun, E.K. Park, Effect of the biodegradation rate controlled by pore structures in magnesium phosphate ceramic scaffolds on bone tissue regeneration in vivo, Acta Biomater. 44 (2016) 155–167. https://doi.org/10.1016/j.actbio.2016.08.039.

[240] M. Bessa-Gonçalves, A.M. Silva, J.P. Brás, H. Helmholz, B.J.C. Luthringer-Feyerabend, R. Willumeit-Römer, M.A. Barbosa, S.G. Santos, Fibrinogen and magnesium combination biomaterials modulate macrophage phenotype, NF-kB signaling and crosstalk with mesenchymal stem/stromal cells, Acta Biomater. 114 (2020) 471–484. https://doi.org/10.1016/j.actbio.2020.07.028.

[241] F. Alvarez, R.M. Lozano Puerto, B. Pérez-Maceda, C.A. Grillo, M. Fernández Lorenzo de Mele, Time-Lapse Evaluation of Interactions Between Biodegradable Mg Particles and Cells, Microsc. Microanal. 22 (2016) 1–12. https://doi.org/10.1017/S1431927615015597.

[242] A. Mantovani, S.K. Biswas, M.R. Galdiero, A. Sica, M. Locati, Macrophage plasticity and polarization in tissue repair and remodelling, J. Pathol. 229 (2013) 176–185. https://doi.org/10.1002/path.4133.

[243] G.E. Glass, J.K. Chan, A. Freidin, M. Feldmann, N.J. Horwood, J. Nanchahal, TNF- promotes fracture repair by augmenting the recruitment and differentiation of muscle-derived stromal cells, Proc. Natl. Acad. Sci. 108 (2011) 1585–1590. https://doi.org/10.1073/pnas.1018501108.

[244] W.L. Chan, E. Chason, Making waves: Kinetic processes controlling surface evolution during low energy ion sputtering, J. Appl. Phys. 101 (2007) 121301. https://doi.org/10.1063/1.2749198.

[245] O.D. Acevedo Rueda, Desarrollo de un metal celular ordenado con recubrimiento continuo como alternativa aplicable a elementos de fijación ósea, Universidad Nacional de Colombia , 2019. http://bdigital.unal.edu.co/75011/ (accessed October 5, 2020).

[246] M. Doube, M.M. Kłosowski, I. Arganda-Carreras, F.P. Cordelières, R.P. Dougherty, J.S. Jackson, B. Schmid, J.R. Hutchinson, S.J. Shefelbine, BoneJ: Free and extensible bone image analysis in ImageJ, Bone. 47 (2010) 1076–1079. https://doi.org/10.1016/J.BONE.2010.08.023.

[247] C. Colosi, M. Costantini, A. Barbetta, R. Pecci, R. Bedini, M. Dentini, Morphological Comparison of PVA Scaffolds Obtained by Gas Foaming and Microfluidic Foaming Techniques, Langmuir. 29 (2013) 82–91. https://doi.org/10.1021/la303788z.

[248] L. Wu, F. Pan, M. Yang, R. Cheng, An investigation of second phases in as-cast AZ31 magnesium alloys with different Sr contents, J. Mater. Sci. 48 (2013) 5456–5469. https://doi.org/10.1007/s10853-013-7339-0.

[249] J. Tao, Y. Zhang, F. Fan, Q. Chen, Microstructural Evolution and Mechanical Properties of AZ31 Magnesium Alloy Prepared by Casting-solid Extrusion Forging During Partial Remelting, Def. Technol. 9 (2013) 146–152. https://doi.org/10.1016/j.dt.2013.09.013.

[250] L. Bourgeois, B.C. Muddle, J.F. Nie, The crystal structure of the equilibrium Φ phase in Mg-Zn-Al casting alloys, Acta Mater. 49 (2001) 2701–2711. https://doi.org/10.1016/S1359-6454(01)00162-8.

[251] Michael Ashby, Tony Evans, NA Fleck, J.W. Hutchinson, H.N.G. Wadley, L. J. Gibson, Properties of metal foams, in: Met. Foam. A Des. Guid., Elsevier, 2000: pp. 42–48.

[252] X.N. Gu, W.R. Zhou, Y.F. Zheng, Y. Cheng, S.C. Wei, S.P. Zhong, T.F. Xi, L.J. Chen, Corrosion fatigue behaviors of two biomedical Mg alloys - AZ91D and WE43 - In simulated body fluid, Acta Biomater. 6 (2010) 4605–4613. https://doi.org/10.1016/j.actbio.2010.07.026.

[253] C. Miura, Y. Shimizu, Y. Imai, T. Mukai, A. Yamamoto, Y. Sano, N. Ikeo, S. Isozaki, T. Takahashi, M. Oikawa, H. Kumamoto, M. Tachi, *In vivo* corrosion behaviour of magnesium alloy in association with surrounding tissue response in rats, Biomed. Mater. 11 (2016) 025001. https://doi.org/10.1088/1748-6041/11/2/025001.

[254] Y. Jang, B. Collins, J. Sankar, Y. Yun, Effect of biologically relevant ions on the corrosion products formed on alloy AZ31B: An improved understanding of magnesium corrosion, Acta Biomater. 9 (2013) 8761–8770. https://doi.org/10.1016/j.actbio.2013.03.026.

[255] F. Tamimi, Z. Sheikh, J. Barralet, Dicalcium phosphate cements: Brushite and monetite, Acta Biomater. 8 (2012) 474–487. https://doi.org/10.1016/j.actbio.2011.08.005.

[256] F. Witte, N. Hort, C. Vogt, S. Cohen, K.U. Kainer, R. Willumeit, F. Feyerabend, Degradable biomaterials based on magnesium corrosion, Curr. Opin. Solid State Mater. Sci. 12 (2008) 63–72. https://doi.org/10.1016/j.cossms.2009.04.001.

[257] F. Witte, J. Fischer, J. Nellesen, H.-A. Crostack, V. Kaese, A. Pisch, F. Beckmann, H. Windhagen, In vitro and in vivo corrosion measurements of magnesium alloys, Biomaterials. 27 (2006) 1013–1018. https://doi.org/10.1016/j.biomaterials.2005.07.037.

[258] D. Zhao, T. Wang, W. Hoagland, D. Benson, Z. Dong, S. Chen, D.-T. Chou, D. Hong, J. Wu, P.N. Kumta, W.R. Heineman, Visual H2 sensor for monitoring biodegradation of magnesium implants in vivo, Acta Biomater. 45 (2016) 399–409. https://doi.org/10.1016/J.ACTBIO.2016.08.049.

[259] N.I. Zainal Abidin, B. Rolfe, H. Owen, J. Malisano, D. Martin, J. Hofstetter, P.J. Uggowitzer, A. Atrens, The in vivo and in vitro corrosion of high-purity magnesium and magnesium alloys WZ21 and AZ91, Corros. Sci. 75 (2013) 354–366. https://doi.org/10.1016/J.CORSCI.2013.06.019.

[260] J. Wang, L. Cui, Y. Ren, Y. Zou, J. Ma, C. Wang, Z. Zheng, X. Chen, R. Zeng, Y. Zheng, In vitro and in vivo biodegradation and biocompatibility of an MMT/BSA composite coating upon magnesium alloy AZ31, J. Mater. Sci. Technol. 47 (2020) 52–67. https://doi.org/10.1016/j.jmst.2020.02.006.

[261] I. Heinonen, J. Kemppainen, K. Kaskinoro, H. Langberg, J. Knuuti, R. Boushel, M. Kjaer, K.K. Kalliokoski, Bone blood flow and metabolism in humans: Effect of muscular exercise and other physiological perturbations, J. Bone Miner. Res. 28 (2013) 1068–1074. https://doi.org/10.1002/jbmr.1833.

[262] J. Walker, S. Shadanbaz, N.T. Kirkland, E. Stace, T. Woodfield, M.P. Staiger, G.J. Dias, Magnesium alloys: Predicting in vivo corrosion with in vitro immersion testing, J. Biomed. Mater. Res. - Part B Appl. Biomater. 100 B (2012) 1134–1141. https://doi.org/10.1002/jbm.b.32680.

[263] S.E. Harandi, P.C. Banerjee, C.D. Easton, R.K. Singh Raman, Influence of bovine serum albumin in Hanks' solution on the corrosion and stress corrosion cracking of a magnesium alloy, Mater. Sci. Eng. C. 80 (2017) 335–345. https://doi.org/10.1016/j.msec.2017.06.002.

[264] M.F. Ulum, W. Caesarendra, R. Alavi, H. Hermawan, M.F. Ulum, W. Caesarendra, R. Alavi, H. Hermawan, In-Vivo Corrosion Characterization and Assessment of Absorbable Metal Implants, Coatings. 9 (2019) 282. https://doi.org/10.3390/coatings9050282.

[265] H. Wu, C. Zhang, T. Lou, B. Chen, R. Yi, W. Wang, R. Zhang, M. Zuo, H. Xu, P. Han, S. Zhang, J. Ni, X. Zhang, Crevice corrosion – A newly observed mechanism of degradation in biomedical magnesium, Acta Biomater. 98 (2019) 152–159. https://doi.org/10.1016/j.actbio.2019.06.013.